# Coastal fracture systems: The relationship between tectonic activity, stratigraphy and the relative timing of fracture formation along the eastern Otway coastline, Victoria

by

**Joel L. Vergunst**

B. Sci (Hons)

A thesis submitted for the degree of

**Masters of Science**

Main supervisor: Professor Mike Hall

Associated supervisor: Professor Alexander Cruden

*School of Earth, Atmosphere and Environment*

*Monash University, Clayton, Victoria, Australia, 3800*

MONASH University

# Copyright Notice

© Joel L. Vergunst (2017). Except as provided in the Copyright Act 1968, this thesis may not be reproduced in any form without the written permission of the author.

# Declaration

I hereby declare that this thesis contains no material which has been accepted for the award of any other degree or diploma at any university or equivalent institution and that, to the best of my knowledge and belief, this thesis contains no material previously published or written by another person, except where due reference is made in the text of the thesis.

This thesis includes three unpublished chapters. The core theme of this thesis is to compare fracture orientations at different stratigraphic depths and structural positions along the Otway coastline, in order to determine the influence that lithology, burial depth and varying tectonic stress conditions have had on the formation of the coastal fracture systems.

The ideas, development and writing up of all the chapters in the thesis were the principal responsibility of myself, the candidate, working within the School of Earth, Atmosphere and Environment under the supervision of Professor Mike Hall and Professor Alexander Cruden.

In the case of Chapters 1, 2 and 3, my contribution to the work involved the following:

| Thesis chapter | Chapter title | Nature and extent (%) of student contribution | Coauthers name(s). Nature and extent (%) of contribution |
|---|---|---|---|
| **1** | An Introduction to the Regional Geology of the eastern Otway Basin | Main research, fieldwork, data analysis and interpretation 80% | Mike Hall, supervisory role 10%<br>Alexander Cruden, supervisory role 10% |
| **2** | Influence of stratigraphic and structual position on the timing and characteristics of fractures along the eastern Otway coastline, Great Ocean Road, Victoria | Main research, fieldwork, data analysis and interpretation 65% | Mike Hall, supervisory role 10%<br>Alexander Cruden, supervisory role 10%<br>Stefan Vollgger, UAV pilot, significant contributions to section 2.3.2. Construction of 2D orthophotographs 15% |
| **3** | Synthesis: Implications for fold-fracture conceptual models | Main research, fieldwork, data analysis and interpretation 80% | Mike Hall, supervisory role 10%<br>Alexander Cruden, supervisory role 10% |

Student signature: [redacted] Date: 05/08/2017

The undersigned hereby certify that the above declaration correctly reflects the nature and extent of the student and co-authors' contributions to this work.

Main Supervisor signature: [redacted] Date: 05/08/2017

# Table of Contents


**1. Chapter 1** **1**

1.1 Project outline/Introduction: . . . 3

1.2 Geological and tectonic setting: . . . 4

1.3 Methods: . . . 8

1.3.1 Fieldwork: Coastal Exposures . . . 8

1.3.2 Airborne Radiometric data: . . . 8

1.4 Lithostratigraphy . . . 10

1.4.1 Eumeralla Formation (Artillery Rocks to Eastern View) . . . 10

1.4.2 Eastern View Formation/ Lower Demons Bluff Group . . . 11

1.4.3 Anglesea Formation . . . 12

1.4.4 Angahook Formation (Aireys Inlet to Anglesea) . . . 14

1.4.5 Torquay Group . . . 16

1.4.6 Stratigraphic correlations . . . 17

1.5 Structural geology: Key localities for structural study . . . 18

1.5.1 Older sequence (Eumeralla Formation) . . . 18

1.5.2 Mount Defiance Anticline . . . 18

1.5.3 Devils Elbow (Eastern View coastal platforms) . . . 21

1.5.4 Younger sequence (Cenozoic sedimentary rocks) . . . 24

1.5.5 Angahook Formation . . . 25

1.6 Discussion . . . 28

1.6.1 Structural trends within the Cretaceous sedimentary rocks . . . 28

1.6.2 Structural trends within the Cenozoic sedimentary rocks . . . 28

1.7 Conclusions . . . 32

**2. Chapter 2** **37**

2.1 Introduction . . . 39

2.2 Sedimentological history . . . 41

2.2.1 Eumeralla Formation (St. George Anticline/ Artillery Rocks) . . . 41

2.2.2 Angahook Formation (Soapy Rocks) . . . 42

2.3 Methods . . . 43
2.3.1 Fracture network analysis . . . 43
2.3.2 Unmanned Aerial Vehicle (UAV) photogrammetry . . . 45
2.4 Structural observations . . . 49
2.4.1 Eumeralla Formation: The St. George Anticline/ Artillery Rocks . . . 49
2.4.2 Angahook Formation: Soapy Rocks . . . 63
2.5 Discussion and interpretations: . . . 66
2.5.1 Analysis of fracture formation . . . 66
2.5.2 Fracture formation during uplift (unloading joints) . . . 66
2.5.3 Interpreted tectonic history of the eastern Otway coastline fracture systems . . . 73
2.5.4 Eumeralla Formation . . . 73
2.5.5 Soapy Rocks (Demons Bluff Group) . . . 76
2.6 Conclusions . . . 78
**3. Chapter 3** **83**
3.1 Introduction . . . 85
3.2 Discussion: Controls on fracture formation . . . 85
3.2.1 Pre-folding fracture formation . . . 86
3.2.2 Syn-folding fracture growth . . . 87
3.2.3 Fracture formation during uplift . . . 88
3.2.4 Post-folding fracture formation . . . 91
3.3 Conclusions . . . 92
**References** **95**
**Appendix 1** **105**
Summary of data collected
**Appendix 2** **123**
Sedimentary stratigraphic columns and bathymetry summary
**Appendix 3** **141**
Summary of fracture interactions and spacing data
**Appendix 4** **167**
Interpreted deformation history of the eastern Otway coastline
**Map Pocket 1** **171**

# List of Figures

## Chapter 1

**Figure 1.1:** Location of the study area (northern Anglesea to southern Lorne) eastern Otway Basin, modified after Holford et al. (2011) & Duddy (2010). Shaded areas represent the extent of the onshore mid Cretaceous uplift, eastern Otway Basin. Offshore inverted normal faults (red) are based on seismic interpretation and cross-sections (purple line) by Matthews (2015). The Victorian extension of the Penola Trough (PT) is based on interpretations made by Boult et al. (2008). . . . . .5

**Figure 1.2:** Geological map showing the stratigraphic units within the field area (onshore eastern Otway Basin). The general stratigraphy of the onshore eastern Otway Basin is provided in the lower right, modified from Abele et al. (1988) & McLaren et al. (2009), with a more comprehensive tectonostratigraphic column provided within Krassay *et al* (2004). The older and younger stratigraphic units of this study are separated by the indicated regional unconformity. The key locations identified within this study are each indicated with a gold star. . . . . .6

**Figure 1.3:** A restored cross section that highlights the temporal evolution of the basin fill (VE = 2) modified from the restored cross-section of (Matthews 2015) and based on seismic line OGF92A-411 collected by Gas and Fuel Exploration N.L. (1992). (A) Early Cretaceous (~113-100 Ma) NW-SE extension. (B) Mid Cretaceous (c. 97-92Ma) NW-SE shortening, erosion and gentle folding. (C) Late Cretaceous (c. 95Ma - ~70Ma) NE-SW extension. (D) Late Cretaceous - mid Cenozoic transgressive sequence. (E) Middle - late Cenozoic (c. 20-0 Ma) NW-SE regional shortening, with forced folding above reactivated faults, centred on the Otway Ranges. (F) Cenozoic erosion. . . . . .7

**Figure 1.4:** (A) airborne radiometric data (GDA94mga54_50m) (B) SRTM digital elevation data with applied 45° shaded relief (1arc_S39_e143/144) from USGS (EarthExplorer) (C) Combined data and interpreted stratigraphic boundary indicated (yellow dotted line), separating the older sediments (K-dominant) from the younger sediments (U/Th-dominant). Painkalac dam is indicated with a gold star. . . . . .9

**Figure 1.5:** Inland exposure of the stratigraphic boundary (southern section) between weathered, light-brown to grey, volcanic sandstone (with nodules and rip-up clasts) of the Eumeralla Formation (lower left), and overlying light brown sandstone of the Eastern View Formation (upper right), northeast of Painkalac Dam (55H 0244145E 5741164N WGS84). . . . . .9

**Figure 1.6:** Partially weathered volcaniclastic sandstone (Eumeralla Formation), northern Lorne coastal cliff exposure (55H 0239165E 5734390N). . . . . 10

**Figure 1.7:** (A) Fluvial silts and sands of the Eastern View Formation, exposed within Coalmine Creek, Eastern View (55H 0242170E 5737754N) WGS84. (B) Duffs Quarry, arkosic sandstone, Boonah Formation (55H 0244151E 5742058N) WGS84. Note the quarry face is ~6 m high, with the photo looking towards the SE. . . . . 11

**Figure 1.8:** Sulphur-rich black sandstone of the lower Anglesea Member, with overlying buff-white fine sands of the upper Anglesea Member, and separated by a disconformity (arrow), northeast of Anglesea (55H 0255172E 5745125N) WGS84. . . . . 12

**Figure 1.9:** Subvertical fracturing within sub-horizontally bedded Anglesea Formation (55H 0260439E 5748269N). . . . . 13

**Figure 1.10:** Jarosite alteration (yellow) of burrows? within the grey-white pyritic siltstone (upper Anglesea Formation) (55H 0254263E 5744344N) +/- 3m WGS84. . . . . 13

**Figure 1.11:** (A) Aireys Inlet coastal cliff exposure, with iron-rich alteration (red arrow) between the uppermost section of the Angahook Formation and overlying brown silts (55H 0248463E;

5739427N) WGS84. (B) Loamy siltstone with Liesegang rings (Angahook Formation) observed ~500 m south of Soapy Rocks (55H 0253758E 5743589N) WGS84. . . . . 15

**Figure 1.12:** Demons Bluff Group and overlying Torquay Group, Point Addis Limestone (55H 0259930E 5747276N). Included is a lower hemisphere equal area stereographic projection (stereonet) of poles (with corresponding 1% area contours) to bedding of the Point Addis Limestone. The stereonet shows gentle folding within the Torquay Group. . . . . 16

**Figure 1.13:** Stratigraphic correlation diagrams, illustrating interpreted unit correlations along coastal cliff exposures between (A) Split Point and Urquharts Bluff (Aireys Inlet) and (B) Point Roadknight and northern Addiscot Beach (Anglesea), with the datum correlated to sea level. Locations of the stratigraphic sections are additionally indicated with gold stars on the accompanying map (Map Pocket 2). For greater resolution of stratigraphic logs see Appendix 2.. . . . . 17

**Figure 1.14:** Interpretation of the major structural trends between Lorne and Eastern View based on field measurements listed in Appendix 1. The southern coastal and inland areas are dominated by NE-trending anticlines and synclines, with overprinting ~NW-oriented sinistral faults. Additionally shown are interpreted NE-oriented inverted normal faults. The area shown on the map is underlain by the Eumeralla Formation. For greater resolution of interpreted structural map see Map Pocket 2. . . . . 19

**Figure 1.15:** Geological map of coastal platforms and road outcrop along Mt. Defiance (south of Cumberland River). Inset lower hemisphere equal area stereographic projection (stereonet) plots poles to measured bedding and corresponding 1% area contours. A cross section of the hinge of the Mt. Defiance Anticline is shown for a section cropping out along the road, after (Vergunst, 2012) with location on the map indicated by a blue (dashed) line. Within the cross section black lines indicate bedding, yellow lines indicate major calcite veins and red lines indicate thrust faults. For increased resolution see Map Pocket 1.. . . . . 20

**Figure 1.16:** (A) The Mt. Defiance fold hinge (dashed arrow) showing ~6m structural offset (54H 0755946E 5725366N) WGS84, with fault shown in red, person for scale. Photo taken along the coastal platforms at the SW end of Figure 1.15. (B) Sinistral offset of sandstone injection structure (54H 0756642E 5725757N) WGS84. . . . . 21

**Figure 1.17:** (A) Geological map of coastal platforms below Devils Elbow with an included lower hemisphere equal area stereographic projection (stereonet) of poles (with corresponding 1% area contours) to measured bedding. For greater resolution see Map Pocket 1. (B) Sedimentary stratigraphic column based on indicated location along the Devils Elbow coastal platforms. For greater resolution of stratigraphic logs see Appendix 2. . . . . 22

**Figure 1.18:** (A) Sinistral fault (150/90) offsetting interbedded volcaniclastic sandstones and mudstones within the Demons Bluff coastal platforms (55H 0241227E 5736871N). Note the compass for scale. (B) Brecciated material with vuggy calcite veins (55H 0241076E 5736306N). Notebook for scale.. . . . . 23

**Figure 1.19:** Interpretation of the major structural and lithological trends between Aireys Inlet and Anglesea based on field measurements. A structural contour map of the top surface of coal seam A depth is shown for the inland Anglesea area, modified after Smith (1998), with inland boundaries of stratigraphic units modified from Abele (1979). Note markers A-E and A′- E′ oriented ~parallel to the coastline, defining the location the cross-sections provided in Map Pocket 2. Included are lower hemisphere equal area stereographic projections (stereonet) of poles (with corresponding 1% area contours) to bedding measured by traditional mapping within (a) The Scrubby Hills Anticline, and (b) The Bald Hills Anticline (Addiscot Beach). Key locations referred to in this study are each indicated with a gold star. For greater resolution of interpreted structural map see Map Pocket 2. . . . . 24

**Figure 1.20:** (A) East-west oriented photo of coarse-grained basaltic tuff (Angahook Formation, Demons Bluff Group), with a cream-coloured surficial coating derived from the overlaying bioclastic grainstone (Torquay Group) (55H 0248437E; 5739732N). Two reverse faults (094/40N and 124/ 59SSW) offset bedding. Note the yellow notebook and hammer for scale (red arrow). (B) Green smectite vein with inclusions of pearl-green altered basalt (55H 0248431E 5739746N). Note the hammer for scale. . . . . 25

**Figure 1.21:** (A) Geologic map of Urquharts Bluff (Aireys Inlet) indicating the transport direction of the volcaniclastic flow (Demons Bluff Group, Angahook Formation) (55H 0249463E; 5741586N). (B) Weathered loamy siltstone slump structures and (A) Slump structures offset by sub-vertical fractures with sinistral strike separation.. . . . . 26

**Figure 1.22:** Thrust fault (55H 0253761E 5743604N) WGS84. (A) drag folding of the upper beds (arrow) in the hanging wall against the fault surface (red-dashed line). (B) drag folding of the lower beds in the footwall. Photograph oriented ~west. . . . . 27

**Figure 1.23:** (A) Regional cross section of Cenozoic deposits within the Anglesea region, after Holdgate et al. (2001), with interpreted stratigraphic correlations of sequence boundaries, derived dominantly from the coal borehole data of Meyer (1982) and Stanley (1994). Given that this interpretation has an applied 73X vertical exaggeration, a second interpretation (B) has been modified from Holdgate et al. (2001) to remove the vertical exaggeration and highlight the very low amplitude of the folds. Locations of minor structural elevation can also be resolved within the basal Cenozoic unconformity depth maps provided by Matthews (2015). . . . 30

**Figure 1.24:** (A) Late Cretaceous - early Eocene ~NE-SW extension within the Anglesea region, forming NW-SE oriented depocentres that are interpreted to have controlled deposition of the Eastern View Formation. (B) Late Eocene deposition of the Anglesea Sandstone. (C) Early Oligocene incursion of volcanic material (Angahook Formation) . (D) Late Oligocene - middle Miocene Torquay Group deposition. . . . . 31

# Chapter 2

**Figure 2.1:** Geological map of the coastal regions of the eastern Otway Basin. The stratigraphy is provided in the lower right, modified from Abele et al. (1988) & McLaren et al. (2009). Studied field areas (Artillery Rocks, St. George Anticline and Soapy Rocks) as well as the location of the Anglesea-1 well are marked as a star. The Eumeralla Fm (green) hosts extensive NE-oriented folds, while the Angahook Fm (red) is significantly less deformed. Within the mini-map (top left corner) offshore inverted normal faults are shown in red, based on seismic interpretations by (Matthews, 2015). A green box indicates the position of the field area. . . . . 41

**Figure 2.2:** Syn-folding fractures, (a-c) fractures oriented perpendicular to the fold strike forming parallel to regional shortening, and (a-b) fractures oriented parallel with the fold strike forming as tensile stress conditions are generated during outer-arc extension of the fold hinge. Shear fractures often form slickenlines on the side of the slickenside surface.. . . 42

**Figure 2.3:** Northeast side of Soapy Rocks (55H 0253787E 5743673N) – Angahook Formation volcaniclastics displaying the contact between grey-light brown debris flow (containing sand and mud clasts), and an overlying cross-bedded sandstone that fines up into a more laminated sandstone, with sub-vertical fracturing. . . . . 42

**Figure 2.4:** (A) UAV map view of the St. George Anticline with applied Victorian nearshore coastal bathymetry 2.5m DEM & 1m contour data, extending up to the 20m-depth contour (DELWP, 2009). Bathymetry data are overlain by a (humidity) colour-ramp. Note the limits of the coastal rock platforms, which are defined by orthophotographs. Red boxes correspond to sampling sites, with each sample site (Locations 1-15) consisting of a 10x10m grid. (B)

Lower hemisphere equal area stereographic projection (poles to bedding planes) with 1% area contours derived from traditional mapping between locations 6-12 within the St. George Anticline. The 60 bedding plane measurements suggest a gently NE plunging fold axis and a subvertical axial plane, and the bathymetric data combined with field measurements between locations 1-3 suggest a possible change in the strike of the fold hinge. . . . . 51

**Figure 2.5:** (A) Fracture orientations on bedding surfaces, observed within an orthorectified photomosaic within the northeastern end of the St. George platform (Location 1). Fracture relationships indicate that fracture set #1 (blue) and #3 (red) abut against fracture set #2 (purple), while fracture set #3 abuts against both fracture sets #1 and #2. (B) SW oriented photograph of a plumose structure on the side of a ~NW-SE (130/80SW) oriented fracture surface (54H 0759267E 5728333N). (C) Fracture cluster groups based on the spread of fracture orientations analysed within UAV orthophotographs, with centres calculated from the mean preferred fracture orientations. (D) Circular histogram corresponding to fracture orientations derived from the high-resolution orthophotograph, weighted for fracture segment length and colour-coded based on orientation, for Location 1. (E) Stereographic projections representing 1% area contours (poles to tensile and shear fracture planes) for Location 1, obtained from field measurements.. . . . . 52

**Figure 2.6:** (A) Northern limb (Location 4) shown in a NW-oriented photograph (yellow notebook for scale). Note the sinistral offset of calcite veins oriented sub-parallel to the fracture set #1. (B) Sinistral strike-slip fault (134/90) within the southern limb, with a person for scale (54H 0759380E 5727785N). (C) Circular histogram corresponding to fracture orientations derived from the high-resolution orthophotograph, weighted for fracture segment length and colour-coded based on orientation, for Location 4. (D) Stereographic projections representing 1% area contours (poles to tensile and shear fracture planes) for Location 4, barren fractures and faults and (E) - Location 4, vein-filled fractures, obtained from field measurements. . . 53

**Figure 2.7:** Matrix of percentage and type of fracture relationships for (A) Northern limb (Location 1), (B) Hinge (Location 10) and (C) Southern limb (Location 13), derived from field measurements within the St. George Anticline. Note that in all locations fracture sets #1 and #3 mostly abut against fracture set #2, while fracture set #3 mostly abuts against all other fracture sets. For the full data sets see Appendix 3. The greater number of ambiguous fracture relationships in the southern limb is due to the increased erosion levels of fracture apertures in this region.. . . . . 54

**Figure 2.8:** Fracture spacing histograms for (A) Northern limb (Location 1), n = 34, (B) Hinge (Location 10), n = 513 & (C) Southern limb (Location 13), n = 76, derived from field measurements within the St. George Anticline. Note that fracture spacing within the hinge region is significantly greater than in the limb regions for fracture sets #1 and #2. For full data set see Appendix 3. . . . . 55

**Figure 2.9:** (A) Fracture orientations on bedding surfaces, observed within an orthorectified photomosaic within the St. George fold hinge (Location 10). Circular histograms corresponding to fracture orientations derived from the high-resolution orthophotograph, weighted for fracture segment length and colour-coded based on orientation, derived from field measurements within, (B) – Fold hinge (Location 10) and (C) – southern limb (Location 12). Stereographic projections representing 1% area contours of poles to fracture planes derived from field measurements within: (D) – Fold hinge (Location 10) and (E) – southern limb (Location 12).. . . . . 56

**Figure 2.10:** Orthophotograph of the coastal platforms around the St. George Anticline, overlain by a fracture density map (max density ~5 fractures/$m^2$ represents the 'hot' regions). Circular histograms are derived from the high-resolution orthophotograph, weighted for fracture segment length. Note the interpreted sinistral offset of the fold hinge. . . . . 57

**Figure 2.11:** (A) UAV acquired high-resolution orthophotograph of the coastal platforms at the southern Artillery Rocks locality. Circular histograms derived from the high-resolution orthophotograph, weighted for fracture segment length and are coloured based on fracture group (#2 purple, #3 red). Red boxes correspond to field sampling sites, with each sample site consisting of a 10x10m grid area. A zoomed in section of the coastal platforms highlights the orientation of fracture set #2 (purple) and fracture set #3 (red). Coordinate system: WGS84. (B) Stereographic projection representing 1% area contours of poles to fracture planes based on field measured within Location 3, and highlights the dominant subvertical dip of fractures in this area. (C) ~NW-SE oriented fracture corridors with a person for scale (location 4). 61

**Figure 2.12:** Orthorectified aerial photomosaic of the Soapy Rocks coastal outcrop (Anglesea). (A) Stereographic projection representing 1% area contours of poles to fracture planes, obtained from field measurements and with a red line indicating the plane of the sinistral fault (152/90). (B) Circular histograms corresponding to fracture orientations are derived from the high-resolution orthophotograph, weighted for fracture segment length and colour-coded based on orientation. (C) Zoomed in section of the coastal platform that highlights the orientation of fracture set #2 (purple) and fracture set #3 (red). (D) Matrix of percentage and type of fracture relationships for the northern area, derived from field measurements. (E) Sinistral faulting of iron rich, coarse granule quartz sandstone laminations. Note the lamination displacement against the sinistral fault. . . . . 64

**Figure 2.13:** Conjugate set of fractures (55H 0253804E 5743678N). (A) Sinistral shear sense defined by offset bedding. (B) Dextral shear sense defined by offset bedding (see zoom). (C) Possible offset of ~WNW-ESE fracture by ~NW-SE fracture (see zoom). . . . . 65

**Figure 2.14:** Mohr criterion for shear stress ($\tau$) (MPa) versus normal stress ($\sigma_n$) (MPa) for volcaniclastic sandstone, taking compression as positive. An average value for the coefficient of internal friction $\mu = 0.75$ has been adopted from Jaeger and Cook (1979) as recommended by Sibson (2000b). A range of differential stress values for maximum burial presented in **Table 2.6** are represented here by the red circle (maximum range of stress values), green circle (minimum range of stress values) and black circle (average stress values). . . . . 71

**Figure 2.15:** A loading path diagram representing how the minimum horizontal stress changes with depth. Tensile fracture formation may be due to the changing horizontal stress conditions during uplift upon reaching the tensile strength ($T_o$) of the rock. As such, the dashed arrows indicate the depth range at which fracture formation may occur. Loading paths are based on values of mechanical properties that vary for each lithology (**Table 2.6**) and are shown with the range of horizontal stress values for each potential loading path. Loading paths have been calculated for volcaniclastic sandstone, Eumeralla Formation (VS, blue), shale, Eumeralla Formation (SH, black) and sandstone, Demons Bluff Group (S, red). . . . . 72

**Figure 2.16:** A schematic representation of deformation and fracture formation within the St. George Anticline, accompanied by 3D block diagrams that illustrate changes to the paleostress orientations. D1 extension: NW-SE extension forms NE-oriented basement faults (Matthews, 2015). D2 folding, Phase 1: NW-SE shortening initiates the formation of the #2 transverse a-c fracture set. D2 folding, Phase 2: Continued NW-SE shortening, reactivation of the underlying normal faults and fold amplification, resulting in outer-arc extension and the formation of the fracture sets #1 and densifying fracture set #2. D3, Unloading: Continued uplift forms the fracture set #3 (unloading joints). D4, faulting: NW-SE shortening results in left-lateral displacement of the fold hinge, with associated sinistral faults forming in the limb regions along prior formed a-c fractures. . . . . 75

**Figure 2.17:** Schematic representation of fracturing within the uppermost stratigraphic units of the Soapy Rocks locality. Observed are two orthogonal fracture sets (A) and several shear fractures (B). (C) Relationships between the shear fractures and the maximum principle stress. The fracture planes are oriented at 24° to the maximum stress ($\sigma 1$=128°) and have a resolved

shear stress of (2θ = 132°). . . . . 76

**Figure 2.18:** Interpreted deformation history of the eastern Otway coastline based on fold and fracture orientations. Red arrows indicate the orientation of the interpreted maximum principal stress. The stratigraphy of the eastern Otway Basin is modified from Abele et al. (1988) and McLaren et al. (2009). . . . . 77

## Chapter 3

**Figure 3.1:** Syn-folding fractures, (A) fractures oriented perpendicular to the fold strike forming parallel to regional shortening, and (B) fractures oriented parallel to the fold axis, forming when tensile stress conditions are generated during outer-arc extension of the fold hinge. . . . 88

**Figure 3.2:** (A) Location of measurement sites (red) for three anticlines south of Cadomin, as well as one unfolded section located northeast of Grande Cache, within the central Alberta Foothills. (B) Rose diagram of fracture orientations with the Cardium Sandstone around Grande Cache, after Jamison (2016). . . . . 89

**Figure 3.3:** A loading path diagram representing effective horizontal stress conditions arising during burial and uplift of the Cardium Sandstone. The loading path is based on the mechanical properties within Table 3.2 and the dashed section represents the range of conditions in which the effective horizontal stress would form unloading joints. . . . . 90

# List of Tables

## Chapter 2

**Table 2.1:** UAV photogrammetry equipment that was used in this study. The compact size and small weight makes it portable and therefore suitable for fieldwork in remote locations. . . 46

**Table 2.2:** Camera settings and survey parameters for UAV photogrammetry northeastern Otway Coastline (Victoria, Australia). The camera automatically adjusts shutter speed in order to minimise motion blur. Note that 2 UAV flights (flight time: 10-12 min each) were necessary to cover the St. George Anticline area and to stay within the legal requirements (flying within line of sight). Prior to the acquisition of aerial photographs by the UAV, wooden markers and high visibility tape were used to mark ground control points. . . . . 47

**Table 2.3:** Fracture data based on field measurements for each sampling area, including the northern limb (blue), the hinge region (green) and the southern limb (red), of the St. George Anticline. Fracture locations are measured from the centre of each counting square. . . . . 58

**Table 2.4:** Fracture data for each sampling area within the Artillery Rocks locality. Fracture locations are measured from the centre of each counting square. . . . . 62

**Table 2.5:** Fracture data for each sampling area within Soapy Rock locality. Fracture locations are measured from the centre of each counting square. . . . . 63

**Table 2.6:** The mechanical properties of representative lithology types for each study area, with values based on equations provided in-text, or as indicated. Numerical ranges are provided, with averaged values in bold. Note that values of **ν**, **E** and **α** are provided for consolidated (C) rock types, while values for unconsolidated sediments (UC) have been used to calculate the horizontal stress change during burial. The horizontal stress change ($\Delta\sigma_h$) is provided for both burial to maximum depth (MD) as well as uplift to surface (S). . . . . 70

## Chapter 3

**Table 3.1:** The Eumeralla Formation and its analogue the Cardium Sandsone, as adopted by Jamison (2016). . . . . 90

**Table 3.2:** The mechanical properties of the Cardium Sandstone, as adopted by Jamison (2016), Numerical ranges are provided, with averaged values in bold. Note that average values of **ν**, **E** and **α** are provided for consolidated (C) rock types, while values for unconsolidated sediments (UC) have been used to calculate the horizontal stress change during burial. The geothermal gradient (~31°C) and surface temperature (~20°C) were derived from Kalkreuth and Mcmech (1988). The horizontal stress change (Δσh) is provided for both burial to maximum depth (MD) as well as uplift to surface (S). . . . . 91

# Acknowledgements

First and foremost, I would like to thank my supervisors for taking the time to mentor me throughout my degree and give me the tools, guidance and constant patience that have allowed me to get to this point.

To my main supervisor Professor Mike Hall, I am constantly amazed that you can get work completed and still maintain an open-door policy. However, I am eternally grateful that you share my enthusiasm for interesting and often off-topic discoveries. I have known you since 2012 and you have always maintained the same vigorous passion for your work during that time. Thank you for sharing your home with me during my fieldwork and for constantly going above and beyond to provide me with the resources I needed.

A special thank you to Professor Sandy Cruden, although the project began with a focus on laser ablation, the finial shape of the project is hopefully more coherent, and the experience I gained under your guidance has become very valuable to me. I doubt that without your guidance I would have been able to maintain focus on a single subject during this project.

On that note, thank you to Massimo Raveggi for both instructing me on the LA-ICPMS, as well as deciphering with me the cathodoluminescence stereomicroscope instruction manual, or lack thereof. While there is more that we could have done, I expect that what we achieved will still become a useful asset to me in the future.

I particularly wish to thank Stefan Vollgger for his assistance during this project. Your help collecting the UAV data, processing the photomosaics and revising the draft of my second chapter, has been a crucial asset to this project. I expect that you will soon have several honours and PhD students working directly under your supervision .

To my compatriots Alastair Tait, Prudence Perry, Nicolas Hunter, Andrew Langendam, Mitchell O'Mara and all the other post-grads. Working each day over the last two years has only been possible because of the support offered by you all. You have honestly made my time at Monash over the last two years the experience of a lifetime.

I would like to acknowledge and thank the hard working administration and technical staff working within the School of Earth, Atmosphere and Environment. To Silvana, Christine, Rob, Katie and Junnel, each of you made working at Monash significantly less strenuous. Without your help I would still be

attempting to enrol into my degree, or I would have spent a much larger portion of my nights trying to create thin-sections.

I would also like to acknowledge the assistance received from the Geological Society of Australia (GSA) as part of the Endowment Fund that helped to support this research. Additionally, thank you to Terry Smith for assisting with high-resolution photography of the Soapy Rocks outcrop, as well as navigating the catacombs of the online GSA database.

Thank you to all my field assistants, Shortaro Naganuma, Yanai Amir, Chris Fielder, Matt van Summeren, Camilo Campillo, Sam Geddes and WWE champion Orlando Jordan, for joining me on my expeditions and assisting my research. We sit on the skin of this planet, and so many of us seem utterly content to be ignorant of what is above us, and below us. I am truly thankful that you all took the time to join me looking at the ground. I hope that the experiences we shared will keep you fascinated by the complexity that geology has to offer.

Lastly, I wish to thank my family for their love and support throughout the completion of my thesis. While we have seen a lot less of each other during the last two years, your continued encouragement has keep me motivated and it will be difficult to return my gratitude.

# Abstract

The Otway Basin, Victoria, Australia formed during the initial breakup of Gondwana (ca. 165 – 100 Ma), as Australia separated from Antarctica. Folded potential reservoir rocks (Eumeralla Formation) within the Otway Basin are of significant exploration interest for their geothermal and tight gas reservoir potential. However, compared with the nearby Gippsland Basin, which has generated significant hydrocarbon resources, the Otway Basin has produced relatively fewer hydrocarbon shows. Brittle deformation within the Eumeralla Formation (ca. 113-100 Ma), along the Otway coastline of Victoria, reflects a protracted history of extension, compression, erosion and uplift, since Australian-Antarctic separation.

This thesis investigates the relative timing of heterogeneously distributed fracture populations within both folded and unfolded regions along the Otway coastline. Data collection occurs across several stratigraphic units spanning the Early Cretaceous to the late Cenozoic in order to measure fracture variation and determine the relative timing of fracture formation.

An unmanned aerial vehicle (UAV) has been used to facilitate the systematic and inexpensive acquisition of high-resolution orthophotographs along coastal platforms, in order to complement traditional field mapping of fracture populations.

The Early Cretaceous Eumeralla Formation rocks have experienced significantly more fold related deformation than the younger (late Cretaceous to late Cenozoic) rocks of the Eastern View Formation and Demons Bluff Group.

Several highly fractured, ENE oriented folds have been documented along the Otway coastline. Fractures have been measured within the fold hinge of the St. George Anticline, as well as within shallow dipping beds at Artillery Rocks. Within the Demons Bluff Group, fractures were measured within shallow dipping beds at the Soapy Rocks locality.

A NE-SW oriented fracture set is observed exclusively within the Eumeralla Formation, while a NW-SE oriented fracture set pre-dates hinge-parallel fractures. Significant fracture formation has been linked to a period of mid Cretaceous uplift within the eastern Otway Basin (ca. 95Ma). For comparison, both the Eumeralla Formation and Demons Bluff Group host a NNW-SSE oriented fracture set that is inferred to largely post-date mid Cretaceous folding.

Additionally, sinistral displacement of fold hinges within the Eumeralla Formation, combined with fracture reshear and thrust faulting within Cenozoic sediments, is interpreted to have occurred during an

episode of late Miocene - early Pliocene shortening.

Ultimately, this thesis provides new insights into the geological history of the eastern Otway Basin. Focusing on outcrop-scale fracture systems, this thesis further advances on conceptual models of fold-related fracturing. By underscoring the methodological limitations in recent publications the finding of this thesis will be applicable to analogous basins.

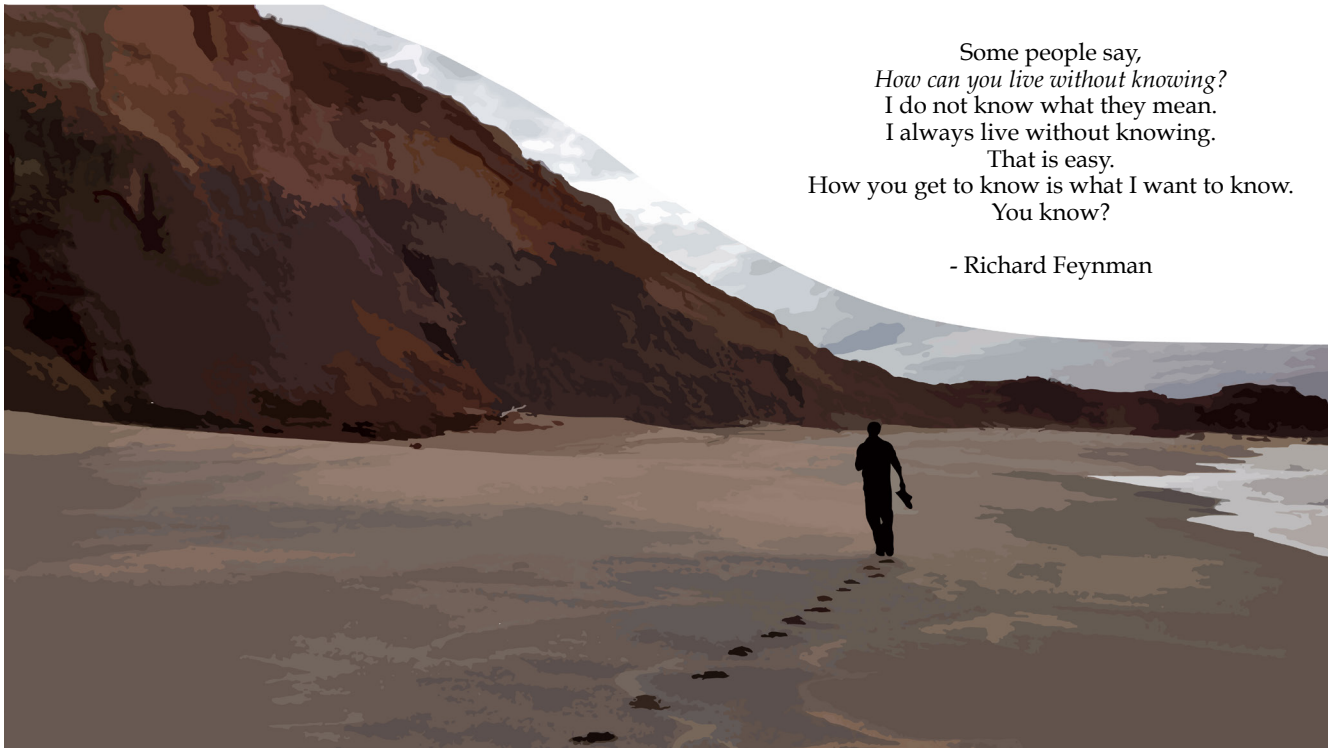

Some people say,
*How can you live without knowing?*
I do not know what they mean.
I always live without knowing.
That is easy.
How you get to know is what I want to know.
You know?

- Richard Feynman

MONASH University

# Declaration for Thesis Chapter 1

Declaration by candidate

In the case of Chapter 1, the nature and extent of my contribution is as follows:

| *Nature of contribution* | *Extent of contribution (%)* |
|---|---|
| Main research, fieldwork, data analysis and interpretation | 80% |

The following co-authors contributed to the work. If co-authors are students at Monash University, the extent of their contribution in percentage terms must be stated.

| *Name* | *Nature of contribution* | *Extent of contribution (%)* |
|---|---|---|
| Mike Hall | Supervisory role | 10% |
| Alexander R. Cruden | Supervisory role | 10% |

The undersigned hereby certify that the above declaration correctly reflects the nature and extent of the candidate's and co-authors' contributions to this work*.

Candidate's signature [redacted] Date: 05/08/2017

Main Supervisor's signature [redacted] Date: 05/08/2017

# Chapter 1

An Introduction to the Regional Geology of the eastern Otway Basin

Joel Vergunst, Mike Hall & Alexander R. Cruden

School of Earth, Atmosphere and Environment, Monash University, Australia;

Email: joel.vergunst1@monash.edu, mike.hall@monash.edu

## 1.1 Project outline/Introduction:

Fold-hosted fracture systems have been the focus of recent hydrocarbon and structural modelling studies (Smart et al., 2009; Zahm & Hennings, 2009; Awdal et al., 2013; Jamison, 2016), with numerous authors (Bergbauer & Pollard, 2004; Bellahsen et al., 2006; Blenkinsop, 2008; Tavani et al., 2012) demonstrating the mechanisms for forming complex fracture patterns within folded regions.

However, such structural models often rely on data sampled from within a single formation (Bergbauer & Pollard, 2004; Fischer & Christensen, 2004; Cooper et al., 2006; Tavani et al., 2012; Jamison, 2016), with only a few authors considering how fracture characteristics vary as a function of lithology and stratigraphic position (Bellahsen et al., 2006; Zahm & Hennings, 2009; Shackleton et al., 2011) and even fewer incorporating the effects of erosion and uplift on fracture formation (Engelder & Geiser, 1980; Hayes & Hanks, 2008; Awdal et al., 2013). These factors can significantly reduce the confidence that can be placed on the interpreted timing of fracture formation, particularly when fracture populations form post-folding, or when the study has been limited by the availability of sufficient outcrop exposure. Furthermore, a complex fracture system will often present significant challenges when determining the historic flow of hydrocarbon systems (Lange, 2009; McLennan et al., 2009).

The eastern Otway coastline (Figure 1.1) hosts excellent platform and cliff exposures that provide a unique opportunity to document in detail the relationships and relative timing of heterogeneously distributed fracture populations within folded and unfolded regions, across several stratigraphic units spanning the Early Cretaceous to the late Cenozoic. This allows for a more complete model on the relative timing of fracture formation within the eastern Otway Basin to be established.

This chapter provides an introduction to the stratigraphic, lithological and structural framework of the study area (Figure 1.2) and defines the major stratigraphic units that will be compared for their potentially different styles of deformation. By understanding how deformation varies throughout the different stratigraphic units, key localities can be identified for further analysis of the associated fracture systems, which have previously not been studied to any significant extent.

## 1.2 Geological and tectonic setting:

The platform and cliff exposures along the eastern Otway coastline (Figure 1.1) dominantly consist of (Early Cretaceous, ca. 113-100 Ma) fluvial sedimentary rocks that were deposited during the initial breakup of Gondwana, as Australia separated from Antarctica, within an eastward-propagating rift system that began in present day Western Australia in the Late Jurassic (~165Ma) and ended in present-day western Victoria in the late Albian (~100Ma) (Duddy, 2003; Krassay et al., 2004). Late Jurassic to Early Cretaceous extension (Figure 1.3) formed a series of E-W to NE-SW oriented half grabens bounded by dominantly north-dipping normal faults (Cooper, 1995; Hall & Keetley, 2009). The Otway Basin formed as a result of this tectonic activity, with the basin-bounding faults controlling deposition of the Eumeralla Formation.

Mid Cretaceous (c. 97-92Ma) NW-SE oriented shortening caused extensive uplift and inversion of the Otway Basin depocentre (Figure 1.1), with an estimated 2km of calculated uplift (Cooper & Hill, 1997; Matthews, 2015) resulting in an initial paleogeographic high, coincident with the present day Otway Ranges, that persisted until the Late Cretaceous (Hill et al., 1995; Green et al., 2004).

Renewed NE-SW oriented extension that commenced in the Late Cretaceous (c. 95Ma) lasted until the Maastrichtian (~70Ma) and lead to the development of mainly NW-oriented normal faults that extended southwards along the west coast of Tasmania, while initiating extension within the Bass Basin and offshore Gippsland Basin (McLaren et al., 2009; Briguglio et al., 2013). Deposition of fluvial to coastal plain sediments of the post Campanian Eastern View Formation (ca. 65Ma - 55Ma) succeeded late Cretaceous extension in the Bass Basin and its northern continuation into the Torquay Sub-basin (McLaren et al., 2009). These sedimentary rocks have been of significant exploration interest for their hydrocarbon potential, with the similar aged Gippsland Basin in Western Victoria producing substantial hydrocarbon resources since the late 1960's (Bernecker et al., 2003). By comparison the underlying, syn-rift Crayfish Group have been a hydrocarbon target in the Western Otway Basin (i.e. Penola Trough, Figure 1.1), where NW-SE and E-W oriented basement faults influenced hydrocarbon migration (Boult et al., 2008).

Within the eastern Otway Basin, the Eastern View Formation was in turn overlain by near-shore to marginal marine sands (Anglesea Formation, ca. 37-34.5Ma) and shallow marine sediments, pyroclastics, tuffs and basalts (Angahook Formation, ca. 28.7Ma) prior to regional deposition of marine limestone (Torquay Group, ca. 24-15 Ma) (Figures 1.2 & 1.3) (Trupp et al., 1994; Holdgate et al., 2001).

In the late Miocene to early Pliocene (ca. 20-2.6 Ma) numerous folds formed along the southeastern Otway coastline as NW-SE oriented shortening was accommodated by the reverse-reactivation of Early Cretaceous, NE-oriented normal faults (Figure 1.1) (Edwards, 1962; Duddy, 1994; Holford et al., 2014; Matthews, 2015). Furthermore, an estimated ~1km of mid-late Cenozoic uplift (Matthews, 2015) established the present topography of the Otway Ranges, as evident by the Paleocene-Eocene coals that lie unconformably on Early Cretaceous sedimentary rocks at an elevation 300-360m around Benwerrin on the crest of the ranges (Figure 1.1) (Holdgate et al., 2001; Holford et al., 2014).

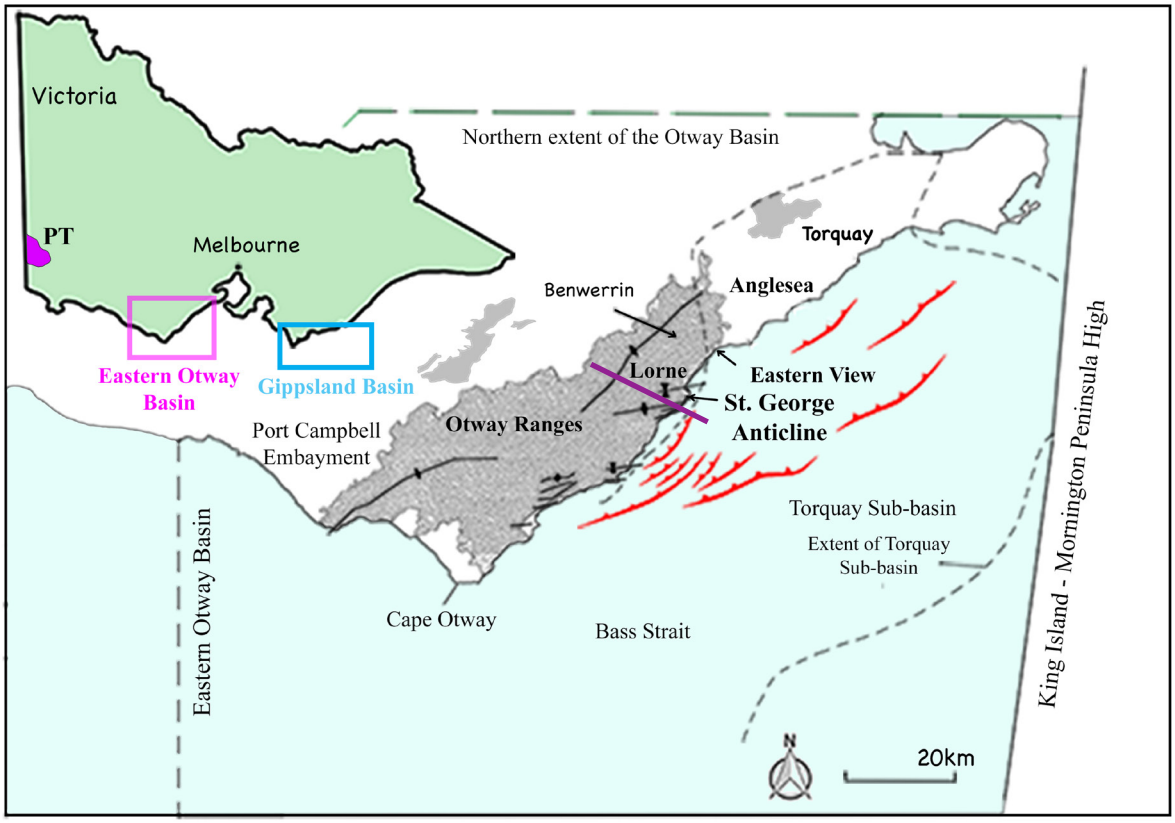


**Figure 1.1:** Location of the study area (northern Anglesea to southern Lorne) eastern Otway Basin, modified after Holford et al. (2011) & Duddy (2010). Shaded areas represent the extent of the onshore mid Cretaceous uplift, eastern Otway Basin. Offshore inverted normal faults (red) are based on seismic interpretation and cross-sections (purple line) by Matthews (2015). The Victorian extension of the Penola Trough (PT) is based on interpretations made by Boult et al. (2008).

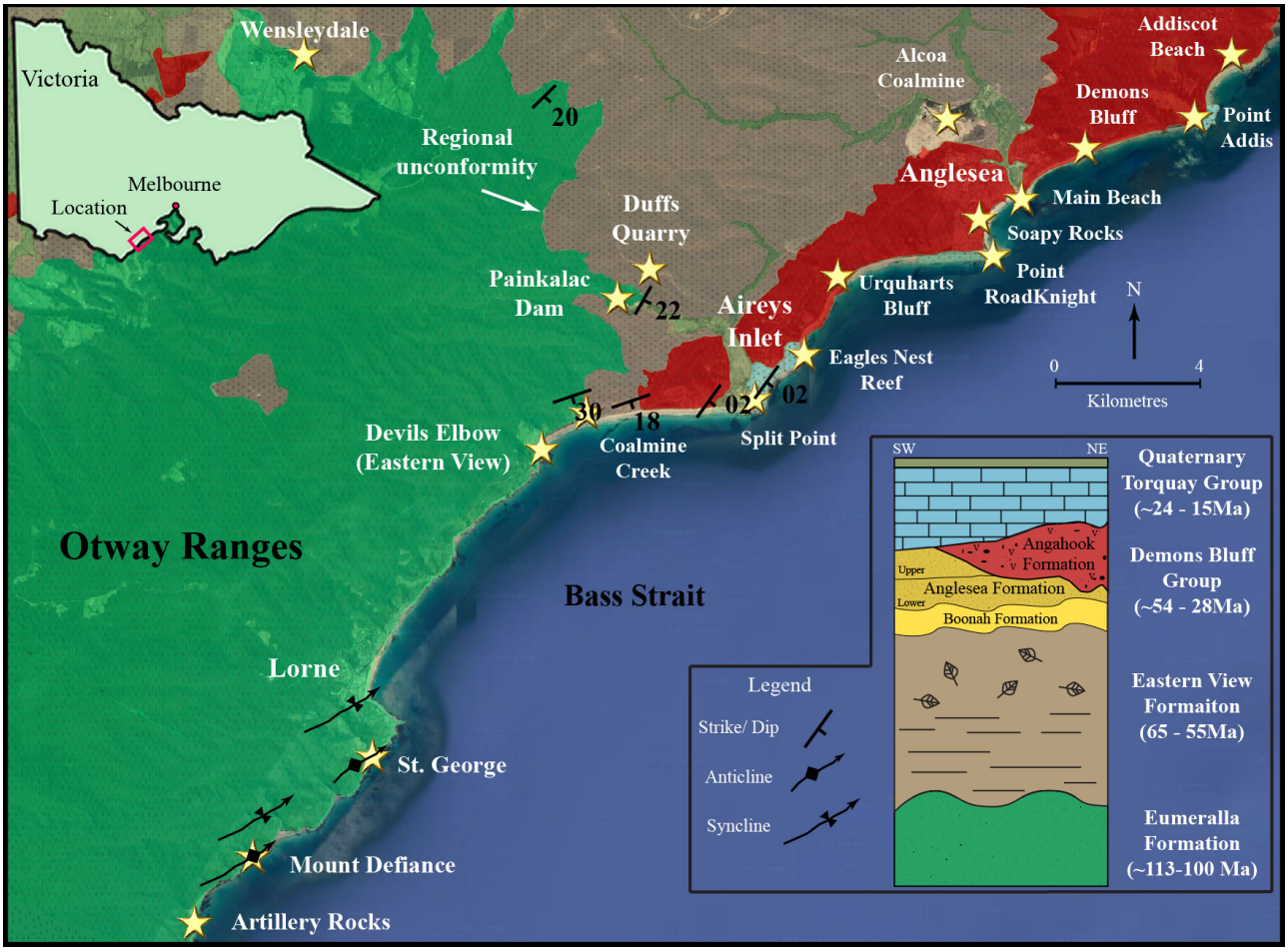


**Figure 1.2:** Geological map showing the stratigraphic units within the field area (onshore eastern Otway Basin). The general stratigraphy of the onshore eastern Otway Basin is provided in the lower right, modified from Abele et al. (1988) & McLaren et al. (2009), with a more comprehensive tectonostratigraphic column provided within Krassay *et al* (2004). The older and younger stratigraphic units of this study are separated by the indicated regional unconformity. The key locations identified within this study are each indicated with a gold star.

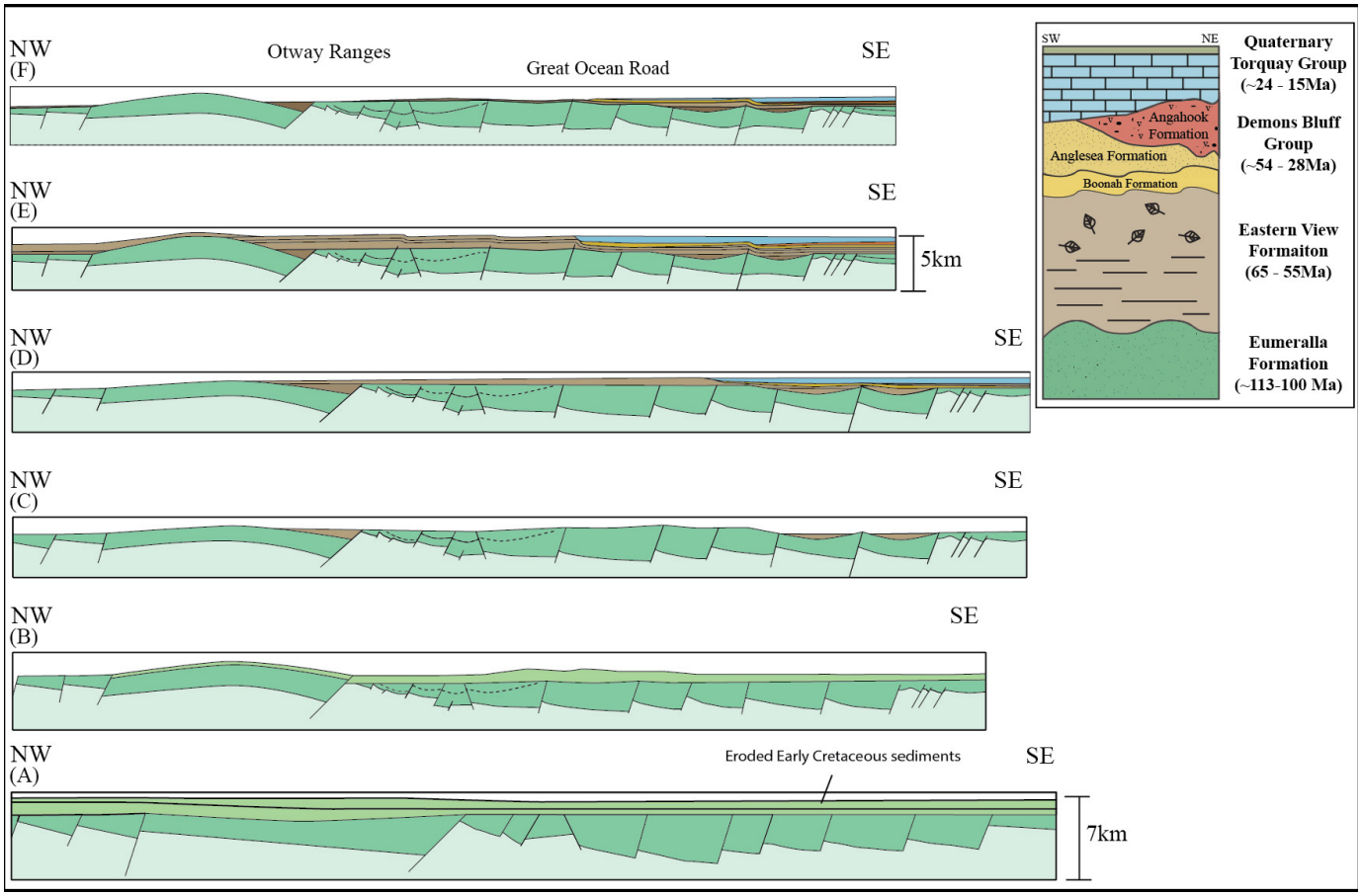


**Figure 1.3:** A restored cross section that highlights the temporal evolution of the basin fill (VE = 2) modified from the restored cross-section of (Matthews 2015) and based on seismic line OGF92A-411 collected by Gas and Fuel Exploration N.L. (1992). (A) Early Cretaceous (~113-100 Ma) NW-SE extension. (B) Mid Cretaceous (c. 97-92Ma) NW-SE shortening, erosion and gentle folding. (C) Late Cretaceous (c. 95Ma - ~70Ma) NE-SW extension. (D) Late Cretaceous - mid Cenozoic transgressive sequence. (E) Middle - late Cenozoic (c. 20-0 Ma) NW-SE regional shortening, with forced folding above reactivated faults, centred on the Otway Ranges. (F) Cenozoic erosion.

## 1.3 Methods:

### 1.3.1 Fieldwork: Coastal Exposures

Field mapping of coastal platforms and cliff exposures focused on documenting lithological contacts, faults, folds and systematic fracture orientations. Coastal platform maps (zone 55 Maps 1-3, zone 54 Maps 4-7) (Map Pocket 1) cover the area between southern Artillery Rocks and Devils Elbow, southern Eastern View (Figure 1.2). Field data are reported in Appendix 1.

### 1.3.2 Airborne Radiometric data:

A regional unconformity exists between the Early Cretaceous sedimentary rocks and overlying very late Cretaceous and Cenozoic sedimentary rocks northeast of the Otway Ranges (Figure 1.2). It conveniently defines the boundary between two subareas that will be compared in terms of their deformation and fracture systems. This largely unexposed regional unconformity has only been previously surveyed using limited inland outcrop exposures around Wensleydale (Abele, 1968), combined with sparse borehole data (Holdgate et al., 2001). In order to constrain this stratigraphic boundary to a higher level of certainty than previous surveys, airborne radiometric data with a 50m resolution have been utilised (Figure 1.4A). Given that the radiometric data have only moderate resolution at this scale, these airborne radiometric data were overlain on the SRTM digital elevation data (Figure 1.4B) in order to increase the apparent contrast in the radiometric signature along the stratigraphic boundary (Figure 1.4C).

It is evident that the older and younger sedimentary rocks have different radiometric signatures, with the older Eumeralla Formation (volcaniclastic sandstone) containing more potassium (K), compared with the more uranium (U) and thorium-rich (Th) Cenozoic sedimentary rocks.

These radiometric data have been supplemented with field observations along coastal and inland exposures, including a newly identified inland exposure of the unconformity located northeast of Painkalac Dam (Figure 1.2). At this outcrop shallow south dipping (18°), weathered, light brown sandstone (Eastern View Formation) unconformably overlies moderately southeast dipping (30°), light brown to grey, weathered volcaniclastic sandstone (Eumeralla Formation) (Figure 1.5).

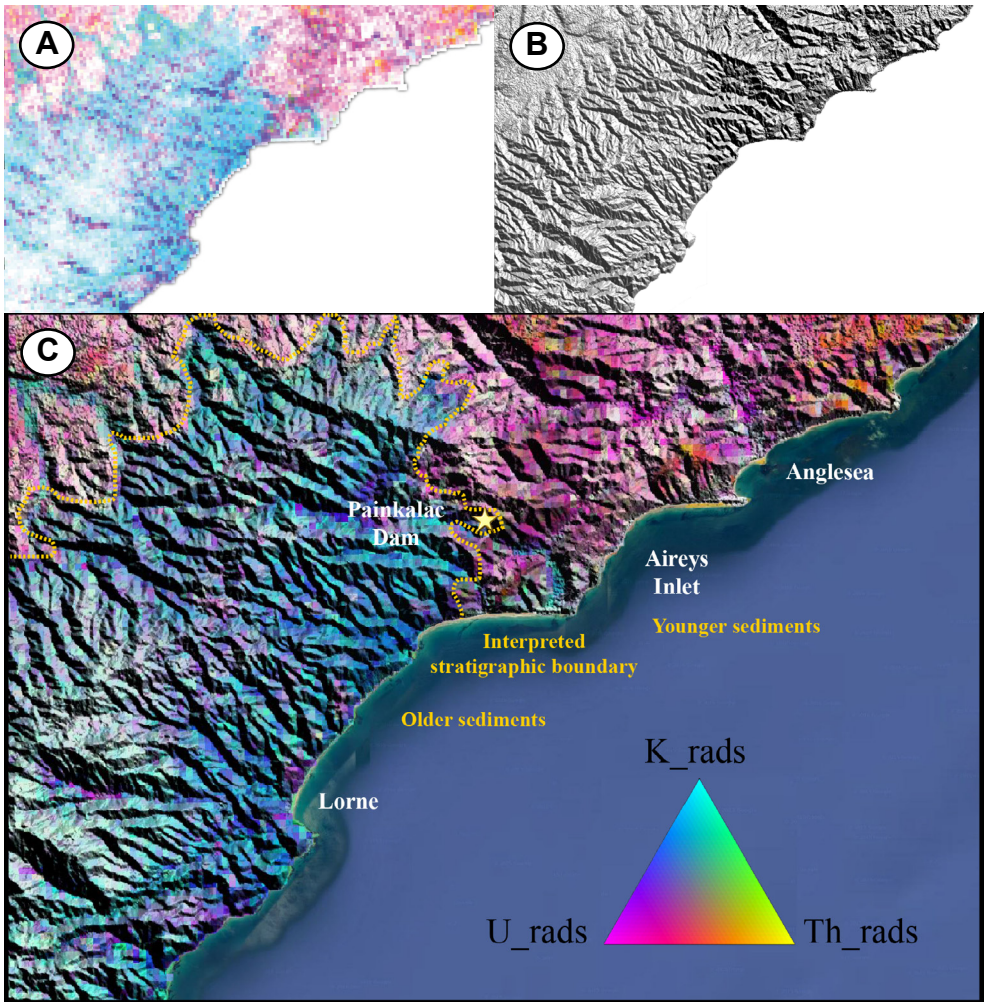


**Figure 1.4:** (A) airborne radiometric data (GDA94mga54_50m) (B) SRTM digital elevation data with applied 45° shaded relief (1arc_S39_e143/144) from USGS (EarthExplorer) (C) Combined data and interpreted stratigraphic boundary indicated (yellow dotted line), separating the older sediments (K-dominant) from the younger sediments (U/Th-dominant). Painkalac dam is indicated with a gold star.

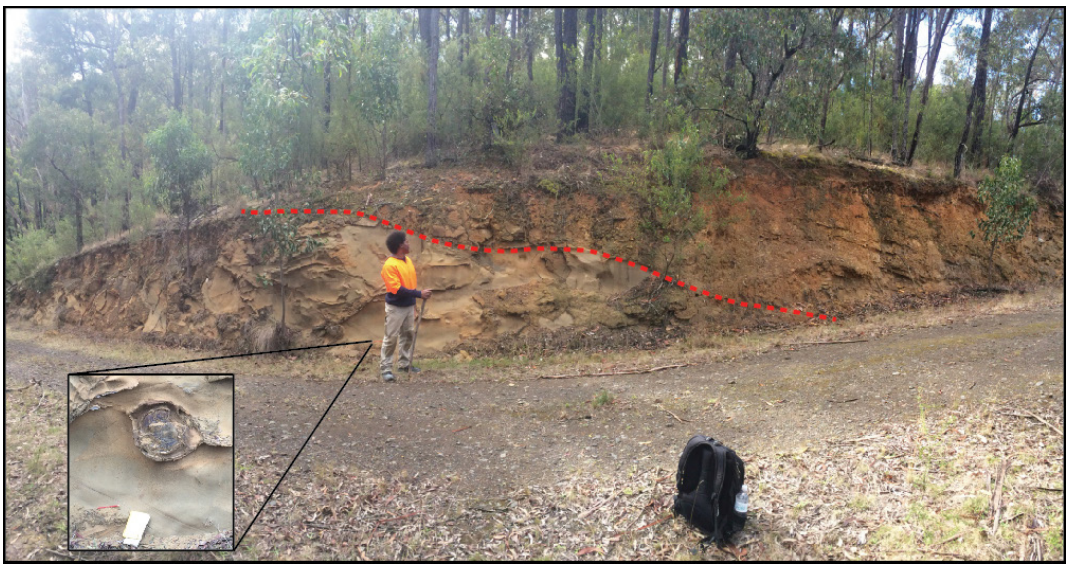

**Figure 1.5:** Inland exposure of the stratigraphic boundary (southern section) between weathered, light-brown to grey, volcanic sandstone (with nodules and rip-up clasts) of the Eumeralla Formation (lower left), and overlying light brown sandstone of the Eastern View Formation (upper right), northeast of Painkalac Dam (55H 0244145E 5741164N WGS84).

## 1.4 Lithostratigraphy

A brief summary of the lithological changes from the oldest to the youngest stratigraphic units, along the coast (Artillery Rocks to northern Addiscot Beach), is provided below. For further lithological descriptions the reader is referred to the larger (91x28.5cm) fold-out cross-sections within Map Pocket 2. Given that the northern coastal section of the field area (Figure 1.2) contains a limited number of wavecut platforms, stratigraphic sections and field observations are dominantly limited to cliff exposures. Stratigraphic sections (logs corrected for true dip) of coastal exposures are provided in Appendix 2, with interpreted correlations between the stratigraphic successions presented in Section 1.4.6.

### 1.4.1 Eumeralla Formation (Artillery Rocks to Eastern View)

Early Cretaceous (ca. 113-100 Ma) fluvial sediments (Krassay et al., 2004) of the Eumeralla Formation (Figure 1.6) are exposed on the wavecut platforms between Artillery Rocks and Eastern View (Figure 1.2). They consist dominantly of fine to medium grained, volcaniclastic sandstone (Quartz: ~25%; Lithics: ~25%; Feldspars: ~30%; Clays ~20%) with interbeds of mudstone.

**Figure 1.6:** Partially weathered volcaniclastic sandstone (Eumeralla Formation), northern Lorne coastal cliff exposure (55H 0239165E 5734390N).

### 1.4.2 Eastern View Formation/ Lower Demons Bluff Group

The Eastern View Formation (65Ma - 55Ma) sedimentary rocks (McLaren et al., 2009) have limited exposure along the coastline north of Eastern View (Figure 1.2). They comprise easily eroded, unconsolidated fluvial sands, silts and impersistent brown coals that dip southeast at 12-26°. The most complete (southern) exposure is observed in a cliff along Coalmine Creek (Figure 1.7A). Duffs Quarry (Figure 1.2) provides one of the best inland exposures of the Boonah Formation (Lower Demons Bluff Group) outside the Alcoa coal mine (Figure 1.7B). At this quarry coarse-grained, quartz-rich, arkosic sandstone with a fine white silt matrix is overlain by fossiliferous (leafy) siltstone that is interbedded with minor brown coal lenses.

**Figure 1.7:** (A) Fluvial silts and sands of the Eastern View Formation, exposed within Coalmine Creek, Eastern View (55H 0242170E 5737754N) WGS84. (B) Duffs Quarry, arkosic sandstone, Boonah Formation (55H 0244151E 5742058N) WGS84. Note the quarry face is ~6 m high, with the photo looking towards the SE.

### 1.4.3 Anglesea Formation

Extensive exposures of the Anglesea Formation occur north of Anglesea Main Beach (Figures 1.2 & 1.8). The Anglesea Formation (ca. 37-34.5Ma) is subdivided into a lower member of weathered, bioturbated, sulphur-rich, black sandstone and an upper member of buff-white, fine sandstone, separated by an extensive disconformity (McLaren et al., 2009). This formation appears to thicken towards the northeast and is best observed around Demons Bluff, where it is over 50m thick and overlain by the lowest 5m of the Angahook Formation (ca. 28.7Ma; McLaren et al., 2009).

**Figure 1.8:** Sulphur-rich black sandstone of the lower Anglesea Member, with overlying buff-white fine sands of the upper Anglesea Member, and separated by a disconformity (arrow), northeast of Anglesea (55H 0255172E 5745125N) WGS84.

The northern end of Addiscot Beach (Figure 1.2) hosts a thick succession (~60 m) of the lower and upper members of the Anglesea Formation, as well as a thin section of the overlying Angahook Formation (Figure 1.9). Exposed is a ~35 m section of the sulphur-rich, black sandstone with jarosite-altered burrows (lower Anglesea Member), with a surficial cream-brown coating of weathered material from the overlying sedimentary rocks. The overlying sedimentary rocks are ~15 m of light cream-coloured, fine grain sandstone (upper Anglesea Member) that are further overlain by the lowermost section of the Angahook Formation, that consists of alternating kaolinite and iron-rich, fine-grained sandstones and siltstones.

One dominant, subvertical fracture set (168/ 90) is oriented at a high angle to the bedding, with a spacing of ~5-30 cm and a vertical height of ~6-10 m, that commonly traverses multiple bedding layers. At the northern end of the beach the fracture characteristics of only the lowest 15 m of the cliff face have been measured due to poor exposure.

Along the northern coastline (Point Roadknight to northern Addiscot Beach) bright yellow jarosite alteration is conspicuous within grey-white pyritic siltstone to fine sandstone (Figure 1.10) and is often observed at the boundary between the upper and lower Anglesea Members.

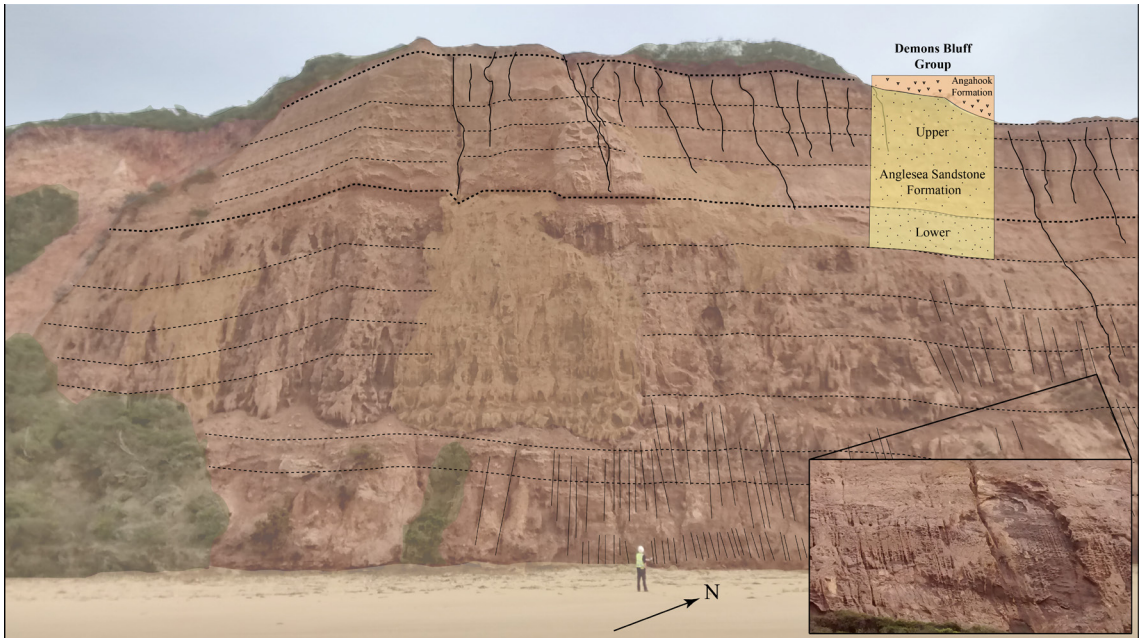


**Figure 1.9:** Subvertical fracturing within sub-horizontally bedded Anglesea Formation (55H 0260439E 5748269N).

**Figure 1.10:** Jarosite alteration (yellow) of burrows? within the grey-white pyritic siltstone (upper Anglesea Formation) (55H 0254263E 5744344N) +/- 3m WGS84.

### 1.4.4 Angahook Formation (Aireys Inlet to Anglesea)

The coastal section at Aireys Inlet (Split Point to Urquharts Bluff, Figure 1.2) exposes a series of partially slumped, diffusely stratified volcaniclastics, tuffs, and weathered basalts of the Angahook Formation (Demons Bluff Group; Cas et al., 1993), that are overlain by brown, fluvial sedimentary rocks containing sub-rounded basalt clasts potentially reworked from the underlying volcanics (Figure 1.11A). The best exposures of the volcanic units are around Split Point, Eagles Nest Reef and Urquharts Bluff (see Appendix 2).

Compared with the coastal sections of Aireys Inlet, volcaniclastic sediments are significantly less represented along the Anglesea coastal section (Pt. Roadknight to northern Addiscot Beach) (Figure 1.2). The Angahook Formation is largely isolated to the upper cliff sections around Demons Bluff, Black Rock and areas within and immediately south of the Soapy Rocks locality (Figure 1.2), where diffusely stratified volcanics (debris flow?) are overlain by black-brown, loamy siltstone (with Liesegang rings, Figure 1.11B), that appear to be laterally correlatable with similar volcaniclastic loamy siltstones observed around Urquharts Bluff. These sedimentary rocks are overlain by bioclastic grainstone (calcarenite) of the Torquay Group (Figure 1.11A).

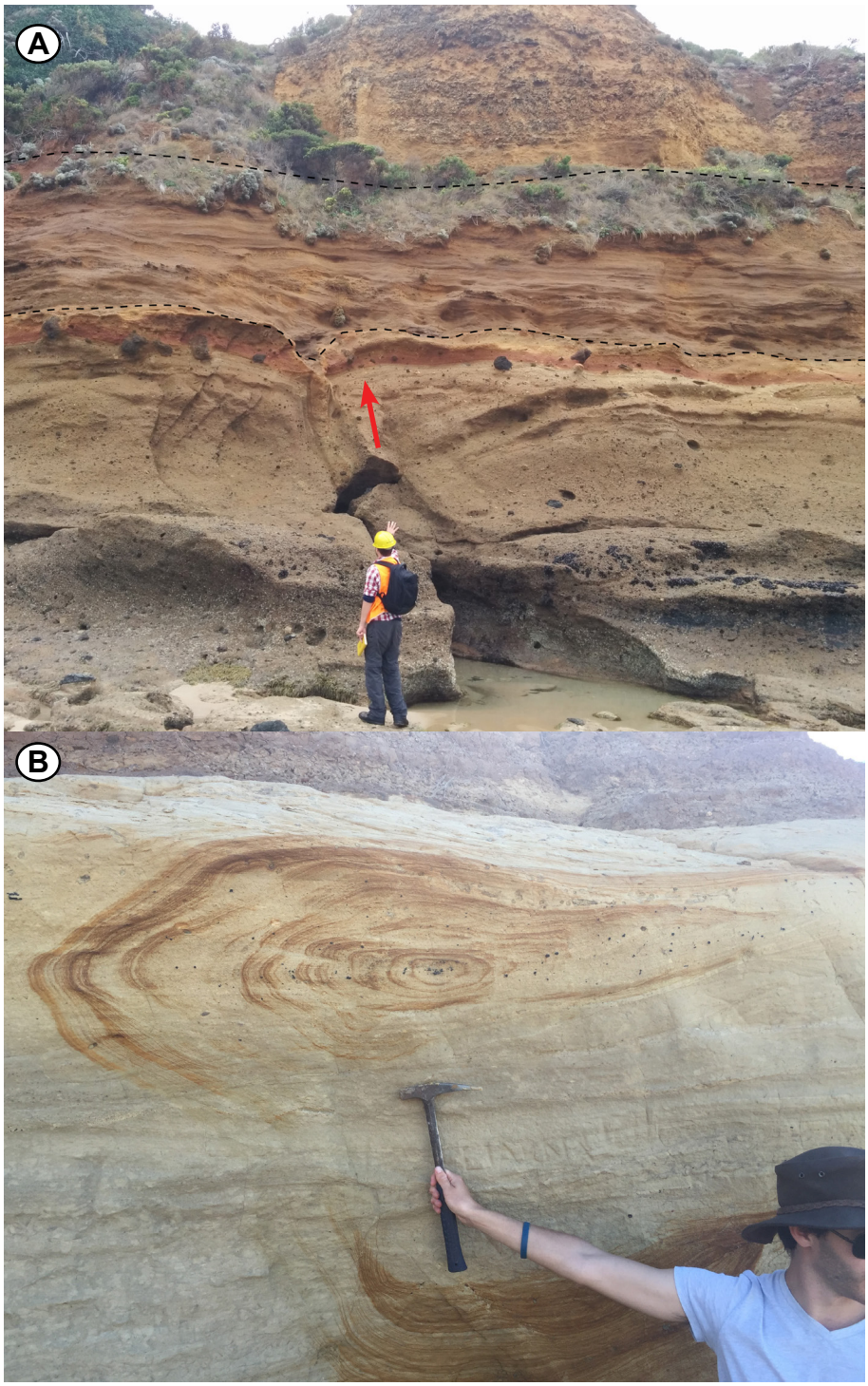


**Figure 1.11:** (A) Aireys Inlet coastal cliff exposure, with iron-rich alteration (red arrow) between the uppermost section of the Angahook Formation and overlying brown silts (55H 0248463E; 5739427N) WGS84. (B) Loamy siltstone with Liesegang rings (Angahook Formation) observed ~500 m south of Soapy Rocks (55H 0253758E 5743589N) WGS84.

### 1.4.5 Torquay Group

The northern coastal section of Point Addis (Figure 1.2) hosts ~1.5 m of alternating, light-tan coloured siltstone and fine-grained, brown quartz sandstone (Angahook Formation), that are onlapped by ~15 m of yellow-grey, bioclastic grainstone (calcarenite) containing abundant bryozoans, foraminifera, crinoids and gastropods (Point Addis Limestone, ca. 24-15 Ma, a lateral equivalent of limestone at Split Point, McLaren et al., 2009). The calcarenite exhibits gentle undulations (Figure 1.12) that appear to be primary depositional features (i.e bedding).

Cross-bedded, bioclastic grainstone (calcarenite) exposed at Point Roadknight (Figure 1.2) is texturally similar to the marine bioclastic grainstone deposits around Pt. Addis and Split Point. This unit is considered to be Pleistocene in age (Abele, 1968) and does not contain in situ bryozoans that are commonly observed in the older Torquay Group calcarenites.

**Figure 1.12:** Demons Bluff Group and overlying Torquay Group, Point Addis Limestone (55H 0259930E 5747276N). Included is a lower hemisphere equal area stereographic projection (stereonet) of poles (with corresponding 1% area contours) to bedding of the Point Addis Limestone. The stereonet shows gentle folding within the Torquay Group.

### 1.4.6 Stratigraphic correlations

Stratigraphic correlations and subdivisions are based on those described within Birch (2003). Stratigraphic units have been separated into individual groups and formations that have been observed and are laterally correlatable along coastal exposures between Split Point (Aireys Inlet) and northern Addiscot Beach (Anglesea) (Figures 1.13A & 1.13B).

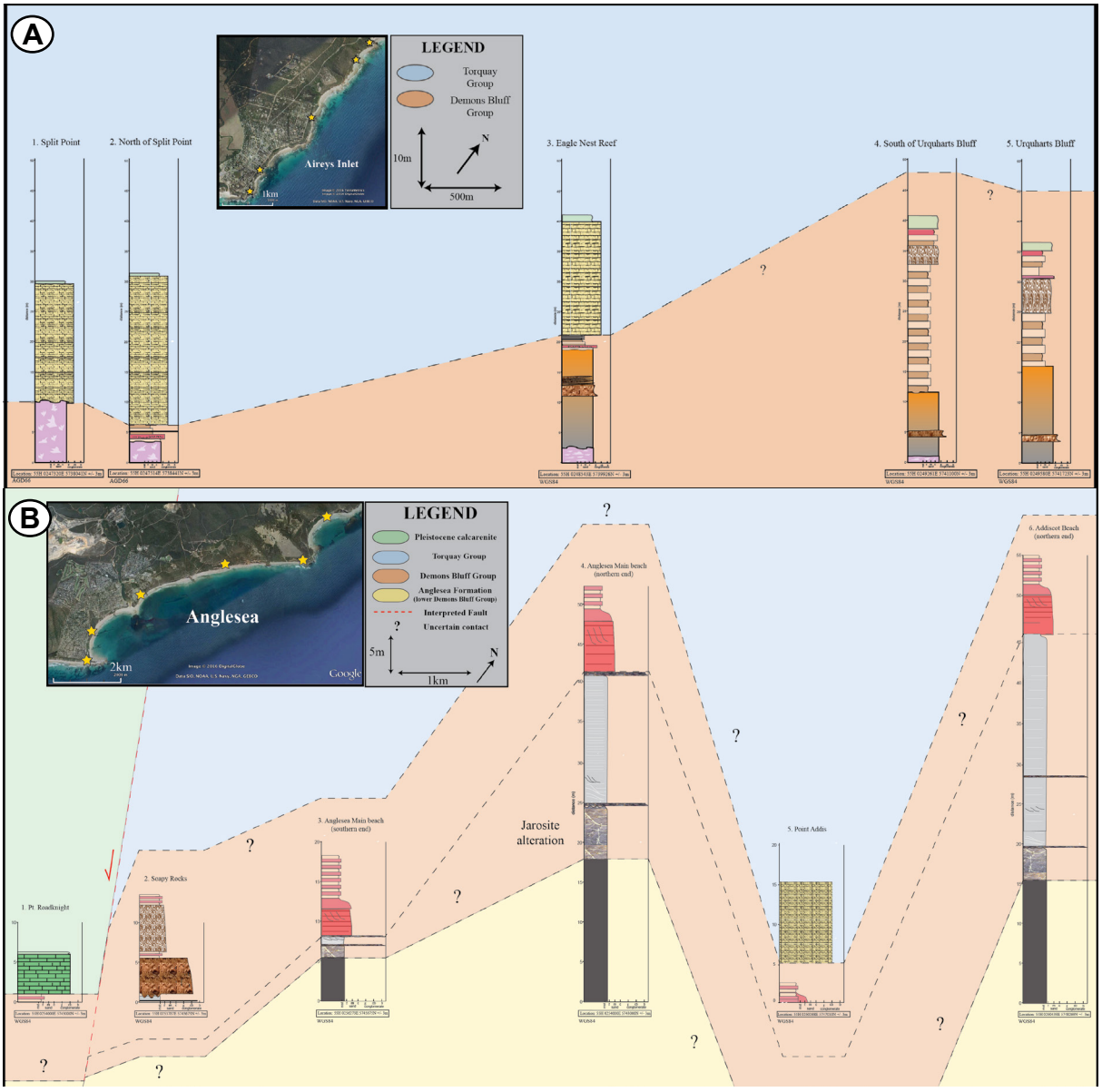


**Figure 1.13:** Stratigraphic correlation diagrams, illustrating interpreted unit correlations along coastal cliff exposures between (A) Split Point and Urquharts Bluff (Aireys Inlet) and (B) Point Roadknight and northern Addiscot Beach (Anglesea), with the datum correlated to sea level. Locations of the stratigraphic sections are additionally indicated with gold stars on the accompanying map (Map Pocket 2). For greater resolution of stratigraphic logs see Appendix 2.

## 1.5 Structural geology: Key localities for structural study

The following section considers key localities identified during field mapping from Artillery Rocks to northern Anglesea that contain significant structural features. These localities are ordered by depositional age (oldest to youngest) and have previously been unreported or only briefly described. The following descriptions will contribute to a more complete understanding of the variation in deformation that exists between each stratigraphic unit encountered. The localities of Artillery Rocks, the St. George Anticline and Soapy Rocks (Figure 1.2) are covered in detail in Chapter 2 and therefore have been excluded from this section.

### 1.5.1 Older sequence (Eumeralla Formation)

The southern coastal platforms host several northeast-trending folds that have been previously described by Edwards (1962), Medwell (1971) and (Cooper, 1995). However, these studies only focused on interpreting the broad structural trends in this region, and did not consider the associated fracture systems. Regional structural trends observed in this region are described below and the associated fracture systems form the basis for Chapter 2.

### 1.5.2 Mount Defiance Anticline

Hosted within the Eumeralla Formation, the hinge zone of the Mount Defiance Anticline is exposed in road cuttings and coastal platform outcrops ~3km south of Lorne (Figure 1.14). It is an upright, asymmetrical anticline with a steep dipping southern limb (maximum dip 89°SE) and a moderately dipping northern limb (maximum dip ~45°NW) (Figure 1.15). The hinge of the anticline plunges ~10° towards 066° (axial plane dip ~70°NNW) and appears to die out northeast into shallow dipping (332/12NE) beds around Cumberland River (Figure 1.14).

The northern part of the Mt. Defiance fold hinge is offset by an inferred fault with a sinistral strike displacement of ~100 ± 20 m (Figure 1.15). Sinistral offset of the fold hinge of ~6m also occurs within the southern coastal platform sections (Figure 1.16A). Faults with a similar orientation (145/90) and movement sense also offset small (~3 m long) sandstone dykes within the southern limb of the fold (Figure 1.16B).

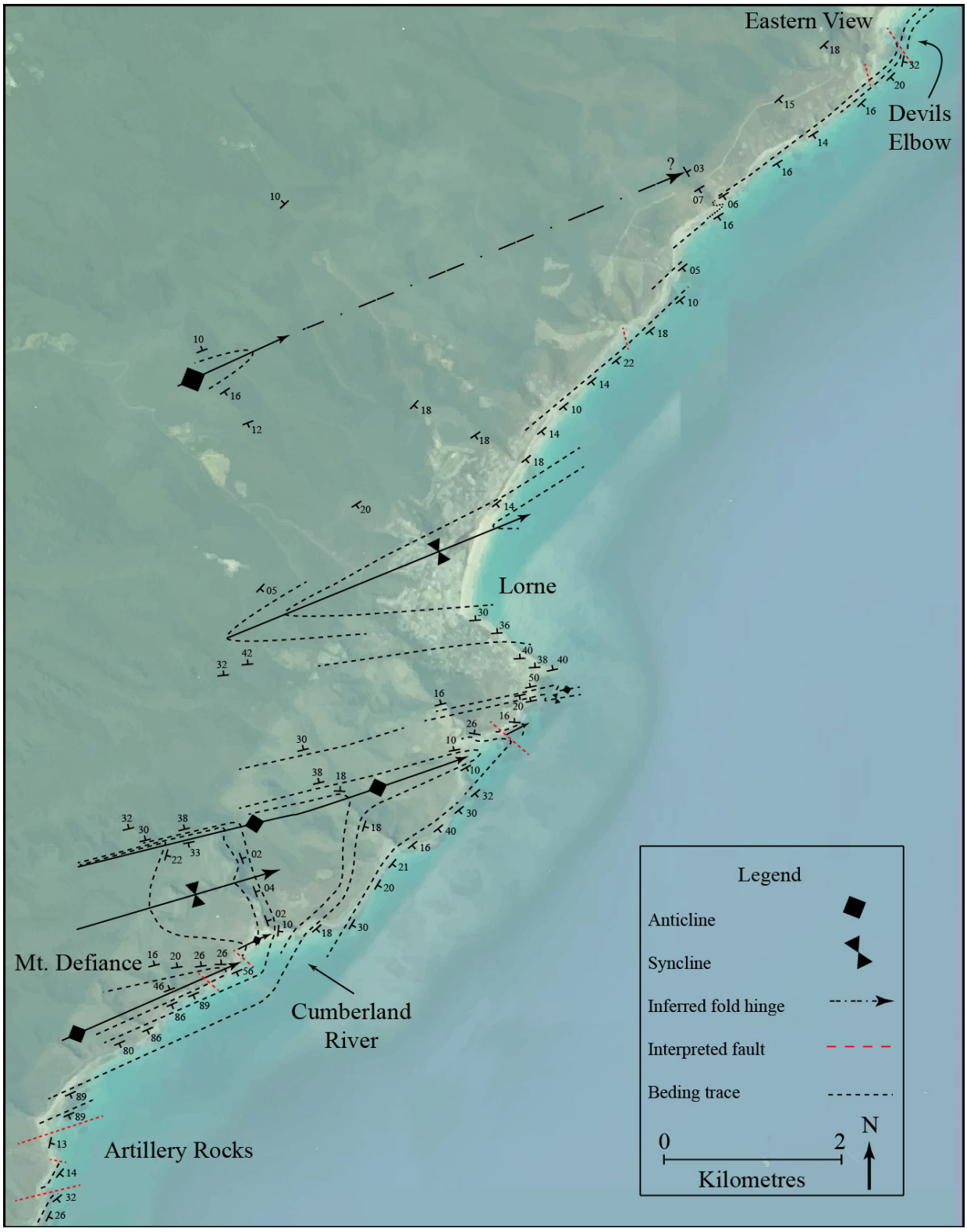


**Figure 1.14:** Interpretation of the major structural trends between Lorne and Eastern View based on field measurements listed in Appendix 1. The southern coastal and inland areas are dominated by NE-trending anticlines and synclines, with overprinting ~NW-oriented sinistral faults. Additionally shown are interpreted NE-oriented inverted normal faults. The area shown on the map is underlain by the Eumeralla Formation. For greater resolution of interpreted structural map see Map Pocket 2.

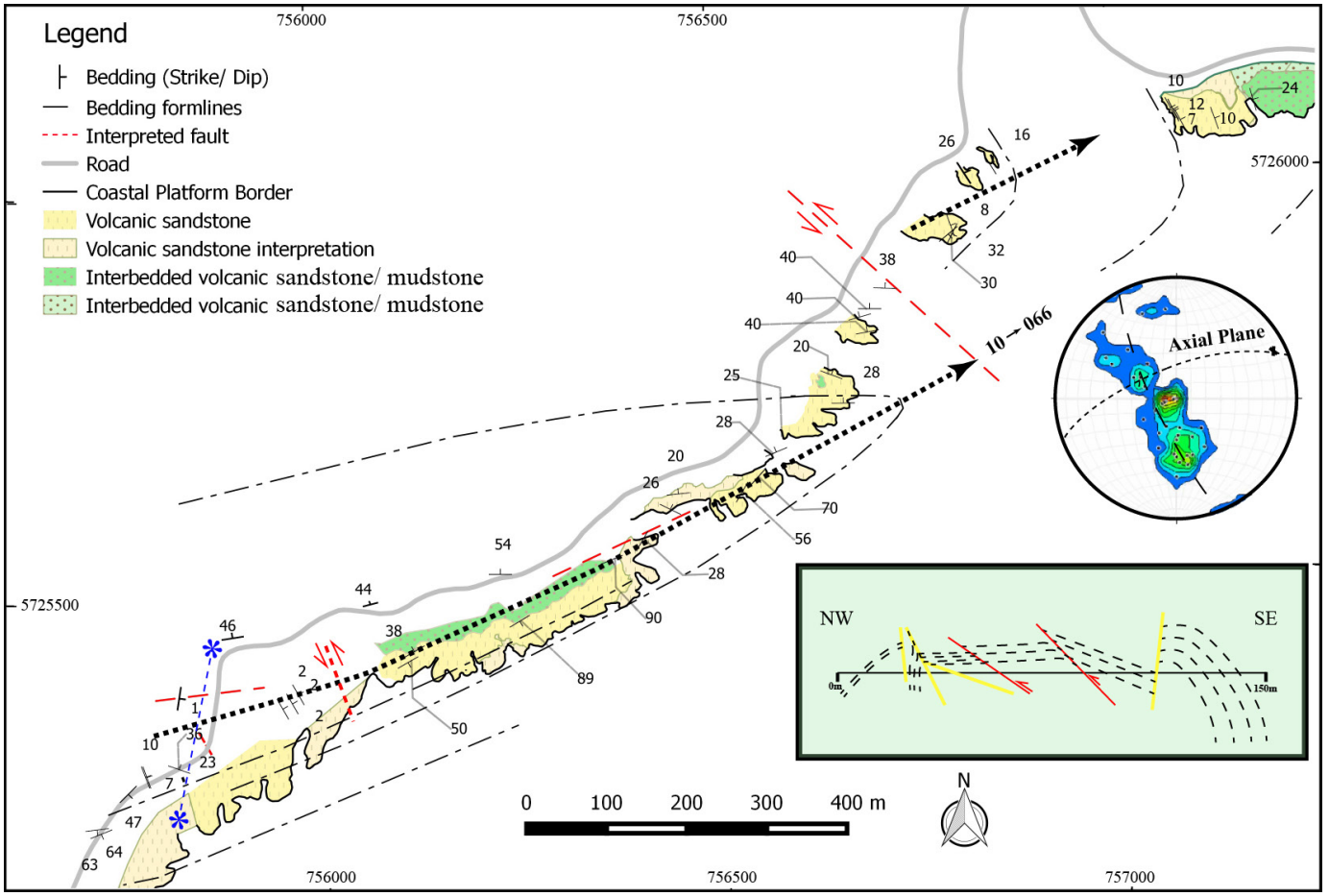


**Figure 1.15:** Geological map of coastal platforms and road outcrop along Mt. Defiance (south of Cumberland River). Inset lower hemisphere equal area stereographic projection (stereonet) plots poles to measured bedding and corresponding 1% area contours. A cross section of the hinge of the Mt. Defiance Anticline is shown for a section cropping out along the road, after (Vergunst, 2012) with location on the map indicated by a blue (dashed) line. Within the cross section black lines indicate bedding, yellow lines indicate major calcite veins and red lines indicate thrust faults. For increased resolution see Map Pocket 1.

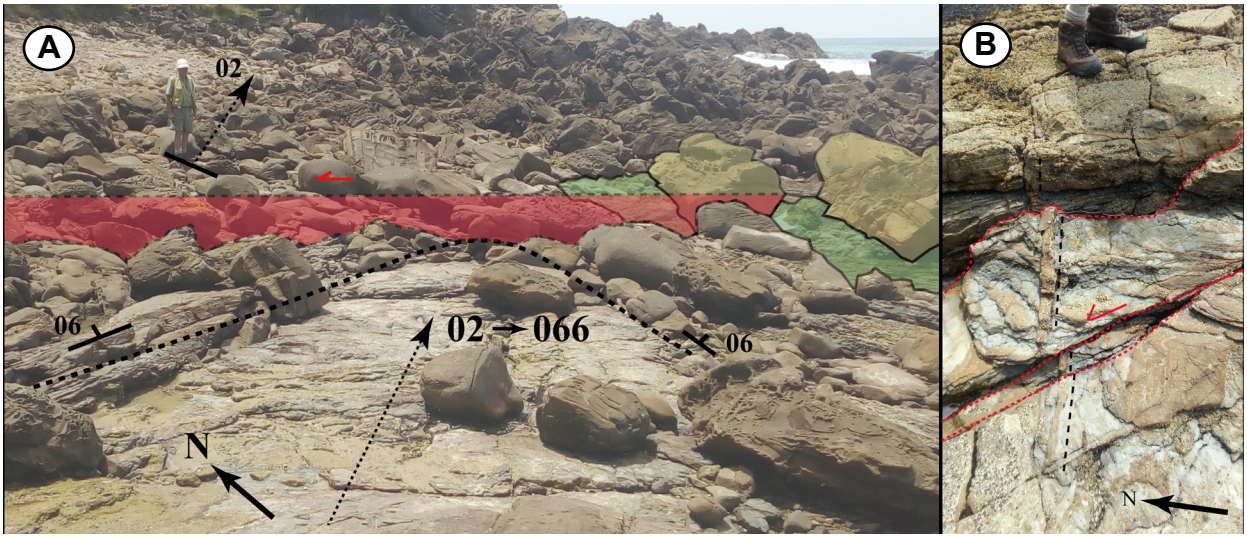


**Figure 1.16:** (A) The Mt. Defiance fold hinge (dashed arrow) showing ~6m structural offset (54H 0755946E 5725366N) WGS84, with fault shown in red, person for scale. Photo taken along the coastal platforms at the SW end of Figure 1.15. (B) Sinistral offset of sandstone injection structure (54H 0756642E 5725757N) WGS84.

### 1.5.3 Devils Elbow (Eastern View coastal platforms)

The Devils Elbow locality is located immediately south of Eastern View and ~8.5 km northeast of Lorne (Figure 1.14), where a sharp bend in the road exposes an outcrop of moderately-steeply dipping (47-60°SE) Eumeralla Formation that is notably steeper than that observed ~500 m northeast (~18°SE) at Spout Creek (55H 0241479E 5737304N). The coastal platforms below the Devils Elbow road outcrop consist of interbedded volcaniclastic sandstones and mudstones (Figure 1.17A/B) that strike northeast (030°) and dip moderately (40°) southeast. Towards the southern margin of the platform the bedding orientation gradually becomes more east-west oriented (070°) and abruptly steeper (~66-52°SE).

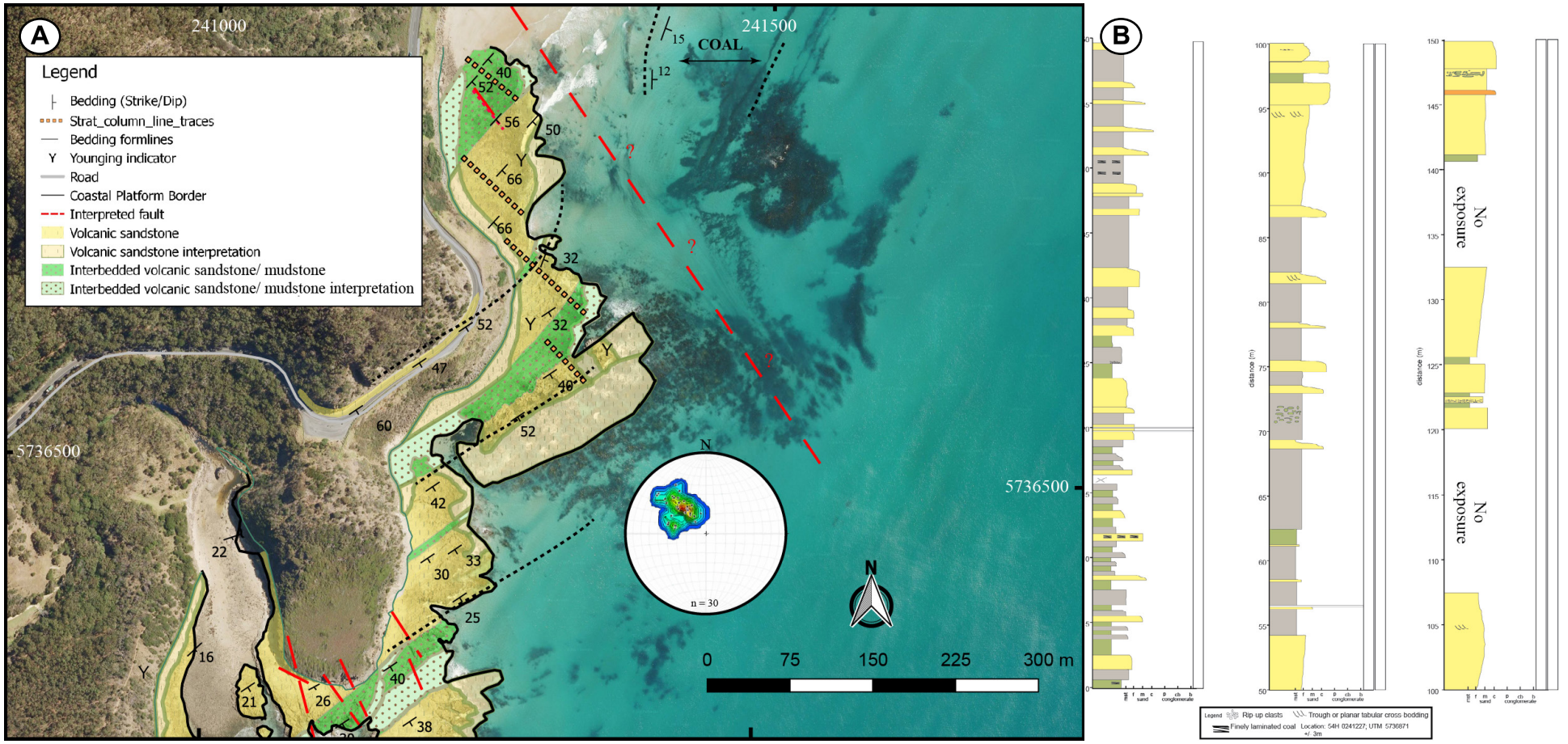


**Figure 1.17:** (A) Geological map of coastal platforms below Devils Elbow with an included lower hemisphere equal area stereographic projection (stereonet) of poles (with corresponding 1% area contours) to measured bedding. For greater resolution see Map Pocket 1. (B) Sedimentary stratigraphic column based on indicated location along the Devils Elbow coastal platforms. For greater resolution of stratigraphic logs see Appendix 2.

Immediately northeast of Devils Elbow, two dark black coal beds are exposed along the beach (Figure 1.17A). The strike of these gradually change from approximately 044° to 024° approaching the Devils Elbow platforms, but are not observed along the platforms. The steep dips of the sedimentary rocks along the Devils Elbow platforms were previously interpreted by Cooper (1995) to be due to a north-northeast (00° to 042°) trending monocline, verging towards the NW. However, as stated by Medwell (1971), the interpretation of the fold position is unclear. Furthermore, bedding measurements collected in this area (Figure 1.17A) are not consistent with significant folding of the sedimentary rocks.

Several NW-SE oriented (150/90) faults with sinistral strike separations (~15 cm offset) occur within the interbedded sandstone and mudstones exposed on the platforms (Figure 1.18A). Several large (>50m long) NW-SE oriented fractures also occur, and contain breccia (with a 5-8m wide deformation zone) and vuggy calcite veins approximately 1-4 cm thick (Figure 1.18B).

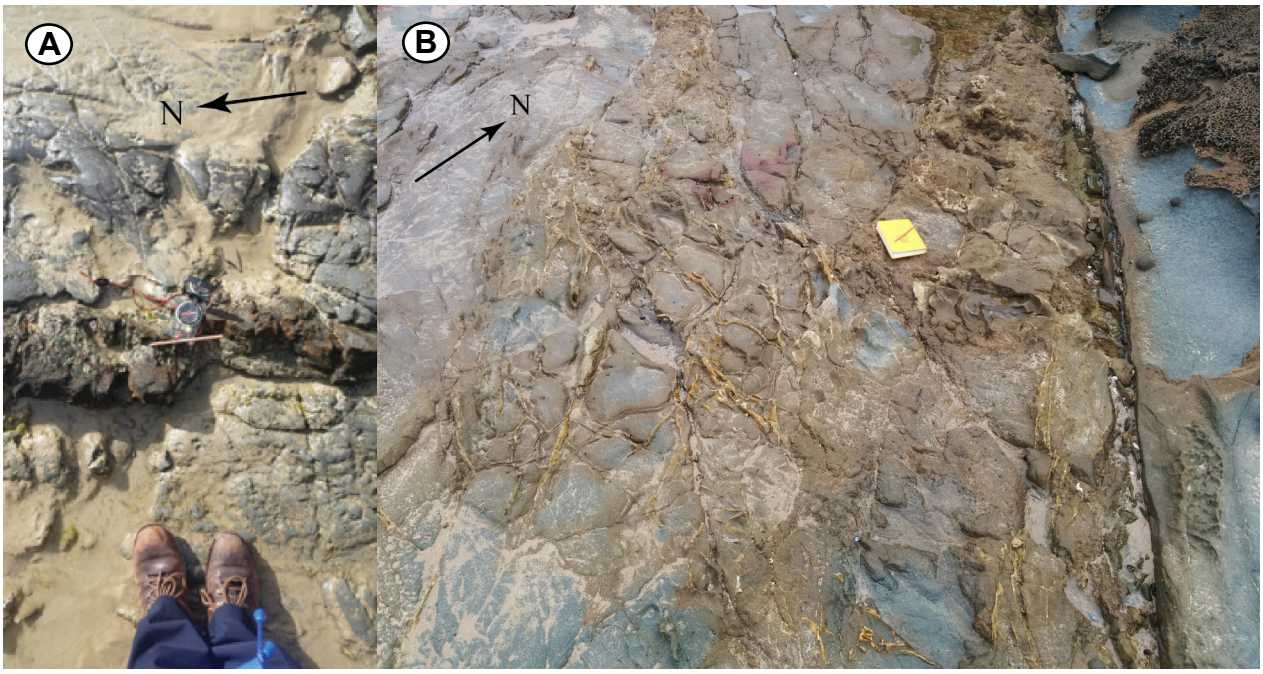


**Figure 1.18:** (A) Sinistral fault (150/90) offsetting interbedded volcaniclastic sandstones and mudstones within the Demons Bluff coastal platforms (55H 0241227E 5736871N). Note the compass for scale. (B) Brecciated material with vuggy calcite veins (55H 0241076E 5736306N). Notebook for scale.

### 1.5.4 Younger sequence (Cenozoic sedimentary rocks)

Previous interpretations by Smith (1998) and Holdgate et al. (2001) suggest that within the Anglesea region the Eastern View Formation occurs within a gentle, southeast plunging basin structure, with more than 100 m of total vertical thickness exposed within the (Anglesea) Alcoa coalmine (Figure 1.19). Given the lack of significant Eastern View Formation outcrop outside of the Alcoa coalmine, structural contours of the uppermost coal surface are shown for the inland Anglesea region (Figure 1.19) and provide a means of comparing the inland structure with coastal observations. The orientation of the inland structure compares well with the very low amplitude folds observed along coastal outcrops, with only minor discrepancies observed along the southern Anglesea Beach where the sedimentary rocks dip continuously southwest (Figure 1.19). Along the coastal outcrops most deformation was observed within the Angahook Formation.

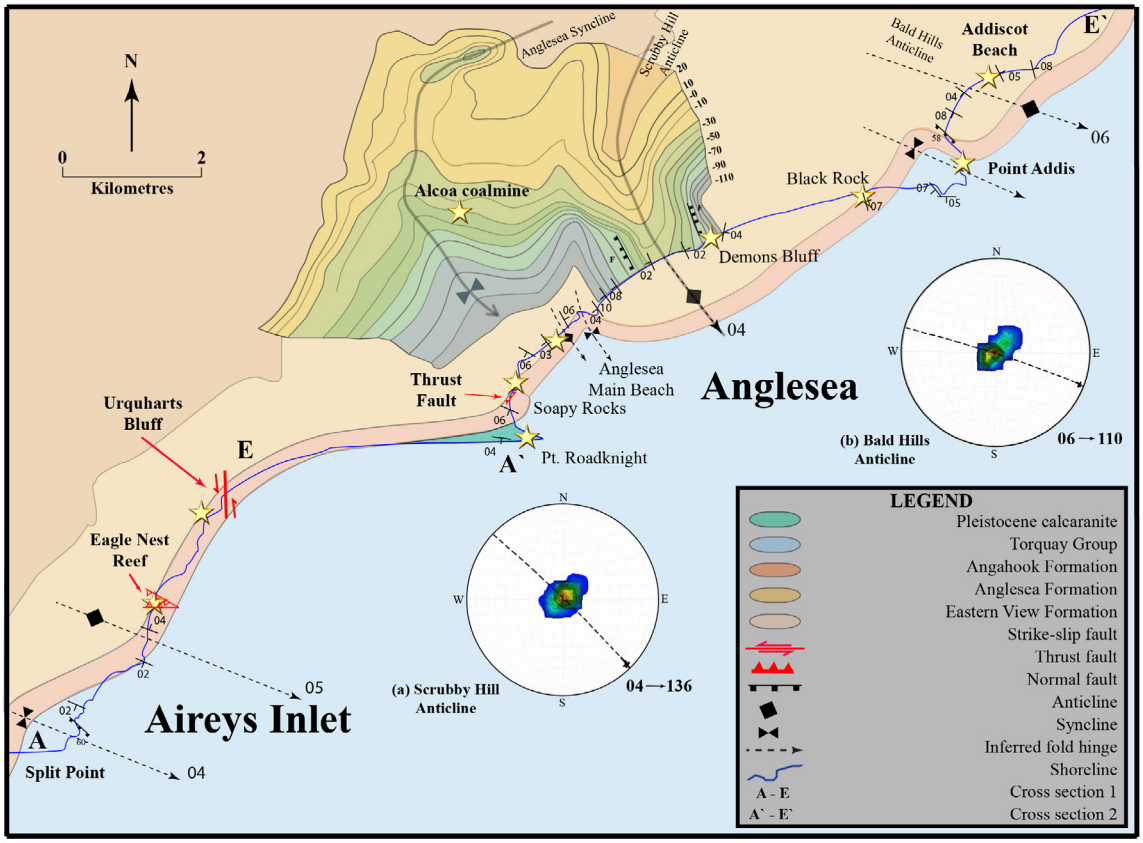


**Figure 1.19:** Interpretation of the major structural and lithological trends between Aireys Inlet and Anglesea based on field measurements. A structural contour map of the top surface of coal seam A depth is shown for the inland Anglesea area, modified after Smith (1998), with inland boundaries of stratigraphic units modified from Abele (1979). Note markers A-E and A′- E′ oriented ~parallel to the coastline, defining the location the cross-sections provided in Map Pocket 2. Included are lower hemisphere equal area stereographic projections (stereonet) of poles (with corresponding 1% area contours) to bedding measured by traditional mapping within (a) The Scrubby Hills Anticline, and (b) The Bald Hills Anticline (Addiscot Beach). Key locations referred to in this study are each indicated with a gold star. For greater resolution of interpreted structural map see Map Pocket 2.

### 1.5.5 Angahook Formation

At Eagle Nest Reef (Figures 1.19 & 1.20A) a ~40 m thick stratigraphic section, consisting of ~20 m of coarse-grained, basaltic tuff with a cream-coloured surficial coating of material derived from the overlying ~15m section of bioclastic grainstone (calcarenite) is exposed within the coarse-grained basaltic tuff; different layers contain different-sized pebble clasts. The basaltic tuffs (Angahook Formation) and bioclastic grainstone (Torquay Group) are separated by a ~5 m section of basaltic conglomerate and laminated brown quartz sands.

Two ~E-W oriented reverse faults (094/40N and 124/ 59SSW) offset bedding ~0.4 m, with local bedding drag (Figure 1.20A). Fracture sets within this location can be subdivided into two preferred orientations; one oriented at a high angle to the bedding and clustered around (096/40N) and the other oriented (~010/ 90), with ~10-20 cm spacing.

Fractures are generally barren, however, significant cementation occurs along bedding planes and within large, vertical vein sets observed immediately north of the outcrop (Figure 1.20B), and with the mineral composition in each of these vein sets varying considerably. Bedding plane mineralisation consists of fibrous calcite crystals, with smooth boundaries and large length-width ratios (Figure 1.20A). Calcite growth is perpendicular to the bedding plane, as indicated by the strongly preferred growth orientation within the crystals. The second vein set identified (010/90) is composed of a light cream-coloured kaolinite mineralisation (1-10 cm thick) that typically contains green smectite material with inclusions of pearl-green altered basalt (Figure 1.20B).

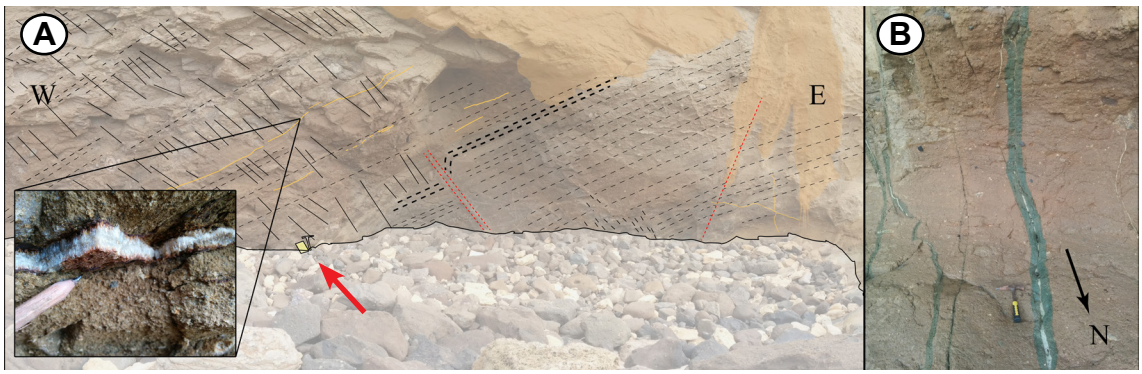


**Figure 1.20:** (A) East-west oriented photo of coarse-grained basaltic tuff (Angahook Formation, Demons Bluff Group), with a cream-coloured surficial coating derived from the overlaying bioclastic grainstone (Torquay Group) (55H 0248437E; 5739732N). Two reverse faults (094/40N and 124/ 59SSW) offset bedding. Note the yellow notebook and hammer for scale (red arrow). (B) Green smectite vein with inclusions of pearl-green altered basalt (55H 0248431E 5739746N). Note the hammer for scale.

To the north, the coastal outcrops below Urquharts Bluff (Figures 1.19 & 1.21A) host ~20 m of massive, coarse-grained, volcaniclastic sandstone (lapilli-tuff?) (Angahook Formation), with pebbles, secondary calcite infilling and some fine-grained basaltic clasts. This is overlain by ~15 m of weathered, loamy siltstone with Liesegang rings (Figure 1.21B), slump structures and brown quartz sands. The volcaniclastic sediments and slump structures (Angahook Formation) contain several sub-vertical fractures filled with weathered, black, fine to coarse grained, unsorted sandy material (sand injection structures?) oriented ~ENE-WSW (077/90), that are offset ~15cm by a series of small faults with sinistral strike separation (016/90) (Figure 1.21C). Within the cliff exposures along the southern platform, the coarse-grained volcaniclastic sandstone hosts sub-horizontal fracturing (186/06W).

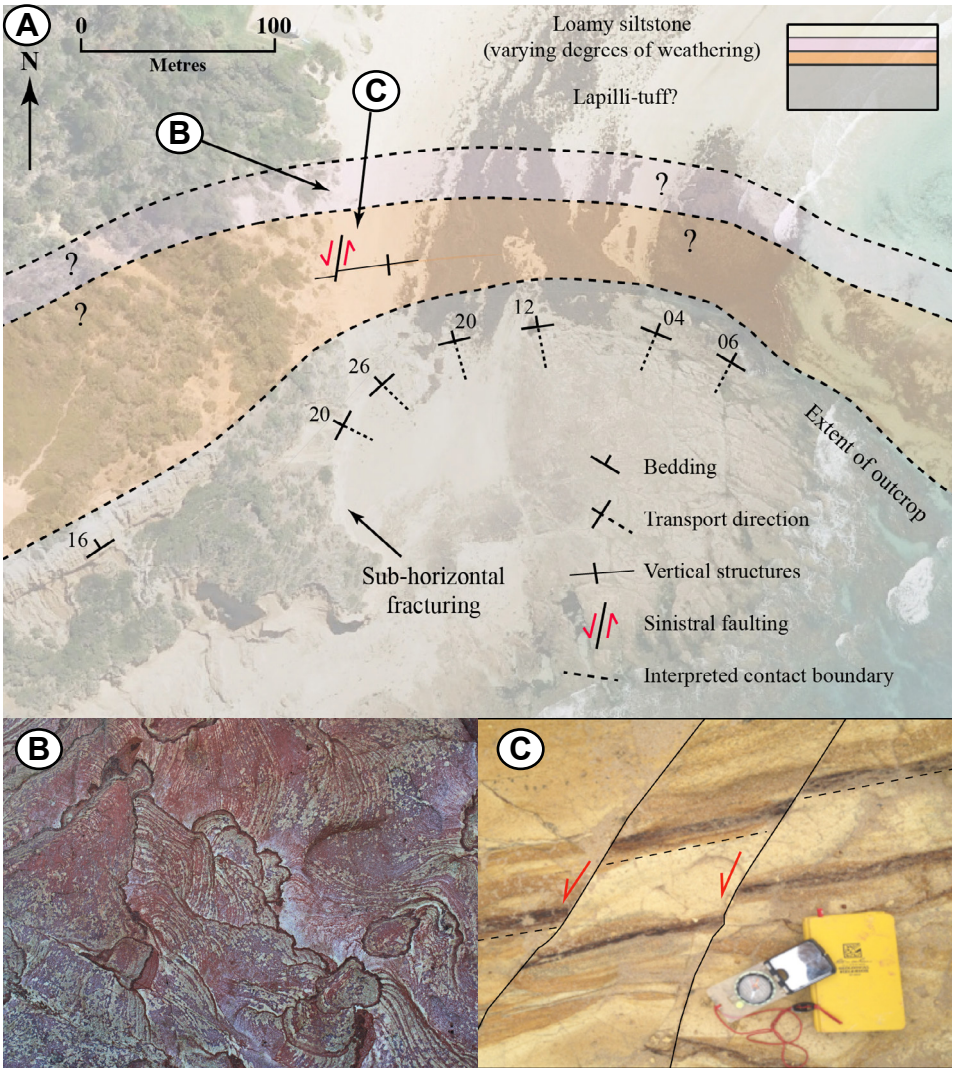


**Figure 1.21:** (A) Geologic map of Urquharts Bluff (Aireys Inlet) indicating the transport direction of the volcaniclastic flow (Demons Bluff Group, Angahook Formation) (55H 0249463E; 5741586N). (B) Weathered loamy siltstone slump structures and (A) Slump structures offset by sub-vertical fractures with sinistral strike separation.

A previously unreported low angle thrust fault is exposed ~500 m south of the Soapy Rocks locality (Figures 1.19 & 1.22) and occurs in black-brown, loamy siltstone and sandstone containing Liesegang rings and channel erosion features (Angahook Formation). This thrust strikes 040°, dips 12° northwest, and displaces bedding ~1-2m. Both the lower and upper bedding surface are folded against the fault surface (Figure 1.22A, B).

**Figure 1.22:** Thrust fault (55H 0253761E 5743604N) WGS84. (A) drag folding of the upper beds (arrow) in the hanging wall against the fault surface (red-dashed line). (B) drag folding of the lower beds in the footwall. Photograph oriented ~west.

## 1.6 Discussion

A broad comparison of the regional structural trends observed throughout each stratigraphic unit has shown that the Cretaceous sedimentary rocks (between Artillery Rocks and Eastern View) have experienced a significantly greater amount of fold-related deformation compared to the Cenozoic sedimentary rocks (Figures 1.14 & 1.19).

### 1.6.1 Structural trends within the Cretaceous sedimentary rocks

Several northeast-trending folds are exposed along the southern coastal platforms and inland areas in the Lorne region (Figure 1.14). There is an average ~3km spacing between the axial planes of each anticline, that increases towards the northwest, while the limited exposure prevents estimates of the average amplidude. The formation of these folds has been previously attributed to the reactivation and reversal of underlying (Early Cretaceous) normal faults (Hall & Keetley, 2009; Matthews, 2015), while abrupt changes in the bedding orientation (Figure 1.14) have previously been attributed to fault offset in areas such as Cumberland River (Medwell, 1971; Cooper, 1995). However, few studies have described the orientation of these significant, NW-SE oriented strike-slip faults that offset the southern fold hinges, for example at Mt. Defiance (Figure 1.15). Furthermore, NW-SE oriented strike-slip faults observed along the Devils Elbow platforms (Figure 1.18A), combined with changes in the strike of bedding (Figure 1.17), suggest that fault movement immediately northeast of the Devils Elbow coastal platforms may have caused rotation of bedding on either side of the fault trace (i.e. drag folding).

### 1.6.2 Structural trends within the Cenozoic sedimentary rocks

Contrary to the intensive, fold-related deformation observed along the southern coastal platforms, folding within the younger stratigraphic units (Figure 1.19) is restricted to very low amplitude folds exposed at Aireys Inlet and Anglesea (Map Pocket 2). The Anglesea Syncline and Scrubby Hill Anticline (Figure 1.19) are upright and open (amplitude ~50 m and wavelength ~6km) and plunge ~04° towards ~144°.

On the basis of a low angle unconformity at the top of the Eastern View Formation (Figure 1.23),

previous studies by Smith (1998) and Holdgate et al. (2001) attributed the gentle folding to a late Eocene (ca. 39.4-38Ma) tectonic event. However, these studies did not provide a tectonic framework for this inferred regional shortening.

The low amplitude of these folds could be due to, a) ~NE-SW oriented shortening or, b) they are not of tectonic origin, but rather an expression of the underlying basement topography. While there is little evidence for ~NE-SW directed shortening both locally, or more regionally within the basin, in the later case, the formation of ~NW-SE oriented depocentres within the Anglesea region may have coincided with Late Cretaceous, NE-SW extension within the Otway and Bass Basins (Briguglio et al., 2013). Holdgate et al. (2001) interpreted the thickest sections of the Eastern View coals to be located within these inland depocentres (Figure 1.23). Based on depocentre-bounding faults observed by Smith (1998) within the Alcoa Coalmine (Figure 1.19), NW-SE oriented graben-bounding faults appear to have controlled deposition of the Eastern View Formation sedimentary rocks (Figure 1.24A).

The Eastern View Formation was then progressively overlain by the Anglesea Formation (Figure 1.24B), the Angahook Formation (Figure 1.24C) and the Torquay Group (Figure 1.24D).

The gentle folds observed within the Anglesea region are therefore likely to be the result of differential compaction of the overlying (post Campanian) sedimentary rocks against the more competent, feldspathic-rich volcaniclastic sandstones of the underlying Eumeralla Formation. The positions of the anticlines are inferred to coincide with 'ridges' in the underlying Eumeralla Formation, interpreted by (Holdgate et al., 2001) from coal borehole data within this region (Figure 1.23A/B), rather than forming during tectonic shortening. Additionally, abandoned channels could provide further increased accommodation space for the deposition of carbonaceous material during the Late Cretaceous to Early Eocene (Anglesea Syncline).

Additionally, the thrust faults observed along the Anglesea shoreline (Angahook Formation, Figure 1.22), appears to have resulted from NW oriented shortening after lithification of the Oligocene-aged sediments (post-ca.28.7Ma).

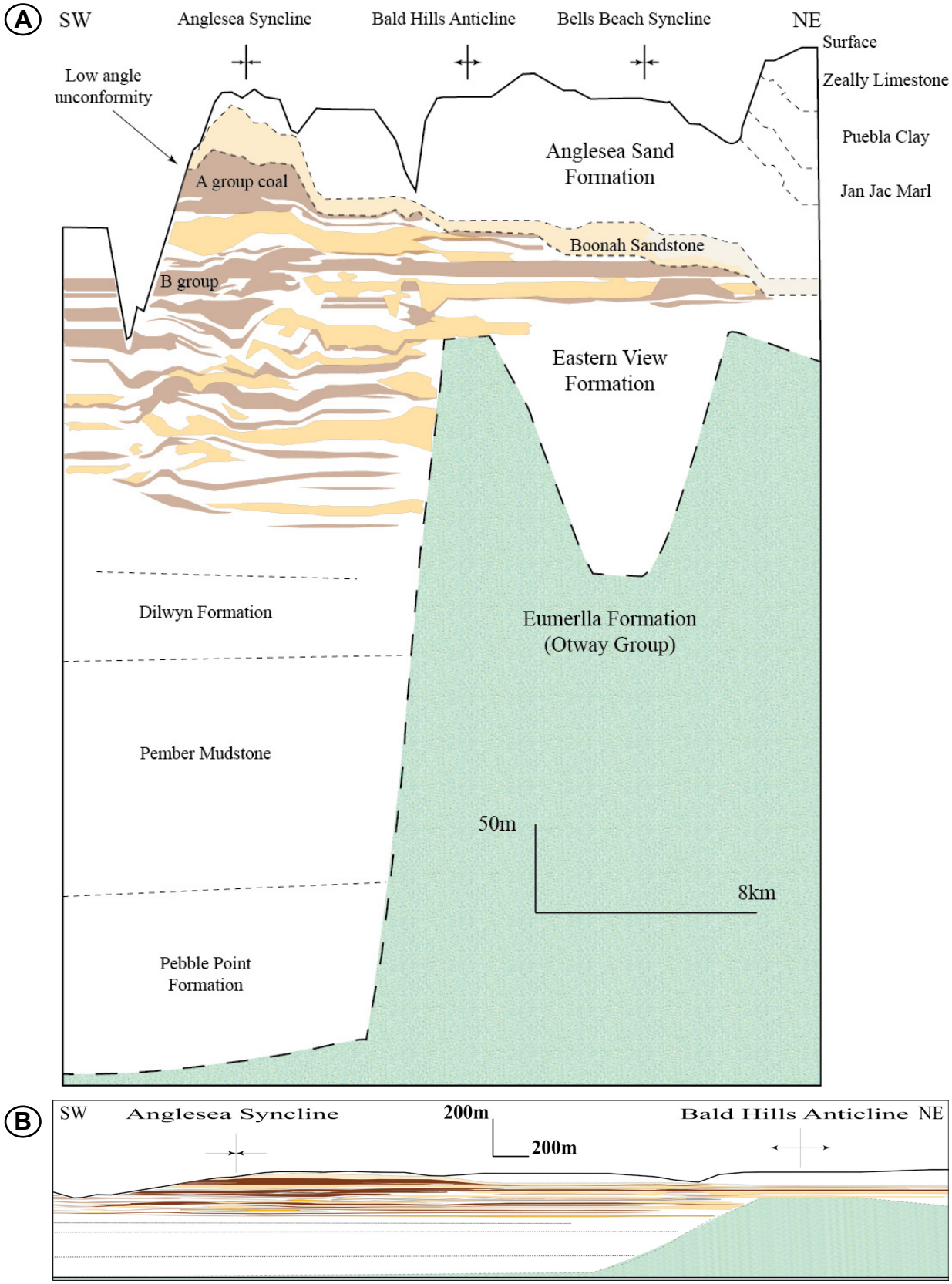


**Figure 1.23:** (A) Regional cross section of Cenozoic deposits within the Anglesea region, after Holdgate et al. (2001), with interpreted stratigraphic correlations of sequence boundaries, derived dominantly from the coal borehole data of Meyer (1982) and Stanley (1994). Given that this interpretation has an applied 73X vertical exaggeration, a second interpretation (B) has been modified from Holdgate et al. (2001) to remove the vertical exaggeration and highlight the very low amplitude of the folds. Locations of minor structural elevation can also be resolved within the basal Cenozoic unconformity depth maps provided by Matthews (2015).

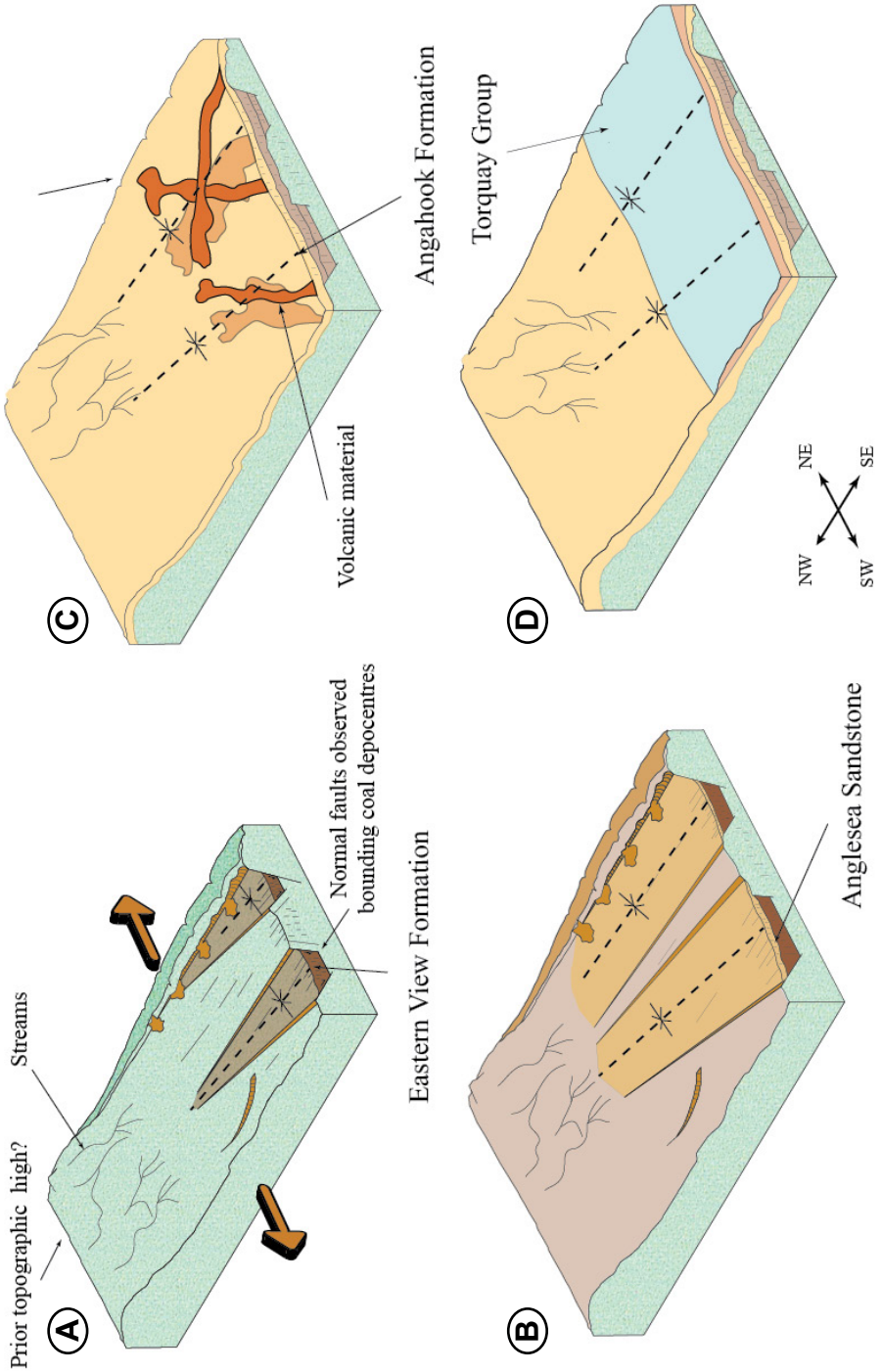


**Figure 1.24:** (A) Late Cretaceous - early Eocene ~NE-SW extension within the Anglesea region, forming NW-SE oriented depocentres that are interpreted to have controlled deposition of the Eastern View Formation. (B) Late Eocene deposition of the Anglesea Sandstone. (C) Early Oligocene incursion of volcanic material (Angahook Formation) . (D) Late Oligocene - middle Miocene Torquay Group deposition.

## 1.7 Conclusions

A regional unconformity separates older (Early Cretaceous) Eumeralla Formation rocks in the south from younger (late Cretaceous to late Cenozoic) rocks (Eastern View Formation, Demons Bluff Group and Anglesea Formation) in the north. Several key differences in deformation and structural trends are observed between the older and younger rock sequences.

(1) Northeast oriented folds are the dominant structure within the Eumeralla Formation (Figure 1.14). These appear to be overprinted by NW-SE oriented strike-slip faults (Figure 1.15).

(2) The younger Eastern View Formation and Demons Bluff Group are significantly less folded, with only very gentle, ~SE oriented folds exposed along coastal outcrops (Figure 1.19).

(3) The orientation of coastal bedding appears to coincide well with changes in the inland structure (Figure 1.19), suggeting that the inland structure is represented by very gentle, ~SE oriented folding.

(4) Late Cretaceous – early Eocene NE-SW extension (Figure 1.24A), combined with differential compaction, may have assisted in forming gentle, ~SE-trending folds around Aireys Inlet and Anglesea.

(5) Faults observed within the Angahook Formation indicate a NW-SE (Figure 1.22) oriented shortening event occurred post. ca 28.7Ma.

MONASH University

# Declaration for Thesis Chapter 2

Declaration by candidate

In the case of Chapter 2, the nature and extent of my contribution is as follows:

| *Nature of contribution* | *Extent of contribution (%)* |
|---|---|
| Main research, data collection, data analysis and interpretation | 65% |

The following co-authors contributed to the work. If co-authors are students at Monash University, the extent of their contribution in percentage terms must be stated.

| *Name* | *Nature of contribution* | *Extent of contribution (%)* |
|---|---|---|
| Stefan A. Vollgger | UAV pilot, construction of 2D orthophotography/ significantt contribtion to section 2.3.2 | 15% |
| Mike Hall | Supervisory role | 10% |
| Alexander R. Cruden | Supervisory role | 10% |

The undersigned hereby certify that the above declaration correctly reflects the nature and extent of the candidate's and co-authors' contributions to this work*.

Candidate's signature [redacted] Date: 05/08/2017

Main Supervisor's signature [redacted] Date: 05/08/2017

# Chapter 2

Influence of stratigraphic and structual position on the timing and characteristics of fractures along the eastern Otway coastline, Great Ocean Road, Victoria

Joel Vergunst, Stefan A. Vollgger, Mike Hall & Alexander R. Cruden

Department of Earth, Atmosphere and Environment, Monash University, Victoria, Australia, 3800

Email: joel.vergunst1@monash.edu, mike.hall@monash.edu

## 2.1 Introduction

The purpose of this chapter is to compare fracture orientations at different stratigraphic and structural positions along the Otway coastline (Figure 2.1), in order to determine the stress conditions that were experienced by the Mesozoic and Cenozoic rocks in the study area during fracture formation. Given the lack of previous work on this topic within this region, the influence that lithology, burial depth and varying tectonic stress conditions have had on the formation of the coastal fracture systems will therefore be considered.

Three study areas have been chosen for comparison based on their different stratigraphic and structural positions. The St. George Anticline and Artillery Rocks localities (Figure 2.1) are located within the oldest stratigraphic unit (Eumeralla Formation) and are at different structural positions with respect to regional folding. Compared with the St. George fold hinge, the southern Artillery Rocks locality is positioned on a shallow dipping (12-18°SE) fold limb that is structurally distal from the nearest (Mt. Defiance) anticline hinge (Figure 2.1). The Soapy Rocks locality (Figure 2.1) by contrast occurs within an unfolded section of younger (Angahook Formation) sediments that are, as explained in Chapter 1, separated from the older stratigraphic unit by a major unconformity. Therefore a significant time gap occurs between these two sequences, so that when these are compared it will be possible for potentially different aged fracture sets to be distinguished. Moreover, documenting the orientation and characteristics of fracture populations along the Otway coastline, in conjunction with their relative timing, allows paleostress orientations to be estimated as a function of time.

Reconstructing the tectonic history of folded and fractured reservoirs requires tight constraints on the timing of deformation, and a sufficient understanding of how the distribution of fracture populations within the reservoir is influenced by their stratigraphic and structural position. The relative timing of deformation and vein emplacement along the Otway coastline has implications for the hydrocarbon prospectively, as vein cementation can severely reduce permeability, while fault and fracture formation may mechanically enhance permeability within the sub-surface (Evans & Fischer, 2012).

Following the fold-fracture relationships described by Stearns (1968), field observations of the distribution and density of present-day systematic fracturing can be linked to fracture formation during fold growth,

while separating out probable pre-existing or post-dating fracture sets. As such, this will allow for changes in the maximum and minimum stress directions to be discerned from field observations. Of the five potential syn-folding fracture sets predicted to form within the model of Stearns (Stearns, 1968), extensional fractures striking perpendicular (a-c) or parallel (b-c) to the fold hinge line (Figure 2.2) (Hancock, 1985) are the most commonly recognised in the field (Florez-Nino et al., 2005; Bellahsen et al., 2006; Cooper et al., 2006; Hayes & Hanks, 2008; Inigo et al., 2012; Tavani et al., 2012; Awdal et al., 2013).

A-c fracture populations form parallel to the maximum principal stress direction during the initial stage of shortening and fold development and are commonly observed as the oldest syn-folding fracture set (Guiton et al., 2003; Bellahsen et al., 2006; Hayes & Hanks, 2008; Inigo et al., 2012; Awdal et al., 2013). Furthermore, based on the work of Savage et al. (2010), who investigated joint pattern variations within the Sheep Mountain Anticline of Wyoming, USA, after the bedding units have undergone a significant amount of pure bending, effective tensile stress conditions will be generated within the outer arc of the fold, which will initiate b-c fracture formation oriented parallel with the fold hinge.

The use of UAVs (Unmanned Aerial Vehicles) for high-resolution photogrammetry enables the collection of large amounts of data within fracture systems exposed in coastal outcrops (Vollgger & Cruden, 2016). When combined with traditional mapping this data contributes to a more comprehensive and detailed understanding of fracture systems that may develop within advanced rift systems, or folded regions.

## 2.2 Sedimentological history

### 2.2.1 Eumeralla Formation (St. George Anticline/ Artillery Rocks)

The St. George Anticline (Figure 2.1) is hosted within Early Cretaceous (~113-100 Ma) volcaniclastic-rich, fine to medium grained sandstone, with only minor sections of interbedded volcaniclastic sandstone and mudstone.

The southern Artillery Rocks locality (Figure 2.1) is approximately 9km south of Lorne and ~500m south of Jamieson River (Map Pocket 1), and is exposed along a ~250m section of wavecut platform that represents the oldest stratigraphic section of Eumeralla Fm encountered along the coastal platforms. The largely homogeneous, fluvial volcaniclastic sediments within this locality are of a similar age to those encountered at the St. George locality. Tafoni weathering (honeycomb weathering) and diagenetic carbonate concretions (nodules) (Gregory et al., 1989; Duddy, 2010) are common surficial features within this locality.

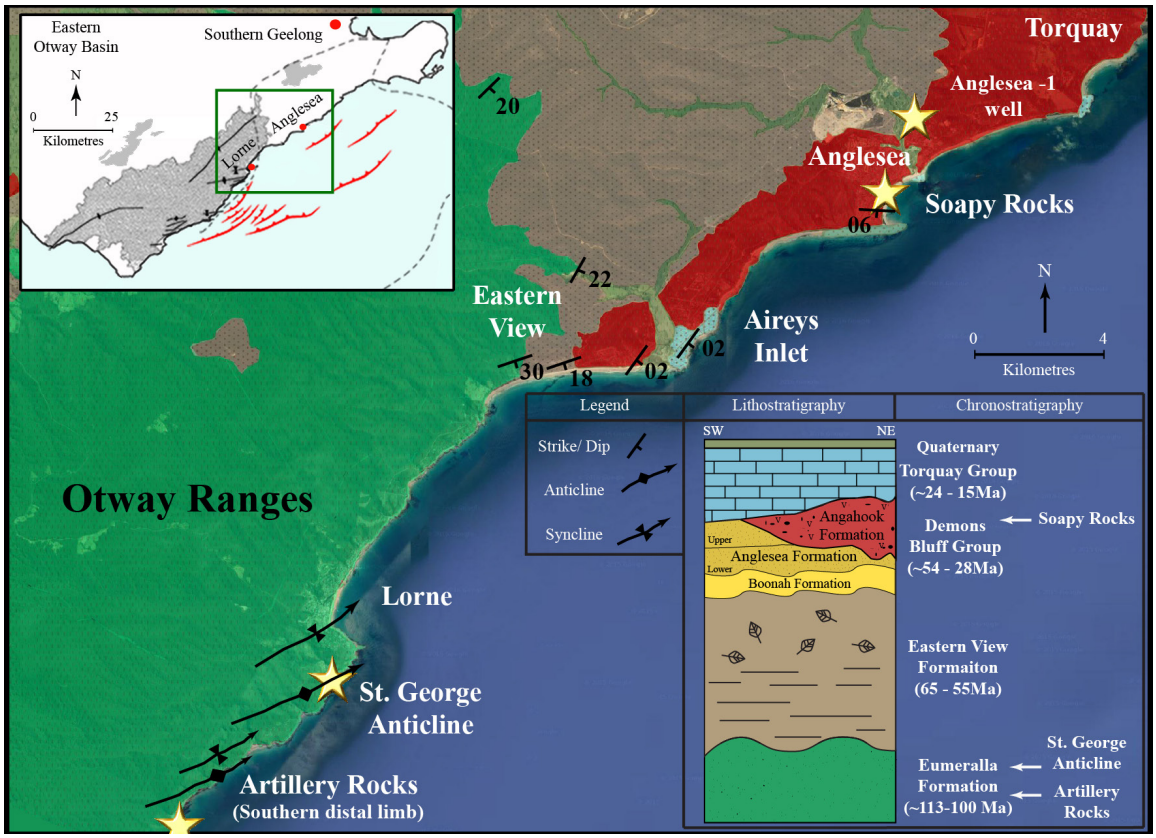


**Figure 2.1:** Geological map of the coastal regions of the eastern Otway Basin. The stratigraphy is provided in the lower right, modified from Abele et al. (1988) & McLaren et al. (2009). Studied field areas (Artillery Rocks, St. George Anticline and Soapy Rocks) as well as the location of the Anglesea-1 well are marked as a star. The Eumeralla Fm (green) hosts extensive NE-oriented folds, while the Angahook Fm (red) is significantly less deformed. Within the mini-map (top left corner) offshore inverted normal faults are shown in red, based on seismic interpretations by (Matthews, 2015). A green box indicates the position of the field area.

### 2.2.2 Angahook Formation (Soapy Rocks)

Soapy Rocks (Figure 2.1) is located approximately 1.3 km southwest of the Anglesea town centre and hosts the Cenozoic Angahook Fm of the Demons Bluff Gp (ca. 28.7 Ma).

At the Soapy Rocks locality, fine-grained, thinly interbedded sandstones and mudstones (~5m) are unconformably overlain by volcaniclastic debris flows, containing clasts of basalt and coarse-grained sandstone (~5m). Overlying the volcaniclastic debris is a succession of cross-bedded, coarse sandstone containing reworked lithic fragments of volcanic material. This cross-bedded sandstone is, in turn, overlain by shallow dipping, finely laminated and moderately sorted, white-grey sandstone (Figure 2.3).

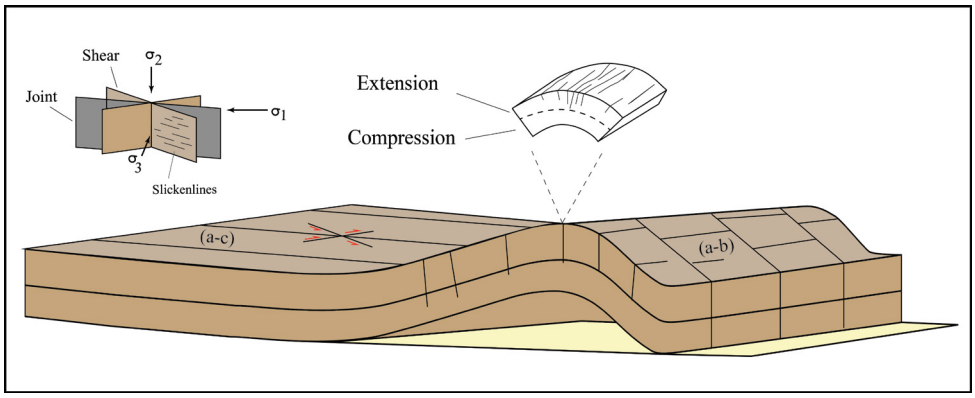


**Figure 2.2:** Syn-folding fractures, (a-c) fractures oriented perpendicular to the fold strike forming parallel to regional shortening, and (a-b) fractures oriented parallel with the fold strike forming as tensile stress conditions are generated during outer-arc extension of the fold hinge. Shear fractures often form slickenlines on the side of the slickenside surface.

**Figure 2.3:** Northeast side of Soapy Rocks (55H 0253787E 5743673N) – Angahook Formation volcaniclastics displaying the contact between grey-light brown debris flow (containing sand and mud clasts), and an overlying cross-bedded sandstone that fines up into a more laminated sandstone, with sub-vertical fracturing.

## 2.3 Methods

### 2.3.1 Fracture network analysis

In order to establish how changes in the maximum and minimum paleostress orientations have influenced the development of the coastal fracture systems, a significant number of joint and shear fracture measurements were acquired along wavecut platforms in the study area.

Fractures have been classified as either tensile or shear fractures based on field observations. For the purpose of this study, a fracture is classified as a tensile fracture (joint, Figure 2.2) where there is no discernable displacement along the fracture plane. Plumose structures further support these interpretations, as they are consistent with a fracture opening perpendicular to the fracture walls (Mode 1) (Pollard & Aydin, 1988). Interpretations of shear fractures are based on observed offset parallel to the plane of the fracture, as well as kinematic indicators or shear sense indicators (slickenlines, Figure 2.2). Fractures that form planar and parallel, or sub-parallel, to each other are considered to be fracture sets (Hancock, 1985).

Principal stress orientations have been interpreted from fracture orientations, attitudes, and crosscutting and abutting relationships. Fracture interactions allow for the relative age of fracture sets to be determined in the field, with younger joints abutting against the side of older joints (Hancock, 1985). Furthermore, crosscutting joints are considered to have formed contemporaneously, while shear-fractures post-date the fracture they offset. Field measurements of fracture relationships have been presented as a matrix representing the percentage and style of fracture interactions observed, for different fracture orientations at varying stratigraphic and structural positions.

In this study, the calculated distribution of fracture orientations is based on conventional field measurements combined with fractures analysed within UAV acquired high-resolution orthophotographs (covered further in Section 2.3.2). The mapping software QGIS (QGIS Development Team, 2015) was used to map and manually digitise fractures, after which circular histograms of fracture orientations were calculated using the ‘line direction histogram’ QGIS plugin by Tveite (2015). Fractures were grouped into 5° azimuth class intervals and weighted based on their segment line length, prior to calculating the mean orientation of the fracture sets from the average distribution of fracture clusters. The mean

orientations were used to define fracture groups, however, the group number has no bearing on the chronological order of fracture formation.

Victorian nearshore coastal bathymetry 2.5 m resolution DEM data (Victorian Department of Environmental, Land, Water and Planning, 2009) has been used to extend viewing of coastal platforms up to a depth of 20 m sub-surface, as the DEM captures the bathymetry to these depths (for further data processing details refer to Appendix 2).

Previous studies that documented fracture distribution in rocks (Pollard & Aydin, 1988; Priest, 1993; Florez-Nino et al., 2005) have routinely collected fracture data using only the linear traverse mapping methods of La Pointe and Hudson (1985), recording fracture data for fractures intersecting a single linear scanline between two measured control points. However, this method under-represents fracture sets oriented parallel or oblique to the scanline (Santos et al., 2015; Watkins et al., 2015) and requires the Terzaghi (1965) method in order to correct for this bias. For this study, fracture properties such as orientation, fracture fill and cross-cutting and abutting relationships, have been collected from field outcrops using a 10x10m square window sampling method, modified from the rectangular window sampling method described by Priest (1993), whereby all fractures are measured within the sampling area. Using a square sampling area has the benefit of collecting fracture data that are unbiased by fracture orientation (Watkins et al., 2015).

After the mean orientation of each fracture set has been established, the distance between fractures within each fracture set is measured along a 10m traverse within each sampling area (Appendix 3), at an orientation perpendicular to the mean orientation of each fracture set. Following the recommendations of Odling et al. (1999) the distribution of fracture spacing within each fracture set is calculated using the coefficient of variation, defined by:

$$Cv = SD/\bar{x} \qquad \text{(Equation 1)}$$

Wherein $\bar{x}$ is the average spacing between individual fractures of a fracture set and SD is the standard deviation of that average. A regularly spaced fracture distribution with only minor variability will result in a low standard deviation and $Cv < 1$, whereas a clustered fracture distribution will comprise a large standard deviation and $Cv > 1$, and lastly, a random fracture distribution will occur when $Cv = 1$.

The fracture density (D) of each fracture set measured in the field has been calculated using the following equation:

$$D = n/A \quad \text{(Equation 2)}$$

where n is the number of systematic fractures of a given set within the square sampling area and A is the area in $m^2$.

Field measurements of fracture density are complemented with qualitative fracture density maps, with a resolution of 5m, using the 'heatmap' QGIS plugin (QGIS Development Team, 2015).

### 2.3.2 Unmanned Aerial Vehicle (UAV) photogrammetry

A UAV photogrammetry workflow was employed to map and analyse different fracture populations in detail. This term was first introduced by Eisenbeiss (2009) to describe the digital photogrammetric processing of images that have been acquired by a remotely controlled, semi-autonomously or autonomously operating airborne platform. UAVs facilitate the systematic and inexpensive acquisition of high-resolution aerial photographic datasets at altitudes between ~10m and a few 100 m, therefore bridging the gap between terrestrial and aerial photography from manned aircraft or satellites.

UAVs allow to systematically capture a sequence of overlapping images from various (aerial) viewpoints which are subsequently processed using advanced computer vision algorithms, that compute spatial datasets such as high-resolution orthophotographs. These can be used for the accurate digital collection of fracture orientation data at higher fidelity and in a fraction of time compared to traditional mapping techniques, and thereby complementing field measurements. Depending on the distance between the camera sensor and the object, as well as the camera/lens setup, mm to cm spatial resolution datasets can be achieved. In this study we employed a commercially available multi-rotor UAV (Table 2.1) that was pre-programmed using the iOS app MapPilot (www.mapsmadeeasy.com) to autonomously collect photographs at a set altitude, speed and image overlap for all survey areas (Table 2.2).

**Table 2.1:** UAV photogrammetry equipment that was used in this study. The compact size and small weight makes it portable and therefore suitable for fieldwork in remote locations.

| | | |
|---|---|---|
| **UAV** | Manufacturer | DJI (www.dji.com) |
| | Model | Inspire 1 |
| | Type | Quadcopter (4 rotors/motors) |
| | Size (diagonal distance) | 559 to 581 mm |
| | Weight (battery included) | 2935 g |
| | Maximum speed | 22 m/s |
| | Battery | TB 47 (4500 mAh @ 22.2V) |
| | Flight time per battery (real world conditions) | 11 – 14 min |
| **Other equipment** | Gimbal | DJI Zenmuse X3 (3-axis gimbal) |
| | Camera | DJI X3 (CMOS, 12 Megapixel) |
| | Tablet computer for waypoint planning | Apple iPad Air |
| | Mission planning app | MapPilot |

Multi-rotor UAVs are able take-off and land vertically, hover over one spot and fly at low horizontal speeds. The latter is essential to maintain optimal camera settings such as shutter speed, ISO and aperture, to minimise motion blur and ensure high quality of images captured at low altitudes (Vollgger & Cruden, 2016). Additionally, a dampened electronic 3-axis gimbal that is attached to the UAV stabilises the camera and removes vibrations inherited from the motors and the airframe. The gimbal also enables the collection of perfect nadir images (camera pointing vertically down), even when the UAV pitches or rolls during the flight (Vollgger & Cruden, 2016). An image overlap of 60 % - 85 % is recommended to achieve spatially accurate datasets using digital photogrammetry (Agisoft LLC, 2015), depending on the scene complexity and geometry. All survey design parameters were based on suggestions outlined by Vollgger and Cruden (2016) and were laid out to attain an image overlap of at least 75% and to achieve a ground sampling distance of less than 2 cm / pixel.

Prior to the acquisition of aerial photographs by UAV, wooden markers were distributed throughout the survey area and used as ground control points. The coordinates of these points were surveyed for georeferencing purposes using either a dual frequency ProMark 500 RTK GPS device with an accuracy of 1-4 cm or a handheld Garmin etrex 10 GPS with an accuracy of 2-5 m, depending on equipment availability.

The surveys were flown in sunny to overcast weather and light to gentle winds that provided good

and safe operating conditions. The UAV take-off time was set to coincide with low tide to ensure maximum exposure of outcrops along the wave-cut platforms that host the coastal fracture networks. The camera was automatically triggered at a set interval, with the survey settings outlined in Table 2.2. After survey completion, all images (JPEG format) were downloaded from the camera and subsequently processed using Agisoft PhotoScan Professional version 1.2.5 (Agisoft LLC, 2015). The resulting orthophotographs were exported in geoTIFF file format for further structural analysis and interpretation in a GIS environment. Limitations in the resolution of the orthophotographs (1.5cm/pixel) did not allow the identification of mm-scale fractures, thus potentially under-representing certain fracture sets. Consequently, in order to ensure the validity of measuring fracture data within the orthorectified photomosaics, these data are additionally complemented with field measurements presented as stereonets plotted from field measurements.

**Table 2.2:** Camera settings and survey parameters for UAV photogrammetry northeastern Otway Coastline (Victoria, Australia). The camera automatically adjusts shutter speed in order to minimise motion blur. Note that 2 UAV flights (flight time: 10-12 min each) were necessary to cover the St. George Anticline area and to stay within the legal requirements (flying within line of sight). Prior to the acquisition of aerial photographs by the UAV, wooden markers and high visibility tape were used to mark ground control points.

| | | |
|---|---|---|
| **Camera** DJI X3 | Image resolution | 12 Megapixel |
| | Image width | 4000 pixel |
| | Image height | 3000 pixel |
| | Focal length (35mm format equivalent) | 20 mm |
| | Aperture | F/2.8 (fixed) |
| | ISO | 100 |
| | Shutter speed | 1/296 sec to 1/3289 sec (variable) |
| **The St. George Anticline** WESTERN part (nadir images) | Average flying altitude | 46 m |
| | Ground resolution | 1.64 cm / pixel |
| | Image side overlap | 75 % |
| | Image forward overlap | 75 % |
| | Flight line spacing | 20 m |
| | Horizontal speed | 5 - 7 m/s |
| | Number of images taken | 137 |
| | Number of images used | 102 |
| | Coverage area | 19800 $m^2$ |
| | Number of Ground control points (GCP) | 18 |
| | Device used to measure coordinates of GCP | ProMark 500 RTK GPS |
| | Accuracy of GPS | 1-4 cm |
| | Survey date | 15/10/2015 |

**Table 2.2 (continued)**

| | | |
|---|---|---|
| **The St. George Anticline** EASTERN part (nadir images) | Average flying altitude | 52.9 m |
| | Ground resolution | 1.92 cm / pixel |
| | Image side overlap | 75 % |
| | Image forward overlap | 75 % |
| | Flight line spacing | 23 m |
| | Horizontal speed | 5 - 7 m/s |
| | Number of images | 122 |
| | Number of images used | 119 |
| | Coverage area | 62400 m2 |
| | Number of Ground control points (GCP) | 7 |
| | Device used to measure coordinates of GCP | Handheld Garmin etrex 10 GPS |
| | Accuracy of GPS | 2-5 m |
| | Survey date | 15/10/2015 |
| **Artillery Rocks** (nadir images) | Average flying altitude | 46 m |
| | Ground resolution | 1.68 cm / pixel |
| | Image side overlap | 75 % |
| | Image forward overlap | 75 % |
| | Flight line spacing | 17 m |
| | Horizontal speed | 5 - 8 m/s |
| | Number of images | 152 |
| | Number of images used | 146 |
| | Coverage area | 23000 m2 |
| | Number of Ground control points (GCP) | 15 |
| | Device used to measure coordinates of GCP | Ashtech ProMark 100/200 (no RTK) |
| | Accuracy of GPS | 0.455-3.286m) |
| | Survey date: | Oct 25, 2016 |
| **Soapy Rocks** (nadir + oblique images) | Average flying altitude | 46 m |
| | Ground resolution | 1.68 cm / pixel |
| | Image side overlap | 75 % |
| | Image forward overlap | 75 % |
| | Flight line spacing (for nadir images) | 17 m |
| | Horizontal speed | 5 - 8 m/s |
| | Number of images | 152 |
| | Number of images used | 146 |
| | Coverage area | 23000 m2 |
| | Number of Ground control points (GCP) | 15 |
| | Device used to measure coordinates of GCP | Ashtech ProMark 100/200 (no RTK) |
| | Accuracy of GPS | 0.455-3.286m) |
| | Survey date | Oct 25, 2016 |

## 2.4 Structural observations

### 2.4.1 Eumeralla Formation: The St. George Anticline/ Artillery Rocks

The St. George Anticline (1km south of Lorne) is one of several ENE trending folds that are well exposed along the coastal platforms of the Otway Ranges, Victoria, (Figure 2.1) and are of significant economic interest for their geothermal and tight gas reservoir potential (Messent et al., 1999; Holford et al., 2014).

The anticline is upright and slightly asymmetrical, with its northern limb dipping up to 25° NW and its southern limb dipping up to 40° SE (Figure 2.4). Based on field measurements between locations 6-12 the hinge plunges ~08° towards 068°, while the axial plane dips 85°NW. When combined with nearshore bathymetric data, the hinge line can be traced for ~1.5km along strike. The anticline geometry changes along the fold axis and in the NE the surface expression of the hinge line terminates against a large fault identified in the nearshore bathymetric data (Figure 2.4).

Fifteen fracture measurement sampling sites were defined on the two limbs and within the hinge zone of the St. George Anticline (Figure 2.4). A total of 660 fractures were recorded in the field (Table 2.3). A further 9448 fractures were measured from orthorectified photomosaics captured along exposed bedding surfaces, with the majority of data collected from along the northern limb and within the fold hinge (Figures 2.3B). The mean orientation calculated from these data was used to determine the three dominant fracture groups (Figure 2.5C).

Fracture sets along the onshore section of the northern limb, around Location 1 (Figure 2.5A) lack discernable displacement along the fracture planes at the scale of observation. Combined with plumose textures observed on the side of a fracture surface (Figure 2.5B) oriented parallel with fracture set #2, suggests that these fractures are dominantly joints. However, a sinistral strike-slip fault oriented 132/90 offsets sub-vertical, NE-oriented, calcite-cemented fractures belonging to fracture set #1 at Location 4 (Figures 2.5A). Gently plunging slickenlines preserved on fault surfaces indicate dominantly strike-slip movement along the sub-vertical fault surface (Figure 2.6D). This indicates that fracture set #2 contains a combination of joints and shear fractures.

Within the northern limb, fracture set #1 is oriented at a high angle to bedding and strikes ~040°. Fracture

set #2 is oriented ~110°, with fracture set #1 abutting against the older fracture set #2 (Figure 2.5D). Fracture set #3 is oriented at ~145° and routinely abuts against both other fracture sets (Figure 2.7A). The majority of fractures in the northern limb are sub-vertical (Figure 2.5E), with fracture set #2 being the most pervasive, with an average density of 0.22/$m^2$, compared to 0.08/m2 for fracture set #1 (Figure 2.8A; Table 2.3). Fractures belonging to fracture set #1 are regularly spaced (Cv = 0.74) while fracture set #2 tends to cluster throughout the northern limb (Cv > 1).

Calcite veins display two dominant orientations (Figure 2.6E) within the northern limb (Locations 4 & 5). Vein set V1 is sub-parallel to fracture set #1 (035°), with ~30° variation in strike within Location 4. Individual veins are thicker (~4cm on average) than those of vein set V2 (~1cm on average), which is oriented sub-parallel to fracture set #2 (120°). The calcite has coarse grained, vuggy texture and locally contains dark host-rock fragments, especially in 0.3-1m wide fault zones (Figure 2.6A) that are characterised by calcite cemented breccias.

The hinge region exhibits an abundance of sub-vertical fractures, oriented sub-perpendicular to the NE-plunging fold axis, belonging to fracture set #2 (~144°) and fracture set #3 (~160°) (Figures 2.8A, B, D). Fracture set #1 is oriented parallel to the fold axis (~070°) and commonly abuts and crosscuts fracture set #2 within the fold hinge (Figures 2.6B). All three fracture sets show high fracture densities between location 9 and location 11 (Figure 2.8B; Table 2.3).

The southern limb exposures are more eroded compared to sections closer to the cliff and along the northern platforms, so that fractures oriented between 030°- 060° have had their apertures significantly enlarged. However, fracture populations are generally well defined by field measurements (Figure 2.9E). Fracture orientations within the southern limb are similar to those within the northern limb (Table 2.3), with two dominant fracture sets of ~030° (#1) and ~115° (#2), as well as a less pervasive fracture set ~168° (#3) (Figure 2.9C). The southern limb exhibits higher fracture densities, ranging from 0.30/$m^2$ to 0.36/$m^2$ for fracture sets #1 and #2, compared to their counterparts on the northern limb (Figure 2.8C; Table 2.3). Several subvertical, sinistral strike-slip faults oriented NW-SE (134/90) offset bedding (~0.4m) within the southern limb, without any noticeable vertical displacement (Figure 2.6B).

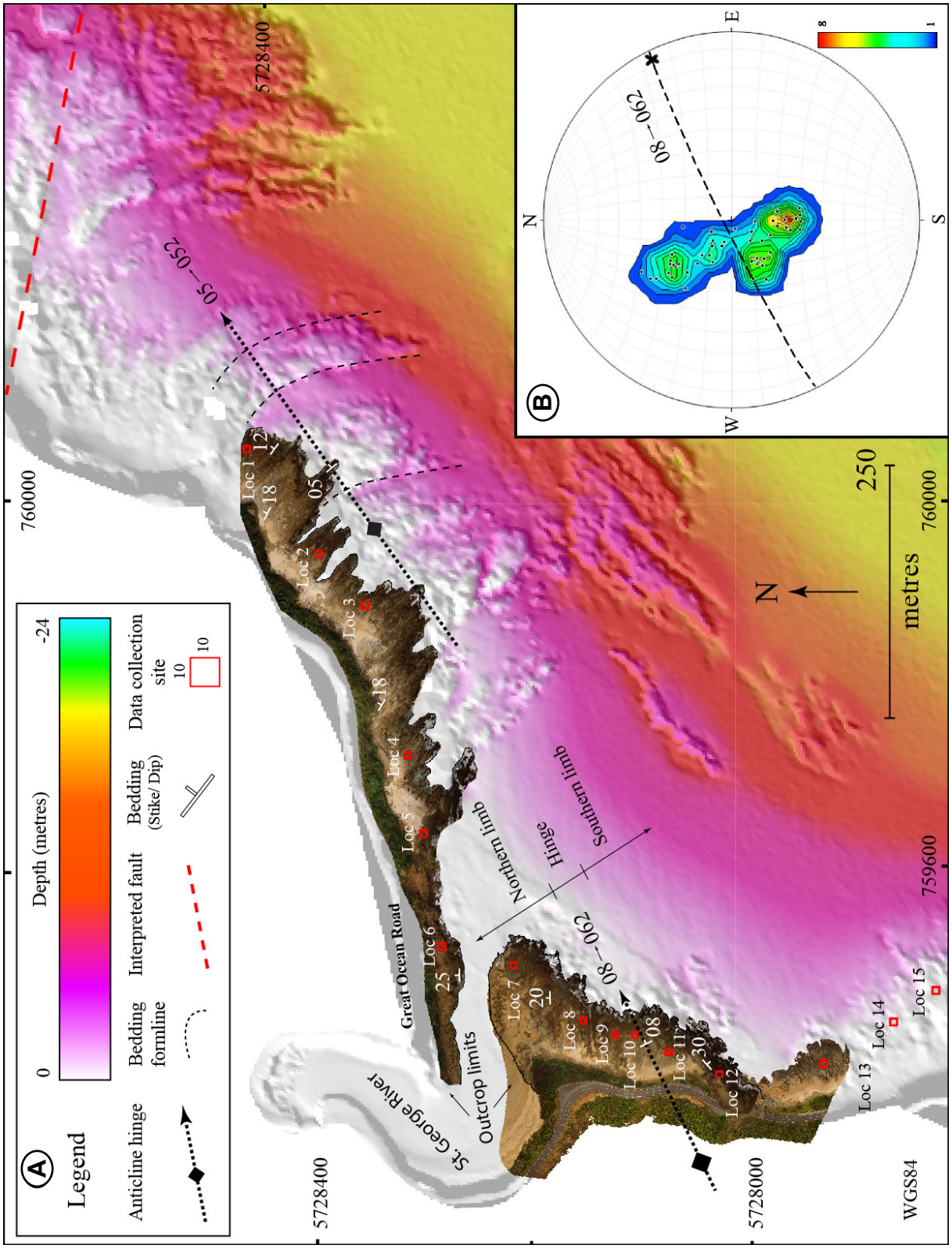


**Figure 2.4:** (A) UAV map view of the St. George Anticline with applied Victorian nearshore coastal bathymetry 2.5m DEM & 1m contour data, extending up to the 20m-depth contour (DELWP, 2009). Bathymetry data are overlain by a (humidity) colour-ramp. Note the limits of the coastal rock platforms, which are defined by orthophotographs. Red boxes correspond to sampling sites, with each sample site (Locations 1-15) consisting of a 10x10m grid. (B) Lower hemisphere equal area stereographic projection (poles to bedding planes) with 1% area contours derived from traditional mapping between locations 6-12 within the St. George Anticline. The 60 bedding plane measurements suggest a gently NE plunging fold axis and a subvertical axial plane, and the bathymetric data combined with field measurements between locations 1-3 suggest a possible change in the strike of the fold hinge.

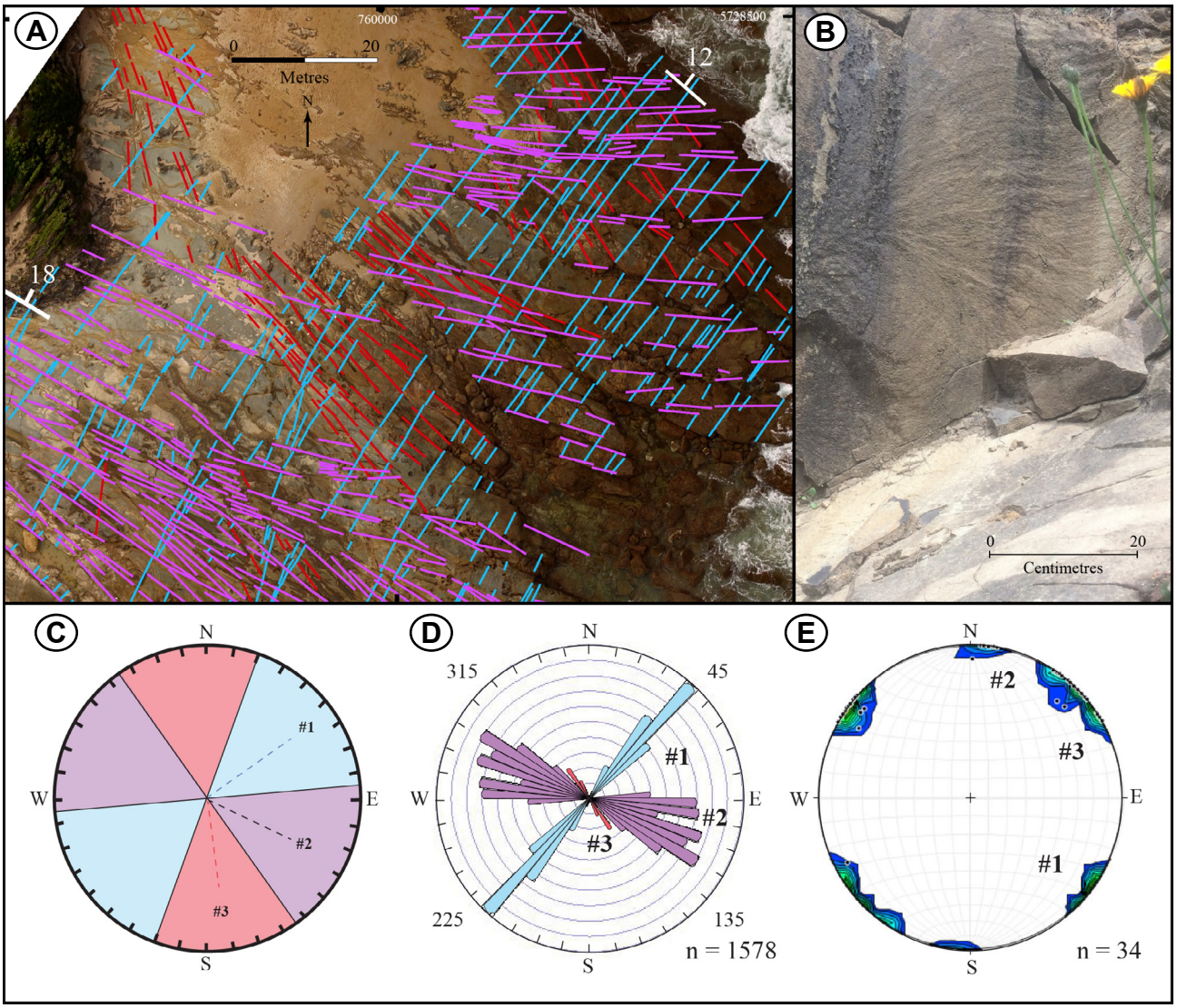


**Figure 2.5:** (A) Fracture orientations on bedding surfaces, observed within an orthorectified photomosaic within the northeastern end of the St. George platform (Location 1). Fracture relationships indicate that fracture set #1 (blue) and #3 (red) abut against fracture set #2 (purple), while fracture set #3 abuts against both fracture sets #1 and #2. (B) SW oriented photograph of a plumose structure on the side of a ~NW-SE (130/80SW) oriented fracture surface (54H 0759267E 5728333N). (C) Fracture cluster groups based on the spread of fracture orientations analysed within UAV orthophotographs, with centres calculated from the mean preferred fracture orientations. (D) Circular histogram corresponding to fracture orientations derived from the high-resolution orthophotograph, weighted for fracture segment length and colour-coded based on orientation, for Location 1. (E) Stereographic projections representing 1% area contours (poles to tensile and shear fracture planes) for Location 1, obtained from field measurements.

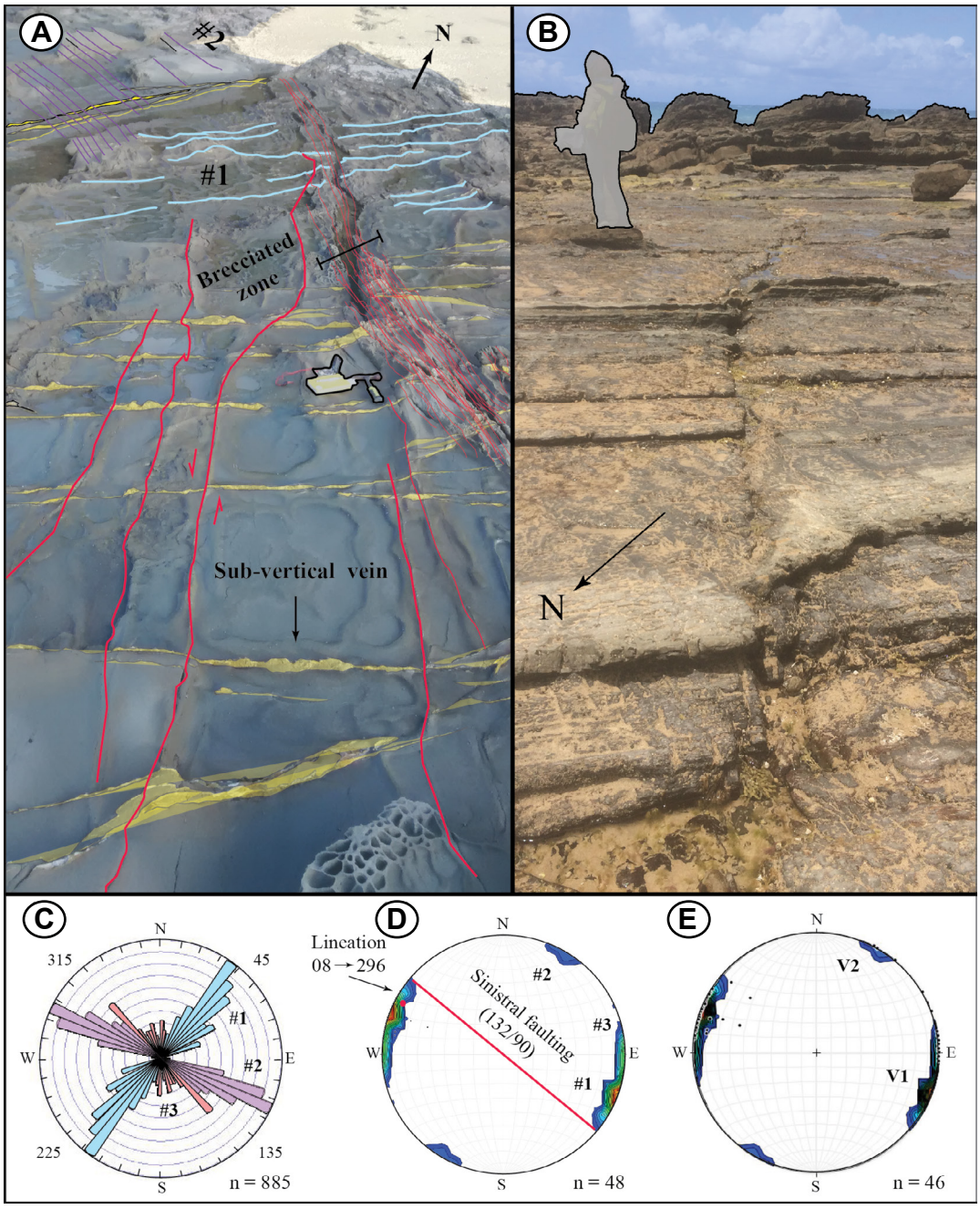


**Figure 2.6:** (A) Northern limb (Location 4) shown in a NW-oriented photograph (yellow notebook for scale). Note the sinistral offset of calcite veins oriented sub-parallel to the fracture set #1. (B) Sinistral strike-slip fault (134/90) within the southern limb, with a person for scale (54H 0759380E 5727785N). (C) Circular histogram corresponding to fracture orientations derived from the high-resolution orthophotograph, weighted for fracture segment length and colour-coded based on orientation, for Location 4. (D) Stereographic projections representing 1% area contours (poles to tensile and shear fracture planes) for Location 4, barren fractures and faults and (E) - Location 4, vein-filled fractures, obtained from field measurements.

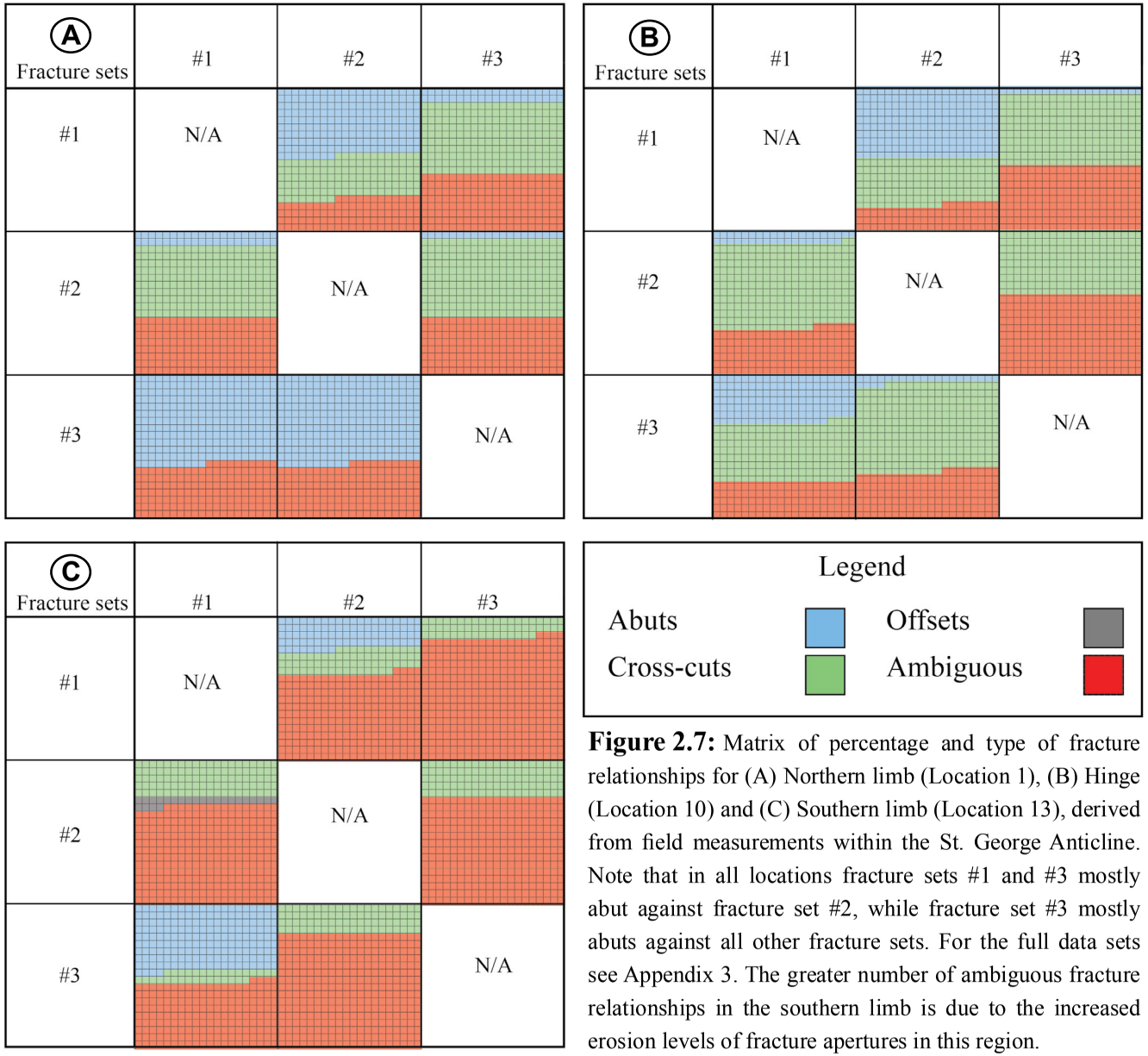


**Figure 2.7:** Matrix of percentage and type of fracture relationships for (A) Northern limb (Location 1), (B) Hinge (Location 10) and (C) Southern limb (Location 13), derived from field measurements within the St. George Anticline. Note that in all locations fracture sets #1 and #3 mostly abut against fracture set #2, while fracture set #3 mostly abuts against all other fracture sets. For the full data sets see Appendix 3. The greater number of ambiguous fracture relationships in the southern limb is due to the increased erosion levels of fracture apertures in this region.

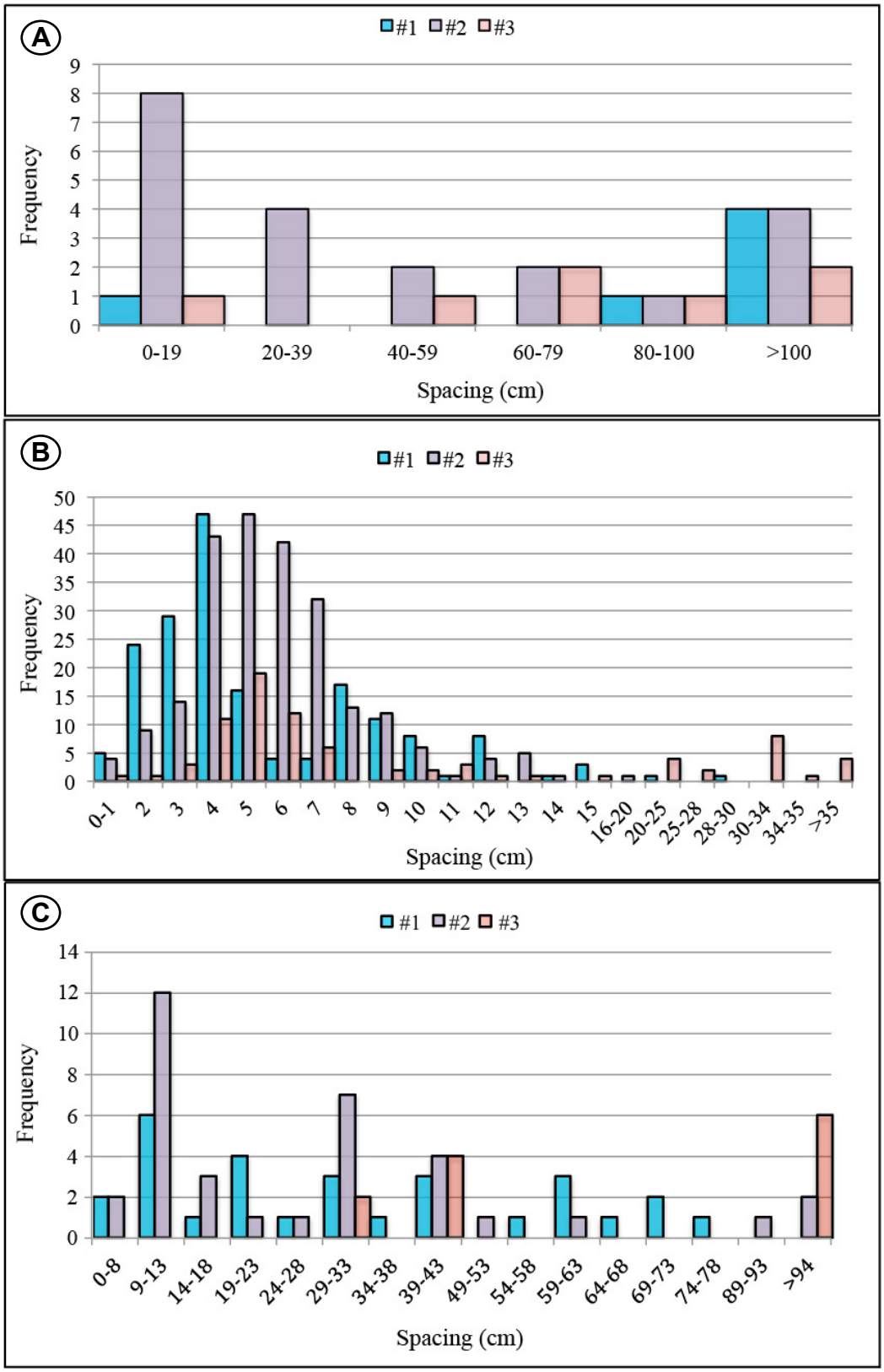


**Figure 2.8:** Fracture spacing histograms for (A) Northern limb (Location 1), n = 34, (B) Hinge (Location 10), n = 513 & (C) Southern limb (Location 13), n = 76, derived from field measurements within the St. George Anticline. Note that fracture spacing within the hinge region is significantly greater than in the limb regions for fracture sets #1 and #2. For full data set see Appendix 3.

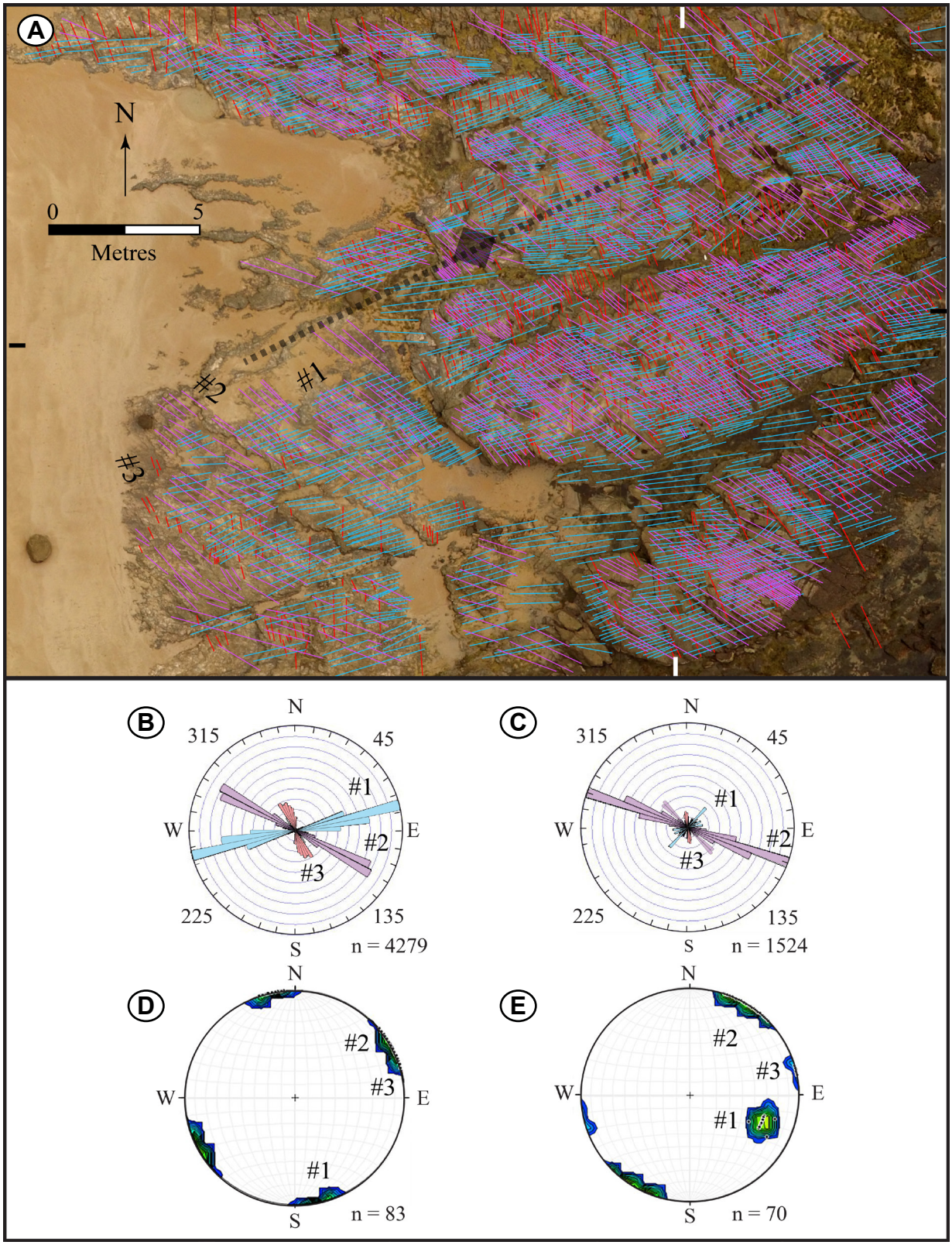


**Figure 2.9:** (A) Fracture orientations on bedding surfaces, observed within an orthorectified photomosaic within the St. George fold hinge (Location 10). Circular histograms corresponding to fracture orientations derived from the high-resolution orthophotograph, weighted for fracture segment length and colour-coded based on orientation, derived from field measurements within, (B) – Fold hinge (Location 10) and (C) – southern limb (Location 12). Stereographic projections representing 1% area contours of poles to fracture planes derived from field measurements within: (D) – Fold hinge (Location 10) and (E) – southern limb (Location 12).

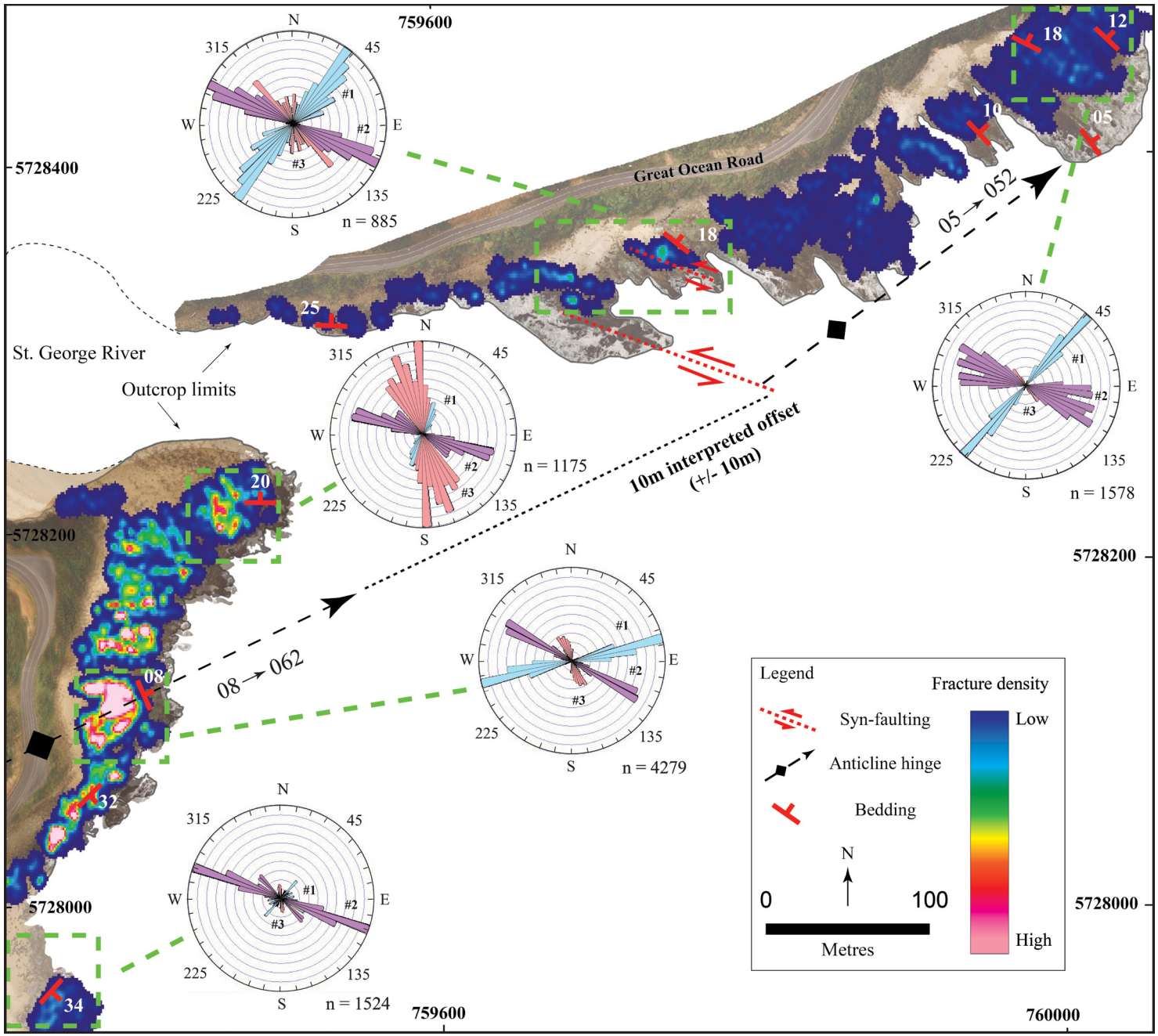


**Figure 2.10:** Orthophotograph of the coastal platforms around the St. George Anticline, overlain by a fracture density map (max density ~5 fractures/m$^2$ represents the 'hot' regions). Circular histograms are derived from the high-resolution orthophotograph, weighted for fracture segment length. Note the interpreted sinistral offset of the fold hinge.

**Table 2.3:** Fracture data based on field measurements for each sampling area, including the northern limb (blue), the hinge region (green) and the southern limb (red), of the St. George Anticline. Fracture locations are measured from the centre of each counting square.

| Location WGS84, 54H | Mean fracture orientations | Average spacing (cm) | Spacing standard deviation (cm) | Cv | Fracture density (f/m²) | Mean total length (m) | Fracture set |
|---|---|---|---|---|---|---|---|
| 0760011E | 040/85S | 165.67 | 123.19 | 0.74 | 0.07 | 5.0 | #1 |
| 5728492N | 110/90 | 47.62 | 45.81 | 0.96 | 0.22 | 8.0 | #2 |
| | 145/90 | 111.43 | 105.42 | 0.84 | 0.08 | 1.0 | #3 |
| | | | | | | | |
| 0759928E | 040/90 | 59.33 | 89.88 | 1.51 | 0.16 | 2.0 | #1 |
| 5728425N | 132/90 | 99.8 | 115.29 | 1.16 | 0.11 | 3.0 | #2 |
| | | | | | | | |
| 0759869E | 032/90 | 51.47 | 19.64 | 0.38 | 0.20 | 5.0 | #1 |
| 5728373N | 130/90 | 78.75 | 95.37 | 1.21 | 0.13 | 9.0 | #2 |
| | | | | | | | |
| 0759746E | 025/90 | 40.35 | 33.24 | 0.82 | 0.24 | 2.0 | #1 |
| 5728344N | 120/85N | 24.89 | 32.94 | 1.32 | 0.37 | 2.0 | #2 |
| | 170/90 | 45.15 | 43.94 | 0.97 | 0.221 | 4.0 | #3 |
| | | | | | | | |
| 0759672E | 044/70SE | 35.00 | 29.84 | 0.85 | 0.27 | 1.0 | #1 |
| 5728331N | 144/90 | 11.34 | 12.09 | 1.07 | 0.88 | 5.0 | #2 |
| | 165/80W | 123.88 | 112.42 | 0.91 | 0.09 | 6.0 | #3 |
| | | | | | | | |
| 0759605E | 032/90 | 35.00 | 10.94 | 0.31 | 0.29 | 4.0 | #1 |
| 5728339N | 110/70E | 24.37 | 6.58 | 0.27 | 0.42 | 6.0 | #2 |
| | | | | | | | |
| 0759488E | 30/90 | 100.00 | 57.39 | 0.57 | 0.10 | 5.0 | #1 |
| 5728207N | 145/65S | 83.00 | 89.57 | 1.08 | 0.13 | 10.0 | #2 |
| | | | | | | | |
| 0759430E | 086/90 | 10.13 | 8.54 | 0.84 | 0.93 | 4.0 | #1 |
| 5728146N | 128/85W | 41.04 | 10.61 | 0.26 | 0.25 | 6.0 | #2 |
| | 165/80W | 9.92 | 6.72 | 0.68 | 1.03 | 6.0 | #3 |
| | | | | | | | |

**Table 2.3: Continued**

| Location WGS84, 54H | Mean fracture orientations | Average spacing (cm) | Spacing standard deviation (cm) | Cv | Fracture density (f/m²) | Mean total length (m) | Fracture set |
|---|---|---|---|---|---|---|---|
| 0759418E | 085/90 | 4.41 | 4.79 | 1.08 | 2.26 | 0.3 | #1 |
| 5728120N | 150/90 | 6.82 | 5.68 | 0.83 | 1.53 | 0.5 | #2 |
| | | | | | | | |
| 0759406E | 070/90 | 5.49 | 3.76 | 0.68 | 1.81 | 0.1 | #1 |
| 5728092N | 144/90 | 5.71 | 2.61 | 0.46 | 1.76 | 0.5 | #2 |
| | 160/90 | 11.66 | 11.37 | 0.98 | 0.83 | 0.6 | #3 |
| | | | | | | | |
| 0759386E | 068/90 | 54.15 | 43.39 | 0.80 | 0.21 | 0.4 | #1 |
| 5728062N | 120/90 | 9.58 | 7.75 | 0.81 | 1.02 | 0.1 | #2 |
| | 174/90 | 40.00 | 23.76 | 0.59 | 0.26 | 0.2 | #3 |
| | | | | | | | |
| 0759355E | 026/70W | 39.54 | 17.00 | 0.43 | 0.25 | 1.0 | #1 |
| 5728001N | 120/85N | 4.90 | 7.71 | 1.58 | 2.05 | 0.3 | #2 |
| | 170/90 | 40.00 | 20.00 | 0.90 | 0.25 | 1.0 | #3 |
| | | | | | | | |
| 0759350E | 030/70W | 33.14 | 22.8 | 0.69 | 0.30 | 4.0 | #1 |
| 5727906N | 115/90 | 28.49 | 26.25 | 0.92 | 0.36 | 0.5 | #2 |
| | 168/90 | 78.25 | 44.88 | 0.57 | 0.13 | 0.1 | #3 |
| | | | | | | | |
| 0759382E | 035/65W | 10.74 | 6.43 | 0.60 | 0.91 | 4.0 | #1 |
| 5727833N | 115/90 | 9.88 | 4.58 | 0.46 | 1.01 | 0.3 | #2 |
| | 170/90 | 50.00 | 8.00 | 1.00 | 0.20 | 0.2 | #3 |
| | | | | | | | |
| 0759409E | 038/80N | 14.43 | 11.58 | 0.80 | 0.70 | 2.0 | #1 |
| 5727755N | 124/80N | 6.84 | 2.42 | 0.35 | 1.33 | 2.0 | #2 |

Fracture orientation and density within the St. George Anticline appears to be controlled by structural position relative to the fold hinge (Figure 2.10; Table 2.3). The density of systematic fractures varies significantly between the hinge and limb regions, with a gradual increase in fracture densities for fracture sets #1 and #2 towards the hinge. Increased fracture densities are also observed proximal to measured shear fractures that are restricted to the fold limbs (Locations 4, 5 and 13; Table 2.3) and oriented NW-SE (~132°).

The southern Artillery Rocks locality is positioned on a gently dipping (12-18°SE) fold limb that is structurally distal from the nearest anticline hinge (~2km, the Mt. Defiance anticline, Figure 2.1). A total of 6 field data sampling sites (Figure 2.11A) were analysed along this section of coastal platform. Only two fracture orientations were observed within southern Artillery Rocks (Figure 2.11A, B; Table 2.4), compared with the three fracture sets observed near the fold hinge (Figure 2.10). The most dominant fracture set #2 is oriented (136/90) (strike/ dip) at a high angle to bedding and commonly occurs as 0.5-1m wide fracture corridors (Peacock et al., 2016) (Figure 2.11C). The orthorectified photomosaics show these fracture corridors to be uniformly distributed along the bedding platform (Figure 2.11A).

Fracture set #3 is oriented 155/80 and is less pervasive than fracture set #2 (Table 2.4). Fracture set #3 is observed abutting the ~NW-SE oriented fracture set in 83% of situations (Figure 2.11A).

The NW-SE oriented fracture set #2 and NNW-SSE oriented fracture set #3 are therefore observed throughout both study localities within the Eumeralla Fm, occurring within both folded regions as well as within areas away from the fold hinge.

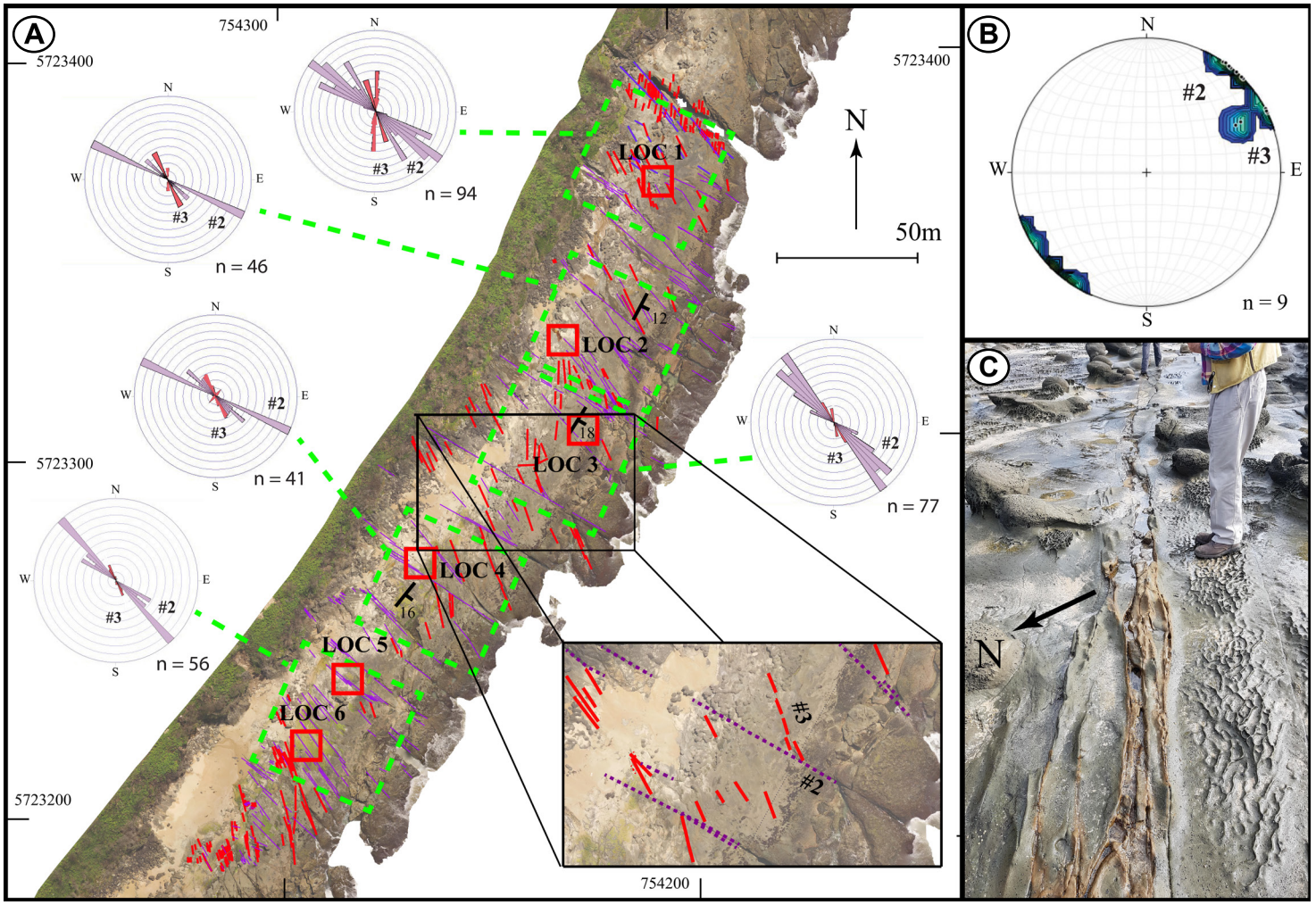


**Figure 2.11:** (A) UAV acquired high-resolution orthophotograph of the coastal platforms at the southern Artillery Rocks locality. Circular histograms derived from the high-resolution orthophotograph, weighted for fracture segment length and are coloured based on fracture group (#2 purple, #3 red). Red boxes correspond to field sampling sites, with each sample site consisting of a 10x10m grid area. A zoomed in section of the coastal platforms highlights the orientation of fracture set #2 (purple) and fracture set #3 (red). Coordinate system: WGS84. (B) Stereographic projection representing 1% area contours of poles to fracture planes based on field measured within Location 3, and highlights the dominant subvertical dip of fractures in this area. (C) ~NW-SE oriented fracture corridors with a person for scale (location 4).

**Table 2.4:** Fracture data for each sampling area within the Artillery Rocks locality. Fracture locations are measured from the centre of each counting square.

| Location WGS84, 54H | Mean fracture orientations | Average spacing (cm) | Spacing standard deviation (cm) | Cv | Fracture density ($f/m^2$) | Mean total length (m) | Fracture set |
|---|---|---|---|---|---|---|---|
| 0754385E | 140/90 | 201.67 | 256.51 | 1.27 | 0.15 | 30.0 | #2 |
| 5723369N | 160/90 | 249.25 | 233.33 | 0.94 | 0.04 | 2.0 | #3 |
| | | | | | | | |
| 0754371E | 130/90 | 211.00 | 182.02 | 0.86 | 0.06 | 50.0 | #2 |
| 5723331N | | | | | | | |
| | | | | | | | |
| 0754364E | 136/90 | 164.20 | 262.33 | 1.60 | 0.06 | 36.0 | #2 |
| 5723310N | 155/64SW | 260.00 | 302.32 | 1.16 | 0.05 | 25.0 | #3 |
| | | | | | | | |
| 0754338E | 144/90 | 179.18 | 367.56 | 2.05 | 0.12 | 42.0 | #2 |
| 5723276N | | | | | | | |
| | | | | | | | |
| 0754318E | 136/90 | 100.81 | 161.45 | 1.60 | 0.17 | 30.0 | #2 |
| 5723259N | | | | | | | |
| | | | | | | | |
| 0754303E | 136/90 | 87.30 | 126.46 | 1.45 | 0.11 | 18.0 | #3 |
| 5723227N | | | | | | | |

### 2.4.2 Angahook Formation: Soapy Rocks

Fracturing within the Soapy Rocks locality is largely confined to the upper two sandstone units (Figure 2.3). Sub-vertical fractures observed in the uppermost, light-grey to light-brown sandstone unit can be subdivided into two dominant fracture sets. The first is oriented ~160° (#3) and the second oriented ~100° (#2), roughly orthogonal to the first fracture set (Figure 2.12A, B), with the WNW- ESE trending fracture set abutting against the older NNW-SSE oriented fracture set (Figure 2.12C, D). Fractures dominantly lack discernable displacement throughout the majority of the outcrop. However, small strike-slip faults (152/90) with minor amounts (~1-2cm) of sinistral offset and associated drag folds (Figure 2.12E) were observed within the second-to-uppermost unit. These shear fractures are sub-parallel to the NNW-SSE oriented joint set (#3), and the joints have an average density of 0.12/$m^2$ (Figure 2.12A; Table 2.5). Furthermore, within southern-most section of the outcrop an ~WNW-ESE oriented (104/90) fracture set crosscuts and appears to be slightly offset (1-2mm) by a NW-SE oriented (152/90) fracture set (Figure 2.13). Fracture set #3 is the most pervasive with an average density of 0.54/ m2 in the northern section of the outcrop compared to the #2 fracture set density of 0.40/$m^2$ (Table 2.5).

**Table 2.5:** Fracture data for each sampling area within Soapy Rock locality. Fracture locations are measured from the centre of each counting square.

| Location WGS84, 54H | Mean fracture orientations | Average spacing (cm) | Spacing standard deviation (cm) | Cv | Fracture density (f/m2) | Mean total length (m) | Fracture set |
|---|---|---|---|---|---|---|---|
| 0253826E | 096/90 | 25.38 | 8.12 | 0.32 | 0.40 | 0.2 | #2 |
| 5743712N | 160/90 | 18.49 | 5.23 | 0.28 | 0.54 | 4.0 | #3 |
| | | | | | | | |
| 0253799E | 104/90 | 100.27 | 102.62 | 1.02 | 0.12 | 1.0 | #2 |
| 5743684N | 152/90 | 55.44 | 62.13 | 1.12 | 0.19 | 1.5 | #3 |

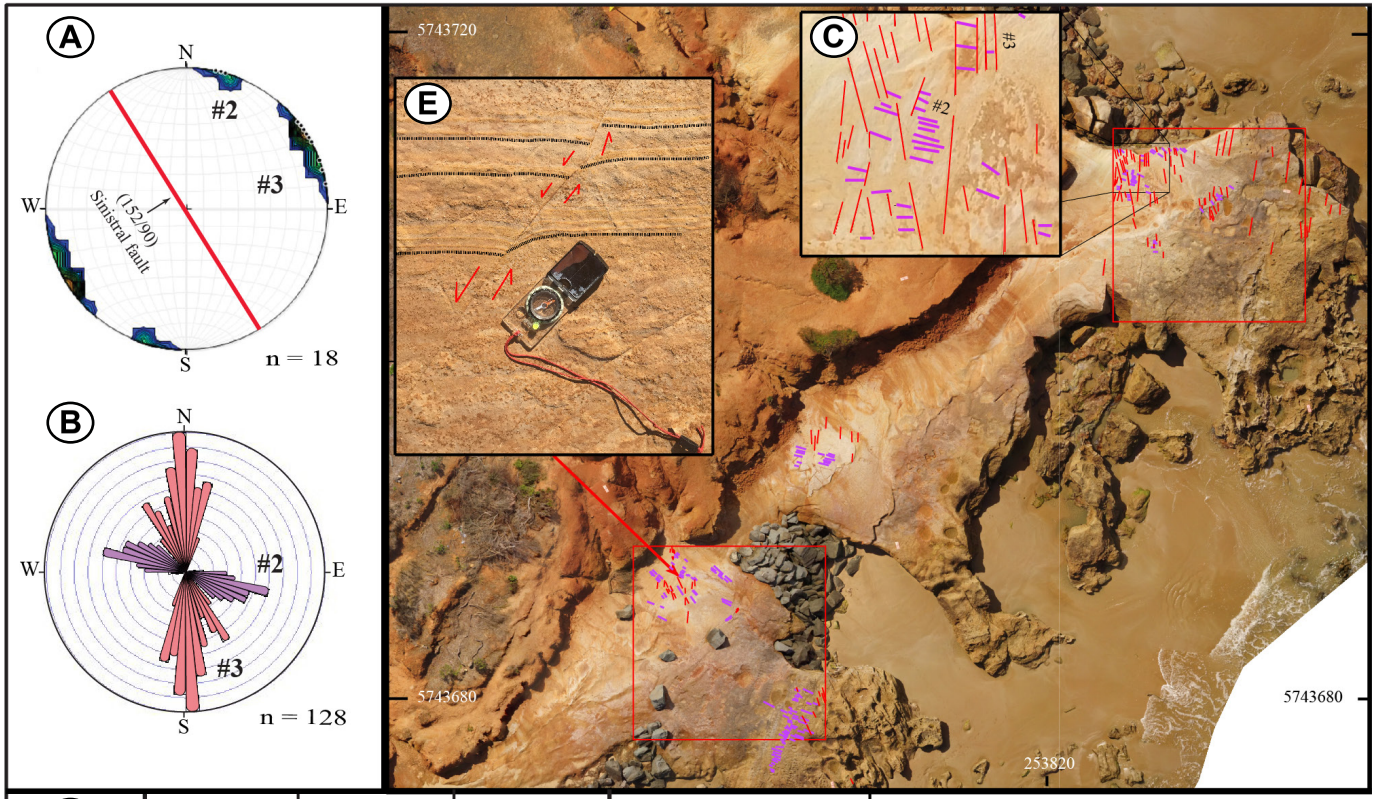


| D Fracture sets | #1 | #2 | #3 |
|---|---|---|---|
| #1 | N/A | N/A | N/A |
| #2 | N/A | N/A | |
| #3 | N/A | | N/A |

Legend
Abuts
Cross-cuts
Offsets
Ambiguous
N
0
10
Metres
10
10
Data sampling areas

**Figure 2.12:** Orthorectified aerial photomosaic of the Soapy Rocks coastal outcrop (Anglesea). (A) Stereographic projection representing 1% area contours of poles to fracture planes, obtained from field measurements and with a red line indicating the plane of the sinistral fault (152/90). (B) Circular histograms corresponding to fracture orientations are derived from the high-resolution orthophotograph, weighted for fracture segment length and colour-coded based on orientation. (C) Zoomed in section of the coastal platform that highlights the orientation of fracture set #2 (purple) and fracture set #3 (red). (D) Matrix of percentage and type of fracture relationships for the northern area, derived from field measurements. (E) Sinistral faulting of iron rich, coarse granule quartz sandstone laminations. Note the lamination displacement against the sinistral fault.

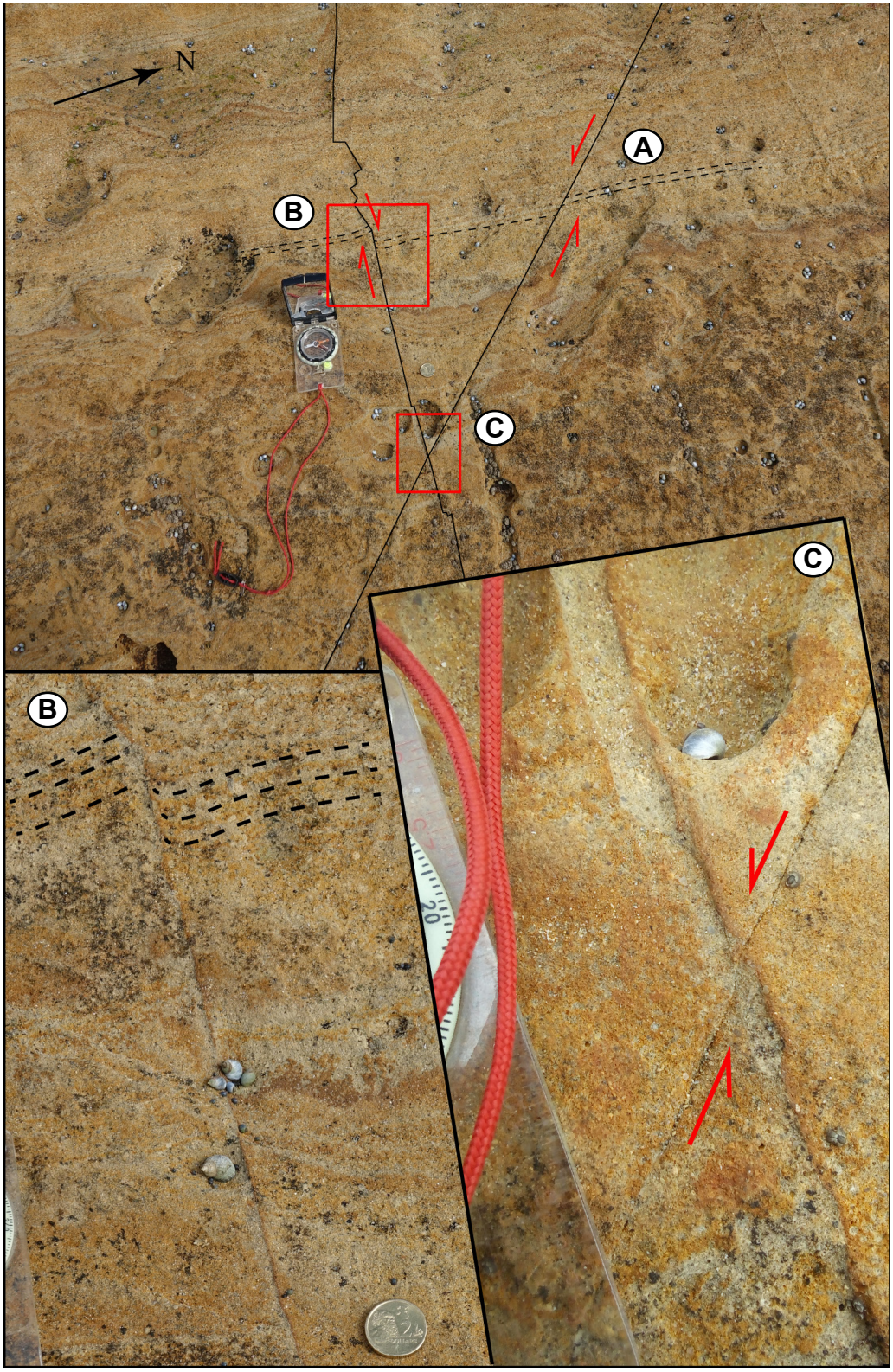


**Figure 2.13:** Conjugate set of fractures (55H 0253804E 5743678N). (A) Sinistral shear sense defined by offset bedding. (B) Dextral shear sense defined by offset bedding (see zoom). (C) Possible offset of ~WNW-ESE fracture by ~NW-SE fracture (see zoom).

## 2.5 Discussion and interpretations:

### 2.5.1 Analysis of fracture formation

This section considers the stress conditions experienced by each unit at maximum burial depth and the potential for fracture formation along the Otway coastline to be the result of uplift and erosion (unloading joints).

The most numerous fracture types observed throughout the study areas are sub-vertical, tensile (mode 1) fractures (Tables 2.3, 2.4 & 2.5) and therefore this discussion will mainly focus on interpreting the potential stress conditions that could form this fracture type.

### 2.5.2 Fracture formation during uplift (unloading joints)

The Mohr diagram (Twiss & Moores, 1992; Fossen, 2010) is a two dimensional graphical visualisation of the state of stress experienced by a rock (Figure 2.14). The diameter of the Mohr circle represents the magnitude of the differential stress such that when shear stress ($\tau$) equals zero its limits are defined by the maximum ($\sigma_1$) and minimum ($\sigma_3$) principal stresses. The origin of the Mohr circle is the mean stress ($\sigma_m$). A Mohr circle that is located entirely within the area bounded by the Mohr-Coulomb failure curve (Figure 2.14) is considered to be safe from failure, with the rock's tensile strength ($T_0$) providing the lower limit of the failure curve (MC). Following the methodology of Sibson (2000a) the cohesive strength (C) is calculated to be ~2x the magnitude of the tensile strength ($T_0$) (Table 2.6). An increase in tensile strength will therefore move the failure curve to the left.

Vitrinite reflectance (VR) measurements provide an indication of the maximum paleotemperature experienced by sediments, based on an optical assessment of the average maximum reflectance ($R_0$) of lignite-rich sediment (Mukhopadhyay & Dow, 1994). Combined with information on the paleogeothermal gradient VR provides an indication of the maximum burial depth for each locality (Appendix 1), however, constraints on paleogeothermal gradients can be poor (Bray *et al*., 1992). The range of vitrinite reflectance (VR) values ($R_0$ = 0.72-0.95 ± 0.049%) measured within the Eumeralla Fm along the St. George platforms (Appendix 1) indicates a maximum burial between 2.0-2.5km for these sediments.

For comparison, these values are much larger than the VR values within the younger sediments ($R_0$ = 0.30 ± 0.05). These data were measured at a depth of ~150m within the Anglesea-1 well (Figure 2.1) and approximate a maximum burial depth of 0.8 ± 0.05km for the Demons Bluff Group, based on a Cenozoic geothermal gradient of ~36°C/km (Green et al., 2004).

Based on the dominantly vertical fracture orientations observed throughout the study area (Table 2.3), the maximum principle stress ($\sigma_1$) within the St. George Anticline is assumed to be equal to the maximum confining lithostatic pressure ($\sigma_v$) (Fossen, 2010). This value is calculated between 48.61 - 60.76 MPa for the maximum burial depth from:

$$\sigma_v = \rho g z = \sigma \qquad \text{(Equation 3)}$$

where g is the gravitation acceleration (9.81 m/s$^2$) and ρ is the host rock average density (2480 ±5 kg/m$^3$) based on 3 concurrent laboratory measurements by weight of a 5cm$^3$ hand sample.

The influence that lithostatic stress has on fracture formation has long been described in the literature (Engelder, 1984; Pollard & Aydin, 1988). Deeper burial and subsequent cementation is linked to an increase in rock strength (Engelder, 1984), defined by the Young's modulus (E) (Table 2.6).

Depending on the Poisson's ratio (ν) (Table 2.6) the minimum principal stress ($\sigma^3$) typically is 30-50% of the magnitude of the maximum principal stress ($\sigma^1$) (Fossen, 2010). Poisson's ratio ranges from 0.05-0.40 for sandstone and 0.05-0.32 for shale (Aadnoy & Looyeh, 2011) depending on the amount of cementation the rock has undergone. The values of 0.21-0.33 (sandstone) and 0.5-0.33 (shale) have been adopted based on the recommendations of Engelder (1984) and references therein (Table 2.6). The range of calculated differential stress values for sandstone (Table 2.6) result in 3 potential Mohr circle stress states (Figure 2.14) representing the various end members of principle stress and burial depth. However, given that these stress estimates are not based on rock mechanical experiments, the values are an approximation. During burial of the volcaniclastic sandstone (Figure 2.15), the pore-fluid pressure (Pf) would reduce the mean normal stress by 19.60-24.50MPa at the time of maximum burial depth, resulting in an effective maximum principle stress of 32.63 ± 3.63MPa defined by the equation:

$$\sigma_1^{eff} = \sigma_1 - Pf \quad \text{(Equation 4)}$$

With the pore-fluid pressure calculated using Equation 3. Given that shallow burial depths (>3km) are unlikely to generate significant hydrostatic overpressures (Fossen, 2010), and therefore unlikely to deviate from the predicated the hydrostatic gradient, the above calculation is considered to still be valid. These calculations assume no tectonic influence, however, in a situation where tectonic compression ($\sigma_1$ horizontal) occurs pore-fluid pressure would be increased (Engelder, 1984). In an extensional tectonic setting the minimum principal stress ($\sigma_3$) is defined by the minimum horizontal stress ($\sigma_3 = \sigma_h$). Tensile fractures form if the tensile strength of the rock (Table 2.6) is exceeded while $\sigma_3$ is within the tensile regime (i.e. $\sigma_3 < 0$ or $\sigma_3 \geq T_o$). As above, this requires the assumption that the differential stress is low to avoid the formation of shear fractures. The required reduction in minimum horizontal stress ($\Delta\sigma_h$) for tectonically induced extensional fracture formation is calculated from the difference between the minimum principle stress and the tensile strength of the rock (i.e. $\Delta\sigma_h = \sigma_3 - T_o$), taking compression as positive.

Vertical tensile fracture formation may have initiated during a period of regional uplift and erosion (unloading joints) (Figure 2.15). Loading paths have been calculated for three rock types encountered at two stratigraphic levels. Loading paths are used to assess the maximum potential variation in horizontal stress ($\sigma_3$) that occurs between different rock types during burial and uplift. Following the advice of Engelder (1984) this requires the assumption that diagenesis and lithification do not occur prior to the maximum burial depth (Voight & St. Pierre, 1974), as lithification during burial will change the rock's mechanical properties (Table 2.6).

Using loading path diagrams (Figure 2.15) it becomes possible to illustrate the predicted change in minimum horizontal stress between the maximum burial depth and at surface level for different rock types, while incorporating effects due to temperature change (Equation 5) (Engelder, 1984; Fossen, 2010). The change in horizontal stress is defined by the equation:

$$\sigma h = (\nu/1 - \nu)\,\Delta\sigma v + [(E/1-\nu)\,\alpha\Delta T] \quad \text{(Equation 5)}$$

where the $\sigma_h$ (horizontal stress) is a function of the $\sigma_v$ (maximum confining lithostatic pressure), $\alpha$ (Thermal expansivity), E (Young's modulus), $\Delta T$ (Temperature change) and $\nu$ (Poisson's ratio) (Table 2.6) (Voight & St. Pierre, 1974).

The horizontal stress change that occurs during burial is calculated to be 10.04 ± 1.13 MPa for the volcaniclastic sandstone at maximum depth (MD) (Table 2.6), with a further horizontal stress change of -44.99 ± 5.44 MPa occurring during uplift to the surface (S). Therefore, although stresses equal zero when the rock is exposed at the surface (Engelder, 1984), at near-surface depths the volcaniclastic sandstone is predicted to have a horizontal stress ($\sigma_h$) of -34.94 ± 4.3MPa ($\Delta\sigma_h$(MD) - $\Delta\sigma_h$(S)) (Engelder, 1984). However, this assumes minimal variation in the stresses and pore fluid pressure during uplift.

A reduction in overburden related pressure during uplift results in an overall decrease in horizontal stress ($\sigma_h$), which facilitates tensile fracturing (Figure 2.14), assuming that the stress circle intercepts the failure curve while within the tensile regime, i.e. $\sigma_3 < 0$. However, tensile fracturing would initiate during the later stages of uplift but prior to reaching the surface, at a depth of ~0.8-1.1km (Figure 2.15) upon reaching the tensile strength ($T_o$) of the rock unit (-6MPa). Furthermore, units that contain a high content of shale are expected to be more resistant to tensile fracture formation during uplift, given that the horizontal stress of shale remains positive during uplift (Figure 2.15). This positive horizontal stress value is partly attributed to the low Poisson's ratio for unconsolidated shale (clay) during burial, which results in the minimum and maximum stress being equal ($\sigma_1 = \sigma_3$) at maximum burial depths (Table 2.6). Given the example provided, a reduction in confining pressure during uplift could spontaneously generate unloading joints. However, given that many of the fracture sets identified during this study are significantly more dense within folded regions (Figure 2.10), fracture formation is suggested to have been largely influenced by regional tectonic stresses, beginning during the early stages of uplift. Furthermore, if the Eumeralla Formation experienced multiple similar periods of burial and uplift this could form several overprinting fracture sets.

**Table 2.6:** The mechanical properties of representative lithology types for each study area, with values based on equations provided in-text, or as indicated. Numerical ranges are provided, with averaged values in bold. Note that values of **ν**, **E** and **α** are provided for consolidated (C) rock types, while values for unconsolidated sediments (UC) have been used to calculate the horizontal stress change during burial. The horizontal stress change ($\Delta\sigma_h$) is provided for both burial to maximum depth (MD) as well as uplift to surface (S).

| Properties & stresses | Volcaniclastic Sandstone (Eumeralla Fm) | Shale (Eumeralla Fm) | Sandstone (Demons Bluff Gp) | Reference |
|---|---|---|---|---|
| Average density of Fm/ Gp ($kg/m^3$) | 2480 ± 5 | | 1720 ± 5 | |
| Tensile strength ($T_0$) (MPa) | ~6 | ~4 | ~3 | (Ahrens, 1995) |
| Cohesive strength (C) (MPa) | ~12.5 | ~8.3 | ~6.2 | Sibson (2000a) |
| Maximum depth (z) (km) | 2.0-2.5 | 2.0-2.5 | 0.75-0.85 | Appendix 1 |
| Temperature change (T) (˚C) | 95-122.5 (**108.7**) | 95-122.5 (**108.7**) | 12-15.6 (**13.8**) | |
| Surface Temp ˚C | 55 ˚C | 55 ˚C | 36 ˚C | Green (2004) |
| Poisson's ratio ν | UC (Sand): 0.21 | UC (Mud): 0.5 | UC (Sand): 0.21 | Engelder (1984) |
| | C (Sandstone): 0.33 | C (Shale): 0.36 | C (Sandstone): 0.33 | Engelder (1984) |
| Young's modulus (E) (GPa) | Sand: 1 | Clay: Negligible | Sand: 1 | Lambe and Whitman (1969) |
| | Sandstone: 16.5 | Shale: 4.9 | Sandstone: 10 | Voight and St. Pierre (1974) |
| Thermal expansivity (α) $10^{-6}C^{-1}$ | UC: 10 | UC: Negligible | UC: 10 | Chong et al. (1980) |
| | C: 10.8 | C: 10.0 | C: 10 | Wilhelmi and Somerton (1967) |
| Lithostatic stress at maximum burial ($\sigma_1$) (MPa) | 48.61-60.76 (**54.7**) | 48.61-60.76 (**54.7**) | 12.64-14.33 (**13.48**) | $\sigma_v = \rho gz$ |
| Pore-fluid pressure (Pf) at max burial (MPa) | 19.60-24.50 (**22.05**) | 19.60-24.50 (**22.05**) | 7.35-8.33 (**7.84**) | $Pf = \sim\rho gz$ |
| Effective principle stress ($\sigma_1^{eff}$) (MPa) at max burial | 29.01-36.26 (**32.63**) | 29.01-36.26 (**32.63**) | 5.25-6.00 (**5.62**) | $\sigma_1^{eff} = \sigma_1 - Pf$ |
| Horizontal stress ($\Delta\sigma_h$) (MPa) | MD:8.91-11.18 (**10.04**) | MD:29.01Ð36.26 (**32.63**) | MD: 1.54-1.79 (**1.66**) | Equation 5 |
| | S: 39.55-50.43 (**44.99**) | S:23.58-29.77 (**26.67**) | S: 4.37-5.27 (**4.82**) | |
| Differential stress ($\sigma_{diff}$) | MD:20.10-25.08 (**22.59**) | MD: 0 | MD: 2.63-4.2 (**3.41**) | $\sigma_1 - \sigma_3$ |
| Surface stress (MPa) | (-)30.64 - (-)39.25 (**-34.94**) | 5.43-6.49 (**5.96**) | (-)2.83 - (-)3.48 (**-3.15**) | (MS-S) Engelder (1984) |

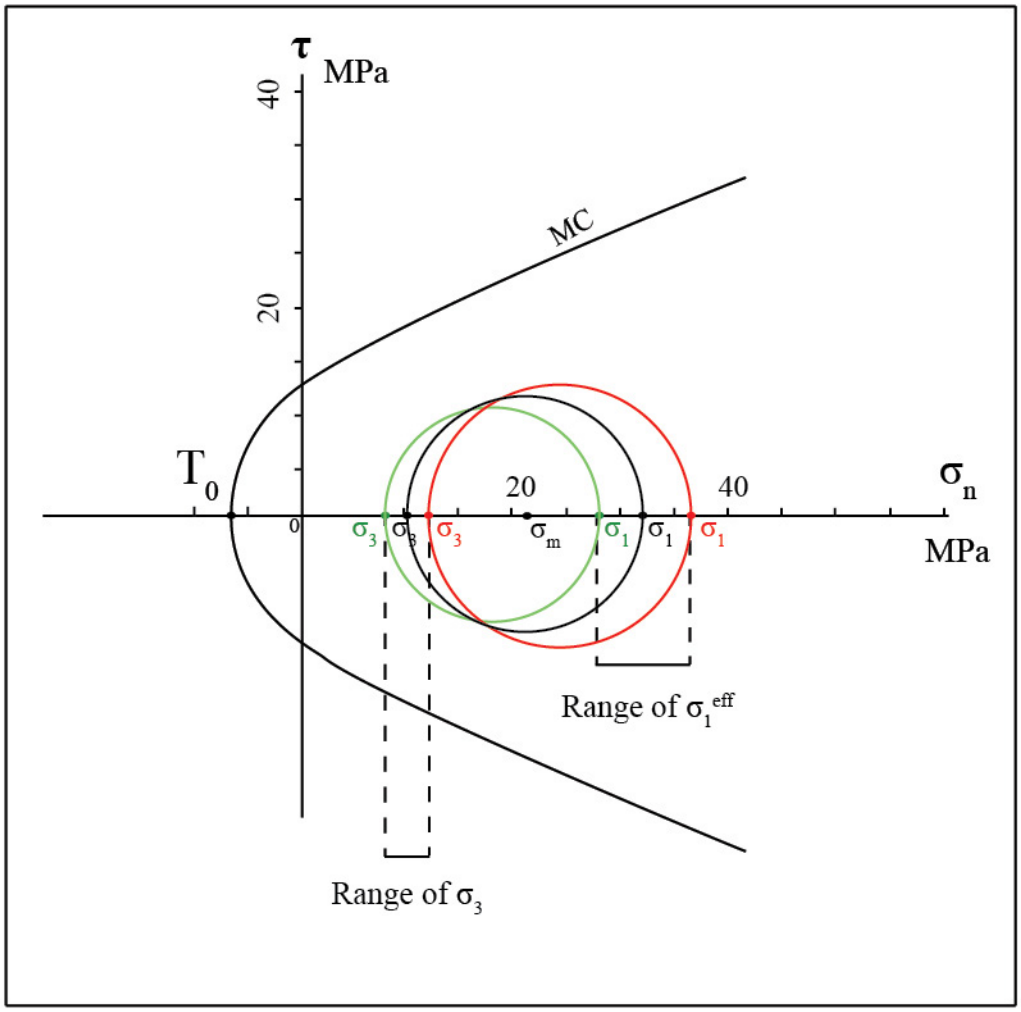


**Figure 2.14:** Mohr criterion for shear stress (τ) (MPa) versus normal stress ($\sigma_n$) (MPa) for volcaniclastic sandstone, taking compression as positive. An average value for the coefficient of internal friction μ = 0.75 has been adopted from Jaeger and Cook (1979) as recommended by Sibson (2000b). A range of differential stress values for maximum burial presented in **Table 2.6** are represented here by the red circle (maximum range of stress values), green circle (minimum range of stress values) and black circle (average stress values).

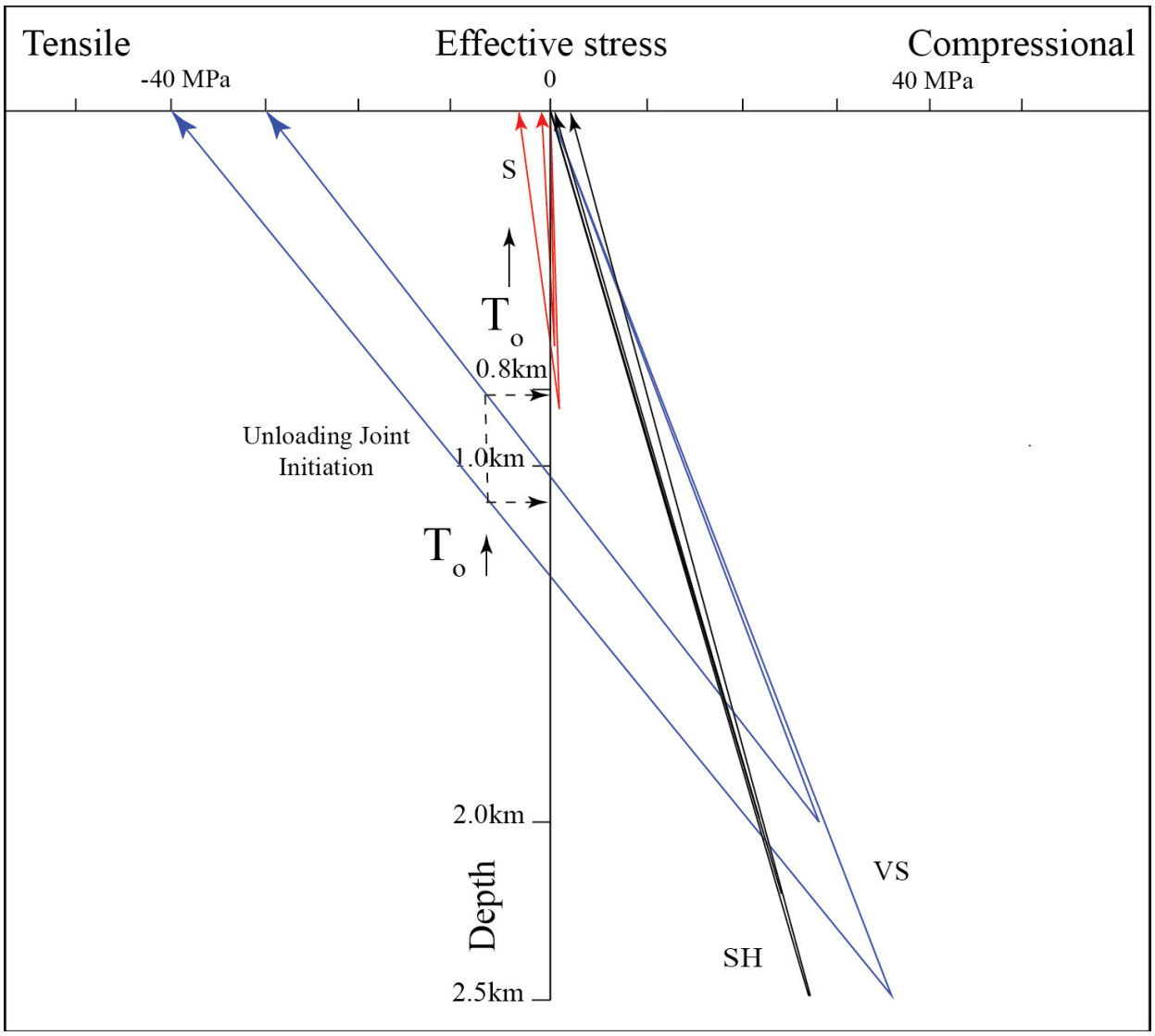


**Figure 2.15:** A loading path diagram representing how the minimum horizontal stress changes with depth. Tensile fracture formation may be due to the changing horizontal stress conditions during uplift upon reaching the tensile strength ($T_o$) of the rock. As such, the dashed arrows indicate the depth range at which fracture formation may occur. Loading paths are based on values of mechanical properties that vary for each lithology (**Table 2.6**) and are shown with the range of horizontal stress values for each potential loading path. Loading paths have been calculated for volcaniclastic sandstone, Eumeralla Formation (VS, blue), shale, Eumeralla Formation (SH, black) and sandstone, Demons Bluff Group (S, red).

### 2.5.3 Interpreted tectonic history of the eastern Otway coastline fracture systems

The following section considers the varying extent to which tectonic activity has influenced the distribution and relative timing of fracture populations at different stratigraphic positions within the study area. This section will conclude by establishing a deformation history that relates the stratigraphic position and relative timing of each fracture set encountered to the principle stress orientations that were active during fracture formation.

### 2.5.4 Eumeralla Formation

Initial deformation D1 is characterised by Early Cretaceous NW-SE extension (Figure 2.16), interpreted to have initiated the formation of NE-oriented, north-dipping, normal faults (Figure 2.1) that were part of an extensive half graben system that controlled deposition of the Eumeralla Fm sediments (Hall & Keetley, 2009).

A second deformation event D2 is interpreted to have involved ~NW-SE oriented shortening that resulted in extensive uplift of the Otway Ranges in the mid Cretaceous (Duddy, 1994; Hall & Keetley, 2009) and probably initiated the formation of a pervasive, transverse a-c fracture set (Set #2) (Figure 2.16) during the earliest stages of folding (Phase 1). Fracture set #2 was oriented parallel to the maximum shortening direction and predates all other fracture sets, based on abutting relationships observed throughout the Eumeralla Fm (Figure 2.7).

The abundance of Set #1 and #2 fractures within the fold hinge of the St George Anticline is interpreted to be the result of strain partitioning during progressive fold development. Fracture set #1 is constrained to the hinge region of the anticline and is oriented subparallel to the fold axis (Figure 2.10). Furthermore, this fracture set is not observed within the Artillery Rocks or Soapy Rocks localities, suggesting a spatial relationship to the hinge of the anticline. It is interpreted as an longitudinal b-c fracture set (Hancock, 1985) formed during convex extension within the outer-arc of the fold (Savage et al., 2010) (Figure 2.16; D2, Phase 2).

Folding-related fracturing and uplift is suggested to have resulted from the reactivation and reversal

of an underlying normal fault, oriented parallel to the fold hinge (Figure 2.16; D2, Phase 2). This is consistent with interpretations of seismic reflection profile data by Matthews (2015) who showed that inverted normal faults controlled fold position within offshore Cretaceous-aged sediments.

The fracture abutting relationships indicate that the sub-vertical fracture set #3 postdates the formation of all other fracture sets throughout the Eumeralla Fm (Figure 2.7). Given that this fracture set is observed regionally throughout the Eumeralla Fm, combined with the loading path calculations provided (Figure 2.15), this fracture set likely formed during uplift as unloading joints. However, based on the average orientation of this fracture set, it may have also formed under the influence of a ~NNW-SSE oriented (~155°) compressional tectonic stress during the uplift process (Figure 2.16, D3).

Given that the ~16° anticlockwise change in the orientation of the fold hinge occurs over a distance of less than 400 meters (Figure 2.10), it is considered unlikely that basement geometry alone has influenced the fold hinge geometry. An overprinting deformation event D4 (Figure 2.16) is inferred from the ~30m left-lateral offset of the northern section of the fold hinge (Figure 2.10), interpreted from field observations (horizontal offset on faults) within the northern and southern limbs (Figure 2.6A, B) combined with bathymetric data (Figure 2.4). Sinistral strike slip faulting along pre-existing (#2) a-c fractures (through locations 4 & 5, Figure 2.10) could have induced block rotation and lead to the ~16° anticlockwise rotation of the fold hinge. The #2 fracture set would provide a favorably oriented plane of weakness (Sibson, 2000a; Wilkins et al., 2001). Furthermore, the fracture corridors observed within Artillery Rocks may have formed during this phase of deformation, as the lack of significant breccia/ gouge observed within the moderately long fracture corridors is considered by Wilkins et al. (2001) to be indicative of fracture reshear along pre-existing fractures.

Calcite veins are heterogeneously distributed, occurring as infilling material in fracture set #1 as well as the matrix to breccia in locations 4 & 5. Fracture set #1 is interpreted to have acted as a fluid conduit in these areas, with one hypothesis being that fracture set #1 was forced open by high fluid pressures resulting from migrating fluids. However, given the restriction of calcite veins to areas within and around highly sheared regions (Figure 2.6A), fluid movement was likely isolated to ~NW-SE oriented brecciated zones, prior to migrating into #1 orientation fractures. Therefore, calcite cementation may have occurred during or after the latest stage of deformation and faulting within the St. George Anticline.

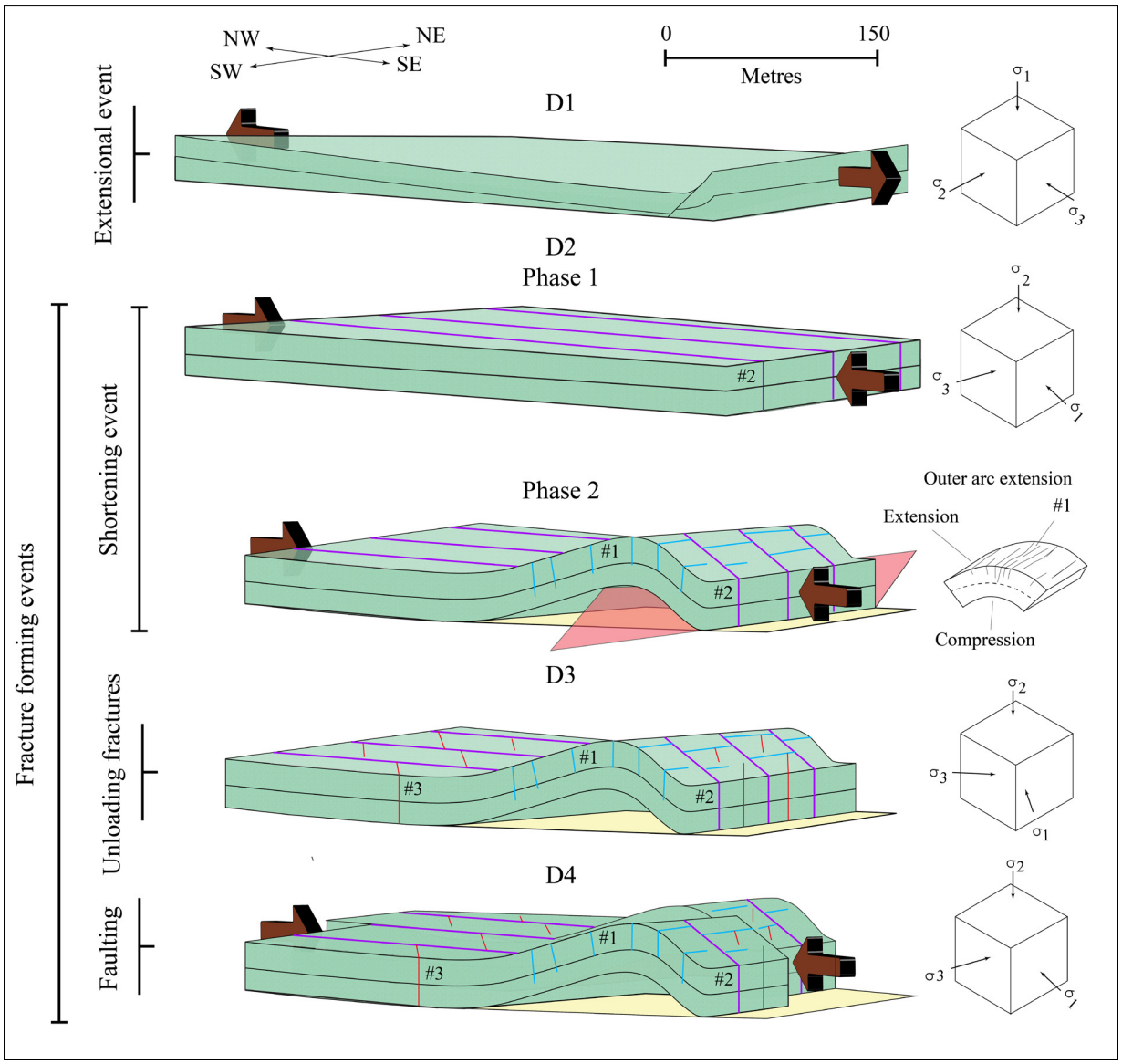


**Figure 2.16:** A schematic representation of deformation and fracture formation within the St. George Anticline, accompanied by 3D block diagrams that illustrate changes to the paleostress orientations. D1 extension: NW-SE extension forms NE-oriented basement faults (Matthews, 2015). D2 folding, Phase 1: NW-SE shortening initiates the formation of the #2 transverse a-c fracture set. D2 folding, Phase 2: Continued NW-SE shortening, reactivation of the underlying normal faults and fold amplification, resulting in outer-arc extension and the formation of the fracture sets #1 and densifying fracture set #2. D3, Unloading: Continued uplift forms the fracture set #3 (unloading joints). D4, faulting: NW-SE shortening results in left-lateral displacement of the fold hinge, with associated sinistral faults forming in the limb regions along prior formed a-c fractures.

### 2.5.5 Soapy Rocks (Demons Bluff Group)

Fracture patterns vary within the uppermost two units of the Soapy Rocks locality, with a combination of joints and shear fractures identified (Figure 2.12C, E). Based on the interpreted loading path for this unit (Figure 2.15), the calculated horizontal stress change generated during uplift from maximum burial to the surface would produce a tensile (-3.15MPa) minimum principle stress at surface depths. The observed orthogonal fracture sets (Figures 2.11C & 2.16A) may have therefore formed as unloading joints, with the subvertical, NNW-SSE oriented fracture set #3 forming slightly prior to the WNW-ESE fracture set #2, based on abutting relationships (Figure 2.12D).

The orientation of shear fractures (Figures 2.12 & 2.16B) at Soapy Rocks appears to suggest several of these unloading joints were subsequently reactivated in shear, with the shear fractures oriented approximately 24° to the maximum shortening direction (Figure 2.17C) (Hancock, 1985; Sibson, 2000a). The southeastern Australian margin has maintained a dominantly NW-SE oriented compressional state of intraplate stress since the mid-late Eocene (ca.43Ma) (Holford et al., 2014). However, given that these early Oligocene-aged sediments are unfolded and only contain minor shear fracture formation, deformation within this locality is interpreted to have occurred during the latest stages of Miocene (12-3Ma) deformation (Green *et al*, 2004). Furthermore, this suggests that folding within the Eumeralla Fm, along the Otway coastline, occurred dominantly prior to deposition of the Angahook Fm, with Soapy Rocks only preserving the latest stage of fracture formation and minor faulting.

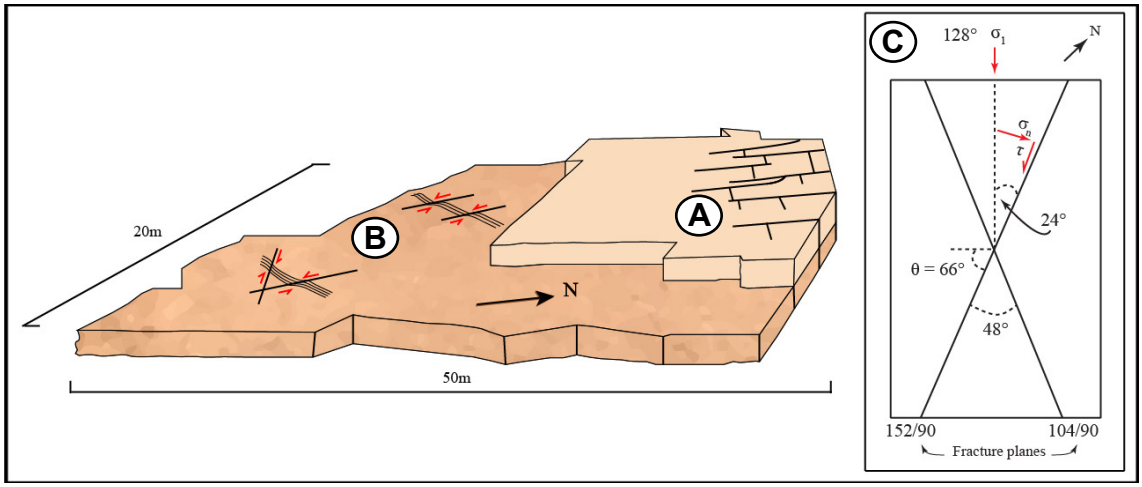


**Figure 2.17:** Schematic representation of fracturing within the uppermost stratigraphic units of the Soapy Rocks locality. Observed are two orthogonal fracture sets (A) and several shear fractures (B). (C) Relationships between the shear fractures and the maximum principle stress. The fracture planes are oriented at 24° to the maximum stress (σ1=128°) and have a resolved shear stress of (2θ = 132°).

Based on a combination of field observations, fracture populations derived from high-resolution orthophotographs and sediment loading paths, this study has identified three main fracture groups along the eastern Otway coastline (Figure 2.5C). A summary of the deformation history below (Figure 2.18) illustrates the relative timing of fracture formation within the two stratigraphic units.

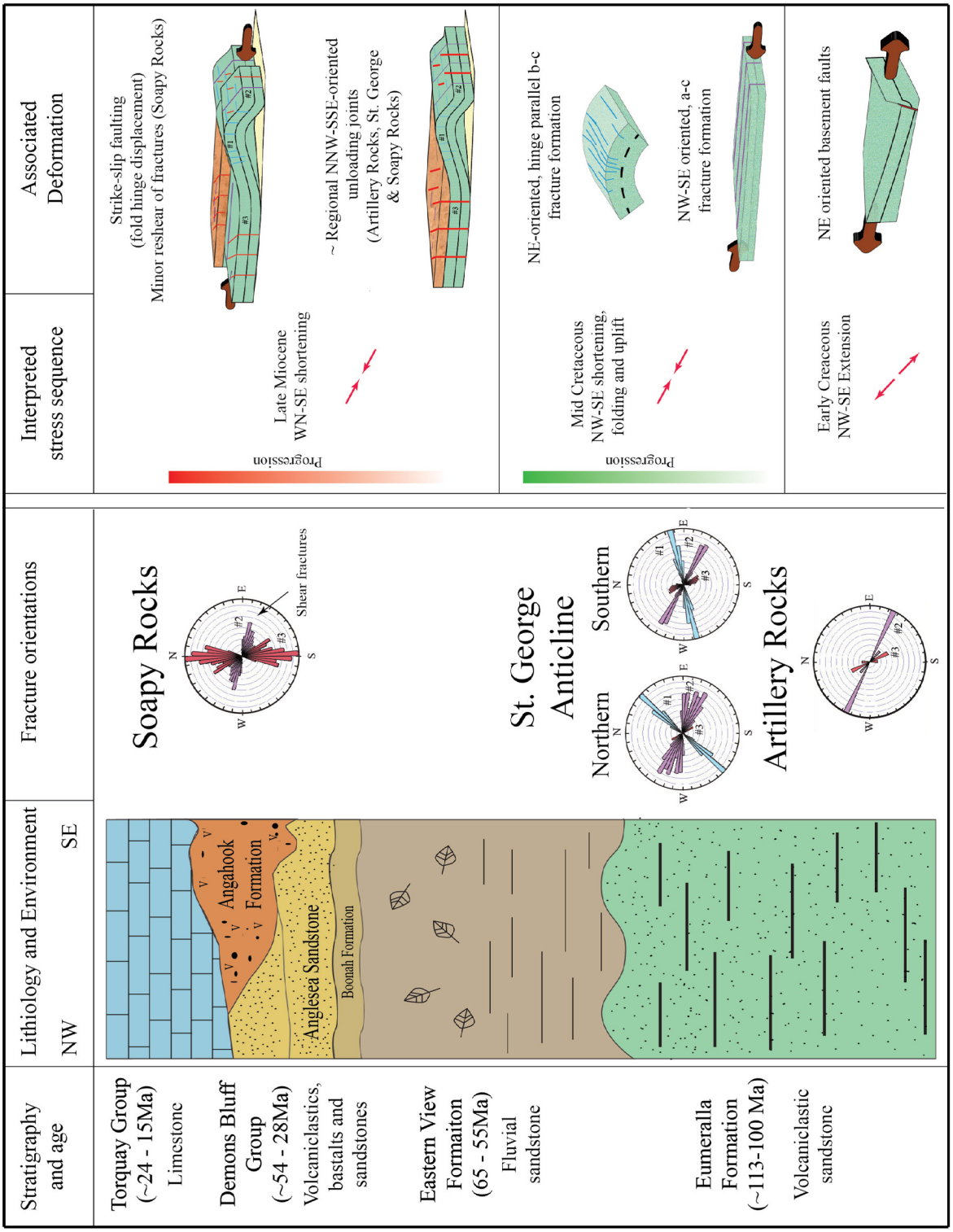


**Figure 2.18:** Interpreted deformation history of the eastern Otway coastline based on fold and fracture orientations. Red arrows indicate the orientation of the interpreted maximum principal stress. The stratigraphy of the eastern Otway Basin is modified from Abele et al. (1988) and McLaren et al. (2009).

## 2.6 Conclusions

This study has shown that fracture patterns along the eastern Otway coastline vary significantly within different stratigraphic and structural positions, with several key features identified:

(1) Within the deepest stratigraphic unit encountered (Eumeralla Fm) fracture formation varies with fold position (Figures 2.9 & 2.10).

(2) Based on the structural and stratigraphic occurrence of fracture set #2, combined with observed abutting relationships, this fracture set is interpreted to have formed during the earliest phases of folding, prior to increasing density syn-folding.

(3) Fracture set #1 is interpreted to relate directly to mid Cretaceous folding, being observed only within folded regions and having an orientation that appears to be influenced by position relative to the fold hinge (Figure 2.10).

(4) Fracture set #3 may have initiated as unloading joints at 0.8-1.1km depth during uplift (Figure 2.15), however, the orientation of this fracture set may have been influenced by tectonic shortening (Figure 2.16, D3).

(5) Sinistral strike-slip movement is interpreted to have displaced the St. George fold hinge (Figure 2.10) along prior formed a-c fractures, while offsetting hinge-parallel fracture sets (Figures 2.5A) and bedding (Figure 2.6B) within the limb regions.

(6) Strike-slip movement observed within the younger stratigraphic units (Figures 2.12 & 2.16B) supports the interpretation that strike-slip faulting (Figure 2.16, D4) coincided late Cenozoic shortening.

(7) At least one fluid flow event is responsible for calcite emplacement within the St. George Anticline, interpreted to be restricted to brecciated shear zones (Figure 2.6A). Fluids may have been derived from external sources migrating along the brecciated zones and then further permeating to proximal NE oriented fractures.

MONASH University

# Declaration for Thesis Chapter 3

Declaration by candidate

In the case of Chapter 3, the nature and extent of my contribution is as follows:

| *Nature of contribution* | *Extent of contribution (%)* |
|---|---|
| Main research, fieldwork, data analysis and interpretaton | 80% |

The following co-authors contributed to the work. If co-authors are students at Monash University, the extent of their contribution in percentage terms must be stated.

| *Name* | *Nature of contribution* | *Extent of contribution (%)* |
|---|---|---|
| Mike Hall | Supervisory role | 10% |
| Alexander R. Cruden | Supervisory role | 10% |

The undersigned hereby certify that the above declaration correctly reflects the nature and extent of the candidate's and co-authors' contributions to this work*.

Candidate's signature [redacted] Date: 05/08/2017

Main Supervisor's signature [redacted] Date: 05/08/2017

# Chapter 3

Synthesis: Fracture formation within the eastern Otway Basin, with implications for fold-fracture conceptual models

Joel Vergunst, Mike Hall & Alexander R. Cruden

School of Earth, Atmosphere and Environment, Monash University, Australia;

Email: joel.vergunst1@monash.edu, mike.hall@monash.edu

## 3.1 Introduction

In order to determine the timing of fracture formation within the eastern Otway Basin it is important to further consider the potential processes involved in forming fractures in folded regions. Recent studies documenting fracture formation within folded regions (Bergbauer & Pollard, 2004; Fischer & Christensen, 2004; Florez-Nino et al., 2005; Bellahsen et al., 2006; Cooper et al., 2006; Hayes & Hanks, 2008; Zahm & Hennings, 2009; Shackleton et al., 2011; Inigo et al., 2012; Tavani et al., 2012; Awdal et al., 2013; Jamison, 2016) have recognised three processes that govern the orientation and timing of fracture formation;

- The orientation of underlying basement structures (Fischer & Christensen, 2004; Cooper et al., 2006; Shackleton et al., 2011).
- Inherent weaknesses introduced by pre-folding deformation (Bergbauer & Pollard, 2004; Inigo et al., 2012)
- Syn-folding fracture formation that incorporates aspects of both the initial fracture formation parallel to regional shortening and fracture growth during fold flexure (Guiton et al., 2003; Florez-Nino et al., 2005; Bellahsen et al., 2006; Hayes & Hanks, 2008; Savage et al., 2010; Tavani et al., 2012; Awdal et al., 2013).

Each of these aspects of fracture formation are important for understanding the geologic history of the eastern Otway Basin, however, modern structural models often neglect the potential for fracture formation accompanying pre- or post-folding erosion and uplift.

## 3.2 Discussion: Controls on fracture formation

The purpose of this chapter is to provide a synthesis of the interpreted chronological history of fracture formation along the eastern Otway coastline, based on the findings of the previous chapters. This interpretation will advance on current models in the literature by comparing fracture variation between multiple stratigraphic formations in order to constrain the timing of fracture formation with respect to folding, while investigating the influence of regional uplift on fracture formation.

### 3.2.1 Pre-folding fracture formation

Many structural models that concentrate on syn-folding fracture development (discussed further in Section 3.2.3) are based on an inferred intact stratigraphy prior to folding (Stearns, 1968; Zahm & Hennings, 2009; Jamison, 2016). However, several authors (Guiton et al., 2003; Bergbauer & Pollard, 2004; Bellahsen et al., 2006; Cooper et al., 2006; Shackleton et al., 2011; Awdal et al., 2013) instead interpret a pre-folding fracture set, on the basis that the oldest observed fracture set has a strike that is inconsistent with the syn-folding principle stress orientations and/or is observed within adjacent unfolded sediments.

Studies frequently attribute the orientations of local pre-folding fracture sets to the position of underlying thrust faults (Bergbauer & Pollard, 2004; Florez-Nino et al., 2005; Shackleton et al., 2011; Inigo et al., 2012; Tavani et al., 2012) or reverse faults (Fischer & Christensen, 2004; Hayes & Hanks, 2008; Holford et al., 2014). In the case of pre-folding fracture sets that occur regionally, these may be due to a prior far-field stress, resulting from plate boundary interactions (Awdal et al., 2013).

Inherent weaknesses in a rock formed by pre-folding deformation will lower the tensile and compressive strength of the rock unit (Sibson, 2000a) so that fractures can preferentially initiate along these planes of weakness. Multiple overprinting periods of tectonic activity are common within older tectonic regimes (Evans & Fischer, 2012), and generally an increase in fracture abundance and complexity will occur within a rock unit over time. Therefore, numerous planes of weakness will be generated, that will gradually reduce the rock unit's strength, and eventually cause a preference for reactivation of older fracture sets over the formation of new ones (Sibson, 2000a).

The orientation of NE-SW striking folds observed in Early Cretaceous rocks of the Eumeralla Fm exposed along the southeastern Otway Range coastline (Figure 1.14) are interpreted to have been influenced by underlying, inverted Early Cretaceous normal faults (Holford et al., 2014; Matthews, 2015). By comparison Late Cretaceous to Cenozoic rocks exposed in the northern onshore region of the Otway Range (Figure 1.19) have experienced significantly less strain. Based on the broad, NW-SE orientation of Late Cretaceous basin-bounding structures northeast of the Otway Ranges (Figure 1.19), these structures may have an origin partly influenced by minor, Late Cretaceous NE-SW extension (Figure

1.24A). Similarly oriented Late Cretaceous basin development has occurred within the southwestern Otway Basin (Hall & Keetley, 2009; Holford et al., 2014).

### 3.2.2 Syn-folding fracture growth

As previously mentioned in Chapter 2, five fracture sets are predicted by the model of Sterns (Stearns, 1968) to form during fold growth. The most common of these being transverse a-c or longitudinal b-c fracture sets (Florez-Nino et al., 2005; Bellahsen et al., 2006; Cooper et al., 2006; Hayes & Hanks, 2008; Inigo et al., 2012; Tavani et al., 2012; Awdal et al., 2013) (Figure 3.1). However, as observed by Cooper et al. (2006) for a basement-cored thrust in Wyoming, USA, fold-related fracture sets may fail to form along orientations predicted by the Stearns model, depending on the mechanism driving crustal shortening.

The distribution of, the NW-SE oriented, fracture set #1 along the eastern Otway coastline appears to be confined to the folded Eumeralla Fm sediments (Figure 2.10), with reduced fracture spacing measured near the hinge of the St. George anticline (Figure 2.8B). Based on the orientation of the #1 fracture set, combined with its relative age as determined from cross-cutting and abutting relationships (Figure 2.7), this bedding perpendicular fracture set is suggested to have formed sub-parallel to the fold axis due to outer-arc extension (Savage et al., 2010) during the mid Cretaceous (ca. 95Ma).

On the basis of the orientations, opening modes and relative chronology of the NW-SE oriented, #2 fracture set, this fracture set is interpreted to have formed during mid Cretaceous uplift. However, Late Cretaceous (ca. 95-70 Ma) NE-SW extension may have contributed to a minor increase in fracture density.

Based on seismic interpretations by Matthews (2015) and Smith (1998), combined with fission track data, within the Anglesea-1 well (Figure 2.1) and interpreted by Green et al. (2004), a second period of uplift occurred in the late Miocene-early Pliocene. Based on the minor bedding dips measured within the Cenozoic sediments, combined with the orientation, distribution and cross-cutting and abutting relationships of the measured fracture sets (Figure 2.12). This episode of tectonic shortening is interpreted to have resulted in only minor amplification of NE striking folds within the Eumeralla Fm (Figure 1.14)

and ~NW-SE oriented Cenozoic compaction features along Anglesea and Addiscot Beach (Figure 1.19).

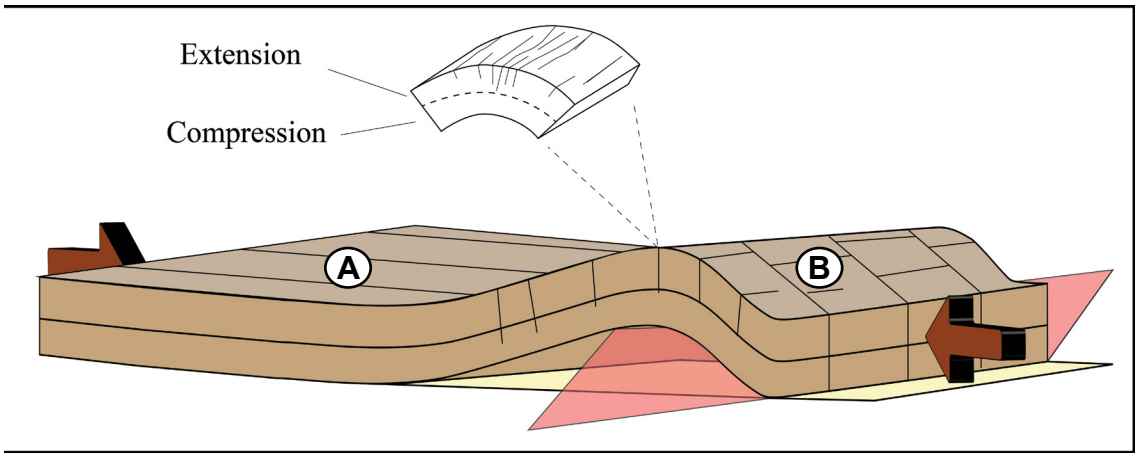


**Figure 3.1:** Syn-folding fractures, (A) fractures oriented perpendicular to the fold strike forming parallel to regional shortening, and (B) fractures oriented parallel to the fold axis, forming when tensile stress conditions are generated during outer-arc extension of the fold hinge.

### 3.2.3 Fracture formation during uplift

As described in Section 2.5.2, extensional unloading joints can spontaneously initiate within sandstone after relatively minor amounts of erosion and uplift, and will readily align with the prevailing regional stress field at the time of their formation (Engelder, 1984). Furthermore, multiple periods of pre- or post-folding uplift can occur within an active tectonic environment, and the principle stress orientations may vary between each of these phases of uplift (Fischer & Christensen, 2004). However, the relative timing in which unloading joints form with respect to regional folding is often ignored in recent fold-fracture studies. A failure to correctly identify potential unloading joints may lead to misinterpretations when integrating measured fracture patterns into conceptual models of fold-fracture formation, or when predicting historical reservoir connectivity, permeability and flow rate (Odling, 1992; Sibson, 2000b; Cooper et al., 2006). This is particularly important for regions such as the eastern Otway Basin where targeted reservoir units commonly lack inherent permeability (Fairbairn & Williams, 1969).

As an example, the Cardium Sandstone within the central Alberta Foothills (Figure 3.2A) can be considered analogous to the Eumeralla Formation within the eastern Otway Basin, given the similarities in age, burial depth and degree of folding of the sediments (Table 3.1).

Jamison (2016) documented fracture populations within the folded Cardium Sandstone with the central Alberta Foothills (Figure 3.2A) and measured fracture variation relative to both fold position and the

degree of fold closure among three anticlines. Significant observations included a regionally pervasive, NE-SW, sub-vertical fracture set that accounted for ~90% of the measured fracture orientations around Grande Cache (Figure 3.2B). These fractures are aligned sub-parallel to the current regional shortening orientation, but lack substantial cross-cutting or abutting relationships (Jamison, 2016). Folding and fracture formation was interpreted to have occurred during maximum burial, prior to 1.5-4km of subsequent, post-folding uplift that occurred over a ~25Ma period (Kalkreuth & Mcmech, 1988; Jamison, 2016).

The physical properties of the sandstone unit within the Cardium Sandstone (Table 3.2) indicate that an optimal depth for unloading joint formation would have been reached 1.9-0.25 kilometres from the surface (Figure 3.3). This suggests that a significant proportion of the documented fractures may instead relate to post-folding fracture formation during regional uplift. Therefore, while formation of the dominant NE-SW fracture set was previously attributed by Jamieson (2016) to be entirely due to syn-folding deformation, the confidence that can be placed in these interpretations is reduced due to the potential for significant post-folding uplift fracture formation.

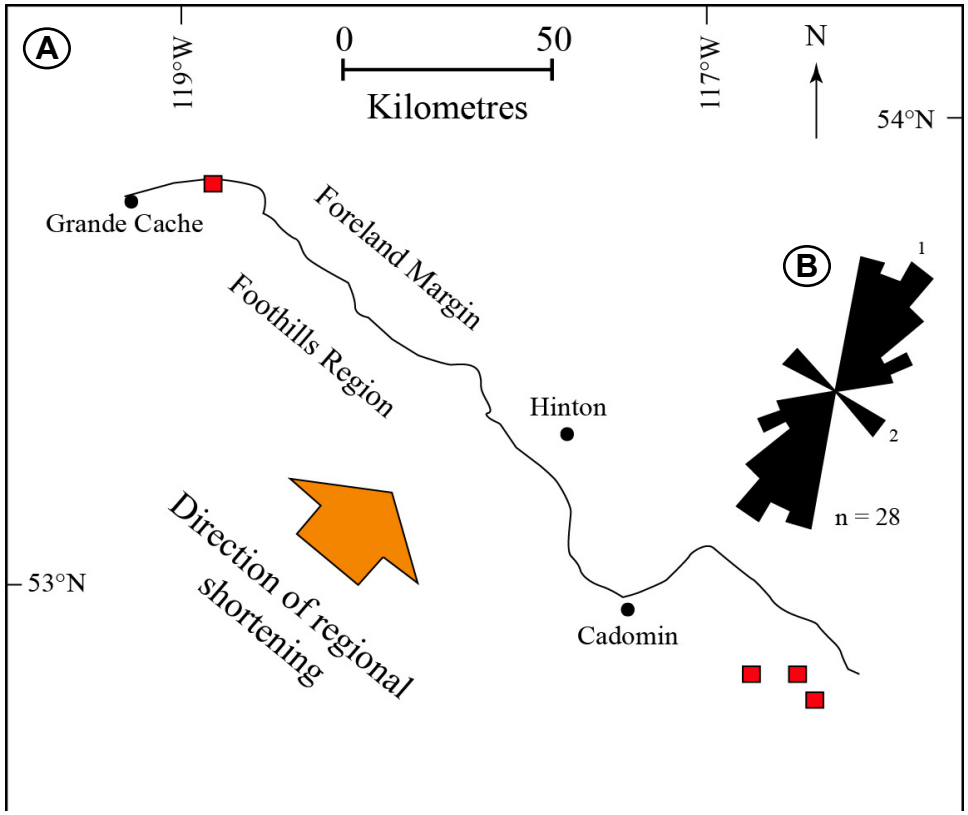


**Figure 3.2:** (A) Location of measurement sites (red) for three anticlines south of Cadomin, as well as one unfolded section located northeast of Grande Cache, within the central Alberta Foothills. (B) Rose diagram of fracture orientations with the Cardium Sandstone around Grande Cache, after Jamison (2016).

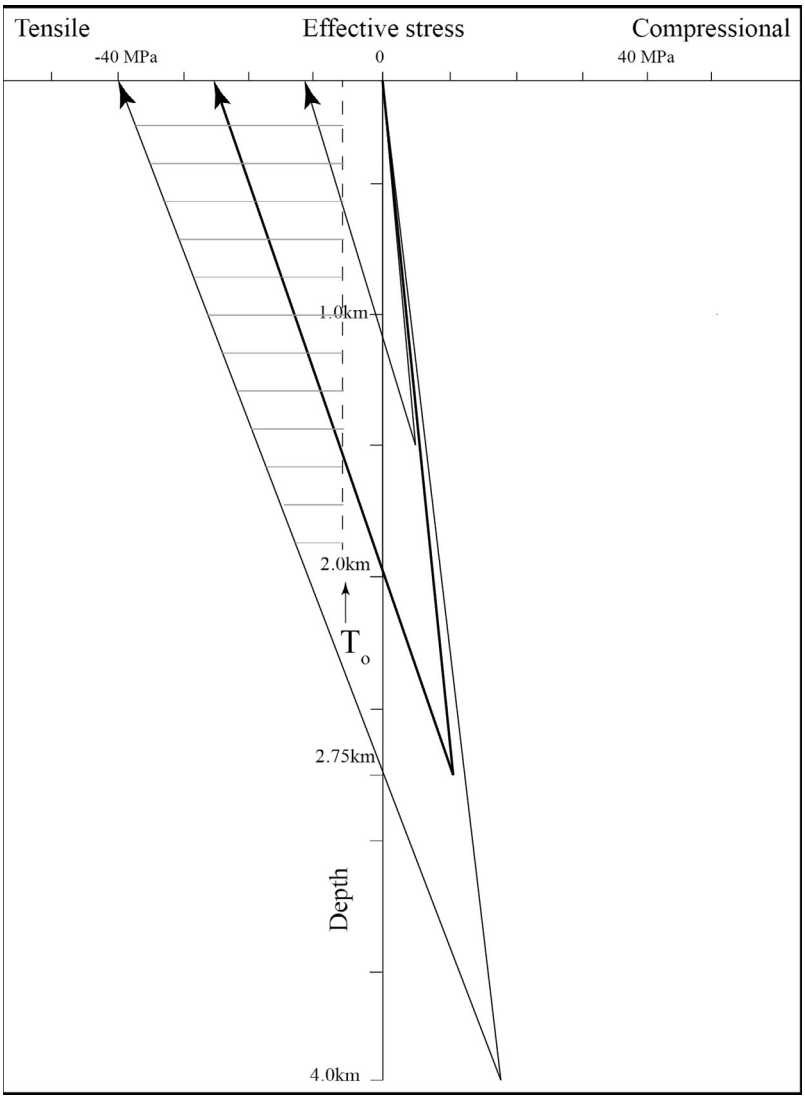


**Figure 3.3:** A loading path diagram representing effective horizontal stress conditions arising during burial and uplift of the Cardium Sandstone. The loading path is based on the mechanical properties within Table 3.2 and the dashed section represents the range of conditions in which the effective horizontal stress would form unloading joints.

**Table 3.1:** The Eumeralla Formation and its analogue the Cardium Sandsone, as adopted by Jamison (2016).

| Properties | Cardium Sandstone | Eastern Otway Basin |
|---|---|---|
| Structural setting | Foreland, fold-thrust belt | Folded, rifted continental margin |
| Age (Ma) | ca. 110-100 | ca. 94-86 |
| Dominant lithology | Fine grained sandstone | Volcaniclastic sandstone |

**Table 3.2:** The mechanical properties of the Cardium Sandstone, as adopted by Jamison (2016), Numerical ranges are provided, with averaged values in bold. Note that average values of **ν**, **E** and **α** are provided for consolidated (C) rock types, while values for unconsolidated sediments (UC) have been used to calculate the horizontal stress change during burial. The geothermal gradient (~31°C) and surface temperature (~20°C) were derived from Kalkreuth and Mcmech (1988). The horizontal stress change (Δσh) is provided for both burial to maximum depth (MD) as well as uplift to surface (S).

| Mechanical properties & stress | Cardium Sandstone | References |
|---|---|---|
| Average density (kg/m$^3$) | 2400 | Ahrens (1995) |
| Tensile strength $T_o$ (MPa) | 6 | |
| Maximum depth (z) (km) | 1.5 - 4 | |
| Temperature change (ΔT) ˚C | 26.5-104 (65.25) | |
| Poisson's ratio (ν) | UC: (Sand): 0.21 | Engelder (1984) Lambe and Whitman (1969) Voight and St. Pierre (1974) Chong et al. (1980) Wilhelmi and Somerton (1967) |
| | C: (Sandstone): 0.33 | |
| Young's modulus (GPa) | Sand: 1 | |
| | Sandstone: 16.5 | |
| Thermal expansivity (α) ($10^{-6}C^{-1}$) | UC: 10 | |
| | C: 10.8 | |
| Maximum effective normal stress ($\sigma_1$) (MPa) | 21 - 63 | |
| Calculated horizontal stress change ($\Delta\sigma_h$) (MPa) | MD: 5.91 - 18.06 (11.98) | |
| | S: 17.39 - 58.68 (38.03) | |
| Surface stress (MPa) | (-)11.48 - (-) 40.62 (-26.05) | |

### 3.2.4 Post-folding fracture formation

Post-folding fracture formation is commonly attributed to the formation of overprinting strike-slip or thrust faults (Guiton et al., 2003; Awdal et al., 2013; Jamison, 2016). This is often after a reorientation of the regional tectonic stress field, or due to the formation of normal faults during a period of regional tectonic stress reduction (Ismat & Benford, 2007).

Along the southeastern Otway coastline, the strike-slip displacement of NE-SW striking folds observed in Early Cretaceous rocks of the Eumeralla Fm (Figure 2.10), combined with the orientation of observed fault slip-surfaces within the limb regions (Figure 2.6), suggests that an episode of faulting post-dated folding. Given that minor strike-slip and thrust faulting is observed within the younger stratigraphic units (Figures 1.22 & 2.12), regional fault development is interpreted to have involved a period of NW-SE oriented shortening, coinciding with the late Miocene-early Pliocene uplift (Green et al., 2004) (Appendix 4).

## 3.3 Conclusions

Based on data collected within multiple stratigraphic formations along the eastern Otway coastline, NE-SW oriented (#1) syn-folding factures are exclusively observed within the folded sections of the Early Cretaceous Eumeralla Fm (Figure 2.10). Furthermore, the density of the NW-SE oriented fracture set #2 increases towards the hinge of NE-striking folds (Figure 2.8). This, combined with the lack of folding within Cenozoic sediments (Figure 1.19), suggests that fracture formation is largely a product of mid Cretaceous uplift (ca. 95Ma, Appendix 4).

On the basis of abutting relationships within the Eumeralla Fm (Figure 2.7), the NNW-SSE oriented #3 fracture set is a late-formed fracture set. Based on its occurrence within Cenozoic sediments, combined with the interpreted loading path of the Eumeralla Fm and Demons Bluff Gp (Figure 2.15), this fracture set is interpreted to have formed as an unloading joint during Cenozoic uplift.

Based on the strike-slip offset of NE striking fold hinges within the Eumeralla Fm (Figure 2.10), combined with shear fractures within the younger sediments, post-folding shear fracture formation is considered to have occurred during a period of late Miocene - early Pliocene NW-SE oriented shortening.

This thesis has shown that complex fracture networks such as those observed along the eastern Otway coastline can be the result of multiple overprinting events, and it is therefore considered unlikely that syn-folding processes alone will account for the complexity observed within folded reservoir rocks. Current fold-fracture models often rely too heavily on comparing the structural positioning of fracture sets within single formations to determine the relative timing of fracture populations. Furthermore, these models often fail to include an adequate evaluation of the potential for unloading joint formation during periods of regional uplift. Therefore these models readily incorporate post-folding unloading joints into a late-stage of the syn-folding process, which can significantly misrepresent the timing of fracture formation. Fold-fracture models can be improved by including observations of fracture characteristics from within multiple stratigraphic formations, in addition to comparing fracture variations at differing structural positions, which will enhance estimates of the relative timing of fracture formation within tectonically active regions.

# References

**Aadnoy B.** & Looyeh R. 2011. Appendix 1. In, Petroleum Rock Mechanics, Drilling Operations and Well Design, Vol. 1, pp 323-326, Burlington, Elsevier Science

**Abele C.** 1968. Explanatory notes on the Anglesea 1:63,360 Geological Map. Mines Department Victoria Geological Survey Report.

**Abele C.** 1979. Geology of the Anglesea area, central coastal Victoria, Memoir 31. Victoria G. S. o. Spencer-Jones, D.

**Abele C.**, Gloe C. S., Hocking J. B., Holdgate G. R., Kenley P. R., Lawrence C. R., Ripper D., Threfall W. F. & Bolger P. F. 1988. Tertiary. In: Douglas J. G. & Ferguson J. A. eds., The Geology of Victoria (2nd edition), pp 252–350, Geological Society of Australia Victorian Division, Melbourne.

**Agisoft LLC 2015.** Agisoft Photoscan Professional [WWW Document] <http://www.agisoft.com>. (retrieved 7.16.15).

**Ahrens T.** J. 1995. Rock physics phase relations; a handbook of physical constants (AGU Reference Shelf, Vol. 3). American Geophysical Union, Washington, DC, United States.

**Anonymous 1992.** Gas and fuel exploration N.L. Seismic Line OGF92A-411. Barwon survey, Otway Basin, Victoria.

**Awdal A.** H., Braathen A., Wennberg O. P. & Sherwani G. H. 2013. The characteristics of fracture networks in the Shiranish Formation of the Bina Bawi Anticline; comparison with the Taq Taq Field, Zagros, Kurdistan, NE Iraq. Petroleum Geoscience 19, 139-155, doi: 10.1144/petgeo2012-036.

**Bellahsen N.**, Fiore P. & Pollard D. D. 2006. The role of fractures in the structural interpretation of Sheep Mountain Anticline, Wyoming. Journal of Structural Geology 28, 850-867, doi: 10.1016/j.jsg.2006.01.013.

**Bergbauer S.** & Pollard D. D. 2004. A new conceptual fold-fracture model including prefolding joints, based on the Emigrant Gap Anticline, Wyoming. Geological Society of America Bulletin 116, 294-307, doi: 10.1130/B25225.1.

**Bernecker T.**, Smith M. A., Hill J. A. & Constantine A. E. 2003. Oil and gas, fuelling Victoria's economy. In: W.D. B. ed., Geology of Victoria, Vol. Special publication 23, pp 469-487, Geoogical society of Australia.

**Birch W.** D. 2003. Geology of Victoria (Special Publication - Geological Society of Australia, Vol. 23). Geological Society of Australia, Sydney, N.S.W., Australia.

**Blenkinsop T.** G. 2008. Relationships between faults, extension fractures and veins, and stress. Journal of Structural Gology 30, 622-632, doi: 10.1016/j.jsg.2008.01.008.

**Boult P.** J., LYON P., CAMAC B. A., HUNT S. & ZWINGMANN H. 2008. Unravelling the complex structural history of the Penola Trough; revealing the St George Fault. Petroleum Exploration Society of Australia Special Publication EABS 2008, 81-93.

**Bray R.** J., GREEN P. F. & DUDDY I. R. 1992. Thermal history reconstruction using apatite fission track analysis and vitrinite reflectance; a case study from the UK East Midlands and southern North Sea. Geological Society Special Publications 67, 2-25.

**Briguglio D.**, Kowalczyk J., Stilwell J. D., Hall M. & Coffa A. 2013. Detailed paleogeographic evolution of the Bass Basin; Late Cretaceous to present. Australian Journal of Earth Sciences 60, 719-734, doi: 10.1080/08120099.2013.826282.

**Cas R.**, SIMPSON C. & SATO H. 1993. Newer Volcanics Province - processes and products of phreatomagmatic activity. IAVCEI Canberra 1993: excursion guide, September, 1993 (Record - Australian Geological Survey Organisation). Geoscience Australia, Canberra, A.C.T., Australia.

**Chong K.** P., Uenishi K., Smith J. W. & Munari A. C. 1980. Non-linear three dimensional mechanical characterization of Colorado oil shale. International Journal of Rock Mechanics and Mining Sciences & Geomechanics Abstracts 17, 339-347.

**Cooper G.** T. & Hill K. C. 1997. Cross-section balancing and thermochronological analysis of the Mesozoic development of the eastern Otway Basin. APPEA Journal 37, 390-414.

**Cooper G.** T. 1995. Structural geology, thermochronology, and tectonic evolution of the Torquay Embayment, Eastern Otway Basin. PhD thesis thesis, Department of Earth Sciences, Monash University, Australia.

**Cooper S.** P., Goodwin L. B. & Lorenz J. C. 2006. Fracture and fault patterns associated with basement-cored anticlines; the example of Teapot Dome, Wyoming. AAPG Bulletin 90, 1903-1920, doi: 10.1306/06020605197.

**Duddy I.** R. 1994. The Otway Basin: thermal, structural, tectonic and hydrocarbon generation histories. Australian Geological Survey Organisation, 35-42.

**Duddy I.** R. 2003. Geology of Victoria (Mesozoic). In: Birch W. D. ed., Special Publication - Geological Society of Australia, Vol. 23, pp 239-286, Geological Society of Australia, Sydney, N.S.W., Australia.

**Duddy I.** R. 2010. The Otway Basin. Geotrack International Pty. Ltd.

**Edwards A.** B. 1962. Notes on the geology of the Lorne District, Victoria. Proceedings of the Royal Society of Victoria 75, Part 1, 101-119.

**Eisenbeiss H.** 2009. UAV Photogrammetry. PhD thesis thesis, ETH Zurich.

**Engelder T.** & Geiser P. 1980. On the use of regional joint sets as trajectories of paleostress fields during the development of the Appalachian plateau, New York. Conference on Magnitude of Deviatoric Stresses in the Earth's Crust and Uppermost Mantle, 29 July-2 Aug. 1979, USA, pp. 6319-6341.

**Engelder T.** 1984. Loading paths to joint propagation during a tectonic cycle: an example from the Appalachian Plateau, U.S.A. Journal of Structural Geology 7, 459-476, doi: 10.1016/0191-8141(85)90049-5.

**Evans M.** A. & Fischer M. P. 2012. On the distribution of fluids in folds; a review of controlling factors and processes. Journal of Structural Geology 44, 2-24, doi: 10.1016/j.jsg.2012.08.003.

**Fairbairn D.** & Williams L. W. 1969. Summary of data and results, Otway Basin, Victoria. Pecten No. I-lA Nerita No. I. 88.

**Fischer M.** P. & Christensen R. D. 2004. Insights into the growth of basement uplifts deduced from a study of fracture systems in the San Rafael Monocline, east central Utah. Tectonics 23, doi: 10.1029/2002TC001470.

**Florez-Nino J.**-M., Aydin A., Mavko G., Antonellini M. & Ayaviri A. 2005. Fault and fracture systems in a fold and thrust belt; an example from Bolivia. AAPG Bulletin 89, 471-493.

**Fossen H.** 2010. Structural Geology. Cambridge University Press Leiden.

**Green P.** F., Crowhurst P. V. & Duddy I. R. 2004. Integration of AFTA and (U-Th)/ He thermochronology to enhance the resolution and precision of thermal history reconstruction in the Anglesea-1 well, Otway Basin, SE Australia. PESA Eastern Australasian Basins Symposium 2, 117-131.

**Gregory R.** T., Douthitt C. B., Duddy I. R., Rich P. V. & Rich T. H. 1989. Oxygen isotopic composition of carbonate concretions from the lower Cretaceous of Victoria, Australia: implications for the evolution of meteoric waters on the Australian continent in a paleopolar environment. Earth and Planetary Science Letters 92, 27-42.

**Guiton M.** L. E., Sassi W., Leroy Y. M. & Gauthier B. D. M. 2003. Mechanical constraints on the chronology of fracture activation in folded Devonian sandstone of the western Moroccan Anti-Atlas. Journal of Structural Geology 25, 1317-1330, doi: 10.1016/ S0191-8141(02)00155-4.

**Hall M.** & Keetley J. 2009. Otway Basin: stratigraphic and tectonic framework. Department of Primary Industries GeoScience Victoria 3D Victoria 2.

**Hancock P.** L. 1985. Brittle microtectonics; principles and practice. Journal of Structural Geology 7, 437-457.

**Hayes M.** & Hanks C. L. 2008. Evolving mechanical stratigraphy during detachment folding. Journal of Structural Geology 30, 548-564, doi: 10.1016/j.jsg.2008.01.006.

**Hill K.** C., Hill K. A., Cooper G. T., O'Sullivan A. J., O'Sullivan P. B. & Richardson M. J. 1995. Inversion around the Bass Basin, SE Australia. Geological Society Special Publications 88, 525-547.

**Holdgate G.** R., Smith T. A. G., Gallagher S. J. & Wallace M. W. 2001. Geology of coal-bearing Palaeogene sediments, onshore Torquay Basin, Victoria. Australian Journal of Earth Sciences 48, 657-679, doi: 10.1046/j.1440-0952.2001.00888.x.

**Holford S.** P., Hillis R. R., Duddy I. R., Green P. F., Tassone D. R. & Stoker M. S. 2011. Paleothermal and seismic constraints on late Miocene-Pliocene uplift and deformation in the Torquay Sub-basin, southern Australian margin. Australian Journal of Earth Sciences 58, 543-562, doi: 10.1080/08120099.2011.565074.

**Holford S.** P., Tuitt A. K., Hillis R. R., Green P. F., Stoker M. S., Duddy I. R., Sandiford M. & Tassone D. R. 2014. Cenozoic deformation in the Otway Basin, southern Australian margin; implications for the origin and nature of post-breakup compression at rifted margins. Basin Research 26, 10-37, doi: 10.1111/bre.12035.

**Inigo J.** F., Laubach S. E. & Hooker J. N. 2012. Fracture abundance and patterns in the Subandean fold and thrust belt, Devonian Huamampampa Formation petroleum reservoirs and outcrops, Argentina and Bolivia. Marine and Petroleum Geology 35, 201-218, doi: 10.1016/j.marpetgeo.2012.01.010.

**Ismat Z.** & Benford B. A. 2007. Deformation in the core of a fold; unraveling the kinematic evolution of tight, multilayer folds developed in the upper crust. Journal of Structural Geology 29, 497-514, doi: 10.1016/j.jsg.2006.09.012.

**Jaeger J.** C. & Cook N. G. W. 1979. Fundamentals of rock mechanics. Chapman and Hall, London.

**Jamison W.** R. 2016. Fracture system evolution within the Cardium sandstone, central Alberta Foothills folds. AAPG Bulletin 100, 1099-1134, doi: 10.1306/03011515082.

**Kalkreuth W.** & Mcmech M. 1988. Burial History and Thermal Maturity, Rocky Mountain Front Ranges, Foothills, and Foreland, East-Central British Columbia and Adjacent Alberta, Canada. AAPG Bulletin 72.

**Krassay A.** A., Cathro D. L. & Ryan D. J. 2004. A regional tectonostratigraphic framework for the Otway Basin. Petroleum Exploration Society of Australia Special Publication 2, 97-116.

**La Pointe P.** R. & Hudson J. A. 1985. Characterization and interpretation of rock mass joint patterns. Special Paper - Geological Society of America 199, 37, doi: 10.1130/SPE199-p1.

**Lambe & Whitman 1969.** Soil Mechanics. John Wiley, New York.

**Lange A.** G. 2009. Assisted history matching for the characterization of fractured reservoirs. AAPG Bulletin 93, 1609-1619, doi: 10.1306/08040909050.

**Matthews J.** 2015. Deformation and uplift in a late Tertiary fold belt, eastern Otway Basin: implications for fault reactivation and petroleum potential. Master of Science thesis, School of Earth, Atmosphere & Environment, Monash University, Clayton.

**McLaren S.**, Wallace M. W., Gallagher S. J., Dickinson J. A. & McAllister A. 2009. Age constraints on Oligocene sedimentation in the Torquay Basin, southeastern Australia. Australian Journal of Earth Sciences 56, 595-604, doi: 10.1080/08120090902806347.

**McLennan J.** A., ALLWARDT P. F., HENNINGS P. H. & FARRELL H. E. 2009. Multivariate fracture intensity prediction; application to Oil Mountain Anticline, Wyoming. AAPG Bulletin 93, 1585-1595, doi: 10.1306/07220909081.

**Medwell G.** J. 1971. Structures in the Otway Ranges in the Otway Basin of South-eastern Australia. Special Bulletin of the Geological Society of South Australia and Victoria 28, 339-362.

**Messent B.** E., COLLINS G. I. & WEST B. G. 1999. Hydrocarbon prospectivity of the offshore Torquay Sub-basin, Victoria: Gazettal area V99-1 (VIMP Report, Vol. 60). Geological Survey of Victoria, Fitzroy, Victoria, Australia.

**Meyer G.** M. 1982. Progress report - EL 659, WMC Hootzpa Coal Project Anglesea.

**Mukhopadhyay P.** K. & Dow W. G. 1994. Vitrinite reflectance as a maturity parameter; applications and limitations (ACS Symposium Series, Vol. 570). American Chemical Society, Washington, DC, United States.

**Nichols** G. 2009. Sedimentology and Stratigraphy In (2 edition), p 411, Wiley-Blackwell, West Sussex, England.

**Odling N.** E. 1992. Network properties of a two-dimensional natural fracture pattern. Pure and Applied Geophysics 138, 95-114.

**Odling N.** E., Gillespie P., Bourgine B., Castaing C., Chiles J. P., Christensen N. P., Fillion E., Genter A., Olsen C., Thrane L., Trice R., Aarseth E., Walsh J. J. & Watterson J. 1999. Variations in fracture system geometry and their implications for fluid flow in fractures hydrocarbon reservoirs. Petroleum Geoscience 5, 373-384.

**Peacock D.** C. P., Nixon C. W., Rotevatn A., Sanderson D. J. & Zuluaga L. F. 2016. Glossary of fault and other fracture networks. Journal of Structural Geology 92, 12-29, doi: 10.1016/j.jsg.2016.09.008.

**Pollard D.** D. & Aydin A. 1988. Progress in understanding jointing over the past century. Geological Society of America Bulletin 100, 1181-1204, doi: 10.1130/0016-7606(1988)100<1181:PIUJOT>2.3.CO;2.

**Priest S.** D. 1993. Discontinuity analysis for rock engineering. Chapman & Hall, London, United Kingdom.

**Santos R.** F. V. C., Miranda T. S., Barbosa J. A., Gomes I. F., Matos G. C., Gale J. F. W., Neumann V. H. L. M. & Guimaraes L. J. N. 2015. Characterization of natural fracture systems; analysis of uncertainty effects in linear scanline results. AAPG Bulletin 99, 2203-2219, doi: 10.1306/05211514104.

**Savage H.** M., Shackleton J. R., Cooke M. L. & Riedel J. J. 2010. Insights into fold growth using fold-related joint patterns and mechanical stratigraphy. Journal of Structural Geology 32, 1466-1475, doi: 10.1016/j.jsg.2010.09.004.

**Shackleton J.** R., Cooke M. L., Verges J. & Simo T. 2011. Temporal constraints on fracturing associating with fault-related folding at Sant Corneli Anticline, Spanish Pyrenees. Journal of Structural Geology 33, 5-19, doi: 10.1016/j.jsg.2010.11.003.

**Sibson R.** H. 2000a. A brittle failure model plot defining conditions for high-flux flow. Economic Geology and the Bulletin of the Society of Economic Geologists 95, 41-47.

**Sibson R.** H. 2000b. Fluid involvement in normal faulting. Journal of Geodynamics 29, 469-499.

**Smart K.** J., FERRILL D. A. & MORRIS A. P. 2009. Impact of interlayer slip on fracture prediction from geomechanical models of fault-related folds. AAPG Bulletin 93, 1447-1458, doi: 10.1306/05110909034.

**Smith T.** 1998. Local geology and the Eastern View Coal Measures, Anglesea area, Victoria. BSc (Hons) thesis, University of Melbourne.

**Stanley D.** 1994. A preliminary appraisal of the groundwater resource potential of the Torquay Basin for urban supply development.

**Stearns D.** W. 1968. Certain aspects of fractures in naturally deformed rock. In: Riecker R. E. ed., NSF Advanced Science Seminar in Rock Mechanics, Air Force Cambridge Research Laboratories.

**Tavani S.**, Fernandez O. & Munoz J. A. 2012. Stress fluctuation during thrust-related folding; Boltana Anticline (Pyrenees, Spain). Geological Society Special Publications 367, 131-140, doi: 10.1144/SP367.9.

**Team.** G. D. 2015. QGIS Geographic Information System. Open Source Geospatial Foundation Project. (2.10 edition). <http://qgis.osgeo.org/en/site/>. (retrieved 7.6.15).

**Terzaghi R.** D. 1965. Sources of error in joint surveys. Géotechnique 13, 287-304.

**Trupp M.** A., Spencer K. W. & Gidding M. J. 1994. Hydrocarbon prospectivity of the Torquay Sub-Basin, offshore Victoria. The APEA Journal 34, Part 1, 479-494.

**Tveite H.** 2015. QGIS Line Direction Histogram. QGIS plugin [WWW Document].

**Twiss R.** & Moores E. 1992. Structural Geology. W.H. Freeman New York.

**Vergunst J.** 2012. The structural history of the Lorne Area, Otway Ranges, Eastern Otway Basin. Bachelor of Science (Honours) Degree thesis, Department of Earth Sciences, Monash University Clayton, Victoria.

**Voight B.** & St. Pierre B. 1974. Stress history and rock stress. Advances in Rock Mechanics. Proceedings of 3rd Congress of ISRM. 2, 580-582.

**Vollgger S.** A. & Cruden A. R. 2016. Mapping folds and fractures in basement and cover rocks using UAV photogrammetry, Cape Liptrap and Cape Paterson, Victoria, Australia. Journal of Structural Geology 85, 168-187, doi: 10.1016/j.jsg.2016.02.012.

**Watkins H.**, Bond C. E., Healy D. & Butler R. W. H. 2015. Appraisal of fracture sampling methods and a new workflow to characterise heterogeneous fracture networks at outcrop. Journal of Structural Geology 72, 67-82, doi: 10.1016/j.jsg.2015.02.001.

**Wilhelmi B.** & Somerton W. H. 1967. Simultaneous Measurement of Pore and Elastic Properties of Rocks Under Triaxial Stress Conditions. Society of Petroleum Engineers Journal 7, 283-294, doi: http://dx.doi.org/10.2118/1706-PA.

**Wilkins S.** J., Gross M. R., Wacker M., Eyal Y. & Engelder T. 2001. Faulted joints; kinematics, displacement-length scaling relations and criteria for their identification. Journal of Structural Geology 23, 315-327.

**Zahm C.** & Hennings P. H. 2009. Complex fracture development related to stratigraphic architecture; challenges for structural deformation prediction, Tensleep Sandstone at the Alcova Anticline, Wyoming. AAPG Bulletin 93, 1427-1446, doi: 10.1306/08040909110.

# Appendix 1

Summary of data collected

The following tables contain bedding and fault measurements collected along coastal and inland areas between April 2015 and February 2017. Two projection systems (AGD66/ WGS84) were used and given that the project area is situated on the boundary between two zones of the Australian UTM system, the tables have been sectioned accordingly.

**Projected in AGD66_AMG zone 54**

| Coordinates | | Accuracy (m) | Strike | Dip | Dip Direction | Type | Lithology | Location | Date |
|---|---|---|---|---|---|---|---|---|---|
| 761550E | 5733094N | 3 | 10 | 12 | SE | Bedding | Volcanic Sandstone | Road outcrop | 10/5/15 |
| 761551E | 5733095N | 3 | 70 | 4 | SE | Bedding | Interbedded Volcanic Sands/ Muds | Road outcrop | 10/5/15 |
| 761503E | 5733073N | 3 | 20 | 10 | S | Bedding | Interbedded Volcanic Sands/ Muds | Road outcrop | 10/5/15 |
| 761463E | 5733059N | 3 | 6 | 9 | SE | Bedding | Interbedded Volcanic Sands/ Muds | Road outcrop | 10/5/15 |
| 761443E | 5733049N | 6 | 22 | 14 | E | Bedding | Interbedded Volcanic Sands/ Muds | Road outcrop | 10/5/15 |
| 761279E | 5732902N | 3 | 30 | 6 | S | Bedding | Interbedded Volcanic Sands/ Muds | Road outcrop | 10/5/15 |
| 760877E | 5732375N | 4 | 58 | 13 | SE | Bedding | Volcanic Sandstone | Road outcrop | 11/5/15 |
| 760812E | 5732375N | 4 | 60 | 9 | SE | Bedding | Volcanic Sandstone | Road outcrop | 11/5/15 |
| 754236E | 5723276N | 3 | 58 | 12 | SE | Bedding | Volcanic Sandstone | Road outcrop | 11/5/15 |
| 759624E | 5728163N | 3 | 320 | 30 | NE | Bedding | Volcanic Sandstone | North of St. George River (platforms) | 27/5/15 |

**Projected in AGD66_AMG zone 55**

| Coordinates | | Accuracy (m) | Strike | Dip | Dip Direction | Type | Lithology | Location | Date |
|---|---|---|---|---|---|---|---|---|---|
| 242028E | 5738103N | 3 | 47 | 22 | SE | Bedding | Volcanic Sandstone (weathered) | Coal Miners Creek | 9/5/15 |
| 241909E | 5738243N | 3 | 95 | 17 | SW | Bedding | Volcanic Sandstone (weathered) | Coal Miners Creek | 9/5/15 |
| 241803E | 5738288N | 3 | 52 | 15 | SE | Bedding | Volcanic Sandstone | Coal Miners Creek | 9/5/15 |
| 241809E | 5738317N | 5 | 37 | 8 | SE | Bedding | Volcanic Sandstone | Coal Miners Creek | 9/5/15 |
| 241458E | 5738284N | 4 | 46 | 19 | SE | Bedding | Volcanic Sandstone, (+ nodules) | Coal Miners Creek | 9/5/15 |
| 241390E | 5738264N | 4 | 20 | 20 | SE | Bedding | Volcanic Sandstone | Coal Miners Creek | 9/5/15 |
| 241260E | 5738356N | 4 | 94 | 10 | S | Bedding | Volcanic Sandstone | Coal Miners Creek | 9/5/15 |
| 240154E | 5736054N | 4 | 83 | 12 | SE | Bedding | Volcanic Sandstone | Road outcrop | 9/5/15 |
| 240171E | 5736064N | 3 | 53 | 10 | S | Bedding | Volcanic Sandstone | Road outcrop | 10/5/15 |
| 240217E | 5736071N | 4 | 72 | 18 | S | Bedding | Volcanic Sandstone | Road outcrop | 10/5/15 |
| 240689E | 5735971N | 6 | 72 | 12 | S | Bedding | Volcanic Sandstone (weathered) | Road outcrop | 10/5/15 |
| 240737E | 5735885N | 3 | 80 | 26 | S | Bedding | Volcanic Sandstone | Road outcrop | 10/5/15 |
| 240050E | 5735459N | 4 | 40 | 14 | SE | Bedding | Volcanic Sandstone | Road outcrop | 10/5/15 |
| 239842E | 5735432N | 3 | 30 | 15 | SE | Bedding | Volcanic Sandstone | Road outcrop | 10/5/15 |
| 239328E | 5734700N | 4 | 80 | 6 | S | Bedding | Interbedded Volcanic Sands/ Muds | Road outcrop (Big Hill) | 10/5/15 |
| 239001E | 5734592N | 3 | 268 | 4 | W | Bedding | Volcanic Sandstone | Road outcrop | 10/5/15 |
| 239027E | 5734331N | 4 | 20 | 10 | SE | Bedding | Interbedded Volcanic Sands/ Muds + coal | Road outcrop | 10/5/15 |
| 238879E | 5734238N | 3 | 36 | 4 | SE | Bedding | Volcanic Sandstone | Road outcrop | 10/5/15 |
| 238704E | 5733773N | 3 | 18 | 2 | S | Bedding | Volcanic Sandstone | Road outcrop | 10/5/15 |
| 247898E | 5739050N | 5 | 122 | 4 | SW | Bedding | Weathered volcaniclastic silts | Aireys Inlet Southern Platforms | 11/5/15 |

| | | | | | | | | | |
|---|---|---|---|---|---|---|---|---|---|
| 247854E | 5739012N | 3 | 177 | 20 | SW | Bedding | Weathered volcaniclastic silts, containing clasts | Aireys Inlet Southern Platforms | 11/5/15 |
| 239060E | 5734520N | 3 | 47 | 7 | SE | Bedding | Volcanic Sandstone | Road outcrop | 11/5/15 |
| 247816E | 5738955N | 4 | 146 | 6 | SW | Bedding | Volcaniclastics, with overlying sands and limestone | Aireys Inlet Southern Platforms | 12/5/15 |
| 247729E | 5738841N | 3 | 230 | 20 | W | Bedding | Volcaniclastics, with overlying sands and limestone | Aireys Inlet Southern Platforms | 12/5/15 |
| 247685E | 5738740N | 6 | 168 | 16 | SW | Bedding | Volcaniclastics | Aireys Inlet Southern Platforms | 12/5/15 |
| 247465E | 5738244N | 3 | 140 | 4 | SW | Bedding | Volcaniclastics | Aireys Inlet Southern Platforms | 12/5/15 |
| 247465E | 5738244N | 3 | 152 | 4 | W | Bedding | Volcaniclastics | Aireys Inlet Southern Platforms | 12/5/15 |
| 247465E | 5738244N | 3 | 149 | 6 | SW | Bedding | Volcaniclastics | Aireys Inlet Southern Platforms | 12/5/15 |
| 240917E | 5736257N | 4 | 68 | 22 | SE | Bedding | Volcanic Sandstone | Platforms Devils Elbow | 13/5/15 |
| 240884E | 5735920N | 3 | 70 | 20 | SE | Bedding | Interbedded Volcanic Sands/ Muds | Platforms Devils Elbow | 13/5/15 |
| 239009E | 5734254N | 4 | 42 | 16 | SE | Bedding | Volcanic Sandstone | North of Lorne | 13/5/15 |
| 239165E | 5734390N | 3 | 60 | 6 | SE | Bedding | Volcanic Sandstone | North of Lorne | 13/5/15 |
| 239229E | 5734437N | 3 | 40 | 6 | SE | Bedding | Volcanic Sandstone | North of Lorne | 13/5/15 |
| 239262E | 5734506N | 3 | 22 | 12 | SE | Bedding | Volcanic Sandstone | North of Lorne | 13/5/15 |
| 239312E | 5734575N | 3 | 36 | 4 | SE | Bedding | Volcanic Sandstone, with fine laminations of coal, calcite & nodules | North of Lorne | 13/5/15 |
| 239238E | 5734479N | 3 | 22 | 6 | SE | Bedding | Volcanic Sandstone, with fine laminations of coal | North of Lorne | 13/5/15 |
| 247320E | 5738041N | 3 | 63 | 1 | SE | Bedding | Weathered Calcaranite | Southern Aireys Inlet, | 25/5/15 |
| 247419E | 5738109N | 3 | 73 | 1 | SE | Bedding | Weathered calcaranite | Aireys Inlet, Southern Beach | 25/5/15 |
| 245727E | 5738048N | 3 | 89 | 2 | SE | Bedding | Highly weathered brown/ pink sands and silts | Aireys Inlet, Southern Beach | 25/5/15 |
| 241278E | 5737075N | 3 | 46 | 30 | SE | Bedding | Volcanic Sandstone | South Side of Spout Creek | 25/5/15 |
| 240322E | 5735362N | 4 | 56 | 20 | SE | Bedding | Volcanic Sandstone, with fine laminations of coal, calcite & nodules | Platforms North of Lorne | 26/5/15 |
| 240217E | 5735350N | 3 | 81 | 22 | E | Bedding | Volcanic Sandstone, with fine laminations of coal, calcite & nodules | Platforms North of Lorne | 26/5/15 |
| 240087E | 5735277N | 3 | 52 | 16 | SE | Bedding | Volcanic Sandstone (with occasional mud clasts) | Platforms North of Lorne | 26/5/15 |
| 239839E | 5735122N | 3 | 60 | 18 | SE | Bedding | Volcanic Sandstone, with fine laminations of coal, calcite & nodules | Platforms North of Lorne | 26/5/15 |
| 239778E | 5735089N | 3 | 66 | 14 | SE | Bedding | Volcanic Sandstone with calcite nodules, coal (4-10cm thick) and mud clasts | Platforms North of Lorne | 26/5/15 |
| 239608E | 5734875N | 5 | 52 | 16 | SE | Bedding | Volcanic Sandstone with calcite nodules, coal and mud clasts | Platforms North of Lorne | 26/5/15 |
| 239526E | 5734772N | 5 | 60 | 16 | SE | Bedding | Volcanic Sandstone | Platforms North of Lorne | 26/5/15 |
| 239489E | 5734676N | 3 | 30 | 14 | SE | Bedding | Volcanic Sandstone | Platforms North of Lorne | 26/5/15 |
| 239427E | 5734680N | 5 | 40 | 12 | SE | Bedding | Volcanic Sandstone | Platforms North of Lorne | 26/5/15 |
| 239289E | 5734504N | 3 | 46 | 2 | SE | Bedding | Interbedded Volcanic Sands/ Muds | Platforms North of Lorne | 26/5/15 |
| 239110E | 5734345N | 3 | 60 | 16 | SE | Bedding | Volcanic Sandstone (with mud clasts) | Platforms North of Lorne | 26/5/15 |
| 244011E | 5741004N | 3 | 44 | 32 | SE | Bedding | Weathered light grey volcanic sandstone, with red altered nodules and mud clasts | Painkalac Dam (NE path) | 26/5/15 |

| | | | | | | | | | |
|---|---|---|---|---|---|---|---|---|---|
| 244021E | 5740996N | 3 | 86 | 12 | SE | Bedding | Light brown-white, highly weathered coarse sandstone | Painkalac Dam (NE path) | 26/5/15 |
| 244018E | 5740948N | 4 | 58 | 31 | SE | Bedding | Volcanic sandstone, with fine laminations of coal and mud clasts | Painkalac Dam (side of the NE cliff) | 26/5/15 |
| 244156E | 5740711N | 3 | 132 | 6 | S | Bedding | Highly weathered light brown-white sandstone | The Glen | 26/5/15 |
| 247576E | 5738475N | 3 | 88 | 14 | SE | Bedding | Basalt | Aireys Inlet Platforms | 27/5/15 |
| 247554E | 5738536N | 4 | 204 | 18 | NW | Bedding | Light Volcaniclastics with clasts | Aireys Inlet Platforms | 27/5/15 |
| 247550E | 5738563N | 3 | 146 | 16 | SW | Bedding | Light Volcaniclastics with clasts | Aireys Inlet Platforms | 27/5/15 |
| 247550E | 5738594N | 5 | 146 | 1 | SW | Bedding | Light coloured Volcaniclastics | Aireys Inlet Platforms | 27/5/15 |
| 249219E | 5741308N | 3 | 258 | 6 | N | Bedding | Light coloured volcaniclastics overlain by sands | South of Urquhart Bluff (Platforms) | 27/5/15 |
| 249225E | 5741294N | 3 | 268 | 16 | NW | Bedding | Light coloured volcaniclastics overlain by sands | South of Urquhart Bluff (Platforms) | 27/5/15 |
| 249215E | 5741234N | 3 | 218 | 6 | W | Bedding | Light coloured volcaniclastics overlain by sands | South of Urquhart Bluff (Platforms) | 27/5/15 |
| 249212E | 5741152N | 3 | 244 | 10 | N | Bedding | Light coloured volcaniclastics overlain by sands | South of Urquhart Bluff (Platforms) | 27/5/15 |
| 249179E | 5741138N | 3 | 246 | 10 | N | Bedding | Light coloured volcaniclastics overlain by sands | South of Urquhart Bluff (Platforms) | 27/5/15 |
| 249134E | 5740972N | 3 | 284 | 18 | N | Bedding | Light coloured volcaniclastics overlain by sands | South of Urquhart Bluff (Platforms) | 27/5/15 |
| 249144E | 5740914N | 3 | 320 | 26 | NE | Bedding | Light coloured volcaniclastics overlain by sands | South of Urquhart Bluff (Platforms) | 27/5/15 |
| 248520E | 5740140N | 3 | 70 | 12 | SE | Bedding | Diffusely stratified volcaniclastics; large clasts of basalt, muds, marl and interbedded sands/ muds | Eagle Nest Reef Aireys Inlet Platforms | 10/6/15 |
| 248435E | 5739674N | 4 | 306 | 24 | N | Bedding | Coarse gained, basaltic tuff | Eagle Nest Reef Aireys Inlet Platforms | 10/6/15 |
| 239535E | 5734778N | 3 | 174 | 90 | N/A | Fault | Volcanic Sandstone | North of Lorne | 26/5/15 |

## Projected in WGS 84_UTM zone 54S

| Coordinates | | Accuracy (m) | Strike | Dip | Dip Direction | Type | Lithology | Location | Date |
|---|---|---|---|---|---|---|---|---|---|
| 759658E | 5731830N | 10 | 48 | 16 | SE | Bedding | Sandstone | Deans Marsh - Lorne Road | 12/4/15 |
| 759173E | 5732665N | 9 | 33 | 18 | E | Bedding | Sandstone | Deans Marsh - Lorne Road | 12/4/15 |
| 757582E | 5734674N | 12 | 226 | 10 | W | Bedding | Sandstone | Deans Marsh - Lorne Road | 12/4/15 |
| 757582E | 5734674N | 12 | 236 | 10 | N | Bedding | Sandstone | Deans Marsh - Lorne Road | 12/4/15 |
| 753360E | 5740891N | 5 | 91 | 18 | S | Bedding | Weathered Sandstone | Deans Marsh - Lorne Road | 12/4/15 |
| 753360E | 5740891N | 5 | 134 | 12 | S | Bedding | Weathered Sandstone | Deans Marsh - Lorne Road | 12/4/15 |
| 757082E | 5726073N | 4 | 333 | 7 | NE | Bedding | Interbedded Volcanic Sandstone/ Mudstone | Cumberland River Platforms | 15/4/15 |
| 759747E | 5728342N | 5 | 310 | 22 | E | Bedding | Volcanic sandstone | NW of St. George | 6/10/15 |
| 760280E | 5731651N | 3 | 22 | 6 | ESE | Bedding | Volcanic sandstone | North of Lorne, Platforms | 6/10/15 |
| 760427E | 5731909N | 3 | 40 | 10 | SE | Bedding | Volcanic sandstone | NW of St. George | 6/10/15 |
| 760492E | 5732026N | 5 | 52 | 12 | SE | Bedding | Volcanic Sandstone | North of Lorne, Platforms | 6/10/15 |
| 760537E | 5732060N | 3 | 74 | 20 | SE | Bedding | Interbedded Volcanic Sandstone/ Mudstone | North of Lorne, Platforms | 6/10/15 |
| 760603E | 5732192N | 3 | 38 | 13 | ESE | Bedding | Volcanic sandstone | North of Lorne, Platforms | 6/10/15 |
| 760761E | 5732377N | 3 | 40 | 14 | SE | Bedding | Volcanic sandstone | North of Lorne, Platforms | 6/10/15 |
| 757406E | 5726061N | 3 | 50 | 16 | SE | Bedding | Volcanic sandstone | Cumberland River Platforms | 7/10/15 |
| 757486E | 5726113N | 5 | 20 | 18 | ESE | Bedding | Volcanic sandstone | Cumberland River Platforms | 7/10/15 |
| 760947E | 5732469N | 3 | 48 | 24 | SE | Bedding | Volcanic sandstone | North of Lorne, Platforms | 7/10/15 |
| 761092E | 5732665N | 3 | 48 | 20 | SE | Bedding | Interbedded Volcanic Sandstone/ Mudstone | North of Lorne, Platforms | 7/10/15 |
| 761092E | 5732665N | 3 | 40 | 20 | SE | Bedding | Interbedded Volcanic Sandstone/ Mudstone | North of Lorne, Platforms | 7/10/15 |
| 761112E | 5732683N | 3 | 55 | 22 | SE | Bedding | Interbedded Volcanic Sandstone/ Mudstone | North of Lorne, Platforms | 7/10/15 |
| 761137E | 5732725N | 3 | 38 | 20 | SE | Bedding | Interbedded Volcanic Sandstone/ Mudstone | North of Lorne, Platforms | 7/10/15 |
| 761209E | 5732805N | 3 | 38 | 22 | SE | Bedding | Volcanic sandstone | North of Lorne, Platforms | 7/10/15 |
| 761225E | 5732825N | 5 | 38 | 20 | SE | Bedding | Interbedded Volcanic Sandstone/ Mudstone | North of Lorne, Platforms | 7/10/15 |
| 761286E | 5732911N | 3 | 22 | 34 | E | Bedding | Interbedded Volcanic Sandstone/ Mudstone | North of Lorne, Platforms | 7/10/15 |
| 761311E | 5732911N | 3 | 56 | 20 | SE | Bedding | Volcanic sandstone | North of Lorne, Platforms | 7/10/15 |
| 761384E | 5732983N | 3 | 52 | 22 | SE | Bedding | Volcanic sandstone | North of Lorne, Platforms | 7/10/15 |
| 761437E | 5733079N | 3 | 40 | 18 | SE | Bedding | Volcanic sandstone | North of Lorne, Platforms | 7/10/15 |
| 761468E | 5733118N | 3 | 56 | 18 | SE | Bedding | Interbedded Volcanic Sandstone/ Mudstone | North of Lorne, Platforms | 7/10/15 |
| 761509E | 5733154N | 3 | 36 | 17 | SE | Bedding | Interbedded Volcanic Sandstone/ Mudstone | North of Lorne, Platforms | 7/10/15 |
| 761569E | 5733139N | 3 | 40 | 22 | SE | Bedding | Volcanic sandstone | North of Lorne, Platforms | 7/10/15 |
| 761401E | 5733129N | 3 | 104 | 12 | S | Bedding | Interbedded Volcanic Sands/ Muds | North of Lorne, Platforms | 7/10/15 |
| 761385E | 5733058N | 5 | 30 | 8 | S | Bedding | Volcanic sandstone | North of Lorne, Platforms | 7/10/15 |
| 761018E | 5732650N | 5 | 48 | 6 | SE | Bedding | Volcanic sandstone | North of Lorne, Platforms | 7/10/15 |
| 756368E | 5725536N | 3 | 68 | 90 | N/A | Bedding | Interbedded sandstone/ shale/ fine sandstone | Mt. Defiance | 19/11/15 |
| 756446E | 5725613N | 3 | 264 | 20 | N | Bedding | Weathered Interbedded Volcanic Sandstone/ Mudstone | Mt. Defiance, platforms | 19/11/15 |
| 756551E | 5725632N | 3 | 42 | 70 | SE | Bedding | Sandstone | Mt. Defiance, platforms | 19/11/15 |
| 756570E | 5725660N | 3 | 247 | 28 | NW | Bedding | Sandstone/ fine sandstone/ laminated coal | Mt. Defiance, platforms | 19/11/15 |
| 756655E | 5725720N | 3 | 269 | 28 | NNW | Bedding | Sandstone | Mt. Defiance, platforms | 19/11/15 |
| 756801E | 5725928N | 3 | 50 | 30 | E | Bedding | Sandstone | Mt. Defiance platforms | 19/11/15 |
| 756818E | 5726004N | 3 | 327 | 26 | N | Bedding | Sandstone | Cumberland River Platforms | 19/11/15 |
| 756850E | 5726014N | 3 | 328 | 16 | N | Bedding | Sandstone | Mt. Defiance, platforms | 19/11/15 |

| | | | | | | | | | |
|---|---|---|---|---|---|---|---|---|---|
| 757078E | 5726077N | 3 | 332 | 30 | NE | Bedding | Sandstone | Cumberland River Platforms | 19/11/15 |
| 757081E | 5726075N | 3 | 332 | 10 | NE | Bedding | Sandstone | Cumberland River Platforms | 19/11/15 |
| 757133E | 5726063N | 3 | 340 | 30 | E | Bedding | Sandstone | Cumberland River Platforms | 19/11/15 |
| 757182E | 5726085N | 3 | 344 | 24 | E | Bedding | Interbedded mudstone/ sandstone | Cumberland River Platforms | 19/11/15 |
| 757279E | 5726091N | 3 | 12 | 20 | E | Bedding | Interbedded mudstone/ sandstone | Cumberland River Platforms | 19/11/15 |
| 757614E | 5726185N | 3 | 46 | 28 | SE | Bedding | Sandstone | Cumberland River Platforms | 19/11/15 |
| 755820E | 5725383N | 5 | 8 | 1 | E | Bedding | Weathered sandstone | Mt. Defiance road outcrop | 19/11/15 |
| 759802E | 5728450N | 3 | 298 | 20 | N | Bedding | Volcanic sandstone | St. George (path) | 30/4/16 |
| 759720E | 5728423N | 4 | 280 | 10 | NE | Bedding | Volcanic sandstone | St. George (path) | 30/4/16 |
| 754170E | 5747183N | 3 | 220 | 30 | NW | Bedding | Gritty sandstone | Northern Road Outcrop | 9/9/16 |
| 761825E | 5745032N | 3 | 52 | 20 | SE | Bedding | Weathered sandstone | Northern Road Outcrop | 9/9/16 |
| 755388E | 5749217N | 3 | 160 | 6 | S | Bedding | Gritty sandstone | Northern Road Outcrop | 9/9/16 |
| 754381E | 5723356N | 3 | 32 | 12 | SE | Bedding | Volcanic sandstone | Artillery Rocks | 11/10/16 |
| 754317E | 5723279N | 3 | 52 | 6 | SE | Bedding | Volcanic sandstone | Artillery Rocks | 11/10/16 |
| 756804E | 5725929N | 3 | 26 | 32 | E | Bedding | Volcanic sandstone | Mt. Defiance, platforms | 9/1/17 |
| 756799E | 5725940N | 3 | 340 | 8 | NE | Bedding | Volcanic sandstone | Mt. Defiance, coastal platforms | 9/1/17 |
| 756712E | 5725861N | 3 | 272 | 38 | N | Bedding | Volcanic sandstone | Mt. Defiance, platforms | 9/1/17 |
| 756692E | 5725836N | 3 | 270 | 40 | N | Bedding | Volcanic sandstone | Mt. Defiance, platforms | 9/1/17 |
| 756679E | 5725825N | 3 | 254 | 40 | NNE | Bedding | Volcanic sandstone | Mt. Defiance, platforms | 9/1/17 |
| 756642E | 5725757N | 3 | 290 | 20 | N | Bedding | Volcanic sandstone | Mt. Defiance, platforms | 9/1/17 |
| 756110E | 5725417N | 3 | 60 | 50 | E | Bedding | Volcanic sandstone | Mt. Defiance, platforms | 9/1/17 |
| 755958E | 5725372N | 3 | 330 | 2 | NE | Bedding | Volcanic sandstone | Mt. Defiance | 9/1/17 |
| 755946E | 5725366N | 3 | 330 | 2 | NE | Bedding | Volcanic sandstone | Mt. Defiance | 9/1/17 |
| 755966E | 5725383N | 3 | 330 | 2 | NE | Bedding | Volcanic sandstone | Mt. Defiance | 9/1/17 |
| 756436E | 5725597N | 3 | 296 | 26 | NE | Bedding | Volcanic sandstone | Mt. Defiance | 9/1/17 |
| 757090E | 5726062N | 3 | 332 | 12 | NE | Bedding | Volcanic sandstone | Mt. Defiance | 9/1/17 |
| 759312E | 5728000N | 3 | 250 | 80 | E | Normal fault | Interbedded Volcanic Sands/ Muds | St. George, southern limb | 25/4/15 |
| 759312E | 5728000N | 3 | 174 | -- | E | Slicks | Interbedded Volcanic Sandstone/ Mudstone | St. George, southern limb | 25/4/15 |
| 759747E | 5728342N | 3 | 126 | 90 | N/A | Fault | Volcanic sandstone | NW of St. George | 6/10/15 |
| 756401E | 5725576N | 6 | 240 | 40 | NE | Fault | Weathered sandstone | Mt. Defiance | 19/11/15 |
| 755820E | 5725383N | 3 | 82 | 30 | S | Thrust fault? | Weathered sandstone | Mt. Defiance road outcrop | 19/11/15 |
| 759380E | 5727785N | 3 | 162 | 90 | N/A | Sinistral fault | Volcanic sandstone | St. George, southern limb | 11/10/16 |
| 755954E | 5725361N | 3 | 160 | 90 | N/A | Sinistral fault | Interbedded Volcanic Sands/ Muds | Mt. Defiance | 9/1/17 |
| 756682E | 5725825N | 3 | 89 | 6 | S | Slicks | Calcite slicks on sandstone | Mt. Defiance, platforms | 9/1/17 |
| 758458E | 5727069N | 3 | 82 | 21 | SSE | Bedding | Volcanic Sandstone | | 5/10/15 |
| 754378E | 5723352N | 3 | 36 | 14 | ESE | Bedding | Volcanic Sandstone | | 7/10/15 |
| 754296E | 5723223N | 3 | 42 | 12 | SE | Bedding | Volcanic Sandstone | | 7/10/15 |
| 759869E | 5728373N | 3 | 300 | 10 | NE | Bedding | Volcanic Sandstone | NW of St. George | 19/2/16 |
| 759323E | 5728012N | 3 | 20 | 12 | E | Bedding | Interbedded Volcanic Sandstone/ Mudstone | Road near St. George | 19/2/16 |
| 759415E | 5728119N | 3 | 271 | 20 | N | Bedding | Volcanic Sandstone | St. George Fold | 19/2/16 |
| 759406E | 5728092N | 3 | 340 | 4 | NE | Bedding | Interbedded Volcanic Sandstone/ Mudstone | St. George Fold | 19/2/16 |
| 759407E | 5728076N | 3 | 20 | 10 | SE | Bedding | IInterbedded Volcanic Sandstone/ Mudstone | St. George Fold | 19/2/16 |
| 759391E | 5728045N | 5 | 60 | 30 | SE | Bedding | Interbedded Volcanic Sandstone/ Mudstone | St. George Fold | 19/2/16 |
| 759339E | 5727976N | 3 | 40 | 30 | SE | Bedding | Volcanic Sandstone | St. George Fold | 19/2/16 |
| 759350E | 5727906N | 3 | 38 | 24 | SE | Bedding | Interbedded Volcanic Sandstone/ Mudstone | St. George Fold | 19/2/16 |

| | | | | | | | | | |
|---|---|---|---|---|---|---|---|---|---|
| 759370E | 5727866N | 3 | 24 | 20 | SE | Bedding | Interbedded Volcanic Sandstone/ Mudstone | St. George Fold | 19/2/16 |
| 759382E | 5727833N | 3 | 32 | 18 | SE | Bedding | Interbedded Volcanic Sandstone/ Mudstone | St. George Fold | 19/2/16 |
| 759396E | 5727797N | 4 | 52 | 42 | SE | Bedding | Interbedded Volcanic Sandstone/ Mudstone | St. George Fold | 19/2/16 |
| 759395E | 5727771N | 3 | 60 | 46 | SE | Bedding | Interbedded Volcanic Sandstone/ Mudstone | St. George Fold | 19/2/16 |
| 759423E | 5727775N | 3 | 54 | 44 | SE | Bedding | Volcanic Sandstone | St. George Fold | 19/2/16 |
| 759370E | 5727729N | 3 | 54 | 33 | SE | Bedding | Volcanic Sandstone | St. George Fold | 19/2/16 |
| 760022E | 5728489N | 3 | 314 | 12 | NE | Bedding | Volcanic Sandstone | NW of St. George | 20/2/16 |
| 759962E | 5728477N | 3 | 304 | 16 | N | Bedding | Volcanic Sandstone | NW of St. George | 20/2/16 |
| 759928E | 5728425N | 3 | 318 | 12 | N | Bedding | Volcanic Sandstone | NW of St. George | 20/2/16 |
| 759878E | 5728358N | 3 | 320 | 22 | N | Bedding | Volcanic Sandstone | NW of St. George | 20/2/16 |
| 759821E | 5728330N | 3 | 334 | 20 | NE | Bedding | Volcanic Sandstone | NW of St. George | 20/2/16 |
| 759760E | 5728333N | 3 | 330 | 22 | NE | Bedding | Volcanic Sandstone | NW of St. George | 20/2/16 |
| 759611E | 5728329N | 3 | 269 | 20 | N | Bedding | Volcanic Sandstone | NW of St. George | 20/2/16 |
| 759657E | 5728333N | 3 | 270 | 23 | N | Bedding | Volcanic Sandstone | NW of St. George | 20/2/16 |
| 759734E | 5728294N | 4 | 326 | 24 | N | Bedding | Volcanic Sandstone | NW of St. George | 20/2/16 |
| 759704E | 5728311N | 3 | 268 | 20 | N | Bedding | Interbedded Volcanic Sandstone/ Mudstone | NW of St. George | 20/2/16 |
| 759506E | 5728318N | 3 | 280 | 26 | N | Bedding | Volcanic Sandstone | NW of St. George | 20/2/16 |
| 759362E | 5728124N | 3 | 260 | 30 | NW | Bedding | Volcanic Sandstone | St. George Fold | 20/2/16 |
| 759488E | 5728207N | 3 | 269 | 20 | N | Bedding | Volcanic Sandstone | St. George Fold | 20/2/16 |
| 759479E | 5728183N | 3 | 278 | 30 | N | Bedding | Volcanic Sandstone | St. George Fold | 20/2/16 |
| 759430E | 5728146N | 3 | 278 | 20 | N | Bedding | Volcanic Sandstone | St. George Fold | 20/2/16 |
| 759385E | 5728091N | 5 | 273 | 10 | N | Bedding | Volcanic Sandstone, surrounded by Mudstone | St. George Fold | 20/2/16 |
| 759386E | 5728062N | 5 | 60 | 10 | E | Bedding | Interbedded Volcanic Sands/ Muds | St. George Fold | 20/2/16 |
| 759400E | 5728039N | 5 | 34 | 36 | SE | Bedding | Volcanic Sandstone | St. George Fold | 20/2/16 |
| 759387E | 5728026N | 5 | 46 | 36 | SE | Bedding | Volcanic Sandstone | St. George Fold | 20/2/16 |
| 760007E | 5728399N | 5 | 316 | 8 | NNE | Bedding | Volcanic Sandstone | St. George Fold | 30/4/16 |
| 760107E | 5728517N | 5 | 324 | 8 | NNE | Bedding | Volcanic Sandstone | St. George Fold | 30/4/16 |
| 759492E | 5728195N | 5 | 269 | 20 | N | Bedding | Volcanic Sandstone | St. George Fold | 30/4/16 |
| 754381E | 5723356N | 3 | 32 | 12 | SE | Bedding | Volcanic sandstone | Artillery Rocks | 11/10/16 |
| 754317E | 5723279N | 3 | 52 | 6 | SE | Bedding | Volcanic sandstone | Artillery Rocks | 11/10/16 |
| 754245E | 5723151N | 3 | 40 | 36 | SE | Bedding | Volcanic sandstone | Artillery Rocks | 11/10/16 |
| 754319E | 5723060N | 3 | 56 | 32 | SE | Bedding | Volcanic sandstone | Artillery Rocks | 11/10/16 |

## Projected in WGS 84_UTM zone 55S

| Coordinates | | Accuracy (m) | Strike | Dip | Dip Direction | Type | Lithology | Location | Date |
|---|---|---|---|---|---|---|---|---|---|
| 246522E | 5738181N | 3 | 86 | 2 | SE | Bedding | Calcarenite | Fairhaven Beach | 26/3/15 |
| 246483E | 5738186N | 3 | 80 | 2 | SE | Bedding | Calcarenite | Fairhaven Beach | 26/3/15 |
| 246203E | 5738138N | 3 | 88 | 14 | SSE | Bedding | Calcarenite | Fairhaven Beach | 26/3/15 |
| 246181E | 5738150N | 3 | 40 | 26 | SE | Bedding | Calcarenite | Fairhaven Beach | 26/3/15 |
| 245960E | 5738125N | 3 | 70 | 2 | E | Bedding | Brown Sandstone | Fairhaven Beach | 26/3/15 |
| 244619E | 5741983N | 3 | 158 | 35 | SW | Bedding | Sandstone | Lookout Hill | 26/3/15 |
| 244604E | 5741988N | 3 | 54 | 10 | S | Bedding | Sandstone | Lookout Hill | 26/3/15 |
| 244587E | 5741991N | 3 | 41 | 18 | SE | Bedding | Sandstone | Lookout Hill | 26/3/15 |
| 244576E | 5741988N | 3 | 137 | 7 | SW | Bedding | Sandstone | Lookout Hill | 26/3/15 |
| 244571E | 5741987N | 3 | 158 | 38 | SW | Bedding | Sandstone | Lookout Hill | 26/3/15 |
| 241227E | 5736871N | 3 | 27 | 40 | E | Bedding | Interbedded Volcanic Sandstone/ Mudstone | Devils Elbow, Eastern View (Platforms) | 27/3/15 |
| 241236E | 5736865N | 3 | 38 | 52 | SE | Bedding | Interbedded Volcanic Sandstone/ Mudstone | Devils Elbow, Eastern View (Platforms) | 27/3/15 |
| 241247E | 5736818N | 3 | 40 | 56 | SE | Bedding | Volcanic Sandstone | Devils Elbow, Eastern View (Platforms) | 27/3/15 |
| 241273E | 5736806N | 3 | 48 | 50 | SE | Bedding | Volcanic Sandstone | Devils Elbow, Eastern View (Platforms) | 27/3/15 |
| 241254E | 5736775N | 3 | 40 | 66 | SE | Bedding | Interbedded Volcanic Sandstone/ Mudstone | Devils Elbow, Eastern View (Platforms) | 27/3/15 |
| 241270E | 5736732N | 3 | 38 | 66 | SE | Bedding | Volcanic Sandstone | Devils Elbow, Eastern View (Platforms) | 27/3/15 |
| 241299E | 5736686N | 3 | 10 | 32 | E | Bedding | Volcanic Sandstone | Devils Elbow, Eastern View (Platforms) | 27/3/15 |
| 241300E | 5736644N | 3 | 52 | 32 | SE | Bedding | Volcanic Sandstone | Devils Elbow, Eastern View (Platforms) | 27/3/15 |
| 241308E | 5736590N | 3 | 43 | 40 | SE | Bedding | Volcanic Sandstone | Devils Elbow, Eastern View (Platforms) | 27/3/15 |
| 241267E | 5736552N | 3 | 48 | 52 | SE | Bedding | Interbedded Volcanic Sandstone/ Mudstone | Devils Elbow, Eastern View (Platforms) | 27/3/15 |
| 244384E | 5738941N | 3 | 310 | 31 | NE | Bedding | Light Sandstone, poor bedding | West side of Berthon Hill | 27/3/15 |
| 247140E | 5741600N | 3 | 89 | 40 | S | Bedding | Weathered Sandstone | Distillery Creek Road | 27/3/15 |
| 241240E | 5736647N | 3 | 58 | 52 | SE | Bedding | Volcanic Sandstone | Devils Elbow, Eastern View (Road) | 28/3/15 |
| 241180E | 5736584N | 3 | 52 | 47 | SE | Bedding | Volcanic Sandstone | Devils Elbow, Eastern View (Road) | 28/3/15 |
| 241170E | 5736550N | 3 | 58 | 60 | SE | Bedding | Volcanic Sandstone | Devils Elbow, Eastern View (Road) | 28/3/15 |
| 241639E | 5737402N | 3 | 80 | 30 | SE | Bedding | Volcanic Sandstone (weathered) | Fairhaven Road | 28/3/15 |
| 241658E | 5737411N | 3 | 28 | 18 | E | Bedding | Volcanic Sandstone (weathered) | Fairhaven Road | 28/3/15 |
| 241666E | 5737418N | 3 | 30 | 40 | SE | Bedding | Volcanic Sandstone (weathered) | Fairhaven Road | 28/3/15 |
| 241690E | 5737433 | 3 | 350 | 10 | NE | Bedding | Sandstone | Fairhaven Road | 28/3/15 |
| 241715E | 5737452N | 3 | 36 | 38 | SE | Bedding | Sandstone, with nodules of calcite | Fairhaven Road | 28/3/15 |
| 241720E | 5737456N | 3 | 12 | 10 | SE | Bedding | Sandstone, with nodules of calcite | Fairhaven Road | 28/3/15 |
| 244135E | 5738116N | 5 | 72 | 33 | SE | Bedding | Lithified Sandstone | Northern Fairhaven Road | 28/3/15 |
| 244135E | 5738116N | 5 | 58 | 50 | SE | Bedding | Lithified Sandstone | Northern Fairhaven Road | 28/3/15 |
| 244135E | 5738116N | 5 | 46 | 50 | SE | Bedding | Lithified Sandstone | Northern Fairhaven Road | 28/3/15 |
| 245850E | 5738234N | 3 | 4 | 3 | E | Bedding | Highly weathered sandstone | Northern Fairhaven Road | 28/3/15 |

| | | | | | | | | | |
|---|---|---|---|---|---|---|---|---|---|
| 245851E | 5738235N | 3 | 356 | 3 | NE | Bedding | Highly weathered sandstone | Northern Fairhaven Road | 28/3/15 |
| 245851E | 5738235N | 3 | 332 | 2 | NE | Bedding | Highly weathered sandstone | Northern Fairhaven Road | 28/3/15 |
| 245851E | 5738235N | 3 | 60 | 5 | SE | Bedding | Highly weathered sandstone | Northern Fairhaven Road | 28/3/15 |
| 245486E | 5738215N | 5 | 286 | 10 | NE | Bedding | Highly weathered sandstone/ clays | Northern Fairhaven Road | 10/4/15 |
| 245476E | 5738206N | 5 | 298 | 4 | NE | Bedding | Highly weathered sandstone/ clays | Northern Fairhaven Road | 10/4/15 |
| 245476E | 5738206N | 5 | 2 | 6 | E | Bedding | Highly weathered sandstone/ clays | Northern Fairhaven Road | 10/4/15 |
| 241229E | 5736475N | 7 | 48 | 42 | E | Bedding | Volcanic Sandstone | Devils Elbow, Eastern View (Platforms) | 11/4/15 |
| 241223E | 5736435N | 4 | 55 | 33 | SE | Bedding | Volcanic Sandstone | Devils Elbow, Eastern View (Platforms) | 11/4/15 |
| 241201E | 5736369N | 4 | 50 | 25 | SE | Bedding | Volcanic Sandstone | Devils Elbow, Eastern View (Platforms) | 11/4/15 |
| 241180E | 5736328N | 5 | 55 | 40 | E | Bedding | Volcanic Sandstone overlaying Mudstone | Devils Elbow, Eastern View (Platforms) | 11/4/15 |
| 241190E | 5736280N | 5 | 42 | 38 | S | Bedding | Volcanic Sandstone overlaying Mudstone | Devils Elbow, Eastern View (Platforms) | 11/4/15 |
| 241184E | 5736405N | 5 | 52 | 30 | SE | Bedding | Volcanic Sandstone | Devils Elbow, Eastern View (Platforms) | 11/4/15 |
| 241441E | 5737299N | 6 | 5 | 30 | E | Bedding | Volcanic Sandstone | Spout Creek | 11/4/15 |
| 241441E | 5737299N | 6 | 4 | 20 | E | Bedding | Volcanic Sandstone | Spout Creek | 11/4/15 |
| 241423E | 5737318N | 6 | 355 | 33 | NE | Bedding | Volcanic Sandstone | Spout Creek | 11/4/15 |
| 241382E | 5737326N | 5 | 16 | 36 | SE | Bedding | Volcanic Sandstone | Spout Creek | 11/4/15 |
| 241348E | 5737325N | 5 | 2 | 30 | SE | Bedding | Volcanic Sandstone | Spout Creek | 11/4/15 |
| 241304E | 5737335N | 4 | 359 | 30 | NE | Bedding | Interbedded Volcanic Sands/ Muds | Spout Creek | 11/4/15 |
| 241304E | 5737335N | 4 | 6 | 29 | E | Bedding | Interbedded Volcanic Sands/ Muds | Spout Creek | 11/4/15 |
| 241303E | 5737340N | 6 | 12 | 29 | SE | Bedding | Interbedded Volcanic Sands/ Muds | Spout Creek | 11/4/15 |
| 242270E | 5737928N | 8 | 57 | 39 | SE | Bedding | Volcanic Sandstone | Coalmine Creek | 11/4/15 |
| 242244E | 5737970N | 9 | 52 | 23 | SE | Bedding | Volcanic Sandstone | Coalmine Creek | 11/4/15 |
| 242239E | 5737975N | 9 | 60 | 30 | SE | Bedding | Volcanic Sandstone | Coalmine Creek | 11/4/15 |
| 242227E | 5738020N | 12 | 76 | 26 | E | Bedding | Volcanic Sandstone | Coalmine Creek | 11/4/15 |
| 242227E | 5738020N | 12 | 44 | 40 | E | Bedding | Volcanic Sandstone | Coalmine Creek | 11/4/15 |
| 241206E | 5736222N | 4 | 63 | 32 | SE | Bedding | Volcanic Sandstone | Devils Elbow, Eastern View (Platforms) | 12/4/15 |
| 241132E | 5736268N | 4 | 45 | 30 | SE | Bedding | Interbedded Volcanic Sandstone/ Mudstone | South of Devils Elbow (Platforms) | 12/4/15 |
| 241001E | 5736212N | 7 | 75 | 21 | SE | Bedding | Volcanic Sandstone | South of Devils Elbow (Platforms) | 12/4/15 |
| 241084E | 5736306N | 5 | 52 | 26 | SE | Bedding | Volcanic Sandstone | South of Devils Elbow (Platforms) | 12/4/15 |
| 241048E | 5736302N | 6 | 56 | 21 | S | Bedding | Volcanic Sandstone | South of Devils Elbow (Platforms) | 12/4/15 |
| 240986E | 5736327N | 7 | 48 | 16 | SE | Bedding | Volcanic Sandstone | South of Devils Elbow (Platforms) | 12/4/15 |
| 241479E | 5737304N | 5 | 2 | 19 | SE | Bedding | Volcanic Sandstone | Spout Creek | 13/4/15 |
| 241240E | 5737346N | 5 | 354 | 18 | NE | Bedding | Volcanic Sandstone | Spout Creek | 13/4/15 |
| 241240E | 5737346N | 5 | 344 | 26 | E | Bedding | Volcanic Sandstone | Spout Creek | 13/4/15 |
| 241042E | 5737472N | 5 | 354 | 12 | E | Bedding | Volcanic Sandstone | Spout Creek | 13/4/15 |
| 241024E | 5737411N | 8 | 326 | 20 | NE | Bedding | Volcanic Sandstone | Spout Creek | 13/4/15 |
| 241024E | 5737411N | 8 | 352 | 25 | NE | Bedding | Volcanic Sandstone | Spout Creek | 13/4/15 |
| 240961E | 5737490N | 6 | 50 | 12 | S | Bedding | Volcanic Sandstone | Spout Creek | 13/4/15 |
| 240955E | 5737531N | 7 | 338 | 25 | NE | Bedding | Volcanic Sandstone | Spout Creek | 13/4/15 |

| | | | | | | | | | |
|---|---|---|---|---|---|---|---|---|---|
| 240747E | 5737630N | 9 | 308 | 9 | NE | Bedding | Volcanic Sandstone | Spout Creek | 13/4/15 |
| 240700E | 5737600N | 9 | 356 | 16 | NE | Bedding | Volcanic Sandstone | Spout Creek | 13/4/15 |
| 240482E | 5737780N | 17 | 337 | 14 | E | Bedding | Volcanic Sandstone | Spout Creek | 13/4/15 |
| 240262E | 5737795N | 17 | 18 | 16 | E | Bedding | Volcanic Sandstone | Spout Creek | 13/4/15 |
| 240252E | 5737795N | 17 | 40 | 12 | SE | Bedding | Volcanic Sandstone | Spout Creek | 13/4/15 |
| 240002E | 5737780N | 15 | 320 | 8 | NE | Bedding | Volcanic Sandstone | Spout Creek | 13/4/15 |
| 240002E | 5737780N | 10 | 340 | 12 | NE | Bedding | Volcanic Sandstone | Spout Creek | 13/4/15 |
| 239902E | 5737780N | 10 | 314 | 10 | NE | Bedding | Volcanic Sandstone | Spout Creek | 13/4/15 |
| 240402E | 5737814N | 15 | 314 | 10 | NE | Bedding | Volcanic Sandstone | Spout Creek | 13/4/15 |
| 248554E | 5740026N | 6 | 74 | 4 | E | Bedding | Volcaniclastics with large clasts of basalt | Eagle Nest Reef (Aireys Inlet) | 14/4/15 |
| 248543E | 5739926N | 7 | 72 | 22 | SE | Bedding | Basaltic tuff with sand/ mud/ basalt/ marl clasts | Eagle Nest Reef (Aireys Inlet) | 14/4/15 |
| 248543E | 5739926N | 7 | 66 | 26 | SE | Bedding | Basaltic tuff with sand/ mud/ basalt/ marl clasts | Eagle Nest Reef (Aireys Inlet) | 14/4/15 |
| 248561E | 5739886N | 6 | 100 | 3 | SW | Bedding | Basaltic tuff with sand/ mud/ basalt/ marl clasts | Eagle Nest Reef (NE of Aireys Inlet) | 14/4/15 |
| 248557E | 5739844N | 7 | 260 | 13 | N | Bedding | Basaltic tuff with sand/ mud/ basalt/ marl clasts | Eagle Nest Reef (Aireys Inlet) | 14/4/15 |
| 248557E | 5739844N | 7 | 280 | 17 | N | Bedding | Basaltic tuff with sand/ mud/ basalt/ marl clasts | Eagle Nest Reef (Aireys Inlet) | 14/4/15 |
| 248571E | 5739753N | 7 | 100 | 2 | SW | Bedding | Basaltic tuff with sand/ mud/ basalt/ marl clasts | Eagle Nest Reef (Aireys Inlet) | 14/4/15 |
| 248540E | 5739705N | 7 | 112 | 6 | S | Bedding | Basaltic tuff with sand/ mud/ basalt/ marl clasts | Eagle Nest Reef (Aireys Inlet) | 14/4/15 |
| 248525E | 5739656N | 8 | 255 | 20 | NW | Bedding | Basaltic tuff with sand/ mud/ basalt/ marl clasts | Eagle Nest Reef (Aireys Inlet) | 14/4/15 |
| 248500E | 5739545N | 12 | 172 | 2 | SW | Bedding | Interbedded basaltic tuff and lighter volcaniclastics | Eagle Nest Reef (Aireys Inlet) | 14/4/15 |
| 248490E | 5739525N | 12 | 261 | 12 | NW | Bedding | Interbedded basaltic tuff and lighter volcaniclastics | Eagle Nest Reef (Aireys Inlet) | 14/4/15 |
| 248494E | 5739442N | 5 | 192 | 2 | NW | Bedding | Coarse volcaniclastics with 1mm-20cm clasts | Eagle Nest Reef (Aireys Inlet) | 14/4/15 |
| 248463E | 5739427N | 5 | 120 | 2 | SW | Bedding | Volcaniclastics | Eagle Nest Reef (Aireys Inlet) | 14/4/15 |
| 246342E | 5739189N | 3 | 88 | 2 | SE | Bedding | Weathered Sands | Berthon Hill (near water treatment plant) | 25/4/15 |
| 245304E | 5738202N | 5 | 15 | 10 | SE | Bedding | Sandstone | | 25/4/15 |
| 248644E | 5740462N | 4 | 266 | 6 | NW | Bedding | Red/ brown Clay and highly weathered Sands | Aireys Inlet, NE platforms | 26/4/15 |
| 248644E | 5740462N | 4 | 200 | 5 | NW | Bedding | Red/ brown Clay and highly weathered Sands | Aireys Inlet, NE platforms | 26/4/15 |
| 248957E | 5740718N | 4 | 110 | 2 | SW | Bedding | Light volcaniclastics, with clasts | Aireys Inlet, NE platforms | 26/4/15 |
| 249015E | 5740761N | 4 | 275 | 21 | N | Bedding | Volcaniclastics and sands | Aireys Inlet, NE platforms | 26/4/15 |
| 249025E | 5740771N | 4 | 322 | 21 | N | Bedding | Interbedded fine grained sands and clast bearing volcaniclastics | Aireys Inlet, NE platforms | 26/4/15 |

| | | | | | | | | | |
|---|---|---|---|---|---|---|---|---|---|
| 249056E | 5740756N | 3 | 295 | 10 | N | Bedding | Interbedded fine grained sandstone and clast bearing volcaniclastics | Aireys Inlet, NE platforms | 26/4/15 |
| 249057E | 5740757N | 6 | 262 | 10 | N | Bedding | Well layered volcaniclastics | Aireys Inlet, NE platforms | 26/4/15 |
| 249105E | 5740869N | 3 | 269 | 18 | NW | Bedding | Well layered volcaniclastics with clasts of mud, scoria and sand | Aireys Inlet, NE platforms | 26/4/15 |
| 249161E | 5741000N | 3 | 202 | 21 | W | Bedding | Well layered volcaniclastics with clasts of mud, scoria and sand | Aireys Inlet, NE platforms | 26/4/15 |
| 249203E | 5741026N | 4 | 288 | 30 | N | Bedding | Well layered volcaniclastics with clasts of mud, scoria and sand | Aireys Inlet, NE platforms | 26/4/15 |
| 249261E | 5741100N | 4 | 280 | 20 | NW | Bedding | Well layered volcaniclastics with clasts of mud, scoria and sand | Aireys Inlet, NE platforms | 26/4/15 |
| 249237E | 5741191N | 5 | 264 | 10 | NE | Bedding | Light coloured volcaniclastics/ sandstone | Aireys Inlet, NE platforms | 26/4/15 |
| 249308E | 5741324N | 5 | 238 | 6 | NW | Bedding | Light coloured volcaniclastics/ sands | Aireys Inlet, NE platforms | 26/4/15 |
| 249580E | 5741723N | 4 | 163 | 94 | W | Bedding | Light sands/ tuffs, containing calcite cement in areas | Urquhart Bluff, Aireys Inlet, NE platforms | 26/4/15 |
| 247063E | 5740415N | 4 | 16 | 8 | SE | Bedding | Weathered, loose, coarse sandstone | Luggs/ Boundary Road | 27/4/15 |
| 244186E | 5742061N | 3 | 349 | 16 | NE | Bedding | Weathered Sandstone | Duffs Quarry | 27/4/15 |
| 244169E | 5742048N | 4 | 51 | 17 | SE | Bedding | Sandstone (large quartz bearing, with silty matrix) | Duffs Quarry | 27/4/15 |
| 244169E | 5742048N | 4 | 35 | 19 | SE | Bedding | Sandstone (large quartz bearing, with silty matrix) | Duffs Quarry | 27/4/15 |
| 244161E | 5742046N | 3 | 49 | 10 | SE | Bedding | Sandstone (large quartz bearing, with silty matrix) | Duffs Quarry | 27/4/15 |
| 246415E | 5738598N | 4 | 86 | 2 | SE | Bedding | Weathered dark brown sands | South of Painkalac Creek (next to road) | 27/4/15 |
| 245347E | 5740980N | 3 | 112 | 10 | S | Bedding | Weathered Sandstone | Dam Creek Road (off Bambra Road) | 28/4/15 |
| 245335E | 5741002N | 4 | 140 | 12 | S | Bedding | Weathered Sandstone | Dam Creek Road (off Bambra Road) | 28/4/15 |
| 244848E | 5741053N | 3 | 100 | 12 | S | Bedding | Weathered Sandstone (red/ brown) | Dam Creek Road (off Bambra Road) | 28/4/15 |
| 244805E | 5741087N | 3 | 78 | 14 | S | Bedding | Weathered Sandstone (red/ brown) | Dam Creek Road (off Bambra Road) | 28/4/15 |
| 244145E | 5741161N | 4 | 100 | 18 | SW | Bedding | Weathered Sandstone (red/ brown) | Dam Creek Road | 28/4/15 |
| 244146E | 5741162N | 4 | 110 | 12 | SSW | Bedding | Weathered Sandstone (red/ brown) | Dam Creek Road (off Bambra Road) | 28/4/15 |
| 244134E | 5741175N | 4 | 55 | 22 | SE | Bedding | Volcanic Sandstone (weathered) | Dam Creek Road (off Bambra Road) | 28/4/15 |
| 244124E | 5741185N | 3 | 59 | 30 | SE | Bedding | Volcanic Sandstone (weathered) | Dam Creek Road (off Bambra Road) | 28/4/15 |
| 244120E | 5741197N | 4 | 61 | 32 | SE | Bedding | Volcanic Sandstone; rounded mud clast conglomerate and coal (weathered) | Dam Creek Road (off Bambra Road) | 28/4/15 |
| 244036E | 5740737N | 3 | 89 | 4 | S | Bedding | Very weathered sandstone, red/ brown | Dam Creek Road (off Bambra Road) | 28/4/15 |

| | | | | | | | | | |
|---|---|---|---|---|---|---|---|---|---|
| 243675E | 5741093N | 5 | 16 | 12 | E | Bedding | Lithified Volcanic Sandstone | Dam Creek Road (off Bambra Road) | 28/4/15 |
| 239343E | 5734665N | 5 | 356 | 10 | NE | Bedding | Volcanic Sandstone | Northern Lorne Coastline | 7/8/15 |
| 238861E | 5733931N | 4 | 46 | 5 | SE | Bedding | Volcanic Sandstone, with small fine beds | Northern Lorne Coastline | 7/8/15 |
| 238531E | 5733214N | 3 | 50 | 10 | SE | Bedding | Volcanic Sandstone | Northern Lorne Coastline | 7/10/15 |
| 238603E | 5733282N | 3 | 50 | 6 | S | Bedding | Volcanic Sandstone | Northern Lorne Coastline | 7/10/15 |
| 238678E | 5733406N | 3 | 20 | 6 | SE | Bedding | Volcanic Sandstone | Northern Lorne Coastline | 7/10/15 |
| 238717E | 5733444N | 3 | 30 | 10 | SE | Bedding | Volcanic Sandstone | Northern Lorne Coastline | 7/10/15 |
| 238731E | 5733474N | 3 | 290 | 4 | N | Bedding | Volcanic Sandstone | Northern Lorne Coastline | 7/10/15 |
| 238749E | 5733568N | 3 | 20 | 4 | SE | Bedding | Volcanic Sandstone | Northern Lorne Coastline | 7/10/15 |
| 238911E | 5733796N | 3 | 58 | 16 | SE | Bedding | Volcanic Sandstone | Northern Lorne Coastline | 7/10/15 |
| 239038E | 5734368N | 3 | 60 | 4 | SE | Bedding | Volcanic Sandstone | Northern Lorne Coastline | 7/10/15 |
| 238675E | 5733489N | 3 | 50 | 4 | SE | Bedding | Volcanic Sandstone | Northern Lorne Coastline | 7/10/15 |
| 238453E | 5733250N | 5 | 22 | 16 | E | Bedding | Volcanic Sandstone | Northern Lorne Coastline | 7/10/15 |
| 241227E | 5736871N | 3 | 150 | 90 | N/A | Sinistral fault | Interbedded Volcanic Sands/ Muds | Devils Elbow, Eastern View (Platforms) | 27/3/15 |
| 241236E | 5736865N | 3 | 325 | 85 | E | Sinistral fault | Interbedded Volcanic Sands/ Muds | Devils Elbow, Eastern View (Platforms) | 27/3/15 |
| 241119E | 5736296N | 5 | 146 | -- | N/A | Fault | Volcanic Sandstone overlaying Mudstone | South of Devils Elbow (Platforms) | 12/4/15 |
| 248543E | 5739926N | 7 | 266 | 40 | N | Fault? | Basaltic tuff with sand/ mud/ basalt/ marl clasts | Eagle Nest Reef Platforms (NE of Aireys Inlet) | 14/4/15 |
| 248821E | 5740636N | 3 | 38 | 90 | N/A | Fault? | Light volcaniclastics, with clasts | Aireys Inlet, NE platforms | 26/4/15 |
| 248973E | 5740735N | 4 | 168 | 68 | S | Incipient fault | Light volcaniclastics, with clasts | Aireys Inlet, NE platforms | 26/4/15 |
| 249572E | 5741781N | 5 | 26 | 90 | N/A | Sinistral fault | Sinistral fault | Urquhart Bluff, Aireys Inlet, platforms | 26/4/15 |
| 241184E | 5736350N | 6 | 148 | 90 | N/A | Incipient fault | Volcanic Sandstone | Devils Elbow, Eastern View (Platforms) | 11/4/15 |
| 241084E | 5736306N | 5 | 119 | 90 | N/A | Fault? | Volcanic Sandstone | South of Devils Elbow (Platforms) | 12/4/15 |
| 248463E | 5739427N | 5 | 332 | 70 | E | Fault? | Volcaniclastics | Eagle Nest Reef (Aireys Inlet) | 14/4/15 |
| 248978E | 5740739N | 4 | 55 | 90 | N/A | Sand injection | Light volcaniclastics, with clasts | Aireys Inlet, NE platforms | 26/4/15 |
| 249163E | 5741006N | 5 | 163 | 70 | W | Fault? | Light coloured volcaniclastics | Aireys Inlet, NE platforms | 26/4/15 |
| 239653E | 5734983N | 4 | 344 | 90 | N/A | Incipient fault | Volcanic sandstone | North of Lorne Coastal Platforms | 7/8/15 |
| 241084E | 5736306N | 3 | 338 | 85 | E | Incipient fault | Volcanic sandstone | Devils Elbow, Eastern View (Platforms) | 6/10/15 |
| 253797E | 5743685N | 3 | 128 | 90 | N/A | Sinistral fault | Sands on top of volcaniclastics | Anglesea Beach (Soapy Rocks) | 15/4/16 |
| 253797E | 5743685N | 3 | 160 | 90 | N/A | Sinistral fault | Sands on top of volcaniclastics | Anglesea Beach (Soapy Rocks) | 15/4/16 |
| 253797E | 5743685N | 3 | 199 | 90 | N/A | Sinistral fault | Sands on top of volcaniclastics | Anglesea Beach (Soapy Rocks) | 15/4/16 |
| 258816E | 5746500N | 3 | 260 | 30 | N | Thrust Fault? | Fe-rich, white-tan sands (with red-orange clasts) on top of silts. | Anglesea Beach (north) - Black Rock | 16/4/16 |

| | | | | | | | | | |
|---|---|---|---|---|---|---|---|---|---|
| 258816E | 5746500N | 3 | 260 | 3 | NW | Thrust Fault? | Fe-rich, white-tan sands (with red-orange clasts) on top of silts. | Anglesea Beach (north) - Black Rock | 16/4/16 |
| 259930E | 5747276N | 3 | 140 | 58 | SW | Normal fault | Fe-rich, white-tan layered sands | Pt. Addis | 16/4/16 |
| 260014E | 5747164N | 3 | 42 | 36 | E | Thrust Fault? | Calcaranite | Pt. Addis | 2/5/16 |
| 260033E | 5747164N | 3 | 200 | 26 | W | Thrust Fault? | Calcaranite | Pt. Addis | 2/5/16 |
| 253761E | 5743604N | 3 | 220 | 12 | NW | Thrust Fault | Loose volcaniclastic sands and silts | South of Soapy Rocks | 8/9/16 |
| 253804E | 5743678N | 3 | 324 | 90 | N/A | Sinistral offset? | Fine laminations of sand and silt overlying volcaniclastics | Soapy Rocks | 11/10/16 |
| 253804E | 5743678N | 3 | 284 | 90 | N/A | Dextral offset? | Fine laminations of sand and silt overlying volcaniclastics | Soapy Rocks | 11/10/16 |
| 254167E | 5744285N | 3 | 128 | 2 | SW | Bedding | Sulphur-rich mudstone layer (1.5m thick) with jarosite on top | Anglesea Beach | 15/4/16 |
| 254132E | 5744260N | 3 | 130 | 3 | SSW | Bedding | Sulphur-rich mudstone layer | Anglesea Beach | 15/4/16 |
| 253989E | 5744135N | 3 | 108 | 5 | SSW | Bedding | Sulphur-rich mudstone layer | Anglesea Beach | 15/4/16 |
| 253889E | 5744019N | 3 | 125 | 5 | S | Bedding | Red sand? layer | Anglesea Beach | 15/4/16 |
| 253826E | 5743916N | 3 | 120 | 6 | SSW | Bedding | Red sand?/ silt on top of grey mud/silt | Anglesea Beach | 15/4/16 |
| 253802E | 5743820N | 3 | 118 | 8 | S | Bedding | Laminated sulphur-rich muds (0.5m), with sands on top (~4.5m), with volcaniclastics on top (1.5m), with sands on top of that. | Anglesea Beach | 15/4/16 |
| 253797E | 5743663N | 3 | 120 | 8 | SSW | Bedding | Layered sandstone on top of volcaniclastics | Anglesea Beach | 15/4/16 |
| 253732E | 5743536N | 3 | 120 | 5 | S | Bedding | Layered mudstone overlying 'slump' (redox) | Anglesea Beach | 15/4/16 |
| 253715E | 5743428N | 3 | 115 | 5 | SSW | Bedding | Fe-rich sands (very weathered) | Anglesea Beach | 15/4/16 |
| 253733E | 5743220N | 3 | 105 | 6 | SSW | Bedding | Fe-rich sands (very weathered), within grey clays/ silts | Anglesea Beach | 15/4/16 |
| 254207E | 5742881N | 3 | 80 | 3 | S | Bedding | Calcaranite (hard but weathered) | Anglesea Beach | 15/4/16 |
| 254949E | 5744773N | 3 | 140 | 8 | SW | Bedding | Pyritic grey sands and jarosite | Anglesea Beach | 16/4/16 |
| 254983E | 5744881N | 3 | 140 | 7 | S | Bedding | Pyritic grey sands and jarosite | Anglesea Beach | 16/4/16 |
| 255056E | 2744985N | 3 | 140 | 5 | SW | Bedding | Sulphur-rich mudstone with overlying pyrite sands | Anglesea Beach | 16/4/16 |
| 255032E | 5744972N | 3 | 140 | 7 | SW | Bedding | Pyritic grey sands and jarosite | Anglesea Beach | 16/4/16 |
| 254988E | 5744897N | 3 | 140 | 8 | SW | Bedding | Pyritic grey sands and jarosite | Anglesea Beach | 16/4/16 |
| 258690E | 5746468N | 3 | 350 | 10 | ENE | Bedding | Boundary between cross-bedded white-tan sands and Fe-rich unit | Anglesea Beach (north) | 16/4/16 |
| 258811E | 5746457N | 3 | 342 | 5 | NE | Bedding | Fe-rich sands | Anglesea Beach (north) | 16/4/16 |
| 258816E | 5746500N | 3 | 84 | 10 | S | Bedding | Fe-rich-white sands with (red-orange) clasts | Anglesea Beach (north) | 16/4/16 |
| 260131E | 5747119N | 3 | 66 | 6 | SE | Bedding | Calcaranite | Pt. Addis | 16/4/16 |
| 259955E | 5747216N | 3 | 128 | 14 | SW | Bedding | Iron-rich sands (layered) | Pt. Addis | 16/4/16 |

| | | | | | | | | | |
|---|---|---|---|---|---|---|---|---|---|
| 259930E | 5747276N | 3 | 140 | 16 | SSW | Bedding | Fe-rich sands (layered) | Pt. Addis | 16/4/16 |
| 259913E | 5747507N | 5 | 140 | 8 | SSW | Bedding | Fe-rich sands (layered) | Pt. Addis | 16/4/16 |
| 260369E | 5748210N | 5 | 340 | 4 | NE | Bedding | Sulphur-rich mudstone with overlying pyrite sands | Pt. Addis | 16/4/16 |
| 260439E | 5748269N | 5 | 340 | 5 | NE | Bedding | Pyritic grey sands and jarosite | Pt. Addis | 16/4/16 |
| 260526E | 5748319N | 5 | 340 | 6 | NE | Bedding | Pyritic grey sands and jarosite | Pt. Addis | 16/4/16 |
| 260693E | 5748390N | 5 | 350 | 8 | NE | Bedding | Pyritic grey sands and jarosite, above sulphur-rich mudstone | Pt. Addis | 16/4/16 |
| 260801E | 5748417N | 5 | 350 | 8 | NE | Bedding | Pyritic grey sands and jarosite, above sulphur-rich mudstone | Pt. Addis | 16/4/16 |
| 261051E | 5748448N | 5 | 350 | 8 | NE | Bedding | Pyritic grey sands and jarosite, above sulphur-rich mudstone | Pt. Addis | 16/4/16 |
| 254263E | 5744344N | 3 | 298 | 6 | NE | Bedding | Pyritic grey sands and jarosite, above sulphur-rich mudstone | Anglesea Surf Beach | 28/4/16 |
| 254308E | 5744410N | 3 | 130 | 4 | SW | Bedding | Contact of pyritic grey sands and jarosite and Fe-rich rock | Anglesea Surf Beach | 28/4/16 |
| 254896E | 5744659N | 3 | 120 | 4 | S | Bedding | Weathered red silts | Anglesea Surf Beach | 28/4/16 |
| 254908E | 5744681N | 3 | 126 | 9 | SW | Bedding | Contact of pyritic grey sands and jarosite with Fe-rich bedded sands | Anglesea Surf Beach | 28/4/16 |
| 254957E | 5744750N | 3 | 140 | 16 | SW | Bedding | Pyritic grey sands and jarosite, above sulphur-rich mudstone | Anglesea Beach | 28/4/16 |
| 254956E | 5744773N | 3 | 146 | 9 | SW | Bedding | Pyritic grey sands and jarosite | Anglesea Beach (north) | 1/5/16 |
| 254964E | 5744799N | 3 | 145 | 10 | SW | Bedding | Pyritic grey sands and jarosite | Anglesea Beach (north) | 1/5/16 |
| 255072E | 5745014N | 5 | 140 | 8 | SW | Bedding | Sulphur-rich mudstone with pyrite sands on top | Anglesea Beach (north) | 1/5/16 |
| 255172E | 5745125N | 3 | 135 | 2 | SW | Bedding | Sulphur-rich mudstone with pyrite sands on top | Anglesea Beach (north) | 1/5/16 |
| 255290E | 5745206N | 3 | 135 | 1 | SW | Bedding | Sulphur-rich mudstone with pyrite sands on top | Anglesea Beach (north) | 1/5/16 |
| 255371E | 5745267N | 4 | 135 | 1 | SW | Bedding | Sulphur-rich mudstone with pyrite sands on top | Anglesea Beach (north) | 1/5/16 |
| 256184E | 5745641N | 3 | 40 | 2 | SE | Bedding | Sulphur-rich mudstone with pyrite sands on top | Anglesea Beach (north) | 1/5/16 |
| 256273E | 5745675N | 3 | 50 | 4 | SE | Bedding | Sulphur-rich mudstone with pyrite sands on top | Anglesea Beach (north) | 1/5/16 |
| 256476E | 5745769N | 3 | 20 | 4 | SE | Bedding | Sulphur-rich mudstone with pyrite sands and then Fe rich rocks on top. | Anglesea Beach (north) | 1/5/16 |
| 257707E | 5746481N | 3 | 30 | 4 | SE | Bedding | Sulphur-rich mudstone with pyrite sands and then Fe rich rocks on top. | Anglesea Beach (north) | 1/5/16 |
| 258120E | 5746494N | 3 | 350 | 5 | NE | Bedding | Sulphur-rich mudstone with pyrite sands and then Fe rich rocks on top. | Anglesea Beach (north) | 1/5/16 |

| | | | | | | | | | |
|---|---|---|---|---|---|---|---|---|---|
| 259953E | 5747221N | 3 | 140 | 8 | S | Bedding | Weathered red-tan sands/ silts | Pt. Addis | 2/5/16 |
| 260027E | 5747168N | 3 | 146 | 4 | S | Bedding | Calcarenite | Pt. Addis | 2/5/16 |
| 260063E | 5747159N | 3 | 150 | 6 | S | Bedding | Calcarenite | Pt. Addis | 2/5/16 |
| 260115E | 5747140N | 3 | 110 | 5 | S | Bedding | Calcarenite | Pt. Addis | 2/5/16 |
| 260137E | 5747119N | 3 | 80 | 8 | S | Bedding | Calcarenite | Pt. Addis | 2/5/16 |
| 260124E | 5747094N | 3 | 160 | 5 | S | Bedding | Calcarenite | Pt. Addis | 2/5/16 |
| 260122E | 5747084N | 3 | 176 | 6 | S | Bedding | Calcarenite | Pt. Addis | 2/5/16 |
| 260130E | 5747078N | 3 | 200 | 5 | W | Bedding | Calcarenite | Pt. Addis | 2/5/16 |
| 260168E | 5747010N | 3 | 102 | 4 | SW | Bedding | Calcarenite | Pt. Addis | 2/5/16 |
| 259950E | 5746589N | 3 | 112 | 3 | W | Bedding | Calcarenite | Pt. Addis | 2/5/16 |
| 259913E | 5746609N | 3 | 126 | 10 | S | Bedding | Calcarenite | Pt. Addis | 2/5/16 |
| 259894E | 5746622N | 3 | 146 | 6 | SW | Bedding | Calcarenite | Pt. Addis | 2/5/16 |
| 259888E | 5746632N | 3 | 150 | 4 | WSW | Bedding | Calcarenite | Pt. Addis | 2/5/16 |
| 259889E | 5746638N | 3 | 210 | 7 | WNW | Bedding | Calcarenite | Pt. Addis | 2/5/16 |

## Summary of vitrinite reflectance data

| Grid Reference | | $R_0$ | Range | Standard Deviation | Number of readings | Location | Date | Temp (˚C) | Max Burial Depth (Km) |
|---|---|---|---|---|---|---|---|---|---|
| 754242E | 5723413N | 0.57 | 0.49 - 0.67 | 0.354 | N/A | Artillery Rocks | 28/6/04 | 98 | 1.78 |
| 754197E | 5723786N | 0.61 | 0.48 - 0.82 | 0.299 | N/A | Jamieson River | 28/6/04 | 103.6 | 1.88 |
| 755830E | 5725135N | 0.58 | 0.44 - 0.71 | 0.363 | N/A | Mt. Defiance | 28/6/04 | 99.1 | 1.8 |
| 756688E | 5725817N | 1.29 | 1.17 - 1.41 | 0.065 | N/A | Cumberland River | 28/6/04 | 156 | 2.83 |
| 760871E | 5732379N | 0.58 | 0.50 - 0.66 | 0.047 | 25 | North of Lorne | 22/3/12 | 99.1 | 1.8 |
| 756429E | 5725461N | 0.85 | 0.74 - 1.02 | 0.062 | 25 | South of Cumberland River | 22/3/12 | 129.5 | 2.35 |
| 754310E | 5723873N | 0.68 | 0.52 - 0.82 | 0.085 | 25 | Jamieson Creek Mouth | 22/3/12 | 112.5 | 2.04 |
| 754221E | 5723465N | 0.66 | 0.53 - 0.78 | 0.064 | 25 | Artillery Rocks | 22/3/12 | 110.3 | 2 |
| 760871E | 5732379N | 0.58 | 0.50 - 0.66 | 0.047 | N/A | North of Lorne | 22/3/12 | 99.1 | 1.8 |
| 759776E | 5729303N | 0.8 | 0.70 - 0.93 | 0.07 | N/A | Lorne | 12/1/12 | 125.3 | 2.27 |
| 760158E | 5728841N | 1.23 | 1.06 - 1.40 | 0.089 | N/A | Point Grey, Lorne | 22/3/12 | 154 | 2.8 |
| 759270E | 5727899N | 0.88 | 0.72 - 0.95 | 0.049 | N/A | South of George River | 22/3/12 | 132 | 2.4 |
| 756564E | 5725652N | 1.05 | 0.88 - 1.20 | 0.09 | N/A | South of Cumberland River | 22/3/12 | 146 | 2.65 |

Data collected by Monash University (2004/ 2012), pers. com M. Hall.

Geothermal gradient 55C°/km – Surface temperature ~15C°

# Appendix 2

Sedimentary stratigraphic columns and bathymetry summary

**Overview of stratigraphic columns**

Twelve locations (Appendix 2.2) were identified for a detailed stratigraphic analysis along the Lorne – northern Anglesea coastline in order to map lithological variations and provide a more comprehensive data set from which to interpreted the regional stratigraphic boundaries and structural trends. The age of the outcropping sediments span the Early Cretaceous (ca. 113-100 Ma) to the late Cenozoic (ca. 24-15 Ma) and were chosen for their excellent lateral and vertical visibility. Stratigraphic sections are presented in true thickness, determined by applying trigonometry to the measured dip and thickness of each unit. Sedimentary stratigraphic data was documented on templates modified from Nichols (2009), prior to being illustrated within CorelDraw and Adobe Illustrator CS6.

**Sedimentary stratigraphic section descriptions**

Facies Code:

**Mst – Mudstone**

**f – Fine-grained sandstone**

**m – Medium-grained sandstone**

**c – Coarse-grained sandstone**

**g – Granular-grained gravel**

**cb – Cobble-grained gravel**

**b – Boulder-grained gravel**

# Eastern View (Devils Elbow) (54H 0241227E; 5736871N)

This stratigraphic section was documented along coastal platforms below Devils Elbow (Eastern View). At this location interbedded units range from interbedded mudstone and coarse grained to massive volcaniclastic sandstone units. On the basis of observed cross-bedding structures and rip-up clasts present in these lithologies, these units are interpreted to represent alternating periods of low to high

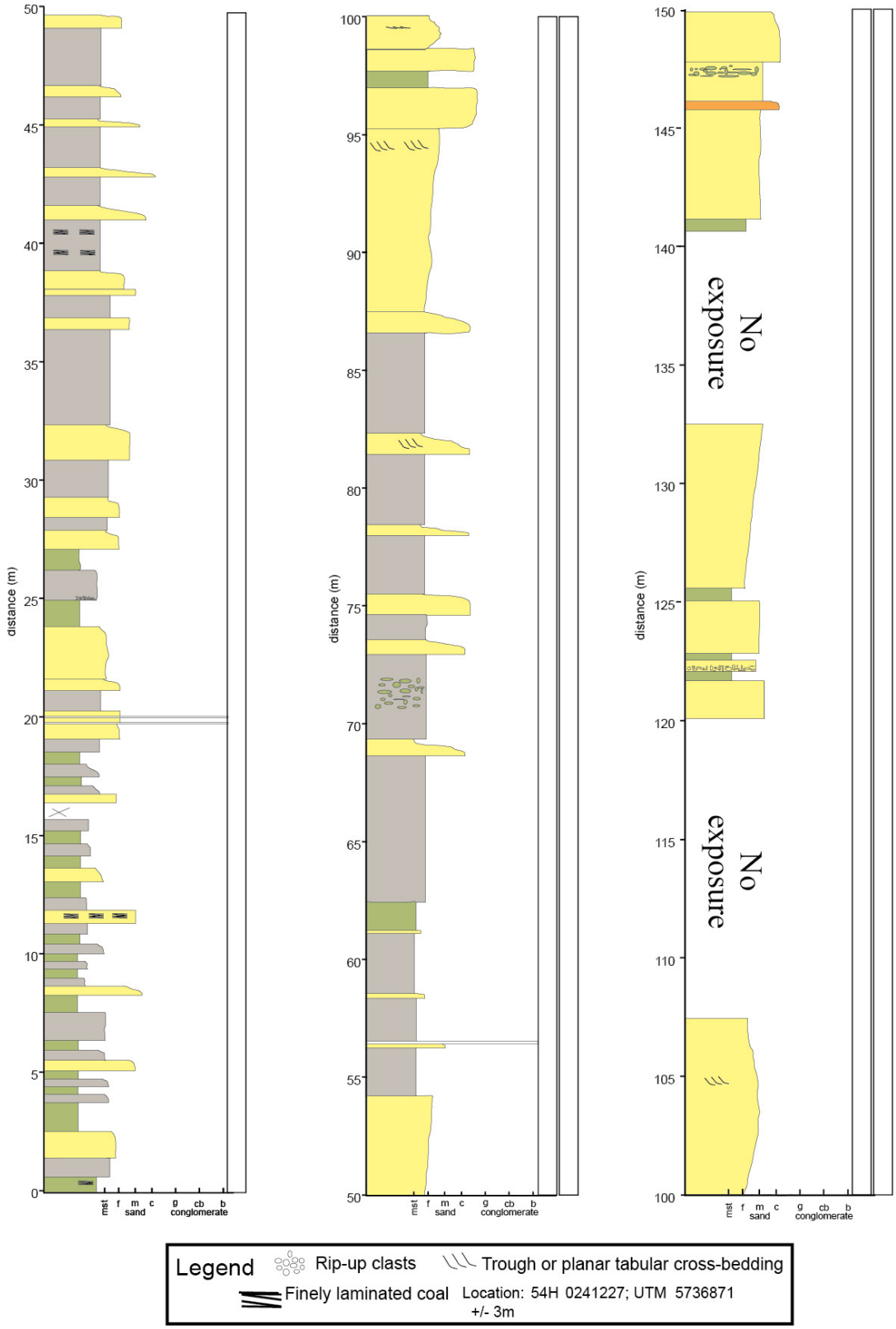

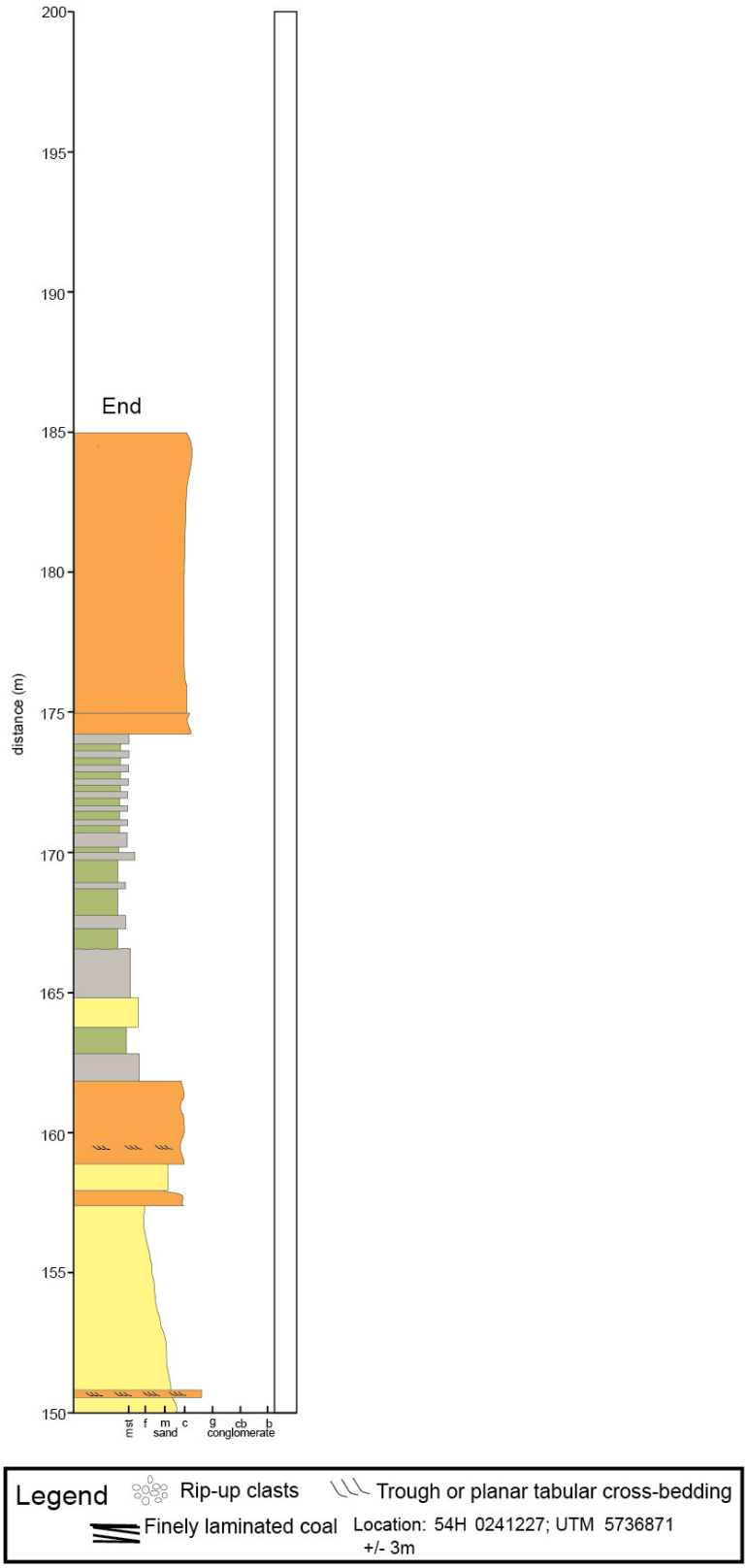
200
195
190
End
185
180
175
170
165
160
155
150
distance (m)
mst
f
m
c
g
cb
b
sand
conglomerate
Legend
Rip-up clasts
Trough or planar tabular cross-bedding
Finely laminated coal
Location: 54H 0241227; UTM 5736871
+/- 3m

# Aireys Inlet Coastal Sections

Figure 1. Split Point

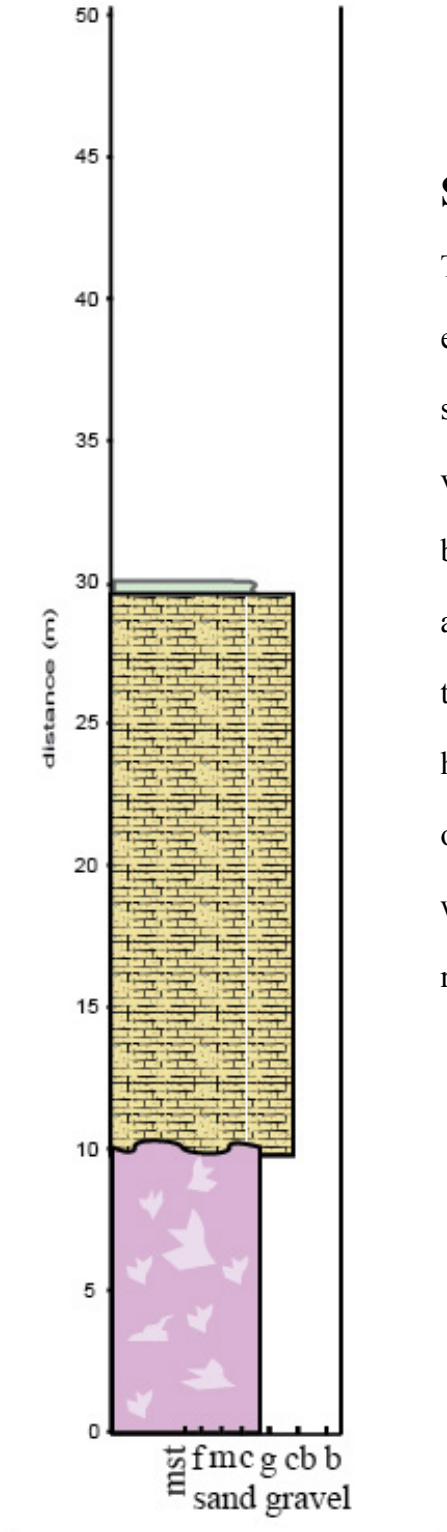


Location: 55H 0247320E 5738041N +/- 3m
AGD66

## Split Point

This stratigraphic section was documented along coastal cliff exposures at Split Point, Aireys Inlet. In this location basalts with surficial flaky weathering contain secondary calcite infilling of the vesicle holes (amygdales). Basalts are unconformably overlain by a light yellow bioclastic grainstone (calcarenite) that displays a fenestral weathering texture. The fossil assemblage within the calcarenite includes crinoids, urchins and pectin (bivalves), however this assemblage lacks corals. Large (~6cm) thick-shelled oysters within the calcarenite fills the eroded channel structures within the basalt (see 10m, figure 1 above), possibly representing a region that experienced higher energy water flow.

Figure 2.
North of Split Point

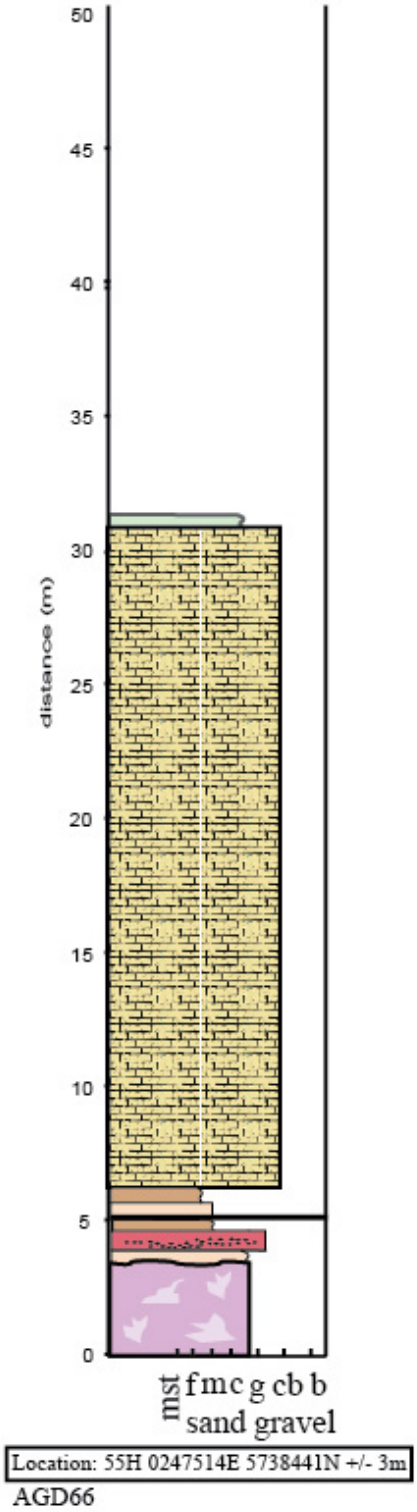


## North of Split Point

Similar to the stratigraphic section at Split Point, this section of the stratigraphy is dominated by a lower unit of weathered basalt (~3-4m) and an upper unit of fossiliferous calcarenite (~25m). However, unlike the southern stratigraphic section (figure 1), to the north of Split Point a unit of cross-bedded brown quartz sandstone (~3m) is observed between the basalt and calcarenite units. This sandstone unit contains black, rounded pebbles, with disseminated hematitic alteration. A ~0.5m thick coal layer is observed within this unit.

Figure 3.
Eagle Nest Reef

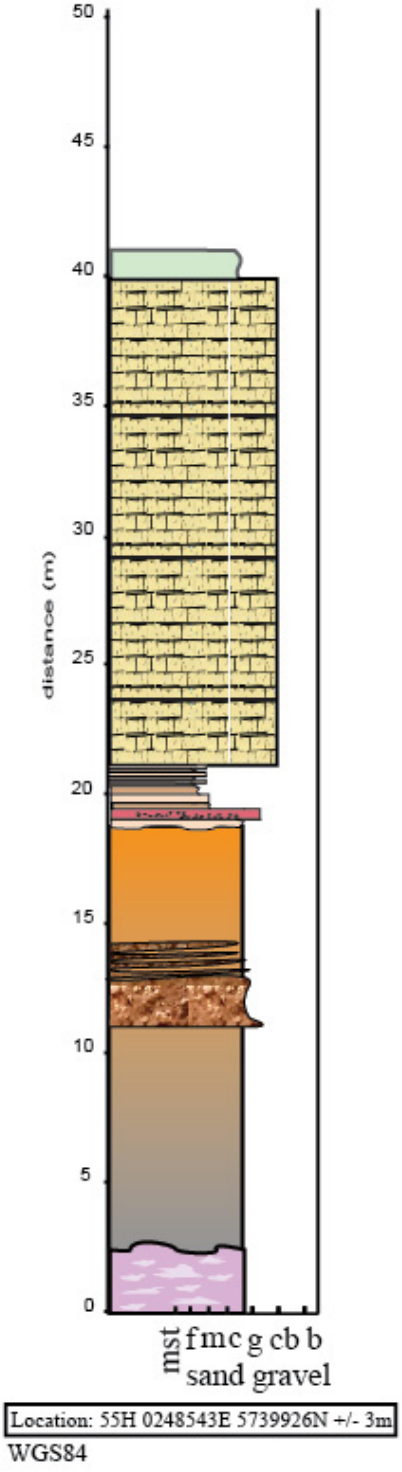


## Eagle Nest Reef

The Eagle Nest Reef cliff exposure hosts a ~40m high stratigraphic section consisting of ~20m of coarse-grained basaltic tuff, that has a cream-coloured surficial coating of material from the overlying ~15m section of bioclastic grainstone (calcaranite). The basaltic tuffs (Angahook Formation) and bioclastic grainstone (calcaranite, Torquay Group) are separated by a ~5m section of basaltic conglomerate and laminated brown quartz sands. Furthermore, ~100m NE of this locality a ~10-20m wide basalt unit is observed intruding into the basaltic tuff, with observed pepperite texture around the basalt margins.

Figure 4.
South of Urquharts Bluff

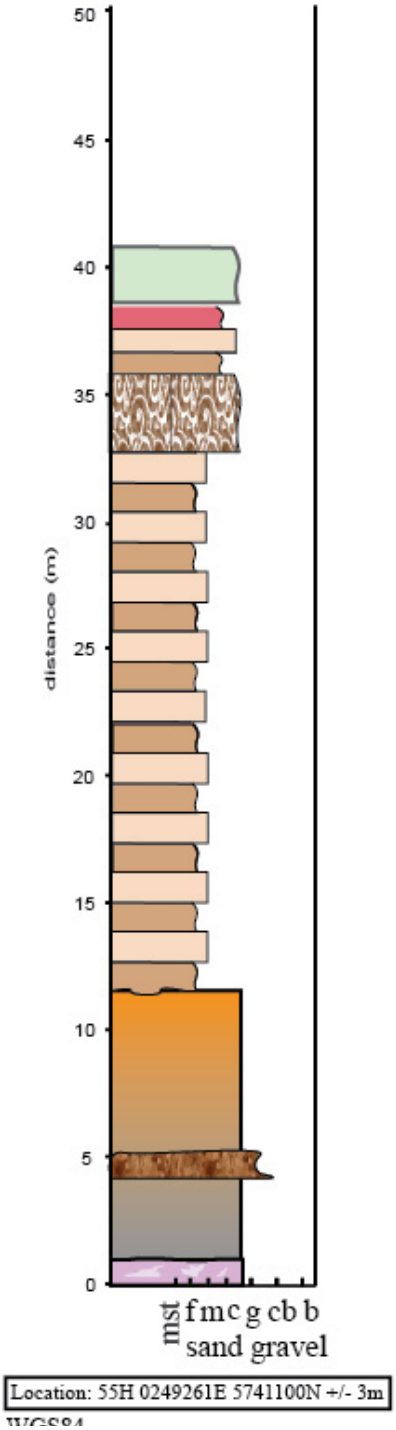


## South of Urquharts Bluff

The coastal outcrops south of Urquharts Bluff host a large succession (~25m high) of cross-bedded, brown quartz sands, underlain by coarse-grained basaltic tuff (~10m high), with minor lenses (each <1m high) of weathered basalt at the base of the stratigraphic section. There is a lateral discordance between the observed basalt wihtin

Figure 5.
Urquharts Bluff

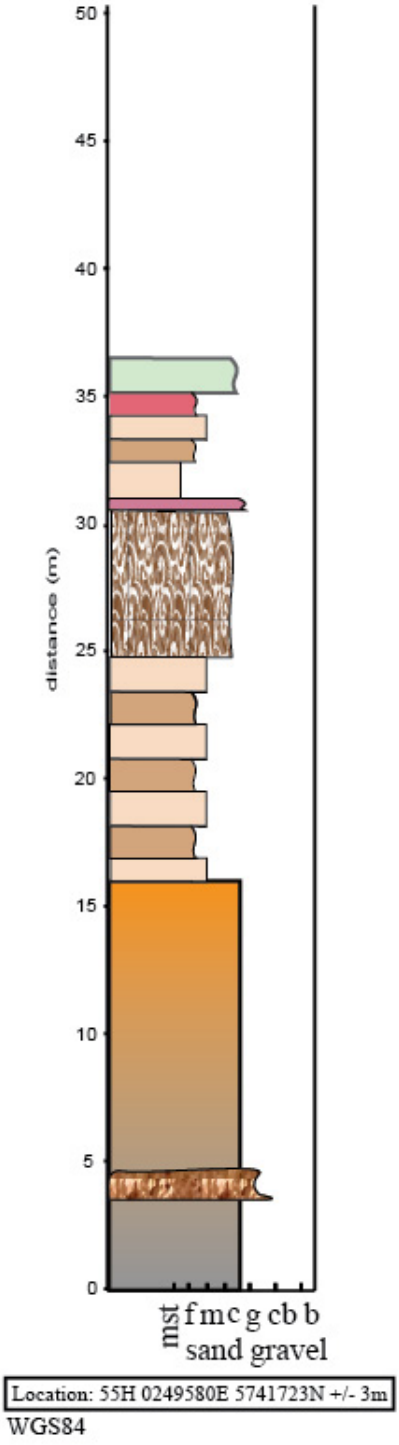


## Urquharts Bluff

The coastal outcrops below Urquharts Bluff host massive (~20m), coarse-grained volcaniclastic sandstone, with pebbles, secondary calcite infilling and some basaltic clasts. This unit is overlain by (~15m) of weathered, loamy siltstone with liesegang rings, slumps and brown quartz sandstone beds (~5m thick).

# Anglesea Coastal Sections

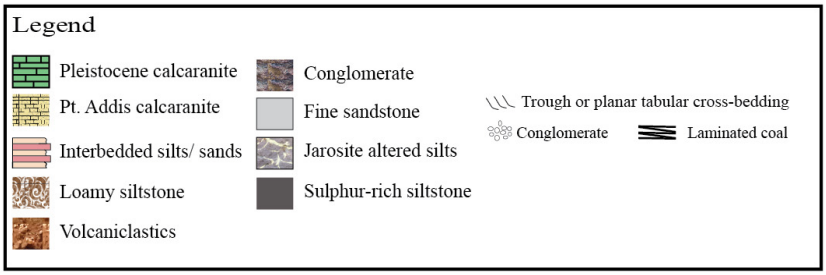


Figure 1.
Pt. Roadknight

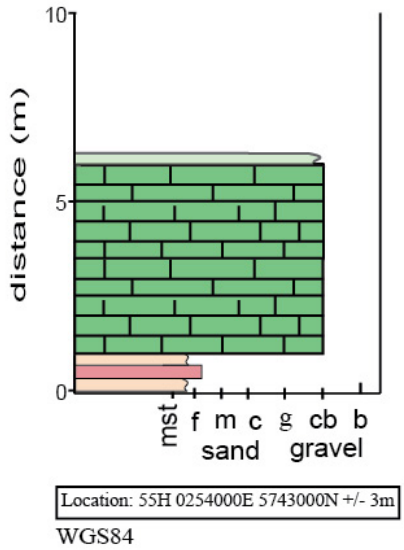


## Pt. Roadknight

Exposed at Point Roadknight are highly weathered brown, red and white sandstone and siltstone that is overlain by cross-bedded, bioclastic grainstone (calcarenite). This calcarenite is texturally similar to the marine bioclastic grainstone deposits around Pt. Addis and Split Point. This Point Roadknight calcarenite is considered to be Pleistocene-aged (Abele, 1968) and does not contain in situ bryozoans that are commonly observed in the older Torquay Group calcarenites.

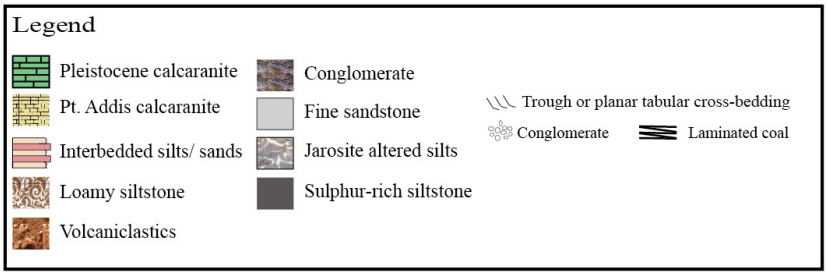


Figure 2.
Soapy Rocks

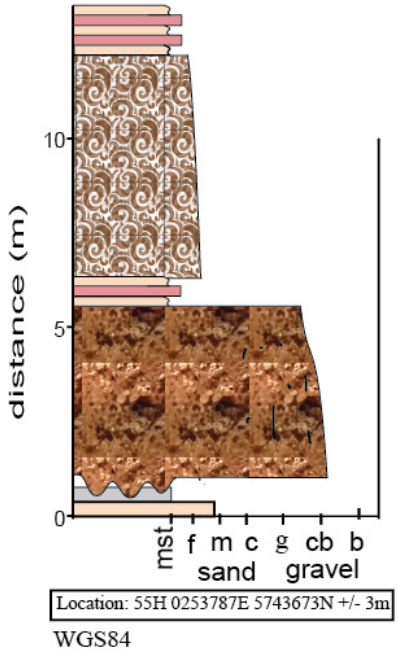


## Soapy Rocks

At the Soapy Rocks locality, fine-grained, thinly interbedded sandstones and mudstones (~5m) are unconformably overlain by volcaniclastic debris flows, containing clasts of basalt and coarse-grained sandstone (~5m). Overlying the volcaniclastic debris is a succession of cross-bedded, coarse sandstone containing reworked lithic fragments of volcanic material. This cross-bedded sandstone is, in turn, overlain by shallow dipping, finely laminated and moderately sorted, white-grey sandstone.

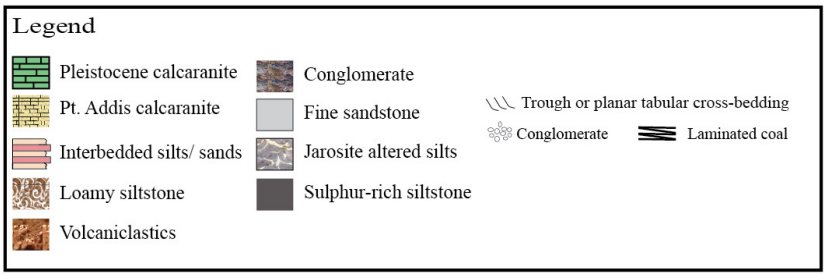


Figure 3.
Anglesea Main beach (southern end)

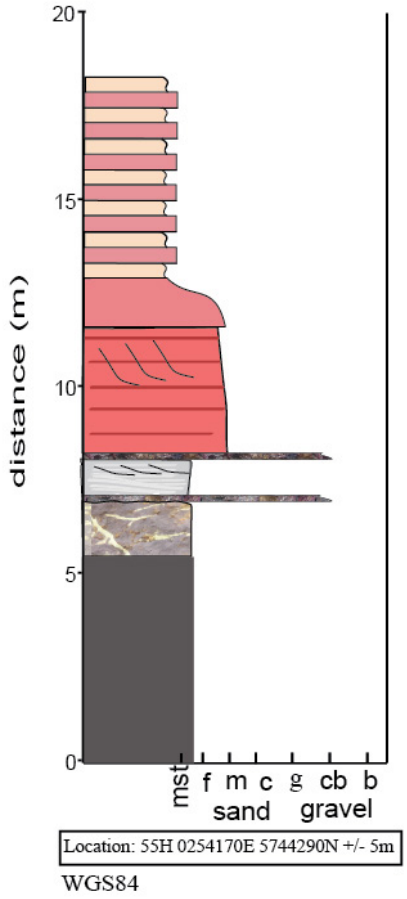


## Anglesea Main Beach (southern end)

The stratigraphic section at Anglesea Main beach (southern end) consists of the Anglesea Formation. This formation is separated into a lower member of weathered, bioturbated, sulphur-rich (anoxic), black sandstone, and an upper member of buff-white, fine sandstone containing weathered pyrite. The uppermost section of this formation appears to be overlain by the lowest sections of the Angahook Formation, while a hematitic rich and laterally confined conglomerates and coarse cross-bedded sandstone are observed within the upper sandstone member.

Figure 4.
Anglesea Main beach (northern end)

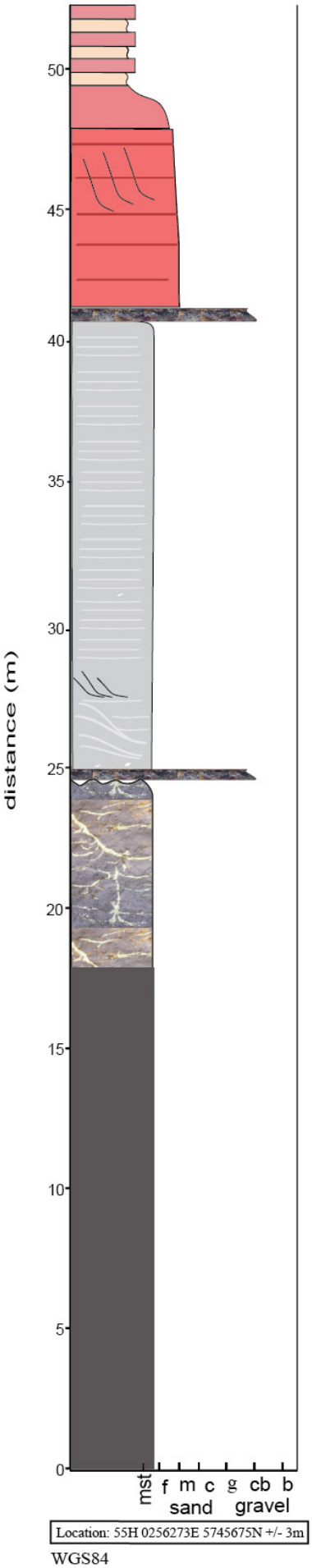


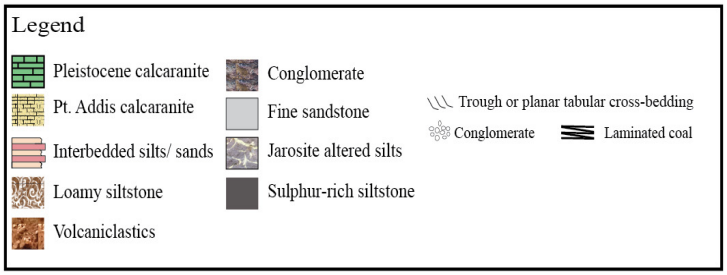


## Anglesea Main Beach (northern end)

The stratigraphic section at Anglesea Main beach (northern end) is similar to the section observed at the southern end of the beach and consists of the Anglesea Formation that is separated into a lower member of weathered, sulphur-rich (anoxic), black sandstone (~18m), and an upper member of buff-white, fine sandstone (~15m). Yellow jarosite alteration is conspicuous within the boundary between the upper and lower Anglesea members.

The lowest (~10m) of the Angahook Formation overlies the upper Anglesea member.

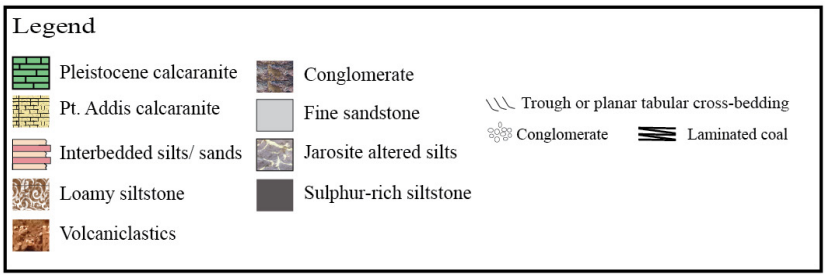


Figure 5.
Point Addis

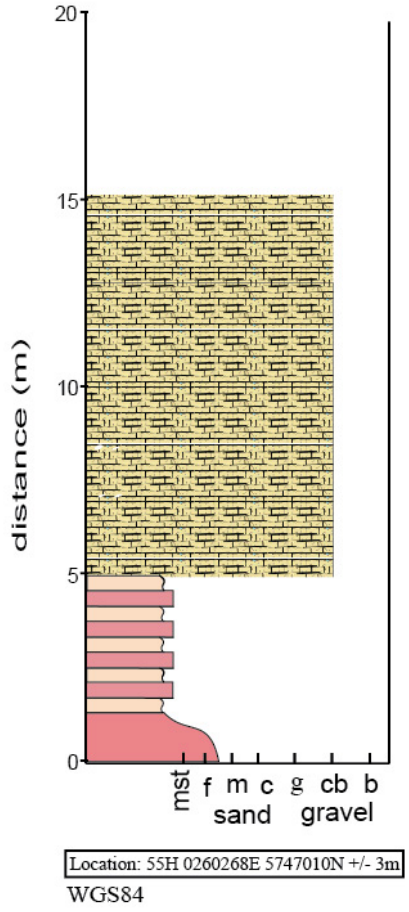


## Point Addis

The northern coastal section of Point Addis hosts ~1.5m of alternating, light-tan coloured, silts and fine-grained brown quartz sands (Angahook Formation), that are onlapped by ~15m of yellow-grey, bioclastic grainstone (calcarenite) containing abundant bryozoans, foraminifera, crinoids and gastropods (Point Addis Limestone, a lateral equivalent of the Split Point Limestone).

Figure 6.
Addiscot Beach
(northern end)

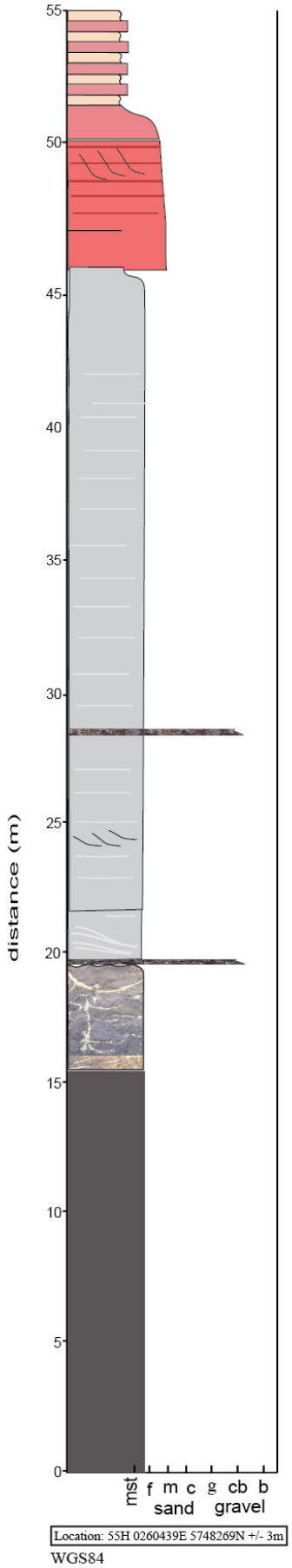


## Addiscot Beach (northern end)

The northern end of Addiscot Beach hosts a thick succession (~60m) of the lower and upper members of the Anglesea Formation, as well as a thin section of the overlying Angahook Formation (Figure 1.9). Exposed is a ~35m section of the sulphur-rich black sandstone with jarosite-altered burrows (lower Anglesea Member), with a surficial cream-brown coating of weathered material from the overlying sediments. The overlying sediments are ~15m of light cream-coloured, fine grain sandstone (upper Anglesea Member) that are further overlain by the lowermost section of the Angahook Formation, that consists of alternating kaolinite and iron-rich, fine-grained sandstones and siltstones.

A bright yellow jarosite alteration is conspicuous within the grey-white pyritic siltstone to fine sandstone, and is observed at the boundary between the upper and lower Anglesea Members (at ~20m).

**Summary of bathymetric data**

In order to apply a color shading to bathymetric data, the bathymetric tiles should be initially merged into a single large raster file.

- Raster: Miscellaneous: Merge
- Select input files
- Name output file (.tif)
- No data value: -9999

Furthermore, the appropriate color ramp should be installed into the plugin list.

- Plugins: Manage and Install Plugins
- Settings: tick “Show also experimental plugins”
- Install Color Ramp Manager
- Plugins: Color Ramp Manager
- Select Full cpt-city package, install cpt-city gradient files (Installation directory - QGIS user directory)

The color ramp will then be available within the properties menu.

Highlight merged .tif layer from step 1 in Layers Panel

- Properties: Style tab:
- Render type: singleband pseudocolor
- Generate new color map: New color ramp: cpt-city: humidity
- Min: -30
- Max: 0
- Classify
- Brightness: 20
- Contrast: 30
- Saturation: -20

Lastly, in order to view the full effect of the color ramp an additional hill shade can be applied.

- Raster: Analysis: DEM (Terrain)
- Input file: initial merged .tif layer
- Add an output name (.tif)
- Apply: Zevenberg & Thorne algorithm
- Azimuth of the light: 315
- Altitude of the light: 40
- A hill shade .tif will be added to the Layers Panel

Properties: Style tab:

- Min: 125
- Max: 200
- Blending mode: Multiply
- Brightness: 50
- Contrast: 20
- Transparency: 65%

# Appendix 3

Summary of fracture interactions and spacing data

**Summary of spacing data**

**Artillery Rocks**

| Coordinates | Fracture orientation and spacing (cm) between fractures | | | | |
|---|---|---|---|---|---|
| Location 1 | #1 | | #2 | | #3 |
| 0754385E | | | 60 | 60 | 324 |
| 5723369N | | | 525 | 50 | 542 |
| Zone 54H | | | 110 | 675 | 113 |
| | | | 15 | 344 | 18 |
| | | | 120 | 20 | |
| | | | 10 | 110 | |
| | | | 120 | 20 | |
| | | | 786 | | |
| **Average spacing (cm)** | N/A | | 201.67 | | 249.25 |
| **Standard deviation (cm)** | N/A | | 256.51 | | 233.33 |
| **CV** | N/A | | 1.27 | | 0.94 |

| Coordinates | Fracture orientation and spacing (cm) between fractures | | | | |
|---|---|---|---|---|---|
| Location 2 | #1 | | #2 | | #3 |
| 0754371E | | | 150 | | |
| 5723331N | | | 500 | | |
| Zone 54H | | | 25 | | |
| | | | 120 | | |
| | | | 260 | | |
| Average spacing (cm) | N/A | | 211 | | N/A |
| Standard deviation (cm) | N/A | | 182.02 | | N/A |
| CV | N/A | | 0.86 | | N/A |

| Coordinates | Fracture orientation and spacing (cm) between fractures | | | | |
|---|---|---|---|---|---|
| Location 3 | #1 | | #2 | | #3 |
| 0754364E | | | 20 | | 620 |
| 5723310N | | | 90 | | 400 |
| Zone 54H | | | 630 | | 10 |
| | | | 67 | | 10 |
| | | | 14 | | |
| **Average spacing (cm)** | N/A | | 164.2 | | 260 |
| **Standard deviation (cm)** | N/A | | 262.33 | | 302.32 |
| **CV** | N/A | | 1.6 | | 1.16 |

| Coordinates | Fracture orientation and spacing (cm) between fractures | | | | |
|---|---|---|---|---|---|
| Location 4 | #1 | | #2 | | #3 |
| 0754338E | | | 959 | 5 | |
| 5723276N | | | 20 | 1 | |
| Zone 54H | | | 2 | 4 | |
| | | | 7 | 2 | |
| **Average spacing (cm)** | N/A | | 125 | | N/A |
| **Standard deviation (cm)** | N/A | | 337.04 | | N/A |
| **CV** | N/A | | 2.7 | | N/A |

| Coordinates | Fracture orientation and spacing (cm) between fractures | | | | |
|---|---|---|---|---|---|
| Location 5 | #1 | | #2 | | #3 |
| 0754318E | | | 20 | 344 | |
| 5723259N | | | 50 | 550 | |
| Zone 54H | | | 2 | 20 | |
| | | | 2 | 6 | |
| | | | 4 | | |
| **Average spacing (cm)** | N/A | | 110.89 | | N/A |
| **Standard deviation (cm)** | N/A | | 197.97 | | N/A |
| **CV** | N/A | | 1.79 | | N/A |

| Coordinates | Fracture orientation and spacing (cm) between fractures | | | | |
|---|---|---|---|---|---|
| Location 6 | #1 | | #2 | | #3 |
| 0754318E | | | 2 | 280 | |
| 5723259N | | | 2 | 250 | |
| Zone 54H | | | 4 | 20 | |
| | | | 15 | 10 | |
| | | | 10 | 280 | |
| **Average spacing (cm)** | N/A | | 87.3 | | N/A |
| **Standard deviation (cm)** | N/A | | 126.46 | | N/A |
| **CV** | N/A | | 1.45 | | N/A |

**St. George Anticline**

| Coordinates | Fracture orientation and spacing (cm) between fractures | | | | |
|---|---|---|---|---|---|
| Location 1 | #1 | | #2 | | #3 |
| 0760011E | 16 | | 20 | 36 | 10 |
| 5728492N | 380 | | 60 | 60 | 200 |
| Zone 54H | 184 | | 13 | 4 | 50 |
| | 194 | | 138 | 6 | 60 |
| | 100 | | 138 | 82 | 70 |
| | 120 | | 30 | 8 | 80 |
| | | | 8 | 6 | 530 |
| | | | 4 | 120 | |
| | | | 50 | 19 | |
| | | | 50 | 30 | |
| | | | 118 | | |
| **Average spacing (cm)** | 165.67 | | 47.62 | | 142.86 |
| **Standard deviation (cm)** | 123.19 | | 45.81 | | 180.53 |
| **CV** | 0.74 | | 0.96 | | 1.26 |

| Coordinates | Fracture orientation and spacing (cm) between fractures | | | | |
|---|---|---|---|---|---|
| Location 2 | #1 | | #2 | | #3 |
| 0759928E | 60 | 16 | 410 | 60 | |
| 5728425N | 10 | 10 | 59 | 111 | |
| Zone 54H | 16 | 200 | 54 | 40 | |
| | 10 | 8 | 9 | 120 | |
| | 250 | 6 | 110 | | |
| | 30 | 12 | 25 | | |
| | 240 | 12 | | | |
| | 10 | | | | |
| **Average spacing (cm)** | 59.33 | | 99.8 | | N/A |
| **Standard deviation (cm)** | 89.88 | | 115.29 | | N/A |
| **CV** | 1.51 | | 1.16 | | N/A |

| Coordinates | Fracture orientation and spacing (cm) between fractures | | | | |
|---|---|---|---|---|---|
| Location 3 | #1 | | #2 | | #3 |
| 0759869E | 70 | 40 | 90 | 6 | |
| 5728373N | 84 | 50 | 74 | 3 | |
| Zone 54H | 40 | 40 | 4 | | |
| | 74 | 40 | 52 | | |
| | 50 | 50 | 180 | | |
| | 40 | 64 | 260 | | |
| | 60 | 66 | 20 | | |
| | 90 | 40 | 240 | | |

| | | | | | |
|---|---|---|---|---|---|
| | 30 | 10 | 10 | | |
| | 40 | | 6 | | |
| **Average spacing (cm)** | 51.47 | | 78.75 | | N/A |
| **Standard deviation (cm)** | 19.64 | | 95.37 | | N/A |
| **CV** | 0.38 | | 1.21 | | N/A |

| **Coordinates** | **Fracture orientation and spacing (cm) between fractures** | | | | | |
|---|---|---|---|---|---|---|
| Location 4 | #1 | | #2 | | #3 | |
| 0759746E | 20 | 60 | 40 | 3 | 10 | 2 |
| 5728344N | 30 | 10 | 30 | 120 | 5 | 130 |
| Zone 54H | 40 | 5 | 20 | 3 | 40 | |
| | 5 | 12 | 40 | 2 | 60 | |
| | 10 | 10 | 30 | 1 | 20 | |
| | 130 | | 20 | 2 | 30 | |
| | 50 | | 40 | 3 | 15 | |
| | 20 | | 30 | 2 | 26 | |
| | 60 | | 20 | 1 | 10 | |
| | 50 | | 40 | 102 | 5 | |
| | 30 | | 30 | 3 | 130 | |
| | 80 | | 20 | 2 | 100 | |
| | 30 | | 40 | 2 | 90 | |
| | 50 | | 30 | 3 | 120 | |
| | 30 | | 20 | 1 | 10 | |
| | 16 | | 140 | 2 | 30 | |
| | 110 | | 30 | 1 | 30 | |
| | 70 | | 20 | 3 | 40 | |
| **Average spacing (cm)** | 40.35 | | 24.89 | | 45.15 | |
| **Standard deviation (cm)** | 33.24 | | 32.94 | | 43.94 | |
| **CV** | 0.82 | | 1.32 | | 0.97 | |

| **Coordinates** | **Fracture orientation and spacing (cm) between fractures** | | | | |
|---|---|---|---|---|---|
| Location 5 | #1 | | #2 | | #3 |
| 0759672E | 40 | | 3 | 40 | 140 |
| 5728331N | 20 | | 4 | 3 | 10 |
| Zone 54H | 15 | | 2 | 3 | 12 |
| | 100 | | 10 | 5 | 158 |
| | 30 | | 5 | 5 | 336 |
| | 35 | | 26 | 10 | 180 |
| | 8 | | 40 | 2 | 145 |
| | 30 | | 10 | 16 | 10 |
| | 40 | | 3 | 5 | |
| | 22 | | 2 | 5 | |
| | 10 | | 5 | 30 | |
| | 47 | | 3 | 50 | |

| | | | | | |
|---|---|---|---|---|---|
| | 35 | | 10 | 40 | |
| | 25 | | 16 | 10 | |
| | 10 | | 5 | 2 | |
| | 103 | | 2 | 5 | |
| | 40 | | 30 | 26 | |
| | 20 | | 25 | 3 | |
| | 10 | | 50 | 10 | |
| | 40 | | 3 | 16 | |
| | 20 | | 4 | 3 | |
| | 10 | | 40 | 5 | |
| | 30 | | 5 | 10 | |
| | 30 | | 10 | 2 | |
| | 125 | | 26 | 5 | |
| | 15 | | 4 | 2 | |
| | | | 10 | 16 | |
| | | | 3 | 25 | |
| | | | 3 | 3 | |
| | | | 25 | 30 | |
| | | | 3 | 3 | |
| | | | 16 | 4 | |
| | | | 10 | 2 | |
| | | | 2 | 5 | |
| | | | 2 | 3 | |
| | | | 30 | 2 | |
| | | | 25 | 10 | |
| | | | 4 | 3 | |
| | | | 3 | 16 | |
| | | | 10 | 3 | |
| | | | 2 | 5 | |
| | | | 10 | 2 | |
| | | | 5 | 10 | |
| | | | 26 | | |
| **Average spacing (cm)** | 35 | | 11.34 | | 123.88 |
| **Standard deviation (cm)** | 29.84 | | 12.09 | | 112.42 |
| **CV** | 0.85 | | 1.07 | | 0.91 |

| **Coordinates** | **Fracture orientation and spacing (cm) between fractures** | | | | |
|---|---|---|---|---|---|
| Location 6 | #1 | | #2 | | #3 |
| 0759605E | 40 | 17 | 35 | 30 | |
| 5728339N | 50 | 29 | 30 | 16 | |
| Zone 54H | 40 | 41 | 20 | 19 | |
| | 30 | 51 | 20 | 30 | |
| | 30 | 39 | 15 | 15 | |
| | 15 | 15 | 30 | 20 | |

| | | | | | |
|---|---|---|---|---|---|
| | 38 | 31 | 20 | 20 | |
| | 52 | 29 | 20 | 15 | |
| | 39 | 41 | 30 | 31 | |
| | 31 | 49 | 34 | 35 | |
| | 32 | | 29 | 30 | |
| | 13 | | 21 | 20 | |
| | 50 | | 15 | 20 | |
| | 40 | | 20 | 30 | |
| | 30 | | 30 | 21 | |
| | 30 | | 20 | 19 | |
| | 40 | | 34 | 30 | |
| | 38 | | 31 | | |
| **Average spacing (cm)** | 35 | | 24.37 | | N/A |
| **Standard deviation (cm)** | 10.94 | | 6.58 | | N/A |
| **CV** | 0.31 | | 0.27 | | N/A |

| **Coordinates** | **Fracture orientation and spacing (cm) between fractures** | | | | |
|---|---|---|---|---|---|
| Location 7 | #1 | | #2 | | #3 |
| 0759488E | 100 | 200 | 100 | 20 | |
| 5728207N | 140 | 150 | 30 | 100 | |
| Zone 54H | 45 | 25 | 210 | 3 | |
| | 100 | | 250 | 20 | |
| | 100 | | 10 | 200 | |
| | 40 | | 3 | 50 | |
| **Average spacing (cm)** | 100 | | 83 | | N/A |
| **Standard deviation (cm)** | 57.39 | | 89.57 | | N/A |
| **CV** | 0.57 | | 1.08 | | N/A |

| **Coordinates** | **Fracture orientation and spacing (cm) between fractures** | | | | | |
|---|---|---|---|---|---|---|
| Location 8 | #1 | | #2 | | #3 | |
| 0759430E | 20 | 10 | 50 | | 10 | 4 |
| 5728146N | 20 | 15 | 60 | | 10 | 13 |
| Zone 54H | 10 | 15 | 40 | | 12 | 4 |
| | 15 | 10 | 50 | | 6 | 4 |
| | 5 | 5 | 45 | | 16 | 22 |
| | 10 | 60 | 54 | | 20 | 4 |
| | 3 | 8 | 40 | | 6 | 13 |
| | 4 | 10 | 20 | | 6 | 7 |
| | 8 | 4 | 30 | | 8 | 19 |
| | 8 | 4 | 30 | | 15 | 7 |
| | 10 | 11 | 35 | | 4 | 11 |
| | 5 | 6 | 40 | | 15 | 5 |
| | 8 | 10 | 40 | | 8 | 4 |
| | 4 | 6 | 21 | | 2 | 8 |

| | | | | | | |
|---|---|---|---|---|---|---|
| | 10 | 6 | 49 | | 2 | 21 |
| | 8 | 12 | 57 | | 10 | 3 |
| | 4 | 8 | 43 | | 15 | 11 |
| | 6 | 8 | 33 | | 3 | 13 |
| | 10 | 12 | 31 | | 6 | 7 |
| | 20 | 59 | 49 | | 20 | 11 |
| | 25 | 22 | 41 | | 10 | 17 |
| | 15 | 12 | 32 | | 18 | 11 |
| | 10 | 16 | 43 | | 3 | 24 |
| | 10 | 8 | 52 | | 10 | 11 |
| | 5 | 11 | | | 12 | 10 |
| | 8 | 8 | | | 3 | 2 |
| | 5 | 5 | | | 40 | 10 |
| | 12 | 10 | | | 10 | 3 |
| | 10 | 8 | | | 8 | 9 |
| | 11 | 14 | | | 2 | 8 |
| | 6 | 7 | | | 10 | 10 |
| | 9 | 9 | | | 8 | 11 |
| | 4 | 5 | | | 15 | 8 |
| | 7 | 7 | | | 8 | 3 |
| | 6 | 13 | | | 10 | 9 |
| | 5 | 5 | | | 10 | 11 |
| | 4 | 5 | | | 9 | 10 |
| | | | | | 10 | 6 |
| | | | | | 11 | 13 |
| | | | | | 10 | 13 |
| | | | | | 3 | 4 |
| | | | | | 4 | 5 |
| | | | | | 5 | 4 |
| | | | | | 4 | 6 |
| | | | | | 6 | 16 |
| | | | | | 24 | 10 |
| | | | | | 10 | 2 |
| | | | | | 2 | 40 |
| | | | | | 10 | 12 |
| | | | | | 20 | 10 |
| | | | | | 10 | 4 |
| **Average spacing (cm)** | 10.13 | | 41.04 | | 10.61 | |
| **Standard deviation (cm)** | 8.54 | | 10.61 | | 6.72 | |
| **CV** | 0.84 | | 0.26 | | 0.68 | |

| **Coordinates** | **Fracture orientation and spacing (cm) between fractures** | | | | | | |
|---|---|---|---|---|---|---|---|
| Location 9 | #1 | | | | #2 | | |
| 0759408E | 20 | 4 | 3 | 4 | 22 | 4 | 5 |
| 5728123N | 3 | 2 | 4 | 3 | 40 | 3 | 4 |

| | | | | | | | |
|---|---|---|---|---|---|---|---|
| Zone 54H | 2 | 3 | 2 | 4 | 33 | 6 | 6 |
| | 4 | 3 | 3 | 5 | 16 | 5 | 5 |
| | 5 | 4 | 5 | 4 | 32 | 4 | 4 |
| | 5 | 3 | 2 | 3 | 20 | 2 | 5 |
| | 2 | 3 | 2 | 4 | 4 | 2 | 6 |
| | 2 | 4 | 9 | 5 | 10 | 4 | 5 |
| | 2 | 3 | 1 | 6 | 23 | 3 | 4 |
| | 2 | 8 | 2 | 7 | 5 | 3 | 5 |
| | 2 | 3 | 14 | 6 | 20 | 5 | 6 |
| | 1 | 1 | 1 | 5 | 10 | 6 | 5 |
| | 2 | 3 | 2 | 6 | 10 | 5 | 4 |
| | 2 | 5 | 13 | 7 | 24 | 4 | 5 |
| | 7 | 4 | 2 | 6 | 10 | 5 | 6 |
| | 3 | 15 | 17 | 5 | 4 | 6 | 5 |
| | 1 | 2 | 1 | 6 | 10 | 5 | 6 |
| | 1 | 1 | 12 | 7 | 6 | 4 | 5 |
| | 1 | 3 | 1 | 6 | 20 | 5 | 6 |
| | 1 | 5 | 3 | 5 | 4 | 6 | 6 |
| | 1 | 7 | 4 | 4 | 4 | 6 | 6 |
| | 1 | 1 | 2 | 5 | 4 | 6 | 6 |
| | 6 | 2 | 1 | 6 | 5 | 6 | 5 |
| | 4 | 1 | 4 | 6 | 5 | 3 | 4 |
| | 10 | 2 | 3 | 6 | 6 | 4 | 5 |
| | 20 | 5 | 4 | 7 | 6 | 5 | 6 |
| | 30 | 1 | 3 | 6 | 5 | 5 | 5 |
| | 4 | 5 | 2 | 5 | 4 | 5 | 6 |
| | 5 | 3 | 5 | 4 | 5 | 5 | 4 |
| | 4 | 3 | 4 | 5 | 6 | 4 | 5 |
| | 3 | 4 | 1 | 3 | 5 | 9 | 4 |
| | 10 | 10 | 14 | 4 | 5 | 5 | 4 |
| | 20 | 1 | 13 | 1 | 6 | 3 | 5 |
| | 1 | 3 | 4 | 2 | 5 | 2 | 4 |
| | 1 | 7 | 1 | 1 | 6 | 5 | 15 |
| | 4 | 5 | 4 | 11 | 7 | 5 | 9 |
| | 4 | 3 | 1 | 1 | 7 | 3 | 9 |
| | 3 | 4 | 6 | 1 | 8 | 9 | 9 |
| | 1 | 1 | 1 | 5 | 7 | 1 | 5 |
| | 1 | 4 | 5 | 6 | 6 | 5 | 4 |
| | 1 | 14 | 3 | 1 | 3 | 1 | 6 |
| | 2 | 1 | 2 | 1 | 4 | 4 | 14 |
| | 3 | 20 | 3 | 3 | 4 | 6 | 5 |
| | 5 | 4 | 6 | 4 | 11 | 11 | 6 |
| | 4 | 1 | 4 | 5 | 4 | 4 | 4 |
| | 2 | 14 | 24 | 6 | 16 | 5 | 5 |
| | 2 | 13 | 1 | 1 | 11 | 5 | 4 |

| | | | | | | | |
|---|---|---|---|---|---|---|---|
| | 5 | 7 | 1 | 1 | 12 | 4 | 5 |
| | 1 | 11 | 1 | 1 | 5 | 5 | 4 |
| | 1 | 1 | 1 | 1 | 10 | 5 | 4 |
| | 1 | 2 | 5 | 2 | 3 | 6 | |
| | 1 | 1 | 1 | 4 | | | |
| | 1 | 1 | 6 | 1 | | | |
| | 1 | 12 | 1 | 2 | | | |
| | 4 | 1 | 4 | | | | |
| | 1 | 1 | 10 | | | | |
| | 1 | 1 | 20 | | | | |
| **Average spacing (cm)** | 4.41 | | | | 6.82 | | |
| **Standard deviation (cm)** | 4.79 | | | | 5.68 | | |
| **CV** | 1.08 | | | | 0.83 | | |

| **Coordinates** | **Fracture orientation and spacing (cm) between fractures** | | | | | | | |
|---|---|---|---|---|---|---|---|---|
| Location 10 | #1 | | | #2 | | | #3 | |
| 0759406E | 10 | 8 | 2 | 10 | 5 | 4 | 11 | 15 |
| 5728092N | 4 | 4 | 3 | 13 | 4 | 4 | 12 | 10 |
| Zone 54H | 20 | 8 | 2 | 12 | 6 | 6 | 13 | 10 |
| | 12 | 8 | 3 | 6 | 7 | 9 | 7 | 30 |
| | 15 | 3 | 1 | 6 | 12 | 9 | 5 | 30 |
| | 4 | 4 | 3 | 6 | 4 | 6 | 7 | 30 |
| | 15 | 5 | 7 | 6 | 7 | 8 | 4 | 45 |
| | 4 | 3 | 2 | 5 | 5 | 4 | 6 | 30 |
| | 5 | 5 | 3 | 4 | 7 | 6 | 6 | 25 |
| | 2 | 4 | 1 | 7 | 17 | 7 | 6 | 20 |
| | 2 | 4 | 3 | 5 | 6 | 5 | 7 | 30 |
| | 10 | 8 | 3 | 5 | 5 | 7 | 5 | 20 |
| | 10 | 8 | 1 | 6 | 9 | 7 | 5 | 25 |
| | 12 | 8 | 3 | 6 | 9 | 8 | 7 | 30 |
| | 10 | 6 | 1 | 6 | 3 | 7 | 6 | 35 |
| | 10 | 8 | 1 | 5 | 7 | 9 | 5 | 20 |
| | 8 | 8 | 4 | 7 | 10 | 8 | 4 | 20 |
| | 10 | 9 | 3 | 4 | 5 | 8 | 5 | 30 |
| | 12 | 2 | 2 | 3 | 7 | 5 | 4 | 30 |
| | 12 | 4 | 3 | 4 | 5 | 4 | 5 | 40 |
| | 15 | 2 | 4 | 4 | 12 | 7 | 5 | 45 |
| | 12 | 6 | 2 | 5 | 4 | 7 | 6 | 45 |
| | 14 | 6 | 2 | 3 | 5 | 12 | 4 | |
| | 8 | 3 | 3 | 3 | 6 | 1 | 4 | |
| | 4 | 3 | 4 | 4 | 4 | 1 | 3 | |
| | 4 | 4 | 3 | 5 | 6 | 9 | 4 | |
| | 5 | 5 | 2 | 5 | 2 | 9 | 5 | |

| | | | | | | | | |
|---|---|---|---|---|---|---|---|---|
| | 28 | 7 | 3 | 5 | 4 | 7 | 5 | |
| | 5 | 5 | 3 | 6 | 7 | 6 | 6 | |
| | 4 | 4 | 3 | 4 | 10 | 7 | 6 | |
| | 8 | 8 | 2 | 4 | 5 | 5 | 6 | |
| | 10 | 8 | 3 | 4 | 6 | 15 | 5 | |
| | 10 | 8 | 9 | 4 | 4 | 5 | 5 | |
| | 12 | 7 | 2 | 3 | 4 | 4 | 6 | |
| | 12 | 8 | 3 | 3 | 6 | 4 | 5 | |
| | 12 | 9 | 4 | 3 | 2 | 5 | 4 | |
| | 11 | 9 | 2 | 2 | 7 | 2 | 5 | |
| | 4 | 4 | 3 | 5 | 6 | 1 | 6 | |
| | 2 | 7 | 3 | 5 | 6 | 7 | 7 | |
| | 9 | 9 | 4 | 10 | 3 | 13 | 11 | |
| | 9 | 9 | 3 | 10 | 8 | 8 | 11 | |
| | 4 | 4 | 5 | 8 | 11 | 5 | 9 | |
| | 5 | 5 | 6 | 8 | 9 | 4 | 9 | |
| | 4 | 4 | 5 | 6 | 4 | 6 | 7 | |
| | 5 | 5 | 4 | 5 | 7 | 6 | 6 | |
| | 4 | 4 | 3 | 5 | 5 | 5 | 6 | |
| | 4 | 4 | 4 | 4 | 8 | 8 | 5 | |
| | 9 | 8 | 5 | 5 | 7 | 7 | 5 | |
| | 9 | 8 | 4 | 4 | 5 | 6 | 5 | |
| | 9 | 2 | 3 | 4 | 6 | 5 | 4 | |
| | 4 | 2 | 4 | 5 | 4 | 4 | 3 | |
| | 4 | 4 | 5 | 4 | 5 | 3 | 4 | |
| | 4 | 2 | 4 | 3 | 3 | 4 | 4 | |
| | 3 | 2 | 3 | 4 | 4 | 4 | 5 | |
| | 4 | 2 | 4 | 4 | 5 | 4 | 5 | |
| | 2 | 2 | 3 | 4 | 5 | | 5 | |
| | 3 | 4 | 4 | 2 | 1 | | 4 | |
| | 2 | 2 | 5 | 2 | 6 | | 3 | |
| | 4 | 4 | 4 | 2 | 4 | | 2 | |
| | 4 | 4 | 4 | 2 | 3 | | 1 | |
| **Average spacing (cm)** | 5.49 | | | 5.71 | | | 11.66 | |
| **Standard deviation (cm)** | 3.76 | | | 2.61 | | | 11.37 | |
| **CV** | 0.68 | | | 0.46 | | | 0.83 | |

| **Coordinates** | **Fracture orientation and spacing (cm) between fractures** | | | | |
|---|---|---|---|---|---|
| Location 11 | #1 | | #2 | | #3 |
| 0759386E | 18 | | 12 | 4 | 40 |
| 5728062N | 30 | | 15 | 10 | 35 |
| Zone 54H | 12 | | 8 | 20 | 45 |

| | | | | | |
|---|---|---|---|---|---|
| | 60 | | 26 | 2 | 42 |
| | 60 | | 6 | 5 | 150 |
| | 40 | | 4 | 9 | 20 |
| | 30 | | 6 | 8 | 25 |
| | 20 | | 4 | 11 | 41 |
| | 59 | | 4 | 6 | 39 |
| | 33 | | 6 | 4 | 42 |
| | 54 | | 15 | 6 | 43 |
| | 126 | | 20 | 4 | 33 |
| | 23 | | 10 | 4 | 34 |
| | 36 | | 26 | 10 | 35 |
| | 156 | | 40 | 9 | 32 |
| | 58 | | 20 | 4 | 40 |
| | 34 | | 10 | 6 | 42 |
| | 42 | | 15 | 13 | 35 |
| | 162 | | 2 | 5 | 37 |
| | 30 | | 15 | 9 | 33 |
| | | | 4 | 8 | 32 |
| | | | 4 | 11 | 40 |
| | | | 6 | 6 | 31 |
| | | | 12 | 4 | 30 |
| | | | 8 | 6 | 24 |
| | | | 2 | 4 | |
| | | | 2 | 3 | |
| | | | 4 | 6 | |
| | | | 6 | 9 | |
| | | | 12 | 3 | |
| | | | 8 | 8 | |
| | | | 2 | 11 | |
| | | | 2 | 6 | |
| | | | 4 | 4 | |
| | | | 6 | 5 | |
| | | | 8 | 4 | |
| | | | 15 | 10 | |
| | | | 12 | 6 | |
| | | | 40 | 9 | |
| | | | 14 | 13 | |
| | | | 25 | 6 | |
| | | | 12 | 5 | |
| | | | 3 | 3 | |
| | | | 22 | 4 | |
| | | | 8 | 5 | |
| | | | 15 | 6 | |
| | | | 3 | 7 | |
| | | | 8 | 15 | |

| | | | | | |
|---|---|---|---|---|---|
| | | | 10 | 30 | |
| | | | 4 | 25 | |
| | | | 32 | | |
| **Average spacing (cm)** | 54.15 | | 9.58 | | 40 |
| **Standard deviation (cm)** | 43.39 | | 7.75 | | 23.76 |
| **CV** | 0.8 | | 0.81 | | 0.59 |

| **Coordinates** | **Fracture orientation and spacing (cm) between fractures** | | | | | | |
|---|---|---|---|---|---|---|---|
| Location 12 | #1 | | #2 | | | | #3 |
| 0759355E | 45 | | 2 | 2 | 10 | 2 | 40 |
| 5728001N | 30 | | 2 | 1 | 2 | 1 | 20 |
| Zone 54H | 44 | | 2 | 2 | 11 | 3 | 60 |
| | 74 | | 10 | 1 | 9 | 1 | 25 |
| | 5 | | 2 | 2 | 2 | 3 | 42 |
| | 44 | | 2 | 1 | 3 | 3 | 47 |
| | 35 | | 4 | 3 | 2 | 18 | 22 |
| | 50 | | 16 | 3 | 17 | 2 | 17 |
| | 50 | | 5 | 3 | 4 | 2 | 31 |
| | 40 | | 4 | 3 | 5 | 2 | 99 |
| | 50 | | 12 | 2 | 14 | 2 | |
| | 30 | | 24 | 2 | 22 | 1 | |
| | 40 | | 10 | 2 | 12 | 4 | |
| | 32 | | 2 | 2 | 3 | 2 | |
| | 49 | | 4 | 2 | 3 | 8 | |
| | 51 | | 8 | 1 | 2 | 18 | |
| | 36 | | 20 | 2 | 2 | 3 | |
| | 43 | | 10 | 3 | 3 | 2 | |
| | 8 | | 2 | 2 | 32 | 3 | |
| | 74 | | 3 | 2 | 1 | 3 | |
| | 32 | | 2 | 3 | 1 | 1 | |
| | 6 | | 2 | 2 | 3 | 10 | |
| | 41 | | 1 | 2 | 1 | 12 | |
| | 40 | | 3 | 2 | 3 | 10 | |
| | | | 3 | 4 | 2 | 10 | |
| | | | 2 | 3 | 3 | 2 | |
| | | | 45 | 2 | 2 | 10 | |
| | | | 2 | 3 | 1 | 1 | |
| | | | 2 | 4 | 2 | 2 | |
| | | | 56 | 2 | 1 | 3 | |
| | | | 2 | 1 | 2 | 2 | |
| | | | 2 | 2 | 3 | 1 | |
| | | | 50 | 3 | 18 | 2 | |
| | | | 3 | 2 | 16 | 3 | |
| | | | 2 | 3 | 2 | 1 | |
| | | | 3 | 3 | 1 | 2 | |

| | | | | | | | |
|---|---|---|---|---|---|---|---|
| | | | 1 | 2 | 2 | 3 | |
| | | | 1 | 3 | 3 | 10 | |
| | | | 2 | 1 | 3 | 3 | |
| | | | 10 | 3 | 2 | 3 | |
| | | | 2 | 2 | 3 | 3 | |
| | | | 1 | 10 | 2 | 30 | |
| | | | 3 | 2 | 3 | 1 | |
| | | | 3 | 3 | 2 | 1 | |
| | | | 3 | 3 | 3 | 1 | |
| | | | 2 | 3 | 2 | 1 | |
| | | | 2 | 2 | 3 | 1 | |
| | | | 1 | 2 | 1 | 2 | |
| | | | 2 | 2 | 2 | | |
| | | | 3 | 2 | 1 | | |
| | | | 10 | 2 | 2 | | |
| | | | 3 | 32 | 2 | | |
| **Average spacing (cm)** | 39.54 | | 4.9 | | | | 40.3 |
| **Standard deviation (cm)** | 17 | | 7.71 | | | | 24.7 |
| **CV** | 0.43 | | 1.58 | | | | 0.61 |

| **Coordinates** | **Fracture orientation and spacing (cm) between fractures** | | | | |
|---|---|---|---|---|---|
| Location 13 | #1 | | #2 | | #3 |
| 0759350E | 30 | 60 | 90 | 20 | 40 |
| 5727906N | 20 | 70 | 60 | 30 | 30 |
| Zone 54H | 10 | 76 | 40 | 15 | 120 |
| | 20 | 70 | 10 | 29 | 140 |
| | 20 | 60 | 40 | 24 | 40 |
| | 16 | 58 | 30 | 30 | 100 |
| | 10 | 68 | 10 | 5 | 121 |
| | 10 | 26 | 10 | 10 | 39 |
| | 30 | 32 | 30 | 30 | 31 |
| | 5 | 35 | 4 | 15 | 42 |
| | 5 | | 10 | 10 | 98 |
| | 10 | | 40 | 15 | 138 |
| | 10 | | 50 | 10 | |
| | 40 | | 100 | 10 | |
| | 20 | | 30 | 10 | |
| | 10 | | 10 | 10 | |
| | 40 | | 10 | | |
| | 40 | | 110 | | |
| | 60 | | 40 | | |
| **Average spacing (cm)** | 33.14 | | 28.49 | | 78.25 |
| **Standard deviation (cm)** | 22.8 | | 26.25 | | 44.88 |
| **CV** | 0.69 | | 0.92 | | 0.57 |

| Coordinates | Fracture orientation and spacing (cm) between fractures | | | | |
|---|---|---|---|---|---|
| Location 14 | #1 | | #2 | | #3 |
| 0759382E | 20 | 7 | 10 | 4 | 50 |
| 5727833N | 10 | 1 | 15 | 4 | 42 |
| Zone 54H | 5 | 15 | 4 | 16 | 40 |
| | 10 | 4 | 15 | 16 | 56 |
| | 10 | 19 | 18 | 8 | 5 |
| | 4 | 11 | 6 | 6 | 3 |
| | 20 | 16 | 10 | 18 | 47 |
| | 10 | 13 | 10 | 8 | 58 |
| | 16 | 24 | 8 | 11 | 6 |
| | 1 | 10 | 14 | 4 | 30 |
| | 6 | 23 | 4 | 4 | 89 |
| | 1 | 2 | 4 | 15 | 63 |
| | 21 | 14 | 4 | 4 | 3 |
| | 3 | 10 | 16 | 11 | 54 |
| | 13 | 6 | 12 | 15 | 134 |
| | 15 | 10 | 5 | 18 | 65 |
| | 4 | 24 | 17 | 15 | 123 |
| | 12 | 4 | 16 | 11 | |
| | 2 | 19 | 9 | 6 | |
| | 11 | 2 | 8 | 14 | |
| | 21 | 16 | 11 | 8 | |
| | 3 | 11 | 5 | 11 | |
| | 13 | 5 | 4 | 4 | |
| | 10 | 10 | 13 | 9 | |
| | 6 | 19 | 5 | 4 | |
| | 10 | 4 | 15 | 5 | |
| | 22 | 14 | 8 | 15 | |
| | 4 | 1 | 6 | 15 | |
| | 18 | 16 | 16 | 6 | |
| | 2 | 9 | 15 | 11 | |
| | 17 | 6 | 9 | 17 | |
| | 11 | 11 | 10 | 8 | |
| | 5 | 5 | 9 | 9 | |
| | 10 | 4 | 4 | 4 | |
| | 20 | 12 | 3 | 4 | |
| | 4 | 10 | 12 | 15 | |
| | 12 | 16 | 14 | 15 | |
| | 1 | 1 | 16 | 10 | |
| | 17 | 18 | 4 | 17 | |
| | 10 | 12 | 10 | 4 | |
| | 5 | | 11 | 15 | |
| | 11 | | 6 | 11 | |
| | 24 | | 18 | 10 | |

| | | | | | |
|---|---|---|---|---|---|
| | 4 | | 15 | 6 | |
| | 11 | | 8 | 15 | |
| | 12 | | 10 | 4 | |
| | 16 | | 11 | 4 | |
| | 11 | | 4 | 7 | |
| | 20 | | 10 | 8 | |
| | 9 | | 8 | 8 | |
| **Average spacing (cm)** | 10.74 | | 9.88 | | 51.06 |
| **Standard deviation (cm)** | 6.43 | | 4.58 | | 38.2 |
| **CV** | 0.6 | | 0.46 | | 0.75 |

| **Coordinates** | **Fracture orientation and spacing (cm) between fractures** | | | | | |
|---|---|---|---|---|---|---|
| Location 15 | #1 | | #2 | | | #3 |
| 0759423E | 25 | 23 | 5 | 6 | 14 | |
| 5727751N | 15 | 13 | 5 | 6 | 7 | |
| Zone 54H | 10 | 10 | 10 | 15 | 7 | |
| | 10 | 9 | 4 | 8 | 13 | |
| | 10 | 11 | 5 | 6 | 7 | |
| | 10 | 10 | 5 | 5 | 7 | |
| | 23 | 10 | 4 | 8 | 4 | |
| | 18 | 10 | 3 | 6 | 4 | |
| | 10 | 10 | 3 | 7 | 10 | |
| | 12 | 10 | 10 | 6 | 7 | |
| | 25 | 15 | 10 | 7 | 6 | |
| | 10 | 10 | 5 | 5 | 8 | |
| | 11 | 25 | 5 | 14 | 6 | |
| | 10 | 15 | 5 | 4 | 5 | |
| | 15 | 25 | 11 | 7 | 7 | |
| | 9 | 10 | 6 | 8 | 6 | |
| | 11 | 11 | 10 | 8 | 6 | |
| | 24 | 10 | 6 | 5 | 8 | |
| | 11 | 24 | 4 | 5 | 7 | |
| | 10 | 16 | 7 | 10 | 5 | |
| | 15 | 10 | 6 | 7 | 7 | |
| | 100 | 9 | 9 | 6 | 4 | |
| | 10 | 10 | 5 | 7 | 8 | |
| | 25 | 12 | 5 | 4 | 4 | |
| | 9 | 13 | 6 | 7 | 8 | |
| | 16 | 11 | 8 | 7 | 7 | |
| | 10 | 14 | 4 | 6 | 7 | |
| | 11 | 13 | 11 | 8 | 8 | |
| | 10 | 9 | 8 | 14 | 6 | |
| | 9 | 10 | 9 | 7 | 9 | |
| | 10 | | 6 | 4 | 8 | |
| | 10 | | 7 | 6 | 7 | |

| | | | | | | |
|---|---|---|---|---|---|---|
| | 11 | | 6 | 5 | 5 | |
| | 22 | | 6 | 7 | 7 | |
| | 17 | | 6 | 5 | 4 | |
| | 10 | | 13 | 5 | 10 | |
| | 12 | | 7 | 4 | 4 | |
| | 10 | | 9 | 4 | 8 | |
| | 12 | | 13 | 10 | 7 | |
| | | | 7 | 6 | 8 | |
| | | | 7 | 6 | 5 | |
| | | | 4 | 6 | 6 | |
| | | | 10 | 4 | 5 | |
| | | | 10 | 6 | 5 | |
| **Average spacing (cm)** | 14.43 | | 6.84 | | | N/A |
| **Standard deviation (cm)** | 11.58 | | 2.42 | | | N/A |
| **CV** | 0.8 | | 0.35 | | | N/A |

**Soapy Rocks**

| **Coordinates** | **Fracture orientation and spacing (cm) between fractures** | | | | | |
|---|---|---|---|---|---|---|
| Location 1 | #1 | | #2 | | #3 | |
| (Northern Area) | | | 23 | 36 | 20 | 16 |
| 0253826E | | | 26 | 34 | 16 | 20 |
| 5743712N | | | 34 | 23 | 14 | 21 |
| Zone 55H | | | 35 | 27 | 14 | 12 |
| | | | 16 | 12 | 17 | 20 |
| | | | 21 | 14 | 17 | 20 |
| | | | 28 | 26 | 26 | 12 |
| | | | 32 | | 26 | 19 |
| | | | 35 | | 20 | 14 |
| | | | 10 | | 12 | 15 |
| | | | 26 | | 30 | 30 |
| | | | 24 | | 22 | 12 |
| | | | 34 | | 20 | |
| **Average spacing (cm)** | N/A | | 25.8 | | 18.6 | |
| **Standard deviation (cm)** | N/A | | 8.07 | | 5.28 | |
| **CV** | N/A | | 0.31 | | 0.28 | |

| **Coordinates** | **Fracture orientation and spacing (cm) between fractures** | | | | | |
|---|---|---|---|---|---|---|
| Location 2 | #1 | | #2 | | #3 | |
| (Southern Area) | | | 40 | 44 | 80 | 16 |
| 0253799E | | | 50 | 44 | 400 | 20 |
| 5743684N | | | 70 | 45 | 90 | 21 |

| | | | | | | |
|---|---|---|---|---|---|---|
| Zone 55H | | | 300 | 42 | 76 | 12 |
| | | | 40 | 30 | 85 | 20 |
| | | | 45 | 20 | 100 | |
| | | | 30 | 18 | 90 | |
| | | | 42 | | 40 | |
| | | | 51 | | 82 | |
| | | | 44 | | 40 | |
| | | | 43 | | 20 | |
| **Average spacing (cm)** | N/A | | 25.8 | | 18.6 | |
| **Standard deviation (cm)** | N/A | | 8.07 | | 5.28 | |
| **CV** | N/A | | 0.31 | | 0.28 | |

**Summary of fracture relationships**

The following tables contain the data used to construct illustrated diagrams of the cross-cutting, abutting and fracture offset relationships measured in each sampling area, along coastal platforms between southern Artillery Rocks and Anglesea.

**Southern Artillery Rocks (Zone 54H)**

| **Location 1** | **Fracture characteristics** | | | |
|---|---|---|---|---|
| 0754385E | | | | |
| 5723369N | | | | |
| **Fractures interacting** | **#3-#2** | **%** | **#2-#3** | **%** |
| **Abuts** | 2 | 40 | 1 | 25 |
| **Cross-cuts** | 0 | 0 | 0 | 0 |
| **Offsets** | 0 | 0 | 2 | 50 |
| **Ambiguous** | 3 | 60 | 1 | 25 |

| **Location 3** | **Fracture characteristics** | |
|---|---|---|
| 0754364E | | |
| 5723310N | | |
| **Fractures interacting** | **#3-#2** | **%** |
| **Abuts** | 5 | 83.3 |
| **Cross-cuts** | 0 | 0 |
| **Offsets** | 0 | 0 |
| **Ambiguous** | 1 | 16.7 |

| **Location 4** | **Fracture characteristics** | |
|---|---|---|
| 0754338E | | |
| 5723276N | | |
| **Fractures interacting** | **#3-#2** | **%** |
| **Abuts** | 2 | 100 |
| **Cross-cuts** | 0 | 0 |
| **Offsets** | 0 | 0 |
| **Ambiguous** | 0 | 0 |

| **Location 5** | **Fracture characteristics** | | | | |
|---|---|---|---|---|---|
| 0754318E | | | | | |
| 5723259N | | | | | |
| **Fractures interacting** | **#3-#2** | **%** | **#1-#2** | **%** | **#3-#2** |
| **Abuts** | 1 | 100 | 2 | 100 | 1 |
| **Cross-cuts** | 0 | 0 | 0 | 0 | 0 |
| **Offsets** | 0 | 0 | 0 | 0 | 0 |
| **Ambiguous** | 0 | 0 | 0 | 0 | 0 |

| Location 6 | Fracture characteristics | |
|---|---|---|
| 0754318E | | |
| 5723259N | | |
| **Fractures interacting** | **#1-#2** | **%** |
| **Abuts** | 1 | 100 |
| **Cross-cuts** | 0 | 0 |
| **Offsets** | 0 | 0 |
| **Ambiguous** | 0 | 0 |

**St. George Anticline (Zone 54H)**

| Location 1 | Fracture characteristics | | | | | | | |
|---|---|---|---|---|---|---|---|---|
| 0760011E | | | | | | | | |
| 5728492N | | | | | | | | |
| **Fractures interacting** | **#1-#2** | **%** | **#2-#1** | **%** | **#3-#1** | **%** | **#3-#2** | **%** |
| **Abuts** | 8 | 47.1 | 1 | 10 | 5 | 62.5 | 5 | 62.5 |
| **Cross-cuts** | 5 | 29.4 | 5 | 50 | 0 | 0 | 0 | 0 |
| **Offsets** | 0 | 0 | 0 | 0 | 0 | 0 | 0 | 0 |
| **Ambiguous** | 4 | 23.5 | 4 | 40 | 3 | 37.5 | 3 | 37.5 |
| **Fractures interacting** | **#1-#3** | **%** | **#2-#3** | **%** | | | | |
| **Abuts** | 2 | 10 | 1 | 5 | | | | |
| **Cross-cuts** | 10 | 50 | 10 | 55 | | | | |
| **Offsets** | 0 | 0 | 0 | 0 | | | | |
| **Ambiguous** | 8 | 40 | 9 | 45 | | | | |

| Location 2 | Fracture characteristics | | | | | | | |
|---|---|---|---|---|---|---|---|---|
| 0759928E | | | | | | | | |
| 5728425N | | | | | | | | |
| **Fractures interacting** | **#1-#2** | **%** | **#2-#1** | **%** | **#3-#1** | **%** | **#3-#2** | **%** |
| **Abuts** | 7 | 38.9 | 2 | 15.4 | 4 | 66.7 | 1 | 33.3 |
| **Cross-cuts** | 5 | 27.8 | 5 | 38.5 | 0 | 0 | 0 | 0 |
| **Offsets** | 0 | 0 | 0 | 0 | 0 | 0 | 0 | 0 |
| **Ambiguous** | 6 | 33.3 | 6 | 46.2 | 2 | 33.3 | 2 | 66.7 |

| Location 3 | Fracture characteristics | | | | | | | |
|---|---|---|---|---|---|---|---|---|
| 0759869E | | | | | | | | |
| 5728373N | | | | | | | | |
| **Fractures interacting** | **#1-#2** | **%** | **#2-#1** | **%** | **#3-#1** | **%** | **#3-#2** | **%** |
| **Abuts** | 4 | 50 | 1 | 20 | 1 | 33.3 | 0 | 0 |
| **Cross-cuts** | 2 | 25 | 2 | 40 | 0 | 0 | 0 | 0 |
| **Offsets** | 0 | 0 | 0 | 0 | 0 | 0 | 0 | 0 |
| **Ambiguous** | 2 | 25 | 2 | 40 | 2 | 66.7 | 2 | 100 |

| Location 4 | Fracture characteristics | | | | | | | |
|---|---|---|---|---|---|---|---|---|
| 0759746E | | | | | | | | |
| 5728344N | | | | | | | | |
| **Fractures interacting** | **#1-#2** | **%** | **#2-#1** | **%** | **#3-#1** | **%** | **#3-#2** | **%** |
| **Abuts** | 7 | 50 | 1 | 6.7 | 3 | 42.9 | 1 | 33.3 |
| **Cross-cuts** | 3 | 21.4 | 3 | 20 | 0 | 0 | 1 | 33.3 |
| **Offsets** | 0 | 0 | 7 | 46.7 | 4 | 57.1 | 0 | 0 |
| **Ambiguous** | 4 | 28.6 | 4 | 26.7 | 0 | 0 | 1 | 33.3 |

| Location 5 | Fracture characteristics | | | | | | | |
|---|---|---|---|---|---|---|---|---|
| 0759672E | | | | | | | | |
| 5728331N | | | | | | | | |
| **Fractures interacting** | **#1-#2** | **%** | **#2-#1** | **%** | **#3-#1** | **%** | **#3-#2** | **%** |
| **Abuts** | 3 | 21.4 | 0 | 0 | 3 | 27.3 | 3 | 37.5 |
| **Cross-cuts** | 6 | 42.9 | 6 | 40 | 0 | 0 | 1 | 12.5 |
| **Offsets** | 0 | 0 | 4 | 26.7 | 5 | 45.5 | 0 | 0 |
| **Ambiguous** | 5 | 35.7 | 5 | 33.3 | 3 | 27.3 | 4 | 50 |

| Location 6 | Fracture characteristics | | | | | | | |
|---|---|---|---|---|---|---|---|---|
| 0759605E | | | | | | | | |
| 5728339N | | | | | | | | |
| **Fractures interacting** | **#1-#2** | **%** | **#2-#1** | **%** | **#3-#1** | **%** | **#3-#2** | **%** |
| **Abuts** | 7 | 58.3 | 0 | 0 | 0 | 0 | 0 | 0 |
| **Cross-cuts** | 2 | 16.7 | 2 | 40 | 0 | 0 | 0 | 0 |
| **Offsets** | 0 | 0 | 0 | 0 | 0 | 0 | 0 | 0 |
| **Ambiguous** | 3 | 25 | 3 | 60 | 0 | 0 | 0 | 0 |

| Location 7 | Fracture characteristics | | | | | | | |
|---|---|---|---|---|---|---|---|---|
| 0759488E | | | | | | | | |
| 5728207N | | | | | | | | |
| **Fractures interacting** | **#1-#2** | **%** | **#2-#1** | **%** | **#3-#1** | **%** | **#3-#2** | **%** |
| **Abuts** | 3 | 33.3 | 0 | 0 | 4 | 66.7 | 1 | 50 |
| **Cross-cuts** | 1 | 11.1 | 1 | 16.7 | 0 | 0 | 0 | 0 |
| **Offsets** | 0 | 0 | 0 | 0 | 0 | 0 | 0 | 0 |
| **Ambiguous** | 5 | 55.6 | 5 | 83.3 | 2 | 33.3 | 1 | 50 |

| Location 8 | Fracture characteristics | | | | | | | |
|---|---|---|---|---|---|---|---|---|
| 0759430E | | | | | | | | |
| 5728146N | | | | | | | | |
| **Fractures interacting** | **#1-#2** | **%** | **#2-#1** | **%** | **#3-#1** | **%** | **#3-#2** | **%** |
| **Abuts** | 10 | 45.5 | 0 | 0 | 2 | 20 | 1 | 14.3 |
| **Cross-cuts** | 2 | 9.1 | 2 | 16.7 | 2 | 20 | 2 | 28.6 |
| **Offsets** | 0 | 0 | 0 | 0 | 0 | 0 | 0 | 0 |
| **Ambiguous** | 10 | 45.5 | 10 | 83.3 | 6 | 60 | 4 | 57.1 |

| Location 9 | Fracture characteristics | | | | | | | |
|---|---|---|---|---|---|---|---|---|
| 0759408E | | | | | | | | |
| 5728123N | | | | | | | | |
| **Fractures interacting** | **#1-#2** | **%** | **#2-#1** | **%** | **#3-#1** | **%** | **#1-#3** | **%** |
| **Abuts** | 0 | 0 | 16 | 40 | 8 | 25.8 | 0 | 0 |
| **Cross-cuts** | 12 | 50 | 12 | 30 | 13 | 41.9 | 13 | 50 |
| **Offsets** | 0 | 0 | 0 | 0 | 0 | 0 | 0 | 0 |
| **Ambiguous** | 12 | 50 | 12 | 30 | 10 | 32.3 | 13 | 50 |

| Location 10 | Fracture characteristics | | | | | | | |
|---|---|---|---|---|---|---|---|---|
| 0759406E | | | | | | | | |
| 5728092N | | | | | | | | |
| **Fractures interacting** | **#1-#2** | **%** | **#2-#1** | **%** | **#3-#1** | **%** | **#1-#3** | **%** |
| **Abuts** | 50 | 50.5 | 5 | 9.3 | 20 | 33.9 | 2 | 4.9 |
| **Cross-cuts** | 32 | 32.3 | 32 | 59.3 | 24 | 40.7 | 24 | 58.5 |
| **Offsets** | 0 | 0 | 0 | 0 | 0 | 0 | 0 | 0 |
| **Ambiguous** | 17 | 17.2 | 17 | 31.5 | 15 | 25.4 | 15 | 36.6 |
| **Fractures interacting** | **#2-#3** | **%** | **#3-#2** | **%** | | | | |
| **Abuts** | 0 | 0 | 2 | 5.8 | | | | |
| **Cross-cuts** | 18 | 45 | 21 | 61.7 | | | | |
| **Offsets** | 0 | 0 | 0 | 0 | | | | |
| **Ambiguous** | 22 | 55 | 11 | 32.5 | | | | |

| Location 11 | Fracture characteristics | | | | | | | |
|---|---|---|---|---|---|---|---|---|
| 0759386E | | | | | | | | |
| 5728062N | | | | | | | | |
| **Fractures interacting** | **#1-#2** | **%** | **#2-#1** | **%** | **#3-#1** | **%** | **#1-#3** | **%** |
| **Abuts** | 4 | 22.2 | 1 | 6.7 | 8 | 50 | 1 | 11.1 |
| **Cross-cuts** | 8 | 44.4 | 8 | 53.3 | 4 | 25 | 4 | 44.4 |
| **Offsets** | 0 | 0 | 0 | 0 | 0 | 0 | 0 | 0 |
| **Ambiguous** | 6 | 33.3 | 6 | 40 | 4 | 25 | 4 | 44.4 |

| Location 12 | Fracture characteristics | | | | | | | |
|---|---|---|---|---|---|---|---|---|
| 0759355E | | | | | | | | |
| 5728001N | | | | | | | | |
| **Fractures interacting** | **#1-#2** | **%** | **#2-#1** | **%** | **#3-#1** | **%** | **#1-#3** | **%** |
| **Abuts** | 10 | 47.6 | 0 | 0 | 4 | 30.8 | 1 | 11.1 |
| **Cross-cuts** | 1 | 4.8 | 1 | 7.1 | 2 | 15.4 | 2 | 22.2 |
| **Offsets** | 0 | 0 | 3 | 21.4 | 1 | 7.7 | 0 | 0 |
| **Ambiguous** | 10 | 47.6 | 10 | 71.4 | 6 | 46.2 | 6 | 66.7 |

| Location 13 | Fracture characteristics | | | | | | | |
|---|---|---|---|---|---|---|---|---|
| 0759350E | | | | | | | | |
| 5727906N | | | | | | | | |
| **Fractures interacting** | **#1-#2** | **%** | **#2-#1** | **%** | **#3-#1** | **%** | **#1-#3** | **%** |
| **Abuts** | 8 | 22.2 | 0 | 0 | 6 | 46.2 | 0 | 0 |
| **Cross-cuts** | 6 | 16.7 | 8 | 25 | 1 | 7.7 | 1 | 14.3 |
| **Offsets** | 0 | 0 | 2 | 6.3 | 0 | 0 | 0 | 0 |
| **Ambiguous** | 22 | 61.1 | 22 | 68.8 | 6 | 46.2 | 6 | 85.7 |
| **Fractures interacting** | **#3-#2** | **%** | **#1-#3** | **%** | | | | |
| **Abuts** | 0 | 0 | 0 | 0 | | | | |
| **Cross-cuts** | 2 | 20 | 3 | 25 | | | | |
| **Offsets** | 0 | 0 | 0 | 0 | | | | |
| **Ambiguous** | 8 | 80 | 9 | 75 | | | | |

| Location 14 | Fracture characteristics | | | | | | | |
|---|---|---|---|---|---|---|---|---|
| 0759382E | | | | | | | | |
| 5727833N | | | | | | | | |
| **Fractures interacting** | **#1-#2** | **%** | **#2-#1** | **%** | **#3-#1** | **%** | **#1-#3** | **%** |
| **Abuts** | 9 | 40.9 | 1 | 7.1 | 3 | 25 | 0 | 0 |
| **Cross-cuts** | 5 | 22.7 | 5 | 35.7 | 2 | 16.7 | 2 | 22.2 |
| **Offsets** | 0 | 0 | 0 | 0 | 0 | 0 | 0 | 0 |
| **Ambiguous** | 8 | 36.4 | 8 | 57.1 | 7 | 58.3 | 7 | 77.8 |

| Location 15 | Fracture characteristics | | | | | | | |
|---|---|---|---|---|---|---|---|---|
| 0759423E | | | | | | | | |
| 5727751N | | | | | | | | |
| **Fractures interacting** | **#1-#2** | **%** | **#2-#1** | **%** | **#3-#1** | **%** | **#1-#3** | **%** |
| **Abuts** | 4 | 23.5 | 0 | 0 | 4 | 33.3 | 0 | 0 |
| **Cross-cuts** | 2 | 11.8 | 2 | 15.4 | 2 | 16.7 | 2 | 25 |
| **Offsets** | 0 | 0 | 0 | 0 | 0 | 0 | 0 | 0 |
| **Ambiguous** | 11 | 64.7 | 11 | 84.6 | 6 | 50 | 6 | 75 |

**Soapy Rocks (Zone 55H)**

| **Location 1** (Northern Area) | **Fracture characteristics** | | | |
|---|---|---|---|---|
| 0253826E | | | | |
| 5743712N | | | | |
| **Fractures interacting** | **#3-#2** | **%** | **#2-#3** | **%** |
| **Abuts** | 0 | 0 | 13 | 81.3 |
| **Cross-cuts** | 0 | 0 | 0 | 0 |
| **Offsets** | 0 | 0 | 0 | 0 |
| **Ambiguous** | 3 | 100 | 3 | 18.8 |

| **Location 2** (Southern Area) | **Fracture characteristics** | | | |
|---|---|---|---|---|
| 0253799E | | | | |
| 5743684N | | | | |
| **Fractures interacting** | **#3-#2** | **%** | **#2-#3** | **%** |
| **Abuts** | 0 | 0 | 0 | 0 |
| **Cross-cuts** | 3 | 37.5 | 3 | 42.9 |
| **Offsets** | 1 | 12.5 | 0 | 0 |
| **Ambiguous** | 4 | 50 | 4 | 57.1 |

| **Combined** | **Fracture characteristics** | | | |
|---|---|---|---|---|
| **Fractures interacting** | **#3-#2** | **%** | **#2-#3** | **%** |
| **Abuts** | 0 | 0 | 13 | 0 |
| **Cross-cuts** | 3 | 27.2 | 3 | 42.9 |
| **Offsets** | 1 | 0.9 | 0 | 0 |
| **Ambiguous** | 7 | 63.6 | 7 | 57.1 |

# Appendix 4

Interpreted deformation history of the eastern Otway coastline

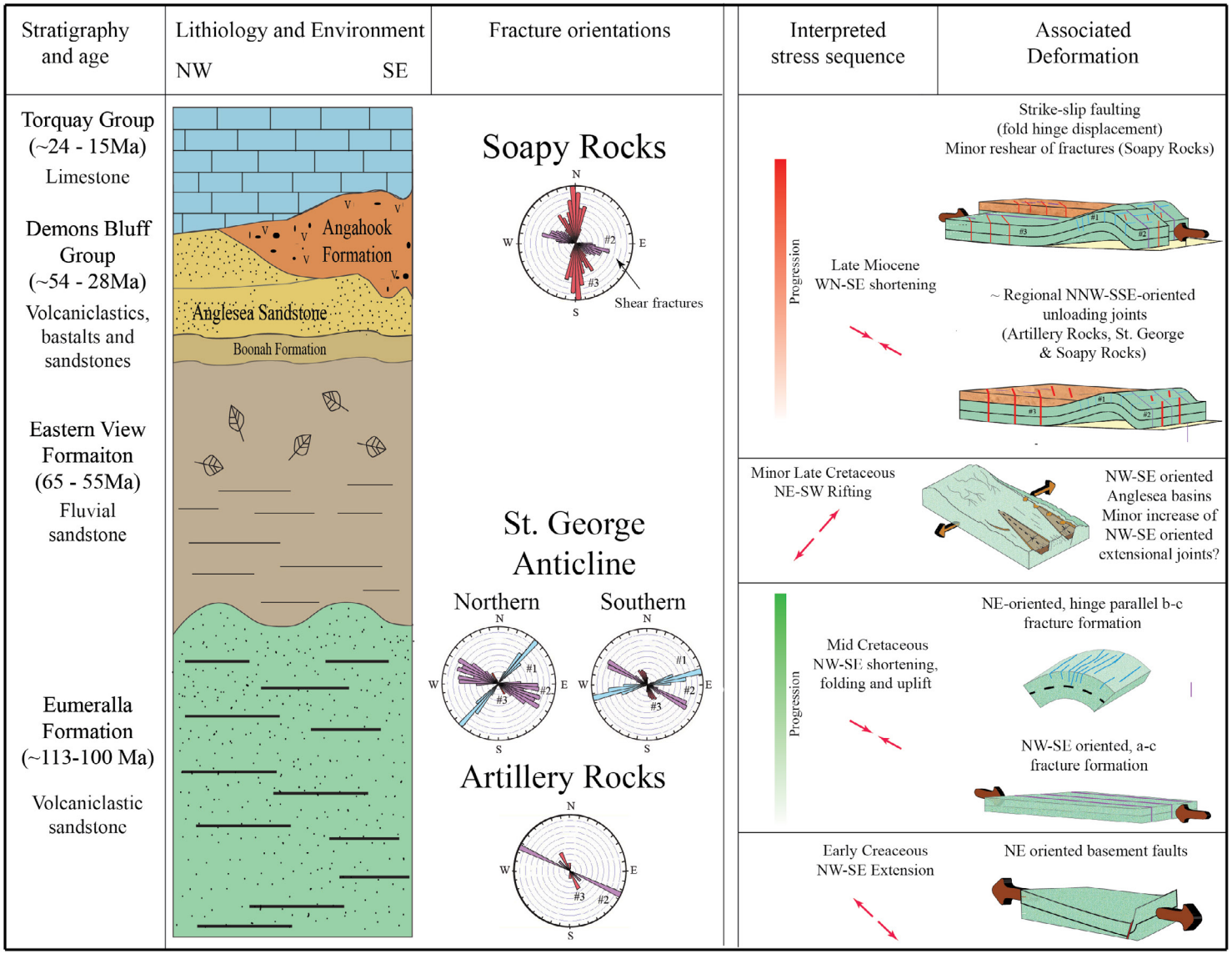


Interpreted deformation history of the eastern Otway coastline based on fold and fracture orientations. Red arrows indicate the orientation of the interpreted maximum principal stress. The stratigraphy of the eastern Otway Basin is modified from Abele et al. (1988) and McLaren et al. (2009).

# Map Pocket 1

Bedding formline maps of the Eastern View to southern Lorne coastline and cross-sections of the Aireys Inlet to northern Anglesea coastline

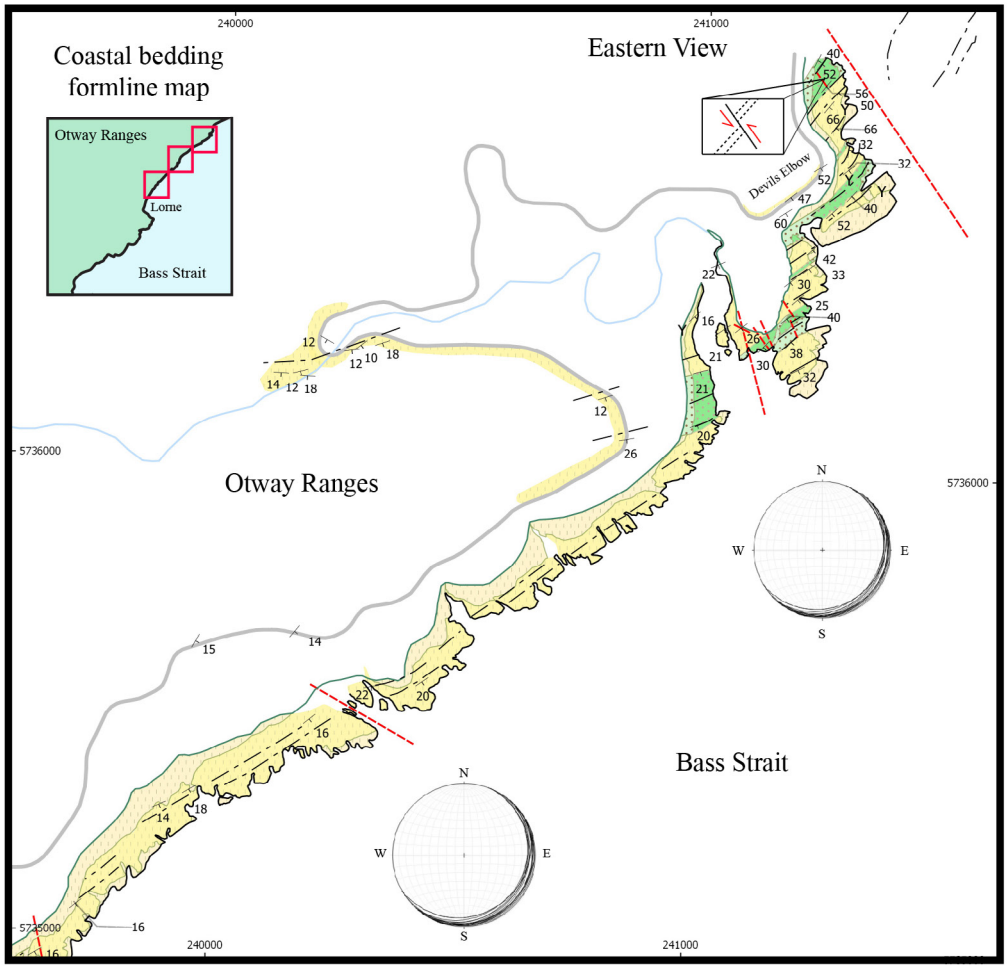
Coastal bedding
formline map
Otway Ranges
Lorne
Bass Strait
Eastern View
Devils Elbow
Otway Ranges
Bass Strait
240000
241000
5736000
5735000
N
S
E
W

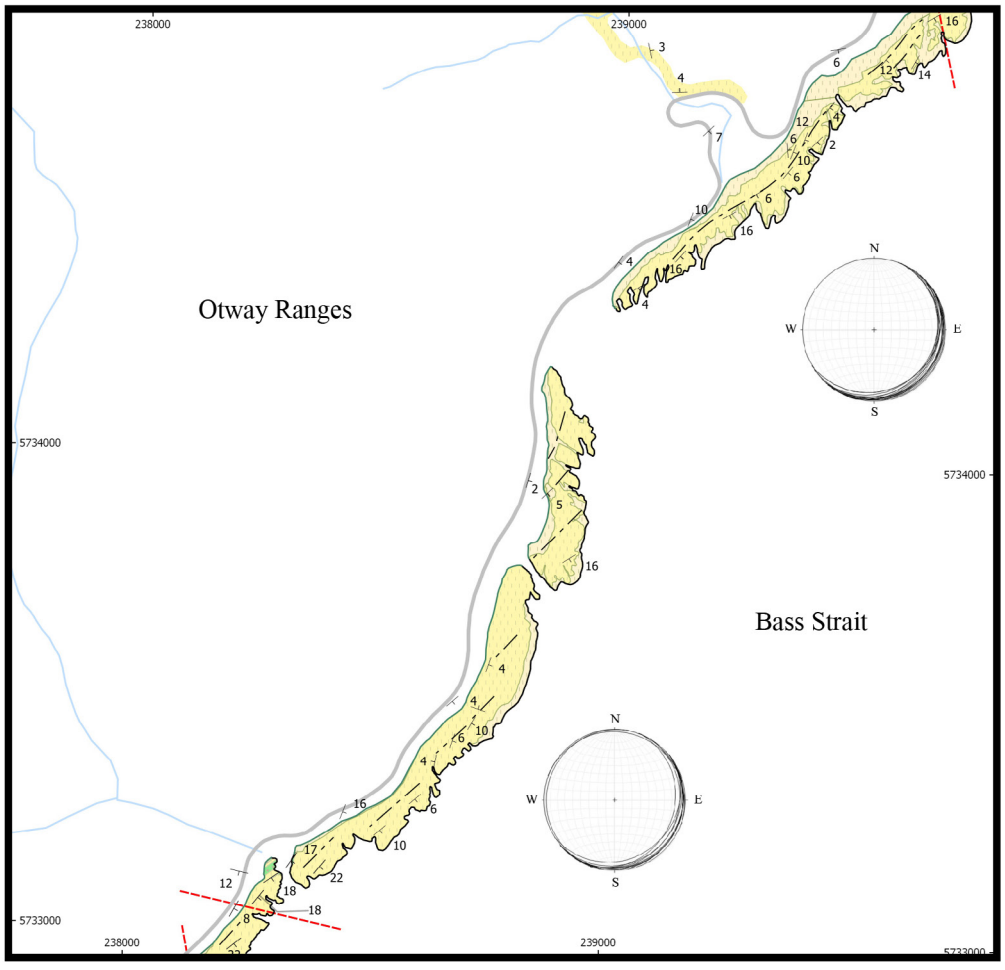
Otway Ranges
Bass Strait
238000
239000
5734000
5733000
N
S
E
W

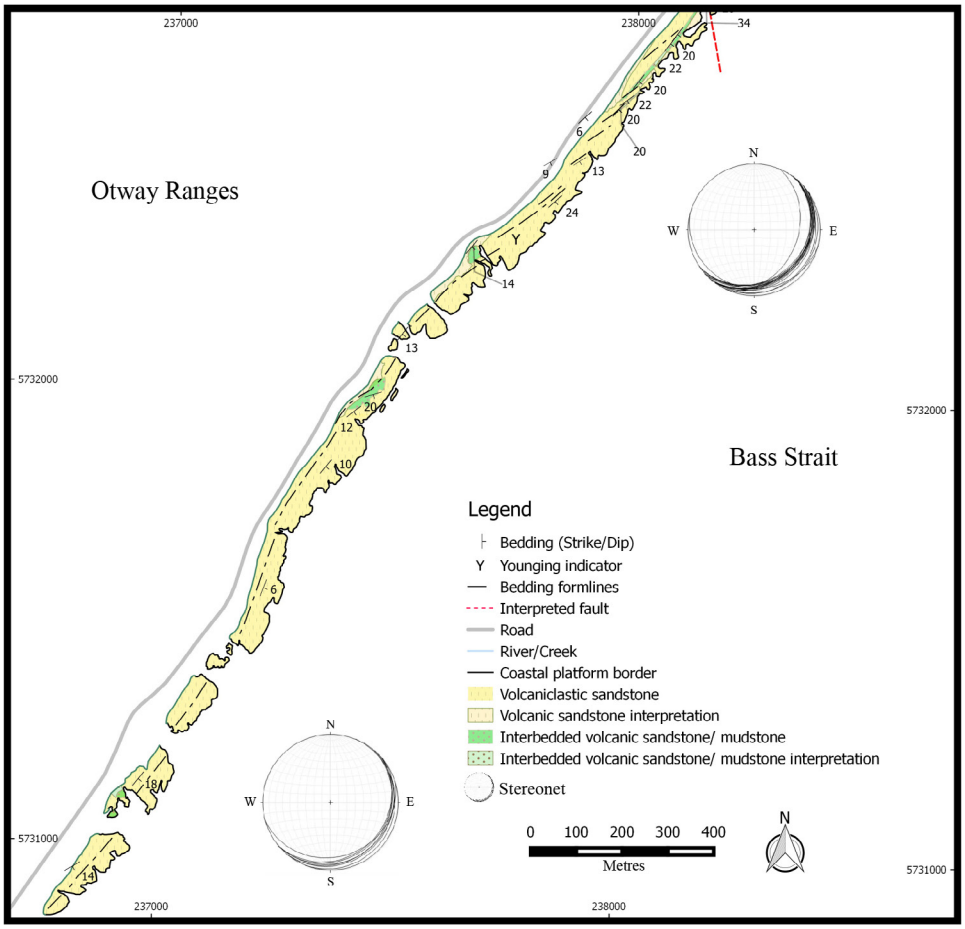
Otway Ranges
Bass Strait
237000
238000
5732000
5731000
Legend
Bedding (Strike/Dip)
Younging indicator
Bedding formlines
Interpreted fault
Road
River/Creek
Coastal platform border
Volcaniclastic sandstone
Volcanic sandstone interpretation
Interbedded volcanic sandstone/ mudstone
Interbedded volcanic sandstone/ mudstone interpretation
Stereonet
0 100 200 300 400
Metres
N
W
E
S

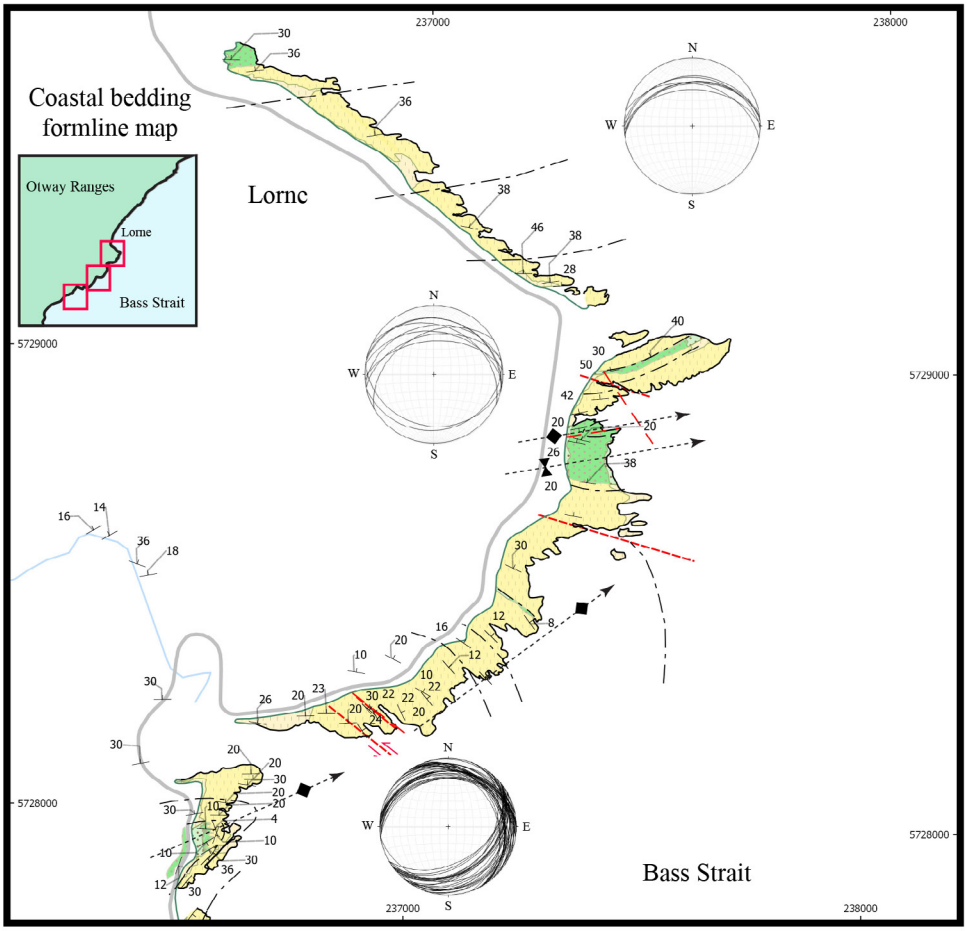
Coastal bedding formline map
Otway Ranges
Lorne
Bass Strait
Lornc
Bass Strait
237000
238000
5729000
5728000
N
W
E
S

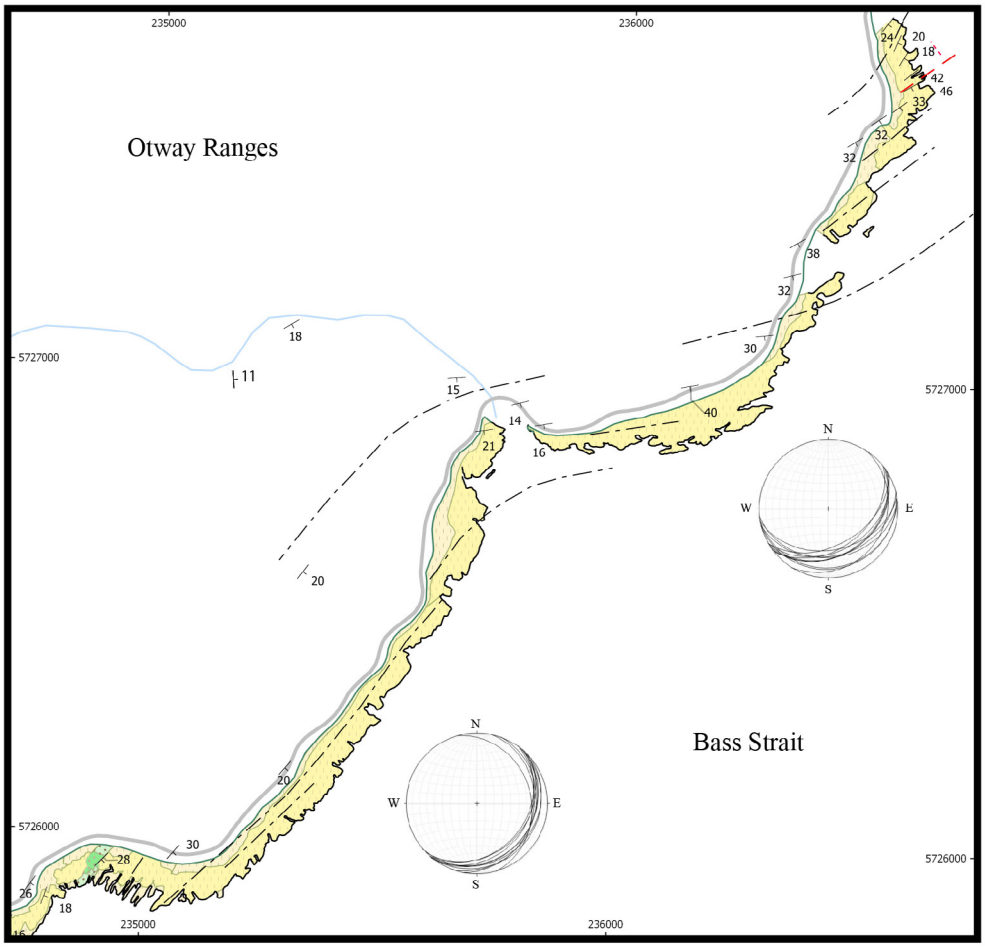
Otway Ranges
Bass Strait
235000
236000
5727000
5726000

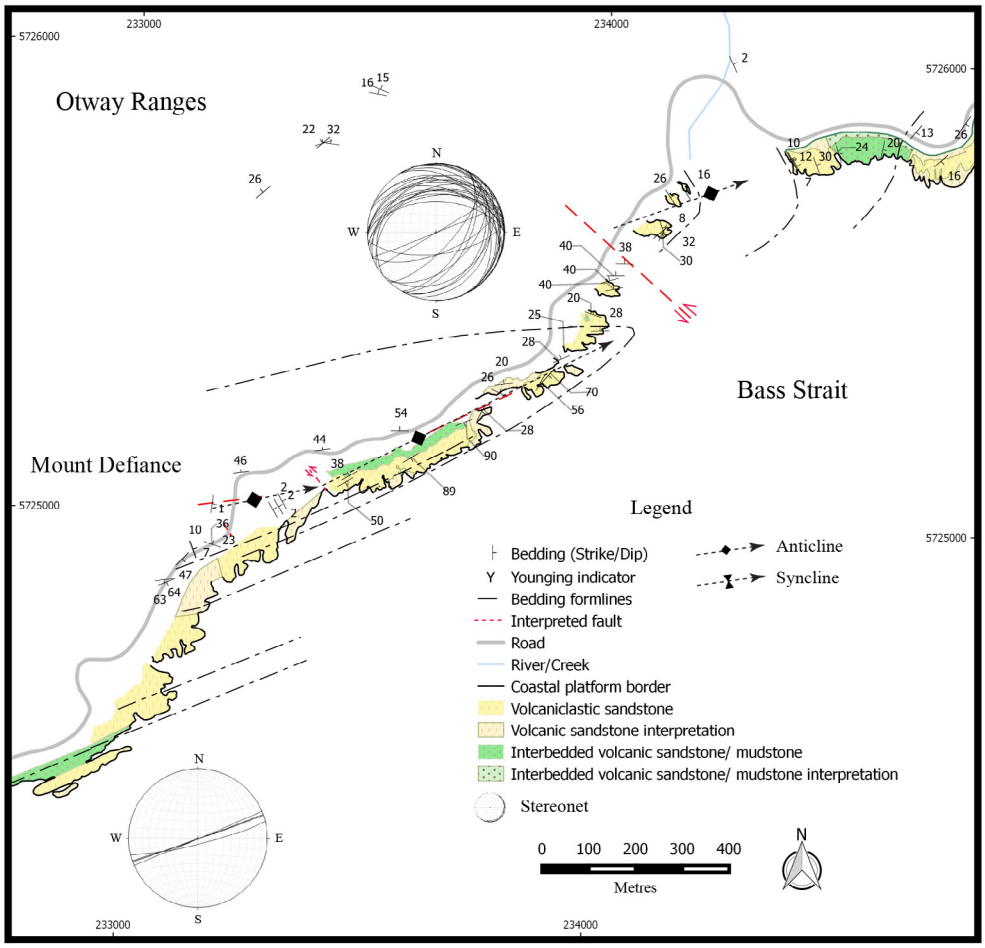
Otway Ranges
Mount Defiance
Bass Strait
Legend
Bedding (Strike/Dip)
Younging indicator
Bedding formlines
Interpreted fault
Road
River/Creek
Coastal platform border
Volcaniclastic sandstone
Volcanic sandstone interpretation
Interbedded volcanic sandstone/ mudstone
Interbedded volcanic sandstone/ mudstone interpretation
Stereonet
Anticline
Syncline
0 100 200 300 400
Metres
233000
234000
5726000
5725000

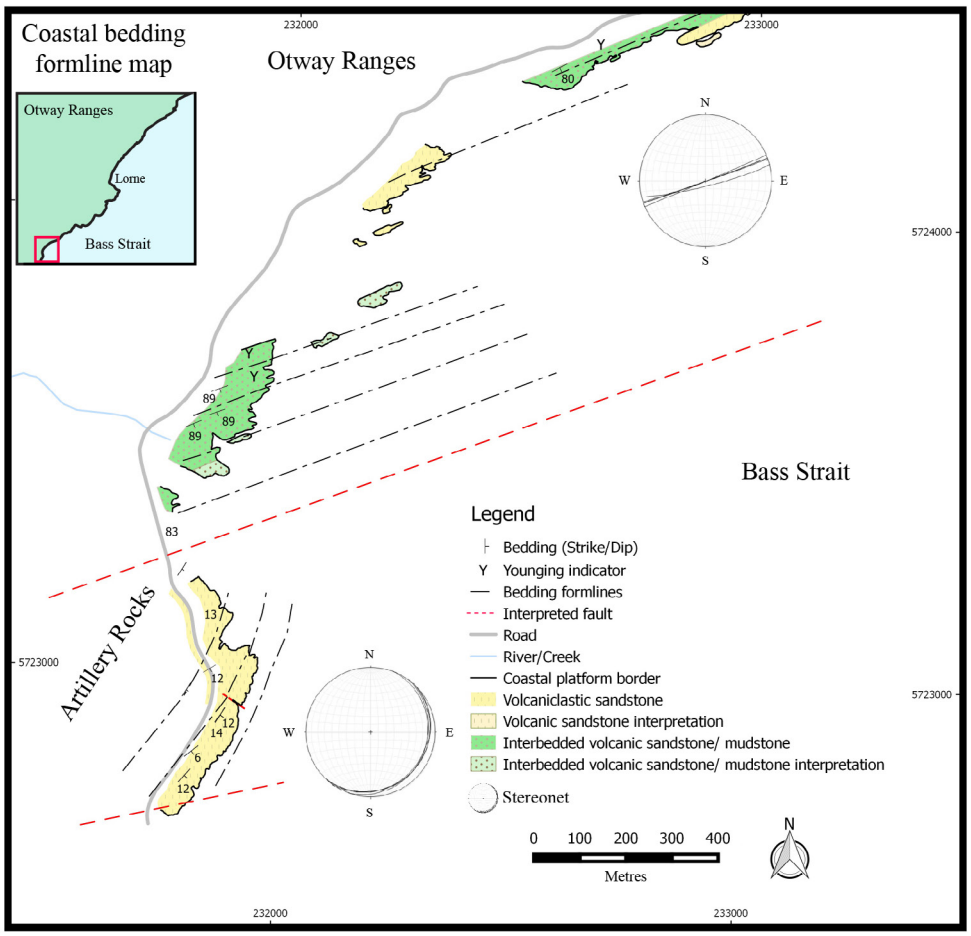
Coastal bedding formline map
Otway Ranges
Lome
Bass Strait
Otway Ranges
232000
233000
5724000
5723000
Bass Strait
Artillery Rocks
N
W
E
S
Legend
Bedding (Strike/Dip)
Younging indicator
Bedding formlines
Interpreted fault
Road
River/Creek
Coastal platform border
Volcaniclastic sandstone
Volcanic sandstone interpretation
Interbedded volcanic sandstone/ mudstone
Interbedded volcanic sandstone/ mudstone interpretation
Stereonet
0 100 200 300 400
Metres

(Top left to bottom right)

Coastal section from Split Point to Urquharts Bluff

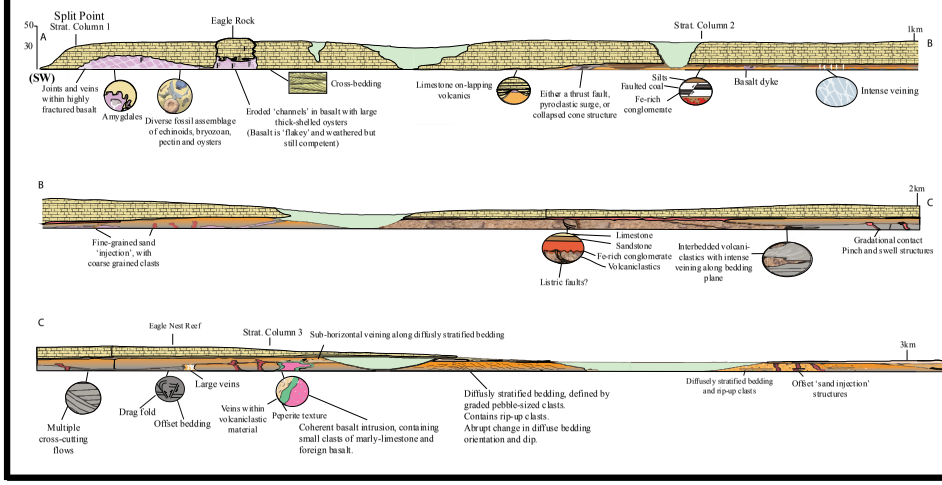


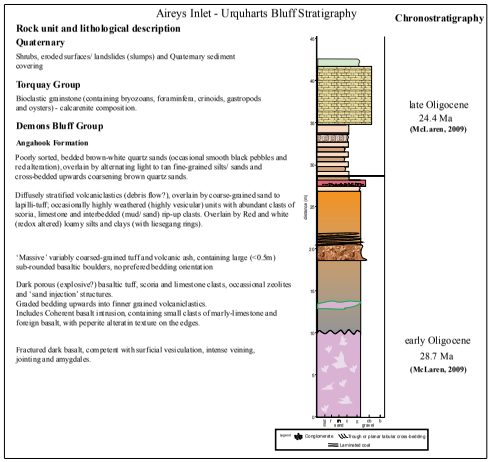


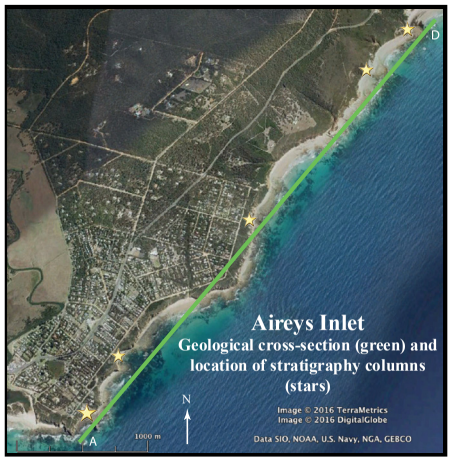

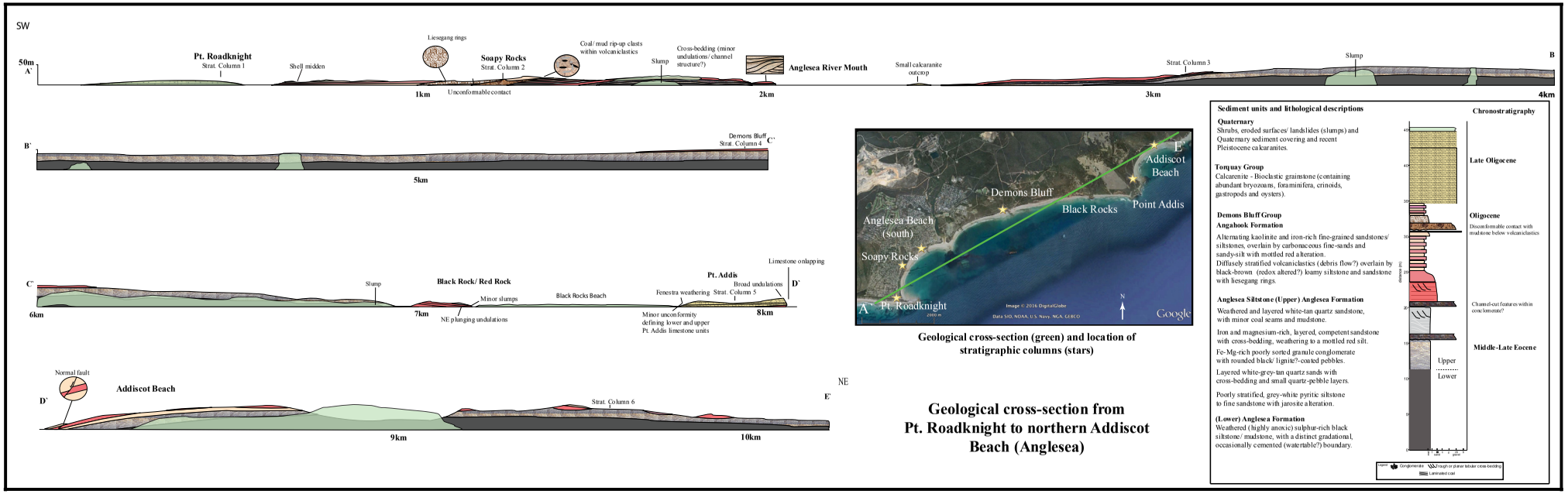


Geological cross-section (green) and location of stratigraphic columns (stars)

# Geological cross-section from Pt. Roadknight to northern Addiscot Beach (Anglesea)